

Code Qualification of Structural Materials for AFCI Advanced Recycling Reactors

Nuclear Engineering Division

About Argonne National Laboratory

Argonne is a U.S. Department of Energy laboratory managed by UChicago Argonne, LLC under contract DE-AC02-06CH11357. The Laboratory's main facility is outside Chicago, at 9700 South Cass Avenue, Argonne, Illinois 60439. For information about Argonne and its pioneering science and technology programs, see www.anl.gov.

Availability of This Report

This report is available, at no cost, at <http://www.osti.gov/bridge>. It is also available on paper to the U.S. Department of Energy and its contractors, for a processing fee, from:

U.S. Department of Energy

Office of Scientific and Technical Information

P.O. Box 62

Oak Ridge, TN 37831-0062

phone (865) 576-8401

fax (865) 576-5728

reports@adonis.osti.gov

Disclaimer

This report was prepared as an account of work sponsored by an agency of the United States Government. Neither the United States Government nor any agency thereof, nor UChicago Argonne, LLC, nor any of their employees or officers, makes any warranty, express or implied, or assumes any legal liability or responsibility for the accuracy, completeness, or usefulness of any information, apparatus, product, or process disclosed, or represents that its use would not infringe privately owned rights. Reference herein to any specific commercial product, process, or service by trade name, trademark, manufacturer, or otherwise, does not necessarily constitute or imply its endorsement, recommendation, or favoring by the United States Government or any agency thereof. The views and opinions of document authors expressed herein do not necessarily state or reflect those of the United States Government or any agency thereof, Argonne National Laboratory, or UChicago Argonne, LLC.

Code Qualification of Structural Materials for AFCI Advanced Recycling Reactors

Prepared for
U.S. Department of Energy
Reactor Campaign

K. Natesan¹, M. Li¹, S. Majumdar¹, R.K. Nanstad², and T.-L. Sham²

¹Nuclear Engineering Division, Argonne National Laboratory

²Oak Ridge National Laboratory

September 2008

Prepared by:

Principal Author



Ken Natesan

Reviewed by:

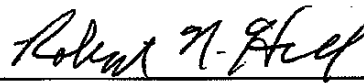
AFCI Work Package Manager



Ken Natesan

Approved by:

AFCI Campaign Manager



Robert N. Hill

Approved by:

Acting Director, Fuel Cycle Research and
Development

Robert Price

EXECUTIVE SUMMARY

This report summarizes the further findings from the assessments of current status and future needs in code qualification and licensing of reference structural materials and new advanced alloys for advanced recycling reactors (ARRs) in support of Advanced Fuel Cycle Initiative (AFCI). The work is a combined effort between Argonne National Laboratory (ANL) and Oak Ridge National Laboratory (ORNL) with ANL as the technical lead, as part of Advanced Structural Materials Program for AFCI Reactor Campaign. The report is the second deliverable in FY08 (M505011401) under the work package “Advanced Materials Code Qualification”.

The overall objective of the Advanced Materials Code Qualification project is to evaluate key requirements for the ASME Code qualification and the Nuclear Regulatory Commission (NRC) approval of structural materials in support of the design and licensing of the ARR. Advanced materials are a critical element in the development of sodium reactor technologies. Enhanced materials performance not only improves safety margins and provides design flexibility, but also is essential for the economics of future advanced sodium reactors. Code qualification and licensing of advanced materials are prominent needs for developing and implementing advanced sodium reactor technologies. Nuclear structural component design in the U.S. must comply with the ASME Boiler and Pressure Vessel Code Section III (Rules for Construction of Nuclear Facility Components) and the NRC grants the operational license. As the ARR will operate at higher temperatures than the current light water reactors (LWRs), the design of elevated-temperature components must comply with ASME Subsection NH (Class 1 Components in Elevated Temperature Service). However, the NRC has not approved the use of Subsection NH for reactor components, and this puts additional burdens on materials qualification of the ARR. In the past licensing review for the Clinch River Breeder Reactor Project (CRBRP) and the Power Reactor Innovative Small Module (PRISM), the NRC/Advisory Committee on Reactor Safeguards (ACRS) raised numerous safety-related issues regarding elevated-temperature structural integrity criteria. Most of these issues remained unresolved today. These critical licensing reviews provide a basis for the evaluation of underlying technical issues for future advanced sodium-cooled reactors.

Major materials performance issues and high temperature design methodology issues pertinent to the ARR are addressed in the report. The report is organized as follows: the ARR reference design concepts proposed by the Argonne National Laboratory and four industrial consortia were reviewed first, followed by a summary of the major code qualification and licensing issues for the ARR structural materials. The available database is presented for the ASME Code-qualified structural alloys (e.g. 304, 316 stainless steels, 2.25Cr-1Mo, and mod.9Cr-1Mo), including physical properties, tensile properties, impact properties and fracture toughness, creep, fatigue, creep-fatigue interaction, microstructural stability during long-term thermal aging, material degradation in sodium environments and effects of neutron irradiation for both base metals and weld metals. An assessment of modified versions of Type 316 SS, i.e. Type 316LN and its Japanese version, 316FR, was conducted to provide a perspective for codification of 316LN or 316FR in Subsection NH. Current status and data availability of four new advanced alloys, i.e. NF616, NF616+TMT, NF709, and HT-UPS, are also addressed to identify the R&D needs for their code qualification for ARR applications. For both conventional and new alloys, issues related to high temperature design methodology are described to address the needs for improvements for the ARR design and licensing. Assessments have shown that there are significant data gaps for the full qualification and licensing of the ARR structural materials. Development and evaluation of structural materials require a variety of experimental facilities that have been seriously degraded in the past. The availability and additional needs for the key experimental facilities are summarized at the end of the report. Detailed information covered in each Chapter is given below.

Chapter 2 describes the five pre-conceptual designs of the ARR proposed by the Argonne National Laboratory and the four industrial consortia selected by the DOE, namely, EnergySolutions, General Atomics, General Electric-Hitachi, and the International Nuclear Recycling Alliance (INRA) led by AREVA and Mitsubishi Heavy Industries (MHI). The current reference designs are sodium-cooled reactors with an outlet temperature in the range of 500-550°C targeted for a design life of 60 years. The main design parameters of these five design concepts are summarized in Chapter 2. It should be noted that the ARR design has not been formally selected. There are incomplete information and uncertainties regarding recommended structural materials for each major component and the corresponding operating conditions (temperature, expected dose and dose rate, loading, pressure, sodium flow rate, etc). Nevertheless, structural materials of interest in all reference designs are austenitic stainless steels (e.g. 316 SS) and low-Cr and high-Cr ferritic steels. The materials assessments presented in this report are based on our best knowledge at the time.

Chapter 3 summarizes the major code qualification and licensing issues pertinent to the ARR. In the preliminary report submitted in February 2008 entitled “Preliminary Assessment of Code Qualification for ABR Structural Materials”, issues raised by the NRC/ACRS during licensing of CRBRP and PRISM were thoroughly reviewed as well as the ASME Section III Subsection NH. Thirteen major issues with regard to material performance and high temperature design technology relevant to the ARR were identified, based on existing experience and the proposed ARR designs. Creep, creep-fatigue, creep ratcheting, and environmental effects are considered the most life-limiting factors in the ARR high temperature structural integrity. Safety issues and concerns associated with liquid sodium exposure are unique to ARR structural materials. A 60-year service life and possible extension beyond presents a significant challenge to materials selection and high temperature design methodology. The ASME Code currently does not provide guidelines that deal with environmental effects (sodium and neutron irradiation) on structural materials. These effects must be considered in licensing by the NRC.

Chapter 4 reviews the existing database for the ASME Code-qualified structural materials. Five materials are currently included in Subsection NH, namely, Type 304 SS, Type 316 SS, 2.25Cr-1Mo, mod.9Cr-1Mo (Grade 91), and Alloy 800H. ARR candidate structural materials fall primarily in two classes, austenitic stainless steels and ferritic steels. Four of the five code-qualified materials, Type 304 and Type 316 stainless steels, low-alloy steel, 2.25Cr-1Mo, and ferritic/martensitic steel, mod.9Cr-1Mo (Grade 91) are reviewed, and their available data are summarized. Material properties that were evaluated include physical properties, tensile properties, impact properties and fracture toughness, creep, fatigue, creep-fatigue, ASME allowables for both base metals and weld metals. Current knowledge of long-term thermal aging effects, effects of sodium exposure, and neutron irradiation effect on materials performance is also assessed. Particular attention is paid to Type 316 SS and Grade 91, two most promising structural alloys for advanced sodium reactor applications in the near-term.

Regarding low-alloy 2.25Cr-1Mo steels, there is a comprehensive database particularly for environmental effects in sodium. There is also extensive industrial experience including nuclear reactor applications. However, 2.25Cr-1Mo steels have inferior high temperature strength and corrosion resistance in sodium environments compared with high-Cr ferritic/martensitic steels, and has been increasingly replaced by high-strength high-Cr steels, in both conventional power plants and in advanced nuclear reactor systems.

The Grade 91 steel has significantly improved high temperature strength and creep resistance compared with 2.25Cr-1Mo steels. It allows thinner wall sections and therefore lower thermal stresses. There is a large database of mechanical performance, microstructural stability, joining technologies, etc for Grade 91. Nevertheless, most of these data have been developed and applied to thermal power boilers, of which materials are subjected to different temperature, loading and environmental conditions from what is expected in the ARR. For the ARR components that are often subjected to high-

temperature, sodium exposure, neutron irradiation and cyclic thermal transients, the structural material is required to have excellent creep-fatigue resistance, sufficient fracture toughness, good sodium compatibility and radiation-tolerance. One of the major differences in dealing with low alloy steels and high-Cr ferritic steels is the microstructural sensitivity of high-Cr steels. It should be noted that the superior properties of Grade 91 depend largely on the creation of precise microstructure of tempered martensite and precipitate particles that give rise to high temperature strength and creep resistance. Failure to maintain such microstructure during fabrication and heat treatments and throughout the service life would seriously degrade the high temperature properties of the materials, and these issues have caused severe failures in the field. The exposure of Grade 91 steel to high temperature for long periods of time can lead to significant microstructural changes, resulting in degradation in mechanical performance, particularly the embrittlement. The microstructural stability, ductility, and toughness are especially required for pipes where leak-before-break has to be ensured. Fracture toughness property is directly related with the leak-before-break characteristics of components and pipes. Long-term thermal aging data are needed for potential embrittlement during long-term service. Some neutron irradiation data are available for Grade 91 from fusion reactor materials programs and previous liquid-metal fast breeder reactor programs.

The emphasis of fusion reactor programs, however, was on the low-temperature irradiation embrittlement in Grade 91. Irradiation data at temperatures specific to the ARR designs are needed. Corrosion damage in Grade 91 in sodium may not be significant based on limited experience. More data on high-Cr F-M steels in sodium are needed to draw firm conclusions. Decarburization/carburization and their effect on mechanical properties may be a more significant issue especially for components to be exposed in sodium for times up to 60 years. R&D on sodium effects in high-Cr F/M steels is required to provide design data and a better understanding that will be needed during licensing. Special consideration should be given to Grade 91 welds and the heat affect zones (HAZs). The microstructure variations and stability in the weldments create complex issues in Grade 91, more so in large-size components. Premature Type IV cracking in the HAZs is a life-limiting failure mechanism. The causes and controls of Type IV cracking need to be well understood, and the issue should be adequately addressed in the design rules. Creep-fatigue data are also lacking for Grade 91 weldments.

Austenitic stainless steels have been widely used in nuclear industry. There is an extensive database and industrial experience for both Type 304 and 316 stainless steels. Knowledge of their performance in sodium reactors is quite extensive as well. Compared to high-Cr F-M steels, austenitic stainless steels have better sodium compatibility, better microstructural stability, smaller heat variations, less sensitive to heat treatments, better control of quality of weldments, and ample experience with their applications in irradiation environments. However, austenitic stainless steels have lower thermal conductivities and higher thermal expansion coefficients, and therefore exhibit high thermal stresses in thick-wall components. Austenitic stainless steels are also more expensive than ferritic steels. For the ARR operating environments, there are few unresolved performance issues in Type 316SS. The primary need for the full qualification and licensing of 316SS for ARR applications is the assessment of their performance for times up to 60 years, especially for the environmental effects of sodium and neutron irradiation. The NRC in their licensing reviews of sodium-cooled reactors raised concerns on sensitization and stress corrosion cracking, carburization, and degradation in sodium in 316SS. These issues need to be addressed in licensing of the ARR.

Chapter 4 also discussed Type 316LN and 316FR (Japanese version of 316LN), small variations to conventional Type 316 SS with lower carbon and higher nitrogen content. Type 316LN and 316FR have higher mechanical strength, good combination of strength and toughness, better resistance to stress corrosion cracking and hot cracking, good compatibility with sodium environment, less prone to irradiation damage of both base metal and weld metal over conventional Type 316SS. 316FR is a prime candidate for structural applications for reactor vessel and internals in the Japanese Sodium Fast Reactors.

Type 316LN is a favorable structural alloy in European fast reactors, and a major structural alloy in fusion reactors (e.g. the International Thermonuclear Experimental Reactor). A comprehensive database exists for Type 316LN and 316FR from the international fast and fusion reactor materials programs. Type 316LN is qualified in the French RCC-MR code. Strong interest has been expressed by the Japanese Fast Reactor Team to qualify 316FR in the ASME Code for elevated temperature structural use in advanced reactors.

Chapter 5 focuses on the four advanced alloys recently selected by the AFCI Advanced Structural Materials Program. They are advanced ferritic/martensitic steels, NF616 and NF616+TMT, and advanced austenitic stainless steels, NF709 and HT-UPS. These alloys offer excellent high temperature strength and creep resistance over the conventional ferritic and austenitic steels. As they are relatively new, the database of these alloys is limited, far from what is needed for nuclear reactor applications. Among these four alloys, NF616 and NF709, two commercially available materials, have been developed for fossil-fired power plants for improved high temperature performance, and they have relatively broader databases and industrial experience. Data are lacking for these steels in sodium environments and after neutron irradiation. The data on the effects of sodium environment are practically zero. Another important aspect is their microstructural stability over long-term periods under high temperature, sodium and neutron exposure. As the excellent high temperature strength and creep resistance of these advanced alloys all rely on stable, fine, and uniformly-distributed precipitate particles, phase stability and phase transformation is a key issue for their applications. In fact, data of long-term thermal aging and of neutron irradiation have already shown inferior impact properties and fracture toughness of NF616. The special thermomechanical treatment in NF616 is believed to be effective in further improvement of its high temperature strength. However, the long-term performance of thermomechanically treated NF616 is uncertain and should be thoroughly investigated. The advanced austenitic alloy HT-UPS (high-temperature, ultrafine precipitation-strengthened) was initially developed for fusion reactor applications. Program was cancelled before testing was completed. The alloy then found its applications in turbine recuperators and in steam tubing in fossil-fired ultrasupercritical steam plants. The development of HT-UPS is still at the early stage, and the available data are very limited.

Chapter 6 addressed a number of prominent issues related to high temperature design methodology. The NRC licensing review of the CRBRP identified a number of concerns covering nine areas including weldment safety evaluation, notch weakening effect, inelastic analysis, elastic follow-up in piping, creep-fatigue evaluation, plastic strain concentration factors, steam generator tubesheet evaluation, intermediate piping transition weld, and elevated-temperature seismic effects. The NRC also expressed significant concerns of environmental effects (sodium and neutron exposure) on material performance. It is critical to build confidence in the regulatory community and show adequate safety margins in the ARR designs. A review of these safety concerns and how Subsection NH currently addresses these issues is presented in Chapter 6. The review will serve as a foundation to initiate communications with the NRC in licensing of the ARR.

Material performance issues and high temperature design methodology issues and the data needs identified above will require extensive testing and evaluation in ARR-specific environments of temperature, loading, irradiation and sodium exposure. Lack of experimental facilities in the U.S. for the development and evaluation of ARR structural materials is a key issue in qualification of advanced materials. A variety of test facilities are needed, including fast-spectrum irradiation facility, general radiological test facility, sodium test facility, creep-fatigue facility, etc. Chapter 7 summarizes the current status and additional needs for the research capability in the sodium reactor technology area. International collaboration for access to experimental reactors and sodium facilities overseas and data sharing can provide a valuable and cost-effective means, and is essential for the near-term deployment of advanced sodium reactor technology.

Based on extensive assessments of material data base and high temperature design methodology issues related to the ARR reactor designs, R&D needs for code qualification and licensing of structural materials are identified and strategies for meeting these needs are discussed.

The priority of the materials code qualification tasks in FY09 will be given to the code-qualified materials with the focus on 316 SS (and its variant, 316L(N) and 316FR) and mod.9Cr-1Mo. Based on the thorough assessment of mechanical properties, weldments, and environmental effects, it is concluded that 316 SS and mod.9Cr-1Mo are the most promising currently available alloys among the Subsection NH materials for the ARR structural applications. The large database and wide industrial experience on these two types of alloys have set a reliable path to their full qualification and licensing of the first reactor and therefore, ultimate utilization in near-term ARRs.

A number of issues remain in the areas of materials performance database and high temperature design methodology for both Type 316 SS and mod.9Cr-1Mo. The FY09 activities will focus on several major safety-related issues. The work plans for addressing these issues are:

- Creep-fatigue evaluation of weldments
 - Review and assess weldment database
 - Conduct creep-fatigue tests to fill the data gaps
 - Develop and verify simplified analysis methodology
 - Review and assess current weldment design rules in the ASME, MCC-MR, and Japanese Codes
 - Address and mitigate Type IV cracking in F-M steels and environmental effects
- Creep-fatigue evaluation in flawed specimens
 - Develop technology of surface treatments to produce realistic surface imperfections
 - Creep-fatigue testing of pre-treated flawed specimens
 - Evaluation and assessment of the effects of surface imperfections on creep-fatigue life
 - Develop flaw evaluation methods to address life prediction
- Assessment of material degradation in sodium environments
 - Thermodynamic and kinetic modeling of the tendency and extent of transfer of nonmetallic elements (C, N, O) under ARR-relevant conditions
 - Assessment of materials database for sodium service
 - Modeling compatibility and mechanical performance in sodium and model validation
 - Prediction of material degradation in sodium for a 60-year design life
- Material property design allowables for a 60-year design life
 - Review and assess current database
 - Identify data needs that impact design rules in ASME Code
 - Develop material property models
 - Confirmatory lab testing

This page is intentionally left blank

CONTENTS

EXECUTIVE SUMMARY.....	iii
1. INTRODUCTION	1
2. PRE-CONCEPTUAL DESIGN OF THE ARR	3
2.1 Introduction	3
2.2 Summary of Key Plant Design Parameters for the ARR	3
2.3 ANL Conceptual Design	3
2.4 EnergySolutions Pre-Conceptual Design	7
2.5 GE-Hitachi Pre-Conceptual Design	7
2.6 General Atomics Pre-Conceptual Design	10
2.7 INRA Conceptual Design.....	10
3. CODE QUALIFICATION AND LICENSING ISSUES FOR THE ARR	11
4. REFERENCE ALLOYS.....	15
4.1 List of Reference Alloys	15
4.2 Austenitic Stainless Steels.....	16
4.2.1 Type 316 Stainless Steel.....	16
4.2.2 Effects of Long-term Thermal Aging	26
4.2.3 Effects of Sodium Exposure	33
4.2.4 Effects of Neutron Irradiation.....	44
4.2.5 316FR and 316LN Stainless Steels.....	54
4.3 Low-Alloy and Ferritic-Martensitic Steels	62
4.3.1 2.25Cr-1Mo Steels	62
4.3.2 Mod.9Cr-1Mo Steel.....	69
4.3.3 Effects of Long-term Thermal Aging	79
4.3.4 Effects of Sodium Exposure	83
4.3.5 Effects of Neutron Irradiation.....	99
4.3.6 Weldments	104
4.3.7 Industrial Experience	109
5. NEW ADVANCED ALLOYS for ARR.....	111
5.1 Selection of Candidate Advanced Alloys.....	111
5.2 NF616.....	112
5.2.1 Base Metal Properties	113
5.2.2 Effects of Long-term Thermal Aging	118
5.2.3 Effects of Sodium Exposure	120
5.2.4 Effects of Neutron Irradiation.....	120
5.2.5 Weldments	121
5.2.6 ASME Code Acceptance	123
5.2.7 Industrial Experience	124
5.3 NF616 + TMT	124
5.4 NF709.....	124
5.4.1 Basic Metal Properties	125

5.4.2	Effects of Long-term Thermal Aging	125
5.4.3	Effects of Sodium Exposure	126
5.4.4	Effect of Neutron Irradiation	126
5.4.5	ASME Code Acceptance	126
5.5	HT-UPS	127
6.	HIGH TEMPERATURE DESIGN METHODOLOGY	129
6.1	Creep-Fatigue Design Rules.....	129
6.1.1	Background on Design Rules Development.....	129
6.1.2	Eddystone Impact	130
6.1.3	Other Approaches Considered.....	131
6.1.4	DOE/ASME Materials Project	133
6.1.5	Creep-Fatigue Code Rule Improvement.....	136
6.2	Weldment Design Methodology	137
6.3	Notch Weakening Effect	138
6.4	Inelastic Design Procedures for Piping	139
6.5	Thermal Striping Design Methodology.....	140
6.6	Buckling	140
6.7	Ratcheting Design Rules	141
6.8	Flaw Assessment Procedures	144
6.8.1	Background.....	144
6.8.2	R5 Procedure	144
6.8.3	A16 Procedure of RCC-MR	145
6.8.4	DOE/ASME Materials Project	145
6.8.5	Required R&D and Testing	146
6.9	Data Extrapolation to 60 Years	146
7.	EXPERIMENTAL FACILITIES	149
7.1	Material Irradiation Facilities.....	149
7.1.1	Domestic Irradiation Facilities	149
7.1.2	International Irradiation Facilities	154
7.2	Radiological Materials Test Facilities.....	164
7.2.1	Facility at Argonne National Laboratory.....	164
7.2.2	Facility at Idaho National Laboratory.....	165
7.2.3	Facility at Oak Ridge National Laboratory.....	165
7.3	Sodium Facility for Materials Testing	166
7.4	Creep-Fatigue Test Facility.....	169
7.4.1	Fatigue and Crack Growth Test Facility at ANL.....	169
7.4.2	Creep-Fatigue Test Facility at INL.....	169
7.4.3	Mechanical Property Test Facility at ORNL	169
8.	SUMMARY.....	171
8.1	Material Data Needs for Reference Alloys	171
8.2	Material Data Needs for New Advanced Alloys.....	174
8.3	High Temperature Design Methodology Needs.....	176
	REFERENCES.....	179

ACRONYMS

ACRS	Advisory Committee on Reactor Safeguards
AFCI	Advanced Fuel Cycle Initiative
AGF	Alpha-Gamma Facility
ALMR	Advanced Liquid Metal Reactor
ANL	Argonne National Laboratory
ARR	Advanced Recycling Reactor
ASME	American Society of Mechanical Engineers
ATR	Advanced Test Reactor
CAMEL	Components and Materials Evaluation Loop
CEA	Atomic Energy Commission
CGHAZ	Coarse Grain Heat Affected Zone
CRBRP	Clinch River Breeder Reactor Project
CRIEPI	Central Research Institute of Power Industry in Japan
CVN	Charpy V-notch
DBTT	Ductile-brittle Transition Temperature
DOE	Department of Energy
dpa	Displacement Per Atom
DWTSG	Double-wall Tube Steam Generator
ECCC	European Creep Collaborative Committee
EDM	Electric Discharge Machine
EM	Electromagnetic
EML	Electron Microcopy Laboratory
EPRI	Electric Power Research Institute
EXIR	Ex-vessel Irradiation Rig
FATT	Fracture Appearance Transition Temperature
FCAW	Flux Cored Arc Welding
FFTF	Fast Flux Test Facility
FGHAZ	Fine Grain Heat Affected Zone
F-M	Ferritic-martensitic
FMF	Fuel Monitoring Facility
FN	Ferrite Number
FP	Fission Product
GE	General Electric
GMAW	Gas Metal Arc Welding
GNEP	Global Nuclear Energy Partnership
GTAW	Gas Tungsten Arc Welding
HAZ	Heat Affected Zone
HCEF	Hot Cell Examination Facility
HFR	High Flux Reactor

HFIR	High Flux Isotope Reactor
HIP	Hot Isostatic Pressing
HSIS	Hydraulic Shuttle Irradiation System
HT	Hydraulic Tube
HT-UPS	High Temperature-Ultrafine Precipitate-Strengthened
HVEM	High Voltage Electron Microscope
ICHAZ	Inter-critical Heat Affected Zone
IFEL	Irradiated Fuels Examination Laboratory
IHTS	Intermediate Heat Transport System
IHX	Intermediate Heat Exchanger
IMET	Irradiated Materials Examination and Testing
IML	Irradiated Materials Laboratory
INL	Idaho National Laboratory
INRA	International Nuclear Recycling Alliance
JAES	Japan Atomic Energy Agency
JDFBR	Japanese Demonstration Fast Breeder Reactor
JSFR	Japanese Sodium-cooled Fast Reactor
LAMDA	Low Activation Materials Design and Analysis
LBB	Leak Before Break
LMFBR	Liquid Metal Fast Breeder Reactor
LMP	Larson-Miller Parameter
LWR	Light Water Reactor
MARICO	Material Testing Rig with Temperature Control
MHR	Modular Helium Reactor
MMF	Material Monitoring Facility
MOTA	Materials Open Test Assembly
MOX	Mixed oxide
MPH	Materials Properties Handbook
NFAs	Nanostructured Ferritic Alloys
NGNP	Next Generation Nuclear Plant
NIMS	National Institute of Material Science
NRC	Nuclear Regulatory Commission
NSFU	National Scientific User Facility
ODS	Oxide Dispersion Strengthened
ORNL	Oak Ridge National Laboratory
PCHE	Printed Circuit Heat Exchanger
PHTS	Primary Heat Transport System
PIE	Post Irradiation Examination
PRISM	Power Reactor Innovative Small Module
PPT	Peripheral Target
R&D	Research and Development

RB	Removable Beryllium
RIS	Radiation Induced Segregation
RPV	Reactor Pressure Vessel
SAW	Submerged Arc Welding
SEM	Scanning Electron Microscope
SG	Steam Generator
SG-ETD	Subgroup on Elevated Temperature Design
SMAW	Shielded Metal Arc Welding
SPTL	Sodium Plugging Test Loop
SSRT	Slow-Strain-Rate Tensile Testing
TEM	Transmission Electron Microscope
TRIGA	Training Research Isotope General Atomics
TRU	Transuranic
UNIS	Un-instrumented Fuel Irradiation Subassembly
UPR	Upper Core Structure Irradiation Plug Rig
USE	Upper Shelf Energy

This page is intentionally left blank

CODE QUALIFICATION OF STRUCTURAL MATERIALS FOR AFCI ADVANCED RECYCLING REACTORS

1. INTRODUCTION

The objectives of the Advanced Fuel Cycle Initiative (AFCI) are to expand the use of nuclear energy to meet the increasing global energy demand and to address the nuclear waste management. Reactor campaign is part of the AFCI to develop advanced recycling reactor (ARR) technologies for commercial use in a closed nuclear fuel cycle in the United States. The campaign is focusing on the sodium-cooled reactor concept because of its technical maturity. The current needs are for larger, more reliable, more economical reactors suitable for commercial nuclear power generation. Research and development focuses on three areas including advanced materials, innovative components and systems, and computer models and simulation.

Economical competitiveness is a key element in the development of advanced reactor technologies. Advanced materials allow compact and simple design of sodium cooling systems and reactor structure, and have the potential to reduce the construction and operational costs for sodium reactors. Heat-, corrosion- and irradiation-resistant alloys are being selected based on economics, reliability, and flexibility of the ARR design. The AFCI Advanced Materials under Reactor Campaign is responsible for developing materials for improved economics, reliability, safety, and design flexibility. The code qualification of Advanced Materials is in support of the ARR design, licensing, and construction activities.

The ARR must demonstrate the technical reliability to obtain a NRC construction and operating license. Nuclear structural component construction in the U.S. complies with the ASME Boiler and Pressure Vessel Code Section III and NRC grants the construction/operation license for the nuclear plant. As the ARR is a sodium-cooled reactor with an outlet temperature of 500-550°C and a 60-year design life, significantly different from the current light water reactors (LWRs), the design of elevated-temperature components must comply with ASME Section III Subsection NH and also must consider time-dependent effects on mechanical properties such as, creep, creep-fatigue, and creep ratcheting. At present, NRC has not approved Subsection NH for high-temperature structural design. The NRC licensing review of the Clinch River Breeder Reactor Project (CRBRP) and the Power Reactor Innovative Small Module (PRISM) project identified a number of technical issues covering nine areas including weldment safety evaluation, notch weakening effect, creep-fatigue evaluation, etc., and many of these issues currently remain unresolved. A review of all the safety issues relevant to Subsection NH and how Subsection currently addresses these issues is required. The review will serve as a foundation to initiate communications with the NRC on these issues.

Subsection NH provides the high temperature design rules for components in nuclear service. The rules were developed in support of the U.S. liquid metal fast breeder reactor (LMFBR) program in 1960s and 70s. Subsection NH has a rather limited choice of materials with only five materials qualified that include Types 304 and 316 austenitic stainless steels, 2.25Cr-1Mo steel, modified 9Cr-1Mo, and Alloy 800H. For these code-qualified alloys, long-term performance and safety-related issues raised by the NRC must be addressed adequately for their applications. The unique environmental conditions of thermal, sodium, and neutron irradiation in the ARR pose a significant challenge to materials selection, development, code qualification, and licensing, particularly for the proposed 60-year design life. To expand the material choice for ARR applications, such as new creep-resistant advanced austenitic stainless steels and high-Cr ferritic/martensitic steels, significant R&D efforts are needed to test, evaluate,

and validate the materials performance in relevant ARR environments. In addition to providing design data for qualification and licensing, high temperature design rules must also be developed to account for high temperature damages such as creep rupture, excessive creep deformation, creep buckling, cyclic creep ratcheting, and creep fatigue and consider environmental effects. Qualification and licensing of both conventional and advanced materials for successful and long-life applications in the ARR environment represents a major component of the ARR Advanced Materials R&D Program.

An initial assessment of materials' qualification and licensing needs was conducted in the first half of FY08. A preliminary report of "Preliminary Assessment of Code Qualification for ABR Structural Materials" was issued in February 2008.

In the current report, detailed assessment of R&D needs for licensing of ASME Code-qualified materials and qualification and licensing of current and advanced alloys is addressed. This report also addresses several of the issues that were raised by NRC/ACRS in licensing of CRBRP and PRISM. Efforts in the DOE initiative to address ASME code issues are also discussed. Major ASME Code and licensing issues relevant to ARR are identified. This report also presents current knowledge of environmental effects (sodium and neutron irradiation) on code-qualified materials and addresses major degradation processes and mechanisms. A strategic plan for code qualification of current and potential new advanced materials is developed.

2. PRE-CONCEPTUAL DESIGN OF THE ARR

2.1 Introduction

The Advanced Recycling Reactor is designed to transmute the recycled transuranics to produce energy while also reducing the long-term radiotoxicity and decay-heat loading in the repository. The primary objectives of the prototype ARR are (1) to demonstrate reactor-based transmutation of transuranics, (2) to qualify the transuranics-containing fuels and advanced structural materials needed for a full-scale ARR, and (3) to support R&D and demonstration required for certification of an ARR standard design by the NRC. Additional objectives include (1) incorporation and demonstration of innovative design concepts and features, (2) demonstration of improved technologies for safeguards and security, and (3) the support of development of the design, fabrication and construction, testing and deployment of systems, structures and components infrastructure for the ARR in the U.S. Based on these objectives, a pre-conceptual design for an advanced recycling test reactor was developed by Argonne National Laboratory (ANL), and a report was issued in 2006 (ANL-ABR-1 2006).

Four industry teams were selected by the U.S. Department of Energy (DOE) in 2007 to further develop pre-conceptual designs, technology development roadmaps, and business plans and to provide industry perspectives for potential deployment and commercialization of recycling and reactor technologies in the U.S. The four industry consortia are *EnergySolutions*, General Atomics, General Electric-Hitachi, and the International Nuclear Recycling Alliance (INRA), led by AREVA and Mitsubishi Heavy Industries. The U.S. DOE released detailed reports and presentations developed by the four industry consortia on May 28, 2008. The reports describe pre-conceptual designs, including cost and schedule for an initial nuclear fuel recycling center and advanced recycling reactor.

A critical review of available ARR conceptual designs has been conducted. The following sections summarize the key plant design parameters in various design concepts, followed by the description of the conceptual designs of the ANL and the four industrial consortia.

2.2 Summary of Key Plant Design Parameters for the ARR

The key plant design parameters for the ARR concept proposed by ANL and four industrial consortia are summarized in Table 2.1. All designs incorporate passive shutdown and decay heat removal features.

2.3 ANL Conceptual Design

Based on the pre-conceptual ARR design, the major structural components can be grouped into (1) reactor system and primary containment boundary, (2) primary heat transport system, (3) intermediate heat transport system, (4) secondary heat transport system, and (5) power conversion system. A schematic view of the primary system is shown in Figure 2.1 (ANL-ABR-1 2006).

Reactor System and Primary Containment Boundary

In the ANL design, the reactor vessel has an inside diameter of 18 ft (≈ 5.5 m), height of 44 ft (≈ 13.4 m), and a wall thickness of 2 in (≈ 50 mm) and it contains the entire primary radioactive sodium inventory. There is no penetration planned in the reactor vessel wall. Components such as the intermediate heat exchanger (IHX), pumps, piping, instrumentation, etc., penetrate the primary enclosure through the top-deck structure. There are no axial welds in the reactor vessel wall. Circumferential welds

Table 2.1. Key design parameters for the ARR concepts.

Key Parameters	ANL Design	Industrial Teams			
		EnergySolutions	GE-Hitachi (PRISM)	GA (ARR)	INRA
Reactor Power	380 MWe	410 MWe	311 MWe	285 MWe	500 MWe
Reactor type	Pool	Pool	Pool	?	Two-loop
Fuel	Metal; Backup: Oxide	Metal; Backup: MOX	Metal	Metal	Oxide
Cladding material	HT-9	HT-9	HT-9	?	ODS ferritic steel
Coolant	Sodium	Sodium	Sodium	Sodium	Sodium
Coolant Outlet/Inlet	510/355°C	550/395°C	499/360°C	?	?
Reactor Vessel Size	5.8 m dia, 14.8 m H	10.5 m ID 20.5 m H	5.74 m dia, 16.9 m H	?	?
Reactor Vessel Material	Austenitic SS	?	316 SS	?	
IHX Design	Tube-Shell	No IHX	Tube-Shell	?	
IHX Material	?		304 SS	?	
Piping	?	?	Single wall	?	Double wall
Piping material	?	?	2.25Cr-1Mo	?	High- Cr steel
Steam Generator Design	?	Double wall, straight/helical	Helical coil	?	Straight double wall
Steam Generator Material	?	?	2.25Cr-1Mo	?	High-Cr steel
Structural and Piping Material	Austenitic stainless steel	?	316 SS	?	?
Primary Pump	4 EM pumps; Backup: mechanical (centrifugal)	4 EM pumps	Two EM pumps	?	?
Power Conversion Cycle	Rankine steam cycle Backup: CO ₂ Brayton cycle	Rankine steam cycle	Rankine steam cycle	?	?
Plant life	30 yr with expectation of 60-yr extension	60 yr	60 yr	60 yr	60 yr
Critical Path	?	Licensing and Economics	Licensing and Commercialization	?	Technology and Licensing

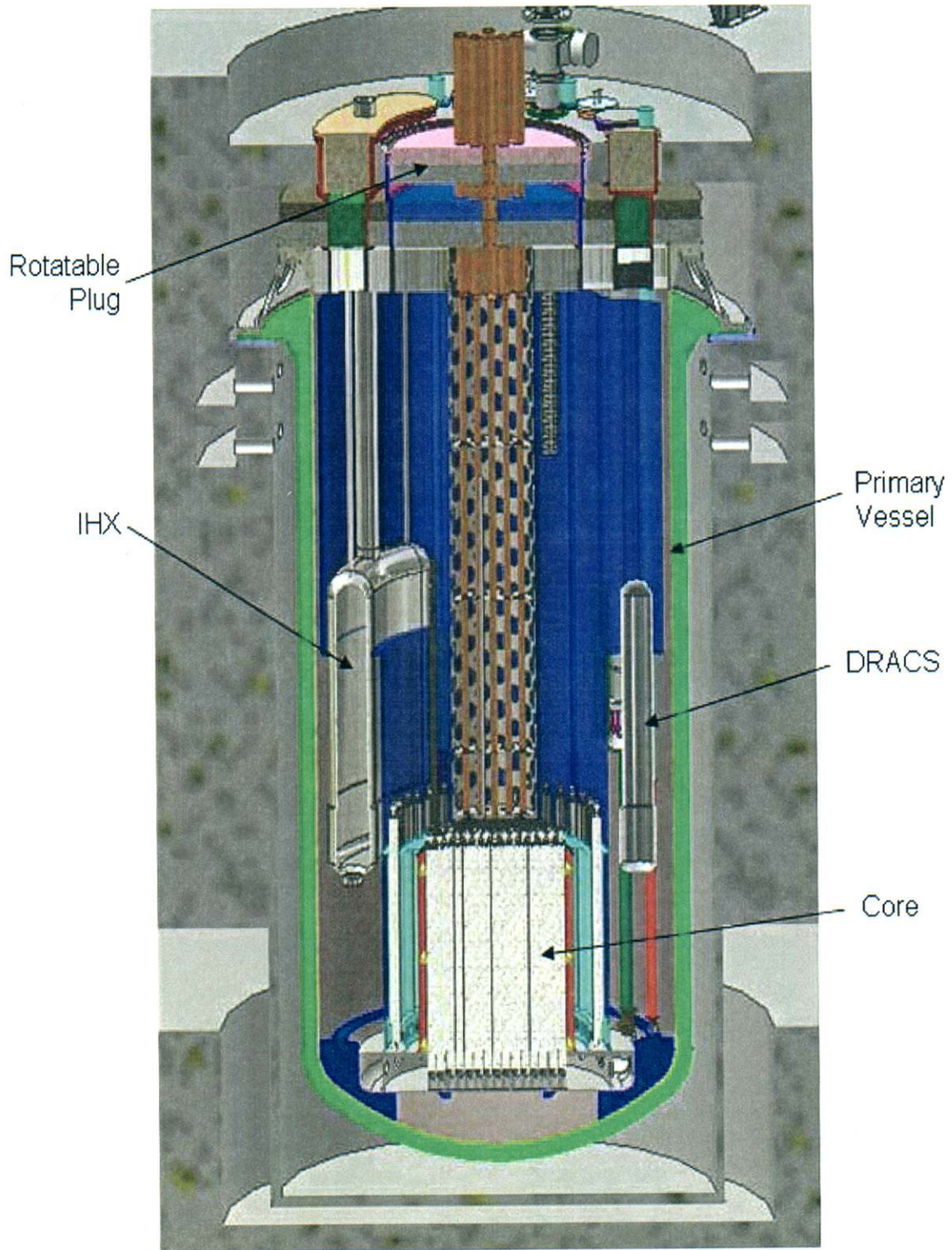


Figure 2.1. Schematic view of primary system in the ANL design (ANL-ABR-1 2006).

will be needed, if the vessel is assembled from ring forgings. The primary sodium coolant outlet temperature is 510°C but most of the reactor pressure vessel (RPV) is at the sodium inlet temperature of 355-410°C. The upper part of the RPV and its cover are in contact with high temperature sodium and the

rules of construction will be based on ASME Code Section III Subsection NH. In addition to the RPV, the structural components of the reactor system include the vessel enclosure, a rotatable plug for the reactor head, the guard vessel, and the core support structure. Austenitic stainless steel was selected for the construction of the reactor vessel and the guard vessel.

The primary containment boundary consists of the reactor vessel, the reactor vessel enclosure, and the IHX tubes. In the case of a breach of the primary containment, the secondary containment comes into play and the containment boundary includes the guard vessel, the reactor containment, the intermediate sodium piping, and the sodium to steam or CO₂ heat exchangers, and others.

Primary Heat Transport System

There are four primary pumps with flexibility to adopt both mechanical and electromagnetic pumps in the ANL design. However, for the rotating-shaft mechanical pump option, there is a need for penetrations through the RPV.

There are two IHXs, which adopt the conventional and well-tested shell-and-tube design, with the primary sodium flow inside the shell and the secondary sodium flow inside the tube. The tube has an outer diameter of 0.625 in (≈ 15.9 mm) and a wall thickness of 0.035 in (≈ 0.89 mm). The pressure drop is expected to be low and is of the order of 0.006 MPa. The ID of the shell and the OD of the tube will be at the temperature of the primary coolant which is at $\approx 500^\circ\text{C}$. This elevated temperature requires the ferritic and austenitic steels to perform in thermal creep regime. Internal piping is used for the mechanical pump option but is not required for the electromagnetic pump option.

Intermediate Heat Transport System

Rankine steam cycle is being considered in the ANL design for power generation, with supercritical CO₂ Brayton cycle being considered as an alternate option. Steam generators with helical coils, similar in design to the PRISM, will be used for the Rankine cycle. The printed-circuit heat exchangers (PCHE) are being considered for the Brayton cycle. The pressure of the secondary sodium is slightly higher than that for the primary sodium.

Power Conversion System

For the reference Rankine steam cycle, the structural components and the associated environment are listed in Table 2.2.

Table 2.2. Structural components and associated environment for the Rankine steam cycle.

Structural Component	Environment
Steam generator shell	Secondary sodium (502-344°C)
Steam generator tubing	Water or steam inside (287-482°C at ≈ 11 MPa) Secondary sodium outside (502-344°C)
Hot-leg steam piping	Steam (482°C)
Cold-leg steam piping	Treated water (287°C)
Steam turbine	Steam

For the alternate supercritical CO₂ Brayton cycle, the structural components and the associated environments are listed in Table 2.3.

Table 2.3. Structural components and associated environment for supercritical CO₂ Brayton cycle.

Structural Component	Environment
Compressor	CO ₂ , moisture, high pressure
Turbine generator	CO ₂ , moisture, high pressure
Sodium to CO ₂ heat exchanger	CO ₂ , moisture, high pressure
Recuperator	CO ₂ , moisture

2.4 EnergySolutions Pre-Conceptual Design

The Advanced Recycling Reactor in the EnergySolutions design will be a sodium-cooled, pool type reactor with a power output of 410 MWe (EnergySolutions 2008). The principal considerations in the ARR design are proliferation resistance, timeliness, economics, safety, and fuel technology. The pertinent details are listed in Table 2.1.

The reactor vessel has an inner diameter of 10.5 m, and a length of 20.5 m. The reactor cover is a hot deck structure. All major primary system components are located inside the vessel. The outlet temperature is 550°C, and the inlet temperature 395°C. Four electromagnetic (EM) pumps are used to circulate the primary sodium coolant.

A double-walled tubing heat exchanger is designed to eliminate the “secondary” sodium loop and thus to reduce the capital cost. Primary system heat is transferred directly to the steam-generating loop.

The steam generator is a helical coil type double-wall tube steam generator (DWTSG), which uses double wall tube with wire mesh between the two concentric tubes with continuous leak detection. Four DWTSG units are installed in the ARR primary vessel.

2.5 GE-Hitachi Pre-Conceptual Design

The GE-Hitachi pre-conceptual design for the ARR is based on the GE Power Reactor Innovative Small Module (PRISM) reactor. The PRISM was a modular, pool-type, sodium cooled reactor. The PRISM design was initiated and studied by GE in the early 1980s. It was the reference design for the DOE-sponsored Advanced Liquid Metal Reactor (ALMR) program. The PRISM design was submitted to the NRC for review and approval. The NRC issued a final Pre-application Safety Evaluation Report for PRISM (Donoghue, et al. 1994) and concluded that no impediments could be identified to prevent future licensing at the level of the PRISM conceptual design. The PRISM construction was stopped due to an abrupt cancellation of the DOE-ALMR program in the mid-1990s. The pertinent system details are listed in Table 2.1.

The major components and systems in the GE-PRISM reactor are summarized as below (GE-Hitachi 2008).

Reactor Vessel and Closure Head

The reactor vessel has an outer diameter of 5.74 m, a height of 16.9 m, and a thickness of 5.08 cm, made of Type 316 stainless steel. The vessel has no penetrations and provides the support for all of

the internal components along with all primary sodium and part of the intermediate heat transport system. All containment penetrations are provided only through the closure head. The vessel closure head is a 0.3 m-thick steel plate with a rotatable plug for refueling, and with penetrations for the primary coolant pumps, the IHX system, and instrumentation and hardware. The closure head and the rotatable plug are designed to operate at relatively low temperatures (<422K). The high-temperature design rules are not required for the closure head and the rotatable plug.

Primary Heat Transport System

The primary heat transport system (PHTS) is contained entirely within the reactor vessel. There are four EM primary pumps to circulate the primary coolant through the core. The heat from the PHTS is transferred to the intermediate heat transport system (IHTS) through the intermediate heat exchanger (IHX). There are two IHXs of shell-and-tube design made from Type 304 SS. The primary sodium flows inside the shell and the secondary sodium flows inside the tube.

Intermediate Heat Transport System

The IHTS transfers heat to the water-steam system through the steam generator (SG). The main components are the tube side of the IHX, the shell side of the SG, the intermediate sodium pump with an auxiliary motor, IHTS piping, and IHTS isolation valves. The IHTS piping is connected to the steam generator through a below-grade pipeway. The IHTS piping is enclosed in a guard pipe to contain possible sodium leaks. The steam generator is made of 2.25Cr-1Mo steel and is 20.42 m high and 3.66 m in diameter. It contains 323 single-walled tubes of 3 cm OD and 2.67 mm in wall thickness.

In the ARR design provided by the GE-Hitachi, new features and design improvements that have been developed include:

1. A compact IHTS design arrangement in which the reactor, the IHTS, and the steam generator system (including the sodium water reaction pressure relief subsystem) are located on a seismically isolated platform.
2. A permanent refueling enclosure for each reactor module.
3. Increased cycle efficiency that is achieved by increasing the mixed mean core outlet temperature to 499°C and the core inlet temperature to 360°C. The net power for a three power-block arrangement is increased to 1,866 MWe.
4. Replacement of the flexible skirt reactor support with sliding brackets attached to the closure to accommodate reactor closure head thermal expansion and seismic and accident loads.
5. Adoption of an improved un-vented duct design for fuel assemblies.
6. Increase of the refueling interval, between 12 to 24 months.
7. Adoption of a superheat steam cycle (2,135 psia/452°C) to increase the net efficiency of the plant. The resulting changes included:
 - a. Adoption of a helical coil tube once through superheated steam generator.
 - b. Deletion of a steam drum and recirculation pump.
 - c. Addition of an auxiliary vessel and startup recirculation pump to allow startup and shutdown heat removal under forced and naturally circulating recirculation conditions.
 - d. Addition of a topping heater to maintain desired feedwater temperature to the steam generator during part load conditions.
 - e. Deletion of water dump subsystem and reaction products separator tank due to the reduced water inventory in the steam generator system.
 - f. Deletion of the high-pressure feedwater heater and two moisture-separator reheaters and associated piping.

- g. Deletion of the blowdown flash tank and cooler and associated piping.
- h. Smaller low pressure feedwater heaters, condenser, and turbine generator.
- i. Replacement of two horizontal sodium dump tanks with one vertical tank.
- 8. Replacement of the unitized turbine generator building design with a totally enclosed turbine generator building arrangement.
- 9. Replacement of the single mechanical pump for the IHTS with two electromagnetic pumps, similar in design to the primary pump.
- 10. Improvements in IHTS piping design to better accommodate seismic and sodium-water reaction events, including a reduction of the rupture disk pressure to 135 psig.
- 11. Adoption of a rail mounted, large component cask transporter with tilt-up mechanisms and side-to-side cask positioning capability.
- 12. Increase in the number of cells in the cooling tower from 8 to 10.
- 13. Use of S-PRISM containment system.

The reactor module of the new design is shown in Figure 2.2 (GE-Hitachi 2008). It consists of the reactor vessel, reactor closure, containment vessel, internal structures, internal components, reactor module supports, and reactor core.

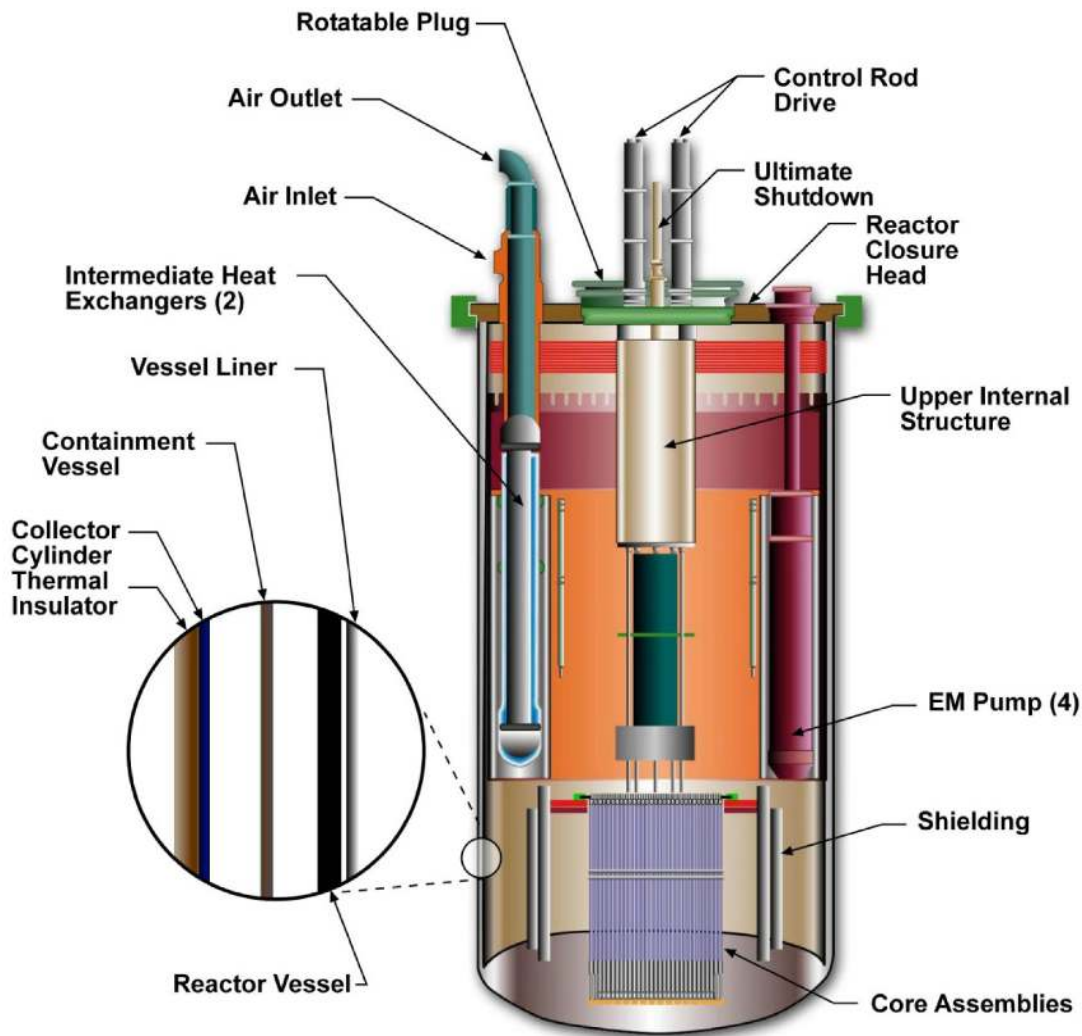


Figure 2.2. PRISM reactor module (GE-Hitachi 2008).

2.6 General Atomics Pre-Conceptual Design

Three scenarios have been proposed by the General Atomics for closing and commercializing the nuclear fuel cycle in the US. These scenarios are (General Atomics 2008):

Scenario A: TRU from LWR spent fuel is processed through an ARR to reduce the waste for depository; this is considered as the standard AFCI fuel cycle.

Scenario B: A two-tier reactor system. LWR spent fuel is sent to the Modular Helium Reactors (MHR) to extract electricity. The MHR spent fuels will have reduced quantity of plutonium and minor actinides, and will then be burned in an ARR with recycle to reduce the TRU waste transfer to the repository.

Scenario D: A similar two-tier system but in this case the MHRs gradually replacing the retiring Gen III LWRs to supply the electricity and satisfy growing non-electricity applications for nuclear energy. The ARR is used to reduce the waste to the repository and eventually to provide new fissile fuel for the growing nuclear industry.

Scenario D is reported as the preferred choice of the GA team. The ARR design in the GA proposal is a sodium reactor with metal fuel. No other design information was disclosed. The pertinent details are listed in Table 2.1.

2.7 INRA Conceptual Design

The INRA ARR design was based on the Japan Atomic Energy Agency's Sodium-Cooled Fast Reactor (JSFR). It is a sodium-cooled, fueled by oxide, 2-loop reactor with a power output of 500 MWe (see Fig. 2.3). Thirteen major technology enhancements have been proposed to achieve the economics, safety, and reliability required for a commercial ARR facility (INRA 2008). The IHX will be integrated with the primary pump and the primary piping will be double-walled structure, made of high-strength high-Cr steel. The steam generator will consist of straight double-walled high-Cr steel tubes. The pertinent details are listed in Table 2.1.

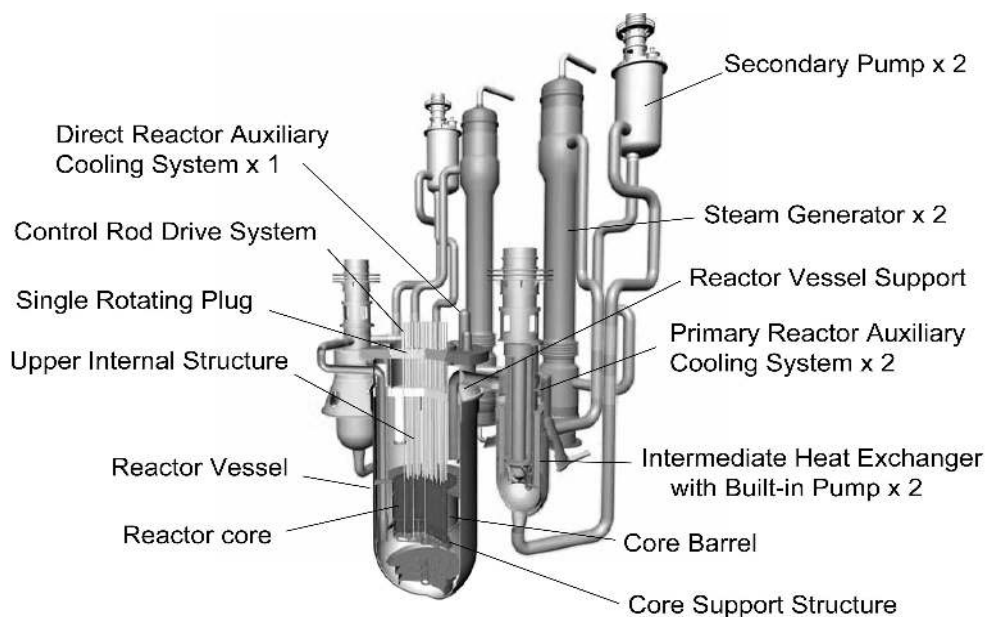


Figure 2.3. The ARR Design by INRA (INRA 2008).

3. CODE QUALIFICATION AND LICENSING ISSUES FOR THE ARR

An extensive review was conducted to identify the major code qualification and licensing issues pertinent to the ARR, and the findings were summarized in a report issued in February 2008 (Natesan et al. 2008). The review was based on the NRC licensing reviews of the CRBRP and PRISM projects, the ASME Subsection NH, and the DOE-NGNP Initiative on the ASME Code. Thirteen major issues relevant to ARR were identified, and are summarized below:

- *Materials property allowable data/curves for 60 year design life*

Subsection NH is applicable to the design life of only up to 34 years (300,000 h). The PRISM and future advanced reactor systems will be designed with a projected life of 60 years. It is essential to develop/modify the material acceptance criteria based on available data and incorporate this information into ASME Code to extend Code allowable stress values to at least 60 years. This issue was investigated in Task 1 of the DOE Code initiative for two Subsection NH code materials, Grade 91 steel and Alloy 800H and their associated weldments. Recommendations have been made on what allowable stresses can be extended to 60 years and what additional testing requirements are needed to extend the remaining allowable stresses to 60 years for these two materials. This effort paves the way to addressing this issue for other Subsection NH coded materials and new advanced structural materials.

- *Validated weldment design methodology*

It is well recognized that lack of weldment-specific design criteria is an issue for advanced reactors. In review of the CRBRP, NRC identified early weldment cracking to be the foremost failure mode. NRC expressed concerns about enhanced creep crack growth in a cracked weldment and enhanced creep in the remaining uncracked wall caused by residual stress and thermal cycling, and effects of creep on stability of the remaining uncracked wall ligament.

Structural integrity of dissimilar metal transition joints was identified as another issue of concern. For example, the tri-metallic joints of the intermediate heat transport system in the CRBRP consisted of 316H S.S, Alloy 800H, and 2¼ Cr-1Mo steel. NRC requested a detailed evaluation of the transition joint, by taking into account the effects of creep, residual stress, and property differences between the component materials. Other types of transition joints such as austenitic to ferritic steels are a possible choice in future advanced reactors and complete information on transition joints need further development.

The weldment integrity is often controlled by numerous factors. There is lack of understanding as to which factors are of primary importance and how these factors should be included in the weld design methodology. NRC identified several areas regarding weldment integrity at elevated temperature that need further evaluation, including crack initiation in the heat-affected zone (HAZ) of the weldment exposed to cyclic sodium temperatures, creep-fatigue, and creep-rupture damage of weldments. Some strength reduction factors are included in Subsection NH. However, a significant amount of R&D is still required in this area. Efforts to address some of these issues are being initiated in Task 8 of the DOE Code initiative.

- *Reliable creep-fatigue design rules*

Creep-fatigue design rules are largely based on the bilinear creep-fatigue model (also called “creep-fatigue damage envelope” or “D diagram”). The idea is that the component lifetime limit is bounded by a linear summation of creep-time fraction and fatigue-cycle fraction in the assessment of the

total accumulated damage. This rule is empirical and often overly conservative. Not all structural materials follow this creep-fatigue rule. Improved and more reliable models need to be developed, validated, and integrated into the design process. Initial steps are being taken to address this issue in Task 10 of the DOE code initiative.

- *Hold time creep-fatigue data*

Creep-fatigue design rules are primarily based on short-time laboratory test data. Whether or not creep-fatigue damage will saturate with increasing hold time is unclear. It is recognized that reactor hold periods can be as long as up to 1500 h in liquid metal reactors. Long hold-time creep-fatigue test data are needed in developing creep-fatigue models and design rules. It should also be noted that loading sequence and waveform types are also important factors in determining creep-fatigue lifetime, particularly for weldments.

- *Improved mechanistically based creep-fatigue life predictive tools*

Given the extension of reactor life from 30 to 60 years, reliable extrapolation of short-term data to 60 years poses a significant challenge to the designers and the regulators. It is imperative to develop a mechanistic understanding of creep-fatigue damage under various loading conditions and to develop improved mechanism-based creep-fatigue life predictive models. These improved and more reliable models need experimental validation and proper integration into the design process.

- *Understanding/validation of notch weakening effects*

Notch weakening effect was listed as one of the key areas that should be resolved in the CRBRP review. Cracks at notches are similar to the situation in the weldment where material discontinuity can lead to high stress concentration. Stress raisers introduce a constraint against plastic deformation (notch strengthening effect) and can cause early crack initiation and rapid crack propagation (notch weakening effect). Overall effects of notches depend on geometry, loading, and material properties. Significant notch weakening is often found for long-term loading at high temperatures. However, design limits of the ASME Code for fatigue and creep rupture are all based on smooth specimen data, though factors accounting for notch effects have been included in the ASME Subsection NH. Confirmatory structural testing is needed to validate the design rules. Some of these issues, such as creep and creep-fatigue crack growth in structural discontinuities and welds, are being addressed in Task 8 of the DOE code initiative.

- *Methodology for analyzing Type IV cracking in 9Cr-1Mo weldment*

Type IV cracking in the HAZ of the weld can be a life-limiting failure mechanism. Type IV cracking often occurs at welded joints in creep-resistant steels, and it has been found to be prominent in 9-12% Cr steels. Cracking is due to enhanced creep void formation in the HAZ of the weld containing coarse carbide particles, leading to premature failure when compared with the base metal. Reduction in creep strength due to Type IV cracking needs consideration in design rules. As the cracking behavior depends on several factors including chemical composition, heat treatment, and the stress state, there has been no satisfactory method that allows for the estimation of Type IV cracking-limited creep rupture life.

- *Inelastic design procedures for piping*

The elastic follow-up concept was used in the “elastic” design rules to account for inelastic effects, particularly for creep strain concentrations in piping systems. Although “elastic follow-up” has been incorporated in the ASME Code, there is no clear definition and a standardized method agreed upon

in the design and regulatory communities. Elastic follow-up is often improperly used to describe plastic and creep concentrations in structural components and has caused confusion. There is a strong need to develop a validated procedure for assessing elastic follow-up and properly integrating it in Code rules.

- *Validated thermal striping materials and design methodology*

Thermal striping can be significant for internal structures in liquid metal reactors in the region where sodium flow streams from different subassemblies mix at the reactor outlet. NRC raised concerns of thermal striping in licensing review of both the CRBRP and the PRISM. There is lack of validated thermal striping materials and design procedures such as high-temperature crack growth methodology. Striping conditions need better characterization and need confirmatory structural testing to establish stress allowables.

- *Material degradation under irradiation*

Neutron embrittlement is of major concern when the components are exposed to neutron irradiation at high temperature over a long period (60 years). Particular attention should be paid on irradiation creep, helium embrittlement, and irradiation-assisted stress corrosion cracking. The ASME code and code cases do not address this important area. Significant efforts are required to develop methods and predictive models to estimate the degree of irradiation-induced degradation and to develop irradiation-tolerant materials for long term service. In review of the PRISM, NRC raised a question about not using real time irradiation data in the design process and the issue remains open.

- *Materials degradation under thermal aging*

The effects of thermal aging on mechanical properties over long term at elevated temperatures are poorly understood. Ductility loss and embrittlement due to formation of new phases have been reported in low-alloy steels, austenitic stainless steels, and bainitic and martensitic steels. Loss of creep strength at elevated temperatures is also reported for Mod.9Cr-1Mo steel, which occurs due to precipitation and coarsening of precipitate particles in the steel. Material performance envelope needs further development to establish material limits. “Knock-down” factors of allowable stresses should be included in the ASME Code to account for degradation from thermal aging. Appropriate “knock-down” factors should be based on aging data obtained in sufficiently long-term tests to validate extrapolation to 60-y lifetime.

- *Materials degradation in sodium environment*

There is insufficient understanding of material degradation due to corrosion over long-term exposure to sodium coolant. Besides general corrosion, several other important degradation mechanisms need to be considered, such as effects of interstitial element C, N, O transfer on mechanical properties, corrosion fatigue, stress corrosion cracking, irradiation-assisted stress corrosion cracking, and creep-fatigue damage. The ASME code and code cases do not provide specific guidelines for environmental effects but are definitely required for NRC licensing. Assessment of data and additional testing are needed to generate materials performance envelope and incorporate “knock-down” factors in design rules.

- *Degradation under sodium-water reaction*

In the PRISM conceptual design, steam generator tubes served as the boundary between the secondary sodium in the IHTS and the steam system. Interaction between sodium and water could occur as a result of steam generator tube rupture. Degradation under this sodium/water reaction should be

considered. The design must consider metal wastage rate, effects of leak rate, tube spacing, sodium temperature, wastage under jet impingement, and progression from small to large leak.

4. REFERENCE ALLOYS

4.1 List of Reference Alloys

Five alloys have been qualified for elevated temperature structural applications by the ASME Code Subsection NH, namely, Type 304 SS, Type 316 SS, 2.25Cr-1Mo, mod.9Cr-1Mo (Grade 91) and Alloy 800H. There has been extensive experimental and operational experience with most of these materials in liquid metal fast breeder reactors. Table 4.1a summarizes the structural applications of these alloys in previous sodium-cooled reactors worldwide, and Table 4-1b summarizes the Subsection NH materials and their allowables for design.

Table 4.1a. Materials used in past sodium-cooled reactors.

Country	Reactor	Vessel	IHX	Steam Generator	
				Evaporator	Superheater
USA	Fermi	304	304	Fe-2.25Cr-1Mo	Fe-2.25Cr-1Mo
	EBR-II	304	304	Fe-2.25Cr-1Mo	Fe-2.25Cr-1Mo
	FFTF	304	316	a	a
	CRBR	304	304	Fe-2.25Cr-1Mo	Fe-2.25Cr-1Mo
UK	DFR	316	316	321	321
	PFR	321	321	Fe-2.25Cr-1Mo	316H
Russia	BOR-60	304	304	Fe-2.25Cr-1Mo	Fe-2.25Cr-1Mo
	BN-350	304	304	Fe-2.25Cr-1Mo	Fe-2.25Cr-1Mo
	BN-600	304	304	Fe-2.25Cr-1Mo	304
Germany	SNR-300	304	Fe-2.25Cr-1Mo-Nb	Fe-2.25Cr-1Mo-Nb	Fe-2.25Cr-1Mo-Nb
France	Rapsodie	316L	316	a	a
	Phenix	316L	316	Fe-2.25Cr-1Mo	321
	SuperPhenix	316	316	Alloy 800 tubes 304, 316L shell	b
Japan	Joyo	304	304	a	a
	Monju	304	304	Fe-2.25Cr-1Mo	304

^asodium to air heat exchanger; ^bevaporator and superheater are combined in a single unit.

Table 4.1b. Materials included in Subsection NH and allowables.

Material	Temperature (°C)	
	Primary stress limits ^a	Fatigue
304	816	704
316	816	704
2.25Cr-1Mo	593 ^b	593
Mod.9Cr-1Mo	649	538
800H	760 ^b	760

^aAllowable stresses extend to 300,000 h (34 years).

^bTemperatures up to 649°C allowed for no more than 1000 h.

4.2 Austenitic Stainless Steels

Austenitic stainless steels have been widely used for fast breeder reactor applications, including reactor core, reactor vessel, grid plate, sodium piping, primary heat exchangers, and sodium pumps. Significant issues related to FBR structural applications identified by the NRC include erosion-corrosion and property degradation in sodium environment, effects of neutron embrittlement for a 60-year lifetime, sensitization and stress corrosion cracking at elevated temperatures, effects of secondary phases, hot cracking and creep-fatigue fracture. Austenitic stainless steels have high thermal expansion coefficient and low thermal conductivity, which limit their application in thick sections and under operating conditions that involve frequent shutdowns and variable power demands.

4.2.1 Type 316 Stainless Steel

Specifications

The specifications, product forms, types, grades, or classes of 316SS that are permitted in Subsection NH are listed in Table 4.2.

Table 4.2. Product forms of 316SS permitted under Subsection NH.

Permitted 316SS for Subsection NH [Notes (1) to (3)]		
Spec. No.	Product Form	Types, Grades, or Classes
SA-182	Fittings & Forgings	F 316, F 316H
SA-213	Seamless Tube	TP 316, TP 316H
SA-240	Plate	316, 316H
SA-249	Welded Tube	TP 316, TP 316H
SA-312	Welded & Seamless. Pipe	TP 316, TP 316H
SA-358	Welded Pipe	316, 316H
SA-376	Seamless Pipe	TP 316, TP 316H
SA-403	Fittings	WP 316, WP 316H, WP 316W, WP 316HW
SA-479	Bar	316, 316H
SA-965	Forgings	F 316, F 316H
SA-430	Forged & Bored Pipe	FP 316, FP 316H
Notes: (1) These materials shall have minimum specified room temperature yield strength of 207 MPa and a minimum specified carbon content of 0.04%. (2) For use at temperatures above 540°C, these materials may be used only if the material is heat treated by heating to a minimum temperature of 1040°C and quenching in water or rapidly cooling by other means. (3) Appendix X of Subsection NH provides non-mandatory guidelines on additional specification restrictions to improve performance when materials are used within the temperature range of 425 to 595°C.		

Baseline Mechanical Properties

Room Temperature Minimum Yield and Tensile Strengths

The specified minimum yield strength at room temperature for all the product forms, types, grades, and classes given in Table 4.2 is 207 MPa (30 ksi). Depending on the product form, type, grade

and class, the specified minimum tensile strength at room temperature for the 316SS listed in Table 4.2 is either 517 MPa (75 ksi) or 483 MPa (70 ksi).

Fatigue Acceptance Testing

In addition to satisfying the minimum room-temperature yield and tensile strength requirements, uniaxial fatigue acceptance test of each lot of material is required for 316SS when conditions for service levels A, B, and C do not satisfy the negligible creep limits of Subsection NH, article T-1324(a) and (b). The fatigue test shall be performed in air at 595°C at an axial strain range of 1.0% with a one-hour hold period at the maximum positive strain point in each cycle. Test-specimen location and orientation shall be in accordance with the general guidance of SA-370, paragraphs 6.1.1 and 6.1.2 and the applicable product specifications. Testing shall be conducted in accordance with ASTM Standard E 606. The test shall exceed 200 cycles without fracture or a 20% drop in the load range.

Maximum Metal Temperature

The maximum metal temperature permitted by Subsection NH for 316SS is 816°C (1500°F).

Yield Strength at Temperature

The yield strength values at temperature (S_y) for 316SS listed in Table 4.3 are tabulated in Section II, Part D, Table Y1 from room temperature to 538°C (1000°F) and in Subsection NH from 538°C to 816°C. These are minimum expected values. The ASME tabulated values for temperatures from 30 to 816°C are shown in Table 4.3. These sets of yield strength values are shown in Figure 4.1.

Table 4.3. Yield strength of 316SS

T (°C)	S_y (MPa)	Source
30	207	Sec II
40	207	Sec II
65	189	Sec II
100	176	Sec II
125	168	Sec II
150	161	Sec II
175	154	Sec II
200	148	Sec II
225	144	Sec II
250	139	Sec II
275	136	Sec II
300	132	Sec II
325	129	Sec II
350	127	Sec II
375	125	Sec II
400	123	Sec II
425	122	Sec II
450	121	Sec II
475	120	Sec II
500	118	Sec II
525	117	Sec II
550	116	NH
575	115	NH
600	114	NH

T (°C)	S _y (MPa)	Source
625	112	NH
650	110	NH
675	107	NH
700	103	NH
725	99	NH
750	94	NH
775	88	NH
800	81	NH
816	75	NH

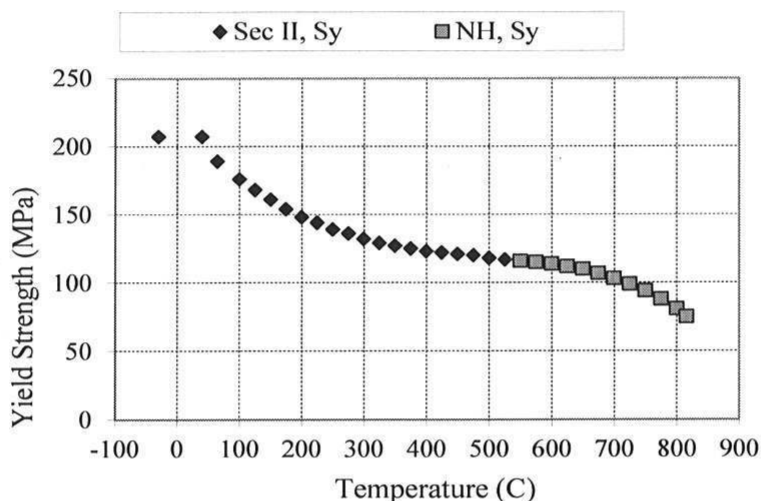


Figure 4.1. Minimum yield strength for Type 316SS.

Tensile Strength at Temperature

The values of tensile strength at temperature (S_u) for 316SS with specified minimum tensile strengths at room temperature of 483 MPa (70 ksi) and 517 MPa (75 ksi), are tabulated in Section II, Part D, Table U, from room temperature to 538°C (1000°F). Subsection NH tabulates only one set of S_u values from above 538 to 816°C. They are shown in Table 4.4. It is apparent from the table that the S_u values listed in Subsection NH are for 316SS that have a room temperature specification minimum tensile strength of 517 MPa (75 ksi). These values are plotted in Figures 4.2 and 4.3.

Table 4.4. Tensile Strengths from Section II and NH, 316SS

T (°C)	Tensile strength, S_u (MPa), at temperature		Source (2007 Edition)
	RT min. S_u = 483 MPa	RT min. S_u = 517 MPa	
30	483	517	Sec II
40	483	517	Sec II
100	482	516	Sec II
150	469	502	Sec II
200	463	496	Sec II
250	462	495	Sec II
300	462	495	Sec II
325	462	495	Sec II

T (°C)	Tensile strength, S_u (MPa), at temperature		Source (2007 Edition)
	RT min. $S_u = 483$ MPa	RT min. $S_u = 517$ MPa	
350	462	495	Sec II
375	462	495	Sec II
400	460	493	Sec II
425	456	489	Sec II
450	450	482	Sec II
475	442	474	Sec II
500	433	463	Sec II
525	421	450	Sec II
550	435		NH
575	417		NH
600	396		NH
625	373		NH
650	347		NH
675	318		NH
700	288		NH
725	255		NH
750	221		NH
775	185		NH
800	149		NH
816	125		NH

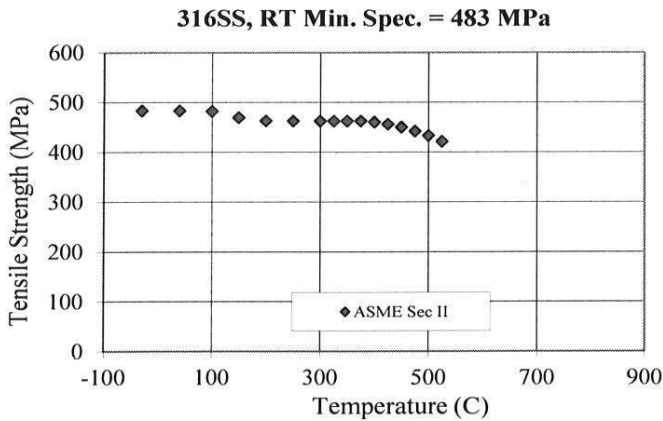


Figure 4.2. Comparison of tensile strengths for 316SS with RT $S_u = 483$ MPa.

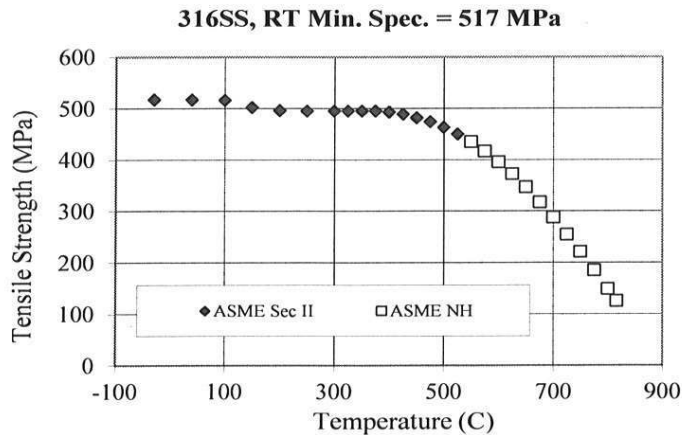


Figure 4.3. Tensile strengths for 316SS with RT $S_u = 517$ MPa.

Modulus of Elasticity

Section II (2007 Edition), Table TM-1 lists the moduli of elasticity, E , for groups of materials. Per the chemical composition, the E values in Sec II, Table TM-1, Group G are applicable to 316SS. A plot of the E values is given in Figure 4.4.

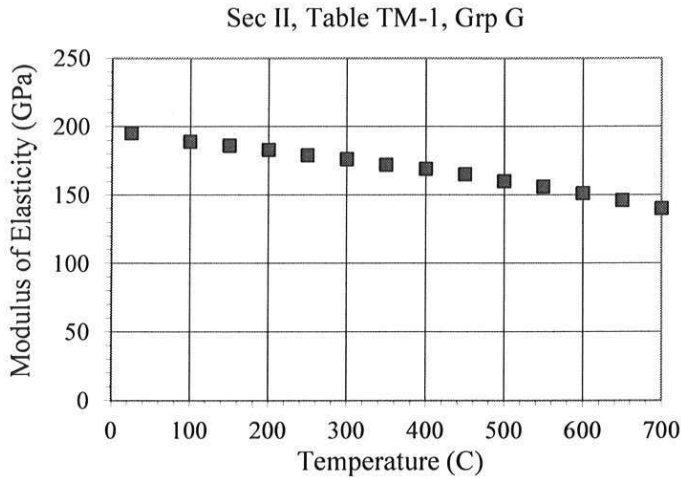


Figure 4.4. Modulus of elasticity (average value), 316SS.

Fatigue

The fatigue design curves for 316SS at temperatures up to 705°C are given in Subsection NH. The design fatigue strain range is given in Table 4.5.

Table 4.5. Design fatigue strain range for 316SS

Nd, No. of Cycles [Note (1)]	Stain Range (m/m) at Temperature				
	40°C	425°C	480°C	595°C	705°C
1x10 ¹	0.0507	0.0438	0.0378	0.0318	0.0214
2x10 ¹	0.0357	0.0318	0.0251	0.0208	0.0149
3x10 ¹	0.0260	0.0233	0.0181	0.0148	0.0105
1x10 ²	0.0177	0.0159	0.0123	0.00974	0.00711
2x10 ²	0.0139	0.0125	0.00961	0.00744	0.00551
3x10 ²	0.0110	0.00956	0.00761	0.00574	0.00431
1x10 ³	0.00818	0.00716	0.00571	0.00424	0.00328
2x10 ³	0.00643	0.00581	0.00466	0.00339	0.00268
3x10 ³	0.00518	0.00476	0.00381	0.00279	0.00226
1x10 ⁴	0.00403	0.00376	0.00301	0.00221	0.00186
2x10 ⁴	0.00343	0.00316	0.00256	0.00186	0.00162
3x10 ⁴	0.00293	0.00273	0.00221	0.00161	0.00144
1x10 ⁵	0.00245	0.00226	0.00182	0.00136	0.00121
2x10 ⁵	0.00213	0.00196	0.00159	0.00121	0.00108
3x10 ⁵	0.00188	0.00173	0.00139	0.00109	0.000954
1x10 ⁶	0.00163	0.00151	0.00118	0.000963	0.000834

Note: (1) Cyclic strain rate: 1x10⁻³ m/m/sec

The design fatigue curves from Subsection NH are shown in Figure 4.5.

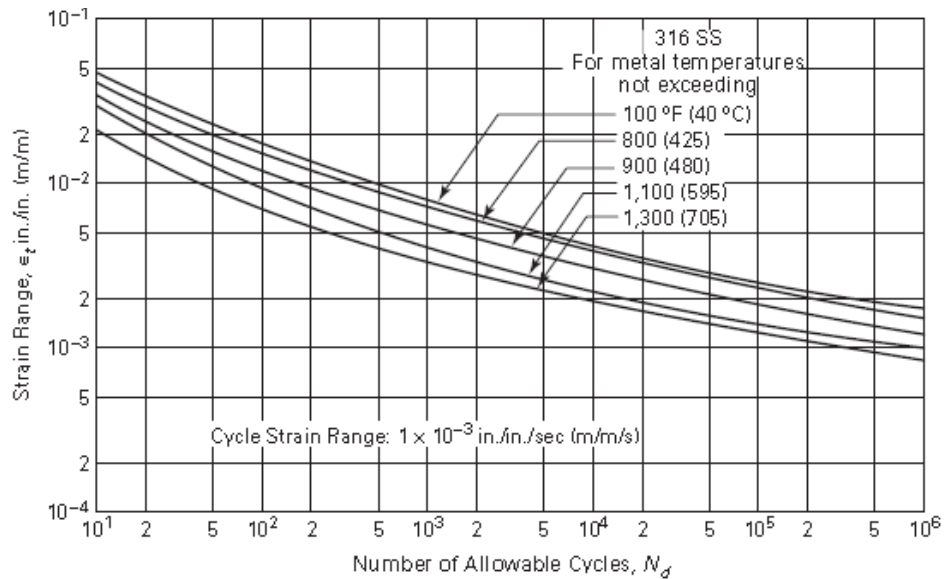


Figure 4.5. Fatigue design curves for 316SS

Creep-Fatigue Interaction

Creep-fatigue tests show that the fatigue life of 316SS is reduced with hold times. Generally for 316SS, tensile hold is more damaging, i.e., more reduction in fatigue life, than compressive hold. Subsection NH employs a creep-fatigue interaction criterion, as shown in Figure 4.6, for designing against creep-fatigue failure of 316SS.

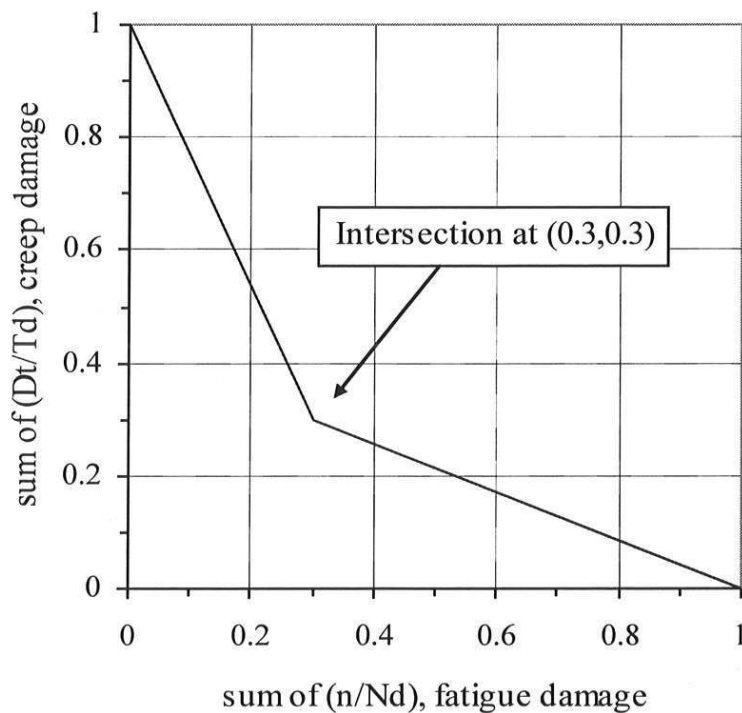


Figure 4.6. Subsection NH creep-fatigue interaction diagram, 316SS

ASME Code Allowables

Design Condition Allowable Stress

The values of the design condition allowable stress S_0 for 316SS are tabulated in Subsection NH and they are shown in Table 4.6.

Table 4.6. S_0 – Design condition allowable stress intensity for design condition calculations, 316SS

Temperature (°C)	S_0 (MPa)
427	110
450	108
475	108
500	107
525	101
550	88
575	77
600	76
625	62
650	51
675	39
700	30
725	23
750	18
775	13
800	11
816	9

Operating Condition Allowable Stress

The values of the operating condition allowable stress (S_{mt}) for 316SS are tabulated in Subsection NH and they are shown in Table 4.7. The maximum time is 300,000 hours. Note that the values in parenthesis are for 316SS with room temperature specified minimum tensile strength of 483 MPa (70 ksi), while the remaining S_{mt} values are valid for both room temperature specified minimum tensile strength values (483 MPa and 517 MPa).

The operating condition allowable stresses are also given in Figure 4.7. The S_{mt} value for each time and temperature condition is given as the smaller of the time independent primary stress S_m and the time dependent primary stress S_t shown in Figure 4.7.

Table 4.7. S_{mt} – Operating condition allowable stress intensity values for 316SS
 (RT $S_y = 207$ MPa, RT $S_u = 483$ MPa)

T (°C)	1 h	10 h	30 h	1E2 h	3E2 h	1E3 h	3E3 h	1E4 h	3E4 h	1E5 h	3E5 h
427	110	110	110	110	110	110	110	110	110	110	110
450	108	108	108	108	108	108	108	108	108	108	108
475	107	107	107	107	107	107	107	107	107	107	107
500	106	106	106	106	106	106	106	106	106	106	106
525	105	105	105	105	105	105	105	105	105	105	105
550	104	104	104	104	104	104	104	104	104	101	87
575	104	104	104	104	104	104	104	104	95	79	67
600	102	102	102	102	102	102	102	91	75	62	51
625	101	101	101	101	101	94	86	72	59	48	40
650	101	101	101	98	84	72	64	57	48	38	31
675	98	98	98	80	69	58	51	44	38	30	24
700	95 (92)	91	78	65	54	46	41	34	28	22	18
725	90 (85)	75	63	52	44	36	31	25	21	16	13
750	82 (76)	62	51	41	35	29	24	19	16	11	9
775	70 (65)	50	40	32	27	23	18	14	12	8	7
816	54 (53)	34	27	22	18	14	11	8	6	4	3

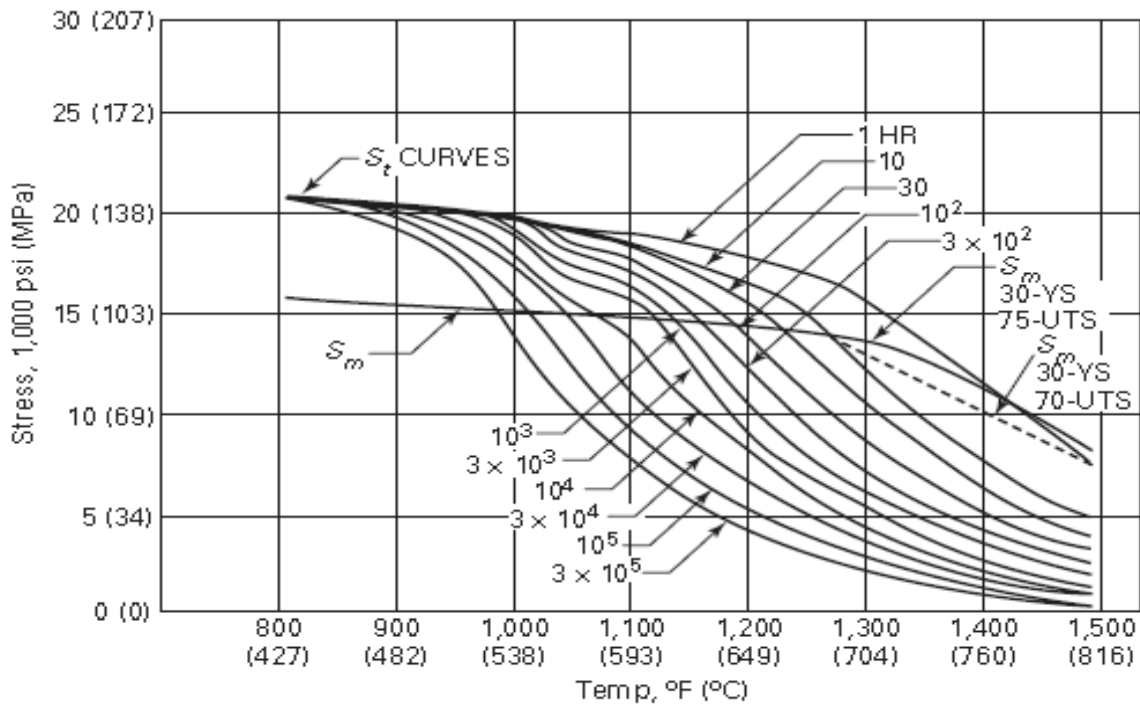


Figure 4.7. S_{mt} for 316SS

Time Dependent Primary Stress

The values of the time dependent primary stress S_t for 316SS are tabulated in Subsection NH and they are shown in Table 4.8. The information is also presented graphically in Figure 4.8. The maximum time is 300,000 hours.

Table 4.8. S_t – Time dependent allowable stress intensity values for 316SS

T (°C)	1 h	10 h	30 h	1E2 h	3E2 h	1E3 h	3E3 h	1E4 h	3E4 h	1E5 h	3E5 h
427	143	143	143	143	143	143	143	143	143	143	143
450	142	142	142	142	142	142	142	142	142	142	140
475	141	141	141	141	141	141	141	141	140	138	135
500	140	140	140	140	140	139	139	138	134	131	125
525	138	138	138	138	138	136	134	130	126	118	108
550	136	136	135	134	132	128	125	119	113	101	87
575	133	133	131	127	124	119	114	105	95	79	67
600	131	129	126	121	116	110	105	91	75	62	51
625	127	121	118	111	103	94	86	72	59	48	40
650	123	116	108	97	84	72	64	57	48	38	31
675	118	106	94	80	69	58	51	44	38	30	24
700	112	91	78	65	54	46	41	34	28	22	18
725	101	75	63	52	44	36	31	25	21	16	13
750	88	62	51	41	35	29	24	19	16	11	9
775	74	50	40	32	27	23	18	14	12	8	7
816	54	34	27	22	18	14	11	8	6	4	3

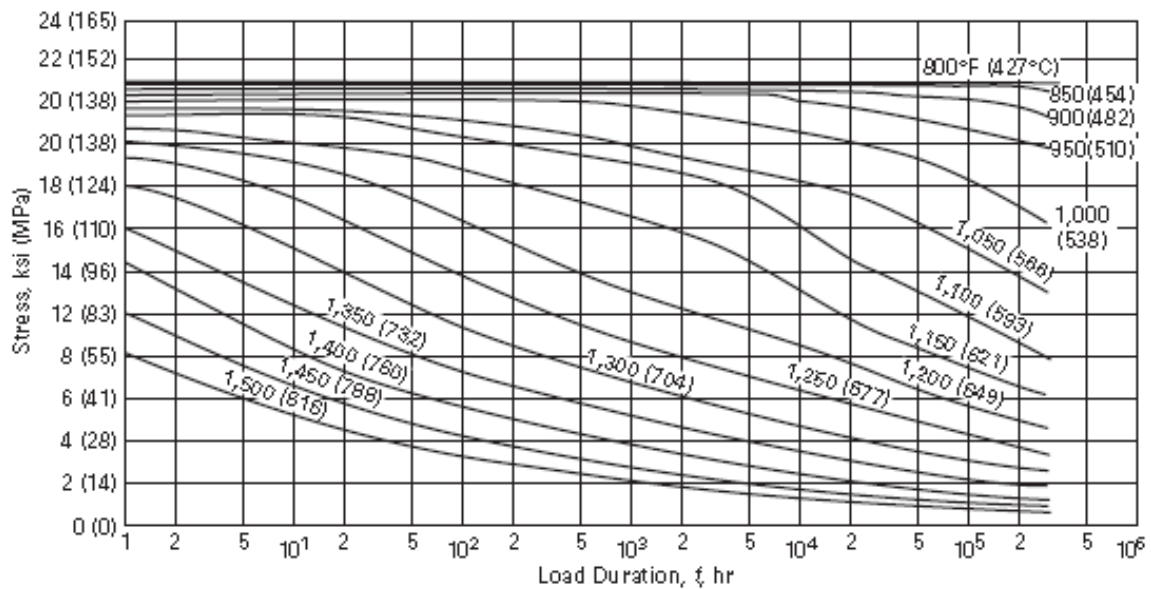


Figure 4.8. S_t -Time dependent allowable stress, 316SS

Stress-to-Rupture

The values of the stress-to-rupture, S_r , for 316SS are tabulated in Subsection NH and they are shown in Table 4.9. The information is also presented graphically in Figure 4.9. The maximum time is 300,000 hours. These are minimum expected values. The values in the table or the graphs in the figure are used to determine the creep rupture time for given stress and temperature in carrying out design calculations.

Table 4.9. S_r – Expected minimum stress-to-rupture values for 316SS

T (°C)	1 h	10 h	30 h	1E2 h	3E2 h	1E3 h	3E3 h	1E4 h	3E4 h	1E5 h	3E5 h
427	445	445	445	445	445	445	445	445	445	445	445
450	437	437	437	437	437	437	437	437	419	395	372
475	431	431	431	431	430	429	409	389	352	317	286
500	419	419	419	419	401	381	349	322	285	248	219
525	406	406	388	371	340	307	275	248	114	183	158
550	393	381	350	323	289	268	230	203	173	147	125
575	380	347	311	283	249	223	194	169	142	120	100
600	357	300	266	241	212	185	159	136	112	94	79
625	315	259	229	205	179	155	130	110	89	72	59
650	275	224	199	176	151	129	107	88	70	57	46
675	244	194	170	150	127	108	89	71	57	44	35
700	212	167	147	128	106	89	72	57	45	34	27
725	186	144	127	108	92	76	60	47	36	27	21
750	163	125	109	91	76	63	50	38	29	21	16
775	144	109	94	78	64	52	41	30	23	16	12
816	117	86	73	61	50	39	29	21	16	11	8

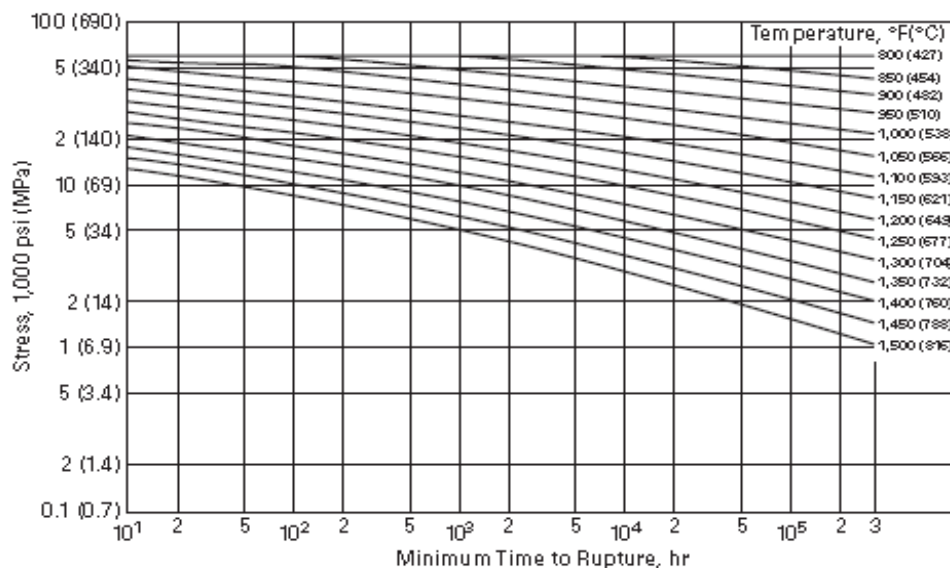


Figure 4.9. Minimum expected stress-to-rupture for 316SS.

4.2.2 Effects of Long-term Thermal Aging

Yukawa (1993) performed a comprehensive review on the long-term elevated temperature exposures on toughness of austenitic steels and nickel alloys. The review focused on the effects of thermal aging on toughness of those materials, but included information on tensile properties as well. The wrought austenitic steels considered were primarily Types 304, 316, 321, 347, and 310, some manganese containing steels of the 200 and XM series, some of the CF series cast austenitic steels, and the welds commonly used for welding of austenitic stainless steels. Another review was performed by Horak et al. (1985) in which Types 304 and 316 stainless steels were thermally aged in air up to 125,000 h at temperatures between 427 to 649°C, with a third report by Sikka (1982) providing some of the same data as well as additional data on Type 316 steel only.

Figures 4.10(a) and (b) show the effects of aging on tensile strengths of type 316 stainless steel after aging times to 91,000 h (Sikka 1982). The data were taken from numerous sources (Cullen 1975, Sikka 1978, Sikka et al. 1975, Van Leeuwen and Schra 1975, US Steel 1972, Cordovi et al. 1968, Steichen 1975, Hoke and Eberle 1957, Blackburn 1975, Fahr 1973) as shown on the figures. For aging to about 600°C, the minimum curves for the unaged material provide a reasonable lower bound of behavior for the aged material, while even to 700°C, the yield strength data are only slightly below the curve. The minimum property curves are based on data analysis reported by Sikka et al. (1975) with the minimum curves for 0.2% yield and ultimate tensile strengths based on room-temperature specified values of 207 and 517 MPa, respectively.

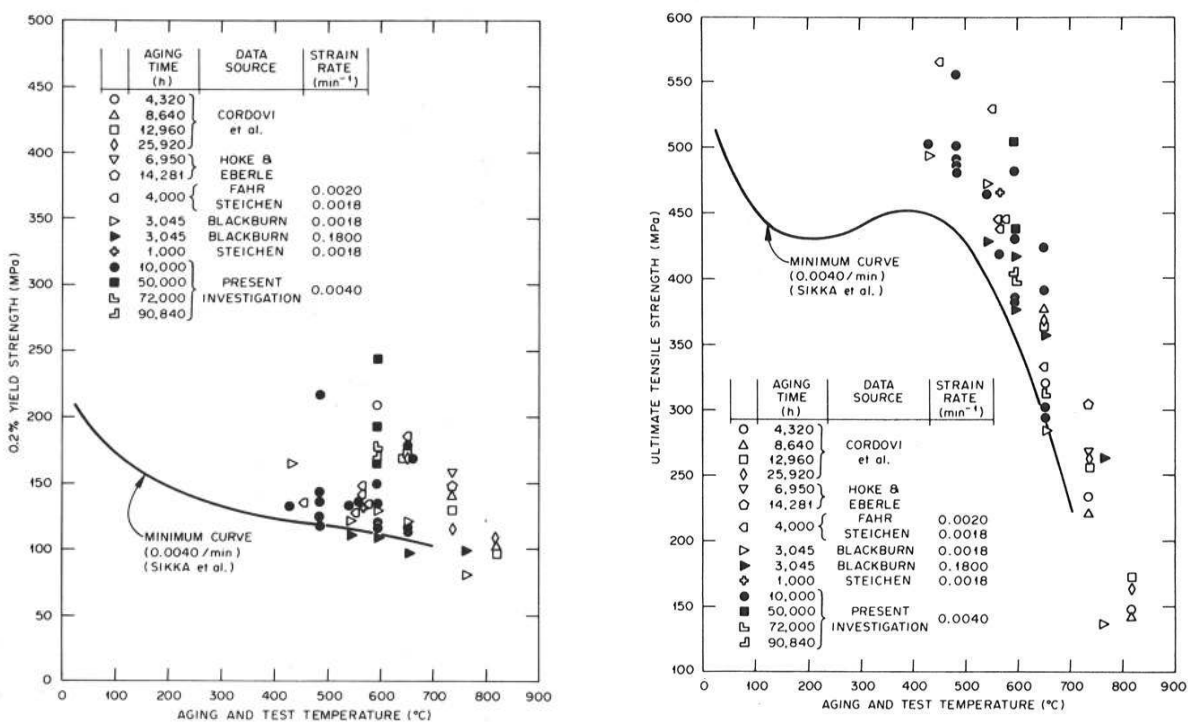


Figure 4.10. Comparison of (a) 0.2% yield strength and (b) ultimate tensile strength data on aged Type 316 stainless steel with the minimum curves for the unaged material. All tests were conducted at the aging temperature (Sikka 1982).

The uniform and total elongation curves are tied to a room-temperature minimum value of 50%, while the reduction of area curve is tied to a value of 60%. Regarding tensile ductility, Figures 4.11 (a)-

(c) show that, contrary to the strength results, some ductility data fall below the minimum curves based on the unaged material. Up to about 600°C, the bulk of the data below the curves are from aging times of 25,000 h and greater, although there are some results below the curves for times as low as 4,000 h. The author points out that, although some of the tensile ductility values are below the minimum property curves, the lowest values observed for the uniform elongation, total elongation, and reduction of area are still at least 10, 25, and 25%, respectively and these values are considered adequate.

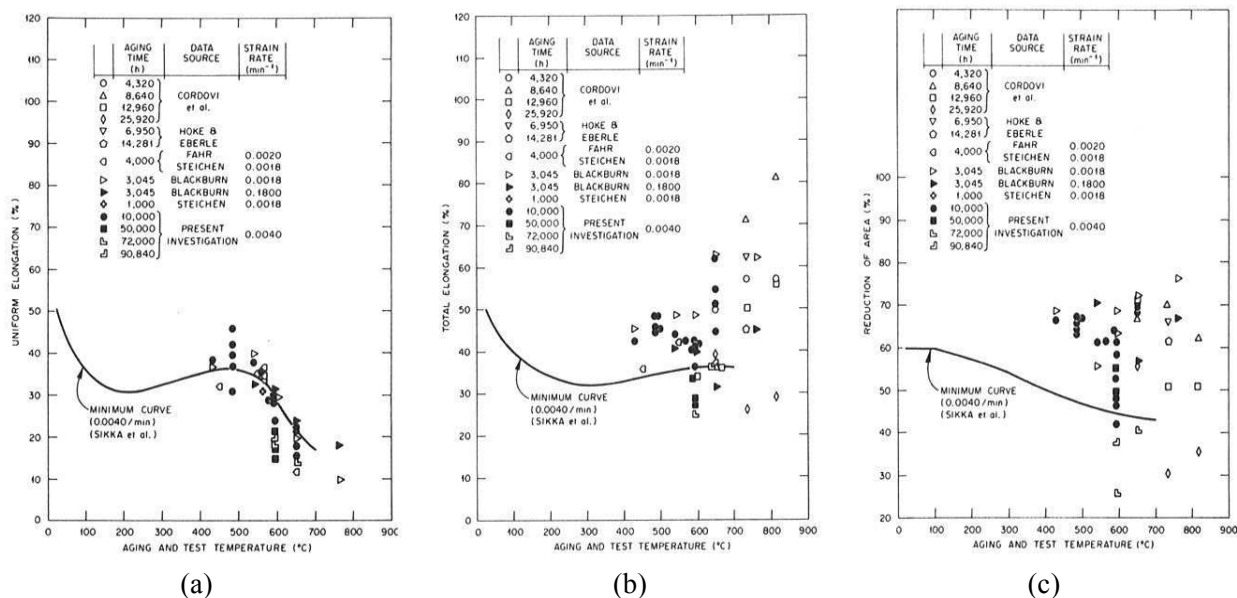


Figure 4.11. Comparison of (a) uniform elongation, (b) total elongation, and (c) reduction in area data on aged Type 316 stainless steel with the minimum curves for the unaged material. All tests were conducted at the aging temperature (Sikka 1982).

Regarding the effects of thermal aging on creep, Figures 4.12(a) and (b) show two examples of aging effects on creep behavior of Type 316 stainless steel at two different stress levels, 172 and 207 MPa, and at 593°C for 44,000 h (Sikka 1982). The data indicate a significant reduction in creep resistance for the aged materials relative to the unaged condition, with the amount of reduction being greater for the higher stress level.

Creep rupture data for Type 316 stainless steel are shown in Figure 4.13 which provides comparison for materials aged at 565°C and 649°C for 10,000 h (Sikka 1982). As shown, none of the data are below the minimum curve in the ASME Code Case N-47 (now incorporated into the Code in Subsection NH of Section III) for Type 316 stainless steel. These results show that thermal aging at 565°C for 10,000 increased the time to rupture, whereas aging at 649°C for the same time decreased the rupture time.

Sikka (1982) reported effects of aging on room-temperature Charpy V-notch (CVN) impact energy and showed that energy values are sharply reduced by thermal aging, especially when the aging temperature is higher than 482°C. After thermal aging for 50,000 h in the WR orientation (now designated TL orientation), the results showed a reduction from about 200J in the unaged condition to about 80J and 27J for aging temperatures of 482 and 649°C, respectively. They further pointed out that changes in minimum creep rate and time to rupture were only slightly more pronounced for the thermal

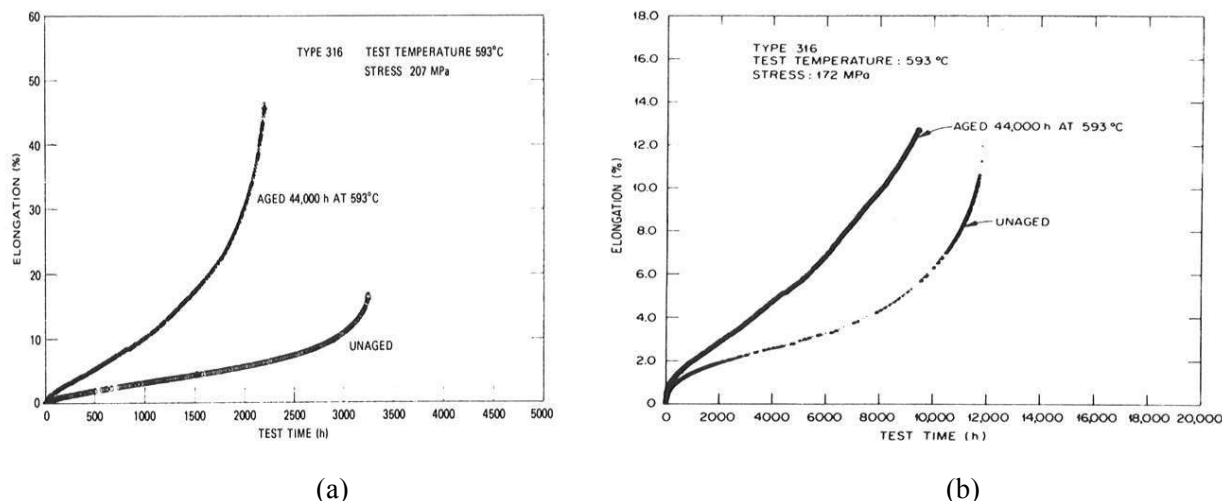


Figure 4.12. Comparison of creep curves at 593°C and for stress levels of (a) 207 MPa and (b) 172 MPa for specimens tested in the unaged condition and after aging for 44,000 h at 593°C. All the specimens were from reference heat 8092297 of Type 316 stainless steel in the as-received condition. (Sikka 1982).

aging results at 649°C than at 565°C, and that the ratio of time to onset of tertiary creep to time to rupture for the aged specimens appears to be slightly lower than that for the unaged material.

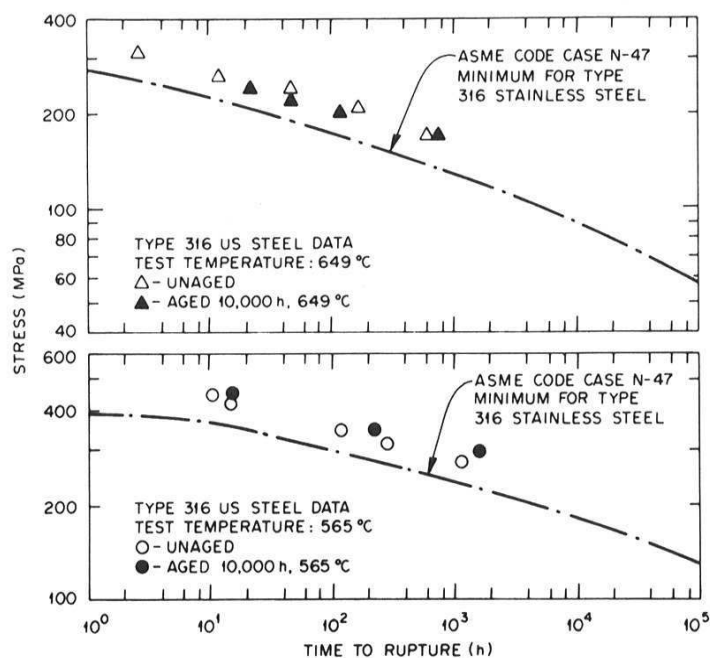


Figure 4.13. Comparison of creep rupture data for type 316 stainless steel after thermal aging for 10,000 h at 649 and 565°C, top and bottom figures, respectively. The curve for ASME Code Case N-47 is now incorporated into Subsection NH of Section III of the ASME Code. (Sikka 1982).

The review of Yukawa (1993) focused on the effects of thermal aging on the toughness of austenitic stainless steels and Figure 4.14 provides a compilation of room temperature CVN data after thermal aging at various temperatures for laboratory exposure times to 31,000 h and for service exposure times to about 140,000 h. The service data include those from the Eddystone power station that experienced a leakage failure (DeLong et al. 1985, Masuyama et al. 1987). It can be observed from the data that a moderate reduction in CVN energy occurs for 538°C exposures, but exposures at 649°C and higher result in severe reductions to as low as about 14J.

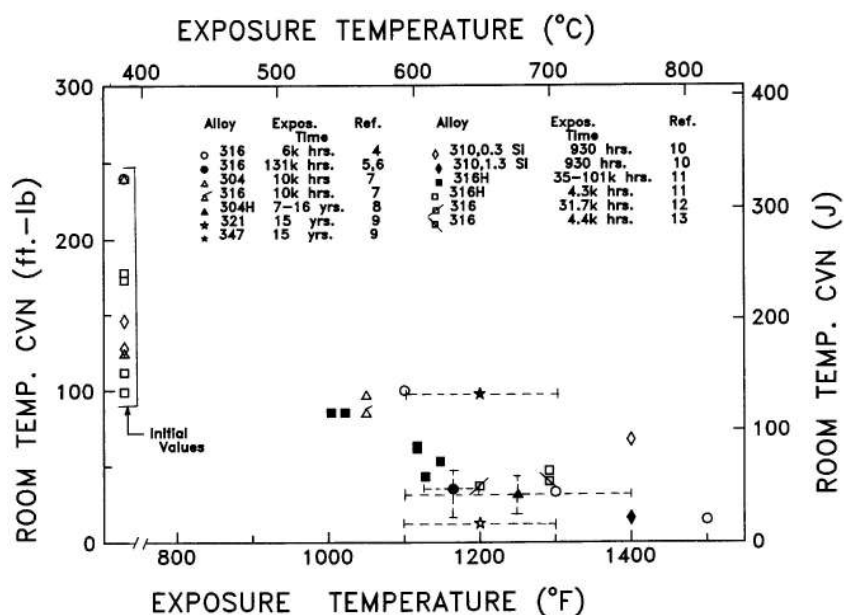


Figure 4.14. Room temperature Charpy V-notch impact energy of thermally exposed wrought austenitic steels. (Yukawa 1993).

Yukawa also discussed work of Spaeder and Brickner (1965) in which they produced a modified version of Type 316 stainless steel that was formulated for minimum sigma phase formation at elevated temperatures. The modification used a so-called Ni-balance procedure, which essentially increased the nickel content and decreased the chromium content, within allowable specifications, such that the standard 316 had a Ni-balance of -1.60 while the modified 316 had a Ni-balance of 2.73. After 6,000 h of thermal aging at 816°C, the modified 316 showed a higher CVN energy compared with that of the standard 316; however, at aging temperatures of 593 and 704°C, both materials exhibited essentially the same behavior.

Another set of results by Horak, et al. (1985) is shown in Figure 4.15 in which room temperature CVN data for a few different austenitic stainless steels are plotted as a ratio of the aged-to-unaged results vs the Holloman-Jaffe time-temperature parameter. The trends with time and temperature are evident, although the scatter is quite large, presumably because the Holloman-Jaffe parameter was not developed for CVN data. For the Type 316 stainless steel data in that figure, the aged CVN energy (after aging at about 538°C) has decreased to about 40% of the unaged value, similar to the results shown in Figure 4.14.

Regarding effects of thermal aging on austenitic stainless steel welds, Figure 4.20 provides a summary following thermal aging for times to 20,000 h at various temperatures (Yukawa 1993). There is a wide variation in the effects of such exposures among the welds, with ferrite number (FN) being one factor. The results for Type 308 welds by Edmonds, et al., (1978) (reference 44 in the figure) and by Alexander et al. (1990) (reference 47 in the figure) indicate increasing sensitivity to thermal aging with increasing ferrite content. On the other hand, data from Myers (1985) (reference 46 on the figure) show a high sensitivity to aging for a Type 316 weld with a nominal ferrite number of zero; thus, ferrite content is apparently only one factor affecting sensitivity to thermal aging. From the data in Figure 4.16, it appears the room temperature CVN energy decreases more rapidly with exposure temperature above about 550-600°C. Additional data from various sources for three types of austenitic stainless steel welds, including Type 316, are also shown for times to about 2,000 h. Exposures of the type 316 at 600°C by Myers (1985) for 2,000 h show the room temperature CVN energy decreased about 40% relative to the unaged value.

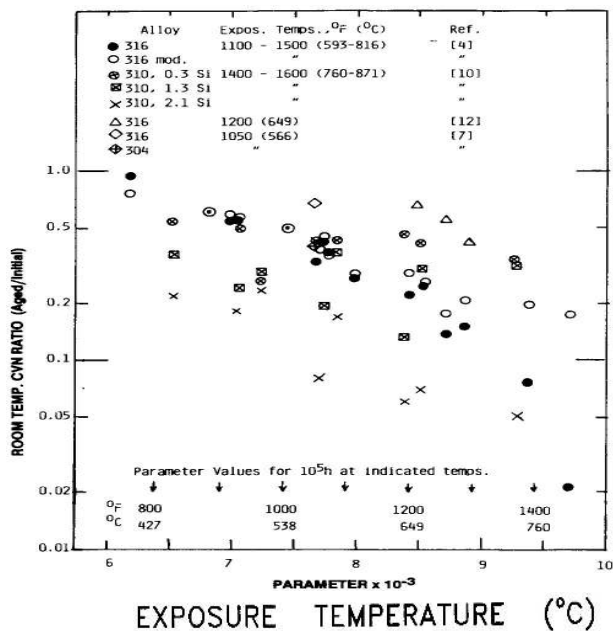


Figure 4.15. Changes in room temperature charpy energy of wrought austenitic steels with exposure temperature and time using the Hollomon-Jaffe parameter per Horak, et al. (1985).

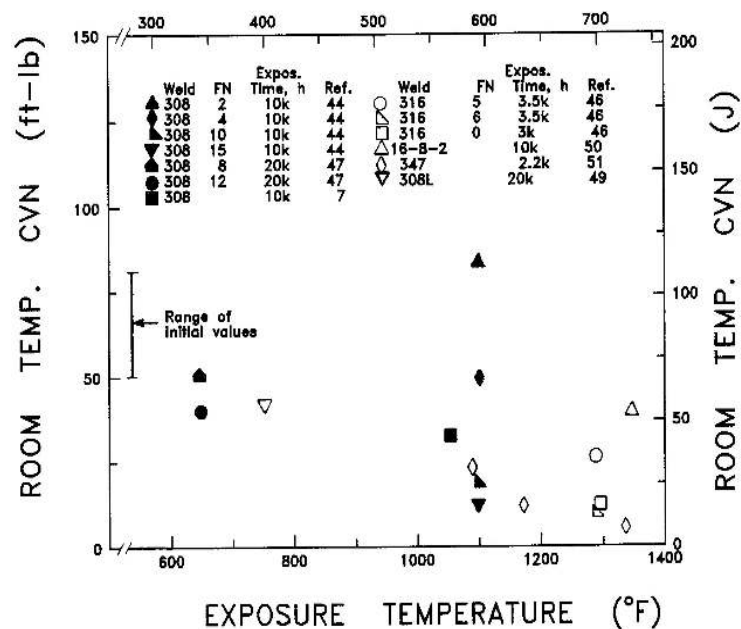


Figure 4.16. Summary of the effect of thermal exposure on the room temperature CVN energy of SMAW and SAW austenitic stainless steel welds. (Yukawa 1993).

The report by Yukawa (1993) also discusses results of elevated temperature testing and effects of thermal aging on the fracture toughness behavior of the austenitic stainless steels, primarily in the form of the ductile initiation fracture toughness, J_{Ic} , and the resistance to crack propagation by ductile tearing as determined by the slope of the J-R curve (J-integral vs crack extension, also characterized as tearing modulus, T). Results from ten different experimental studies with only unaged materials were reviewed, with Types 304, 316L, 316, 321, and 347 stainless steels included. Representative J-R curves for Types 304 and 316 stainless steels at room temperature and at two different elevated temperatures are presented and reveal that the J-R curves for both materials are decreased at high temperatures relative to those at room temperature. This is commonly observed for both stainless steels and low-alloy ferritic steels. Figure 4.17 shows a plot of both room temperature fracture toughness (J_c) and CVN results in terms of the ratios of aged to initial values for a type 308 gas-tungsten-arc weld, based on data from Vitek, et al. (1991) quoted as reference 56 in the figure. The fracture toughness and CVN energy present similar

trends of decreasing toughness with aging time, with some indication of a decreasing rate of change with increasing time.

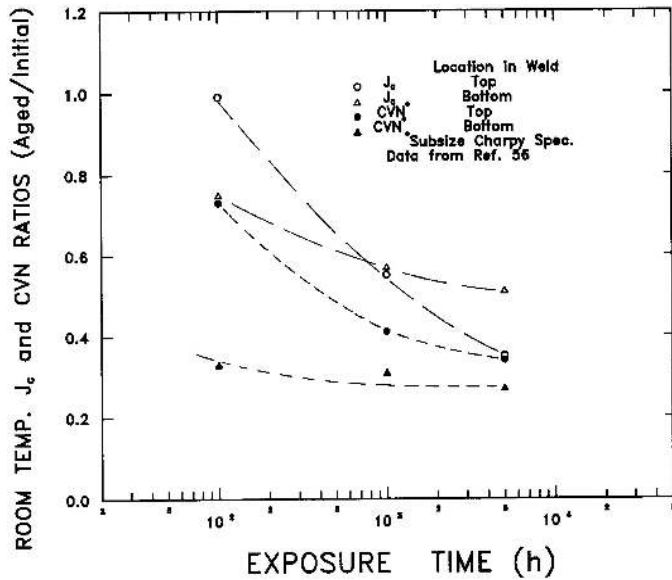


Figure 4.17. Room temperature initiation J-integral (J_c) and Charpy energy of a 308 GTAW weld after thermal exposure at 474°C for times to 5,000 h (Yukawa 1993).

Mills (1989) performed J-R fracture toughness testing at 538°C after thermal aging of Types 304 and 316 wrought stainless steels and a type 308 stainless weld at 566°C for 10,000 h. Figure 4.18 shows J-R curves for those three materials, respectively, in both the unaged and aged conditions and at two displacement rates. Mills points out that the load-displacement records were found to be very similar under static, semi-dynamic, and dynamic loading conditions. Thus, as shown in the three figures, the fracture toughness results do not indicate any significant effects of loading rate. Thermal aging at 566°C for 10,000 h reduced J_c and tearing modulus by ≈ 10 -20% and 20-30%, respectively, for all three materials. However, at a very slow loading rate of 0.006 mm/min, Mills observed a greater effect of thermal aging on the type 304 stainless steel and extensive intergranular cracking on the fracture surfaces. He concluded that creep crack growth along the grain boundaries was the cause of large degradation in fracture toughness that could, “negate the exceptionally high fracture resistance exhibited by SS alloys.”

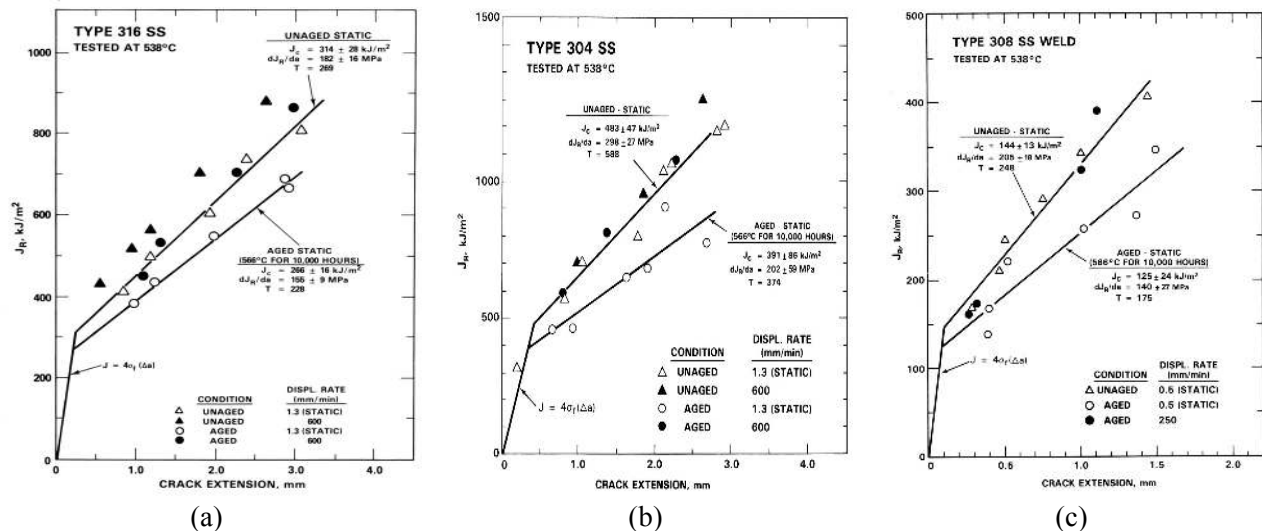


Figure 4.18. J_R curves for (a) unaged and aged 316 stainless steel, (b) unaged and aged 304 stainless steel, and (c) unaged and aged 308 stainless steel weld (Mills 1989).

Thermal Aging Effect on Code Allowables

Reduction in the yield and tensile strengths of a material may result from prior long-time, elevated temperature service. As the time independent primary stress S_m is determined from the yield and tensile strengths, it is necessary to appropriately reduce the values of S_m , and hence the operating condition allowable stress due to prior elevated temperature service. In Subsection NH, yield and tensile strength reduction factors are introduced to allow for the effects of prior elevated temperature service. For 316SS, these reduction factors are listed in Table 4.10 and plotted in Figure 4.19.

Table 4.10. Yield and tensile strength reduction factor due to prior long-time elevated temperature service, 316SS

Temp. (°C)	YS Reduction Factor	TS Reduction Factor
427	1	1
482	1	0.8
816	1	0.8

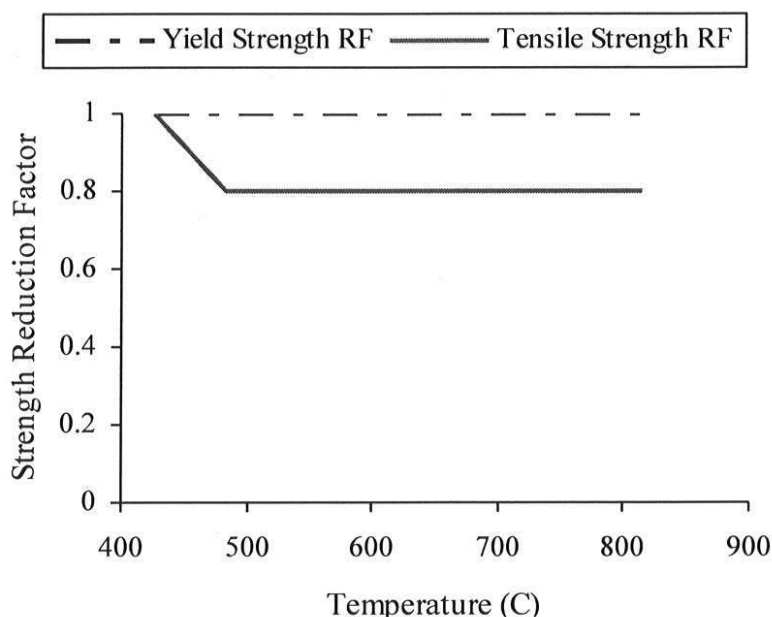


Figure 4.19. Yield and tensile strength reduction factors, 316SS.

To account for the effect of long-time elevated temperature service for 316SS, the S_{mt} values of Table 4.7 should be redefined as the smaller of

- S_{mt} value from Table 4.7
- $0.33 \times$ specified minimum TS at room temperature \times TS reduction factor of Table 4.10
- $0.33 \times$ tensile strength at temperature of $4.4 \times$ tensile strength reduction factor of Table 4.10
- $0.67 \times$ specified minimum YS at room temperature \times YS reduction factor of Table 4.10
- $0.9 \times$ yield strength at temperature of Table 4.3 \times yield strength reduction factor of Table 4.10

4.2.3 Effects of Sodium Exposure

Sodium Corrosion and Carburization/Decarburization

Austenitic stainless steels are generally compatible with high-purity sodium. Sodium corrosion of austenitic stainless steels is significantly enhanced by presence of oxygen even at low levels. Formation of the ternary NaCrO_2 phase leads to leaching of Cr out of the steel. Leaching of Ni also occurs in austenitic stainless steels due to its high solubility in sodium. In a dynamic sodium system such as reactor coolant circulation systems, typical mass transfer occurs in austenitic stainless steels due to solubility difference caused by temperature gradients. Alloying elements such as Ni, Cr, and Mn dissolve in the high temperature region and deposit at the lower temperature region. Selective leaching of these alloying elements (Ni and Cr) causes destabilization of the austenite phase and promotes the formation of ferrite phase. The layer containing ferrite is referred to as “surface degraded layer.” Depletion of Ni and Cr is, generally, more severe at grain boundaries.

Corrosion behavior of austenitic stainless steels is well understood over the temperature range of 455 to 755°C. It is known that after the initial period of exposure (500 to 1000 h), the steady state corrosion is reached, governing the corrosion rate for long-term behavior. The steady-state corrosion rates of austenitic stainless steels can be expressed by the following equations:

$$R/\phi = (2.9728 \times 10^8 + 2.9133 \times 10^8 V) \cdot \exp\left(-\frac{150.6}{RT}\right), \text{ for sodium velocities } < 3 \text{ m/s}$$

$$R/\phi = (1.6981 \times 10^9) \cdot \exp\left(-\frac{150.6}{RT}\right), \text{ for sodium velocities } > 3 \text{ m/s}$$

where ϕ is the oxygen concentration in sodium in ppm, V is the sodium velocity in m/s, T is the temperature in K, and R is the gas constant, 8.31 J/mol-K. The apparent activation energy for this corrosion process is 150.6 kJ/mol. It is noted that the corrosion rate of austenitic stainless steels are mainly influenced by temperature, oxygen contents in sodium and sodium velocities. The corrosion rate increases exponentially with temperature and linearly with oxygen content. The corrosion rate increases with increasing sodium velocity up to ≈ 3 m/s, and becomes independent of velocity at higher values. Figure 4.24 shows the corrosion rates for Type 316 SS as a function of temperature, oxygen concentration and sodium velocity.

Other factors affecting sodium corrosion include material composition, thermo-mechanical treatment, material position (downstream effect), and heat flux (Ganesan and Ganesan 1998). For instance, addition of Mo to 316SS improves the corrosion resistance by forming Fe-Mo nodes. Annealed stainless steel was found to be more prone to corrosive attack than cold worked material. High heat flux can increase the corrosion rate by a factor of 2. These effects are however, of secondary importance to the corrosion rate compared with temperature, oxygen concentration and sodium velocity.

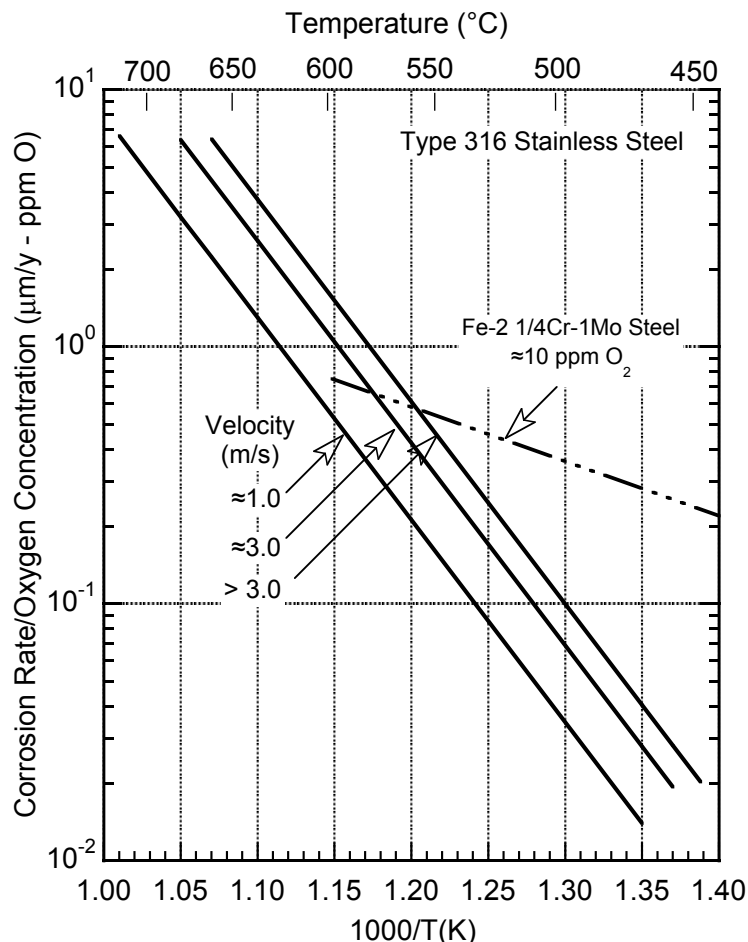


Figure 4.20. Corrosion rates of Type 316 SS in flowing sodium.

Nonmetallic elements such as carbon and nitrogen in sodium have significant effects on austenitic stainless steels as well. Transfer of C and N in flowing sodium circuits results in carburization/decarburization and nitridation/denitridation, which can significantly affect microstructural stability and mechanical properties of austenitic stainless steels. In a monometallic sodium system, austenitic stainless steels decarburize in the high temperature region and carburize in the low temperature region; in bimetallic sodium loops constructed of austenitic and ferritic steels, the ferritic steel located in the low temperature region tends to decarburize and the austenitic stainless steel located in the high temperature region tend to carburize.

Carburization/decarburization depends on the temperature, the C activity in sodium, materials' composition, and thermo-mechanical treatments. The carbon activity in sodium is affected by temperature, material composition, effectiveness of carbon sinks (cold trap), and presence of carbon sources (e.g. ingress of CO₂ and hydrides and hydrocarbon from oil leak). Figure 4.21 gives an example of carburization/decarburization in 304 SS and 316 SS in EBR-II and FFTF environments (Snyder et al. 1976). The carbon concentration-penetration-temperature diagrams shown in Figure 4.22 represent the influence of time, temperature, carbon concentration in sodium, and thermal-mechanical treatment on the carburization/decarburization behavior of Types 304 and 316 SS (Snyder et al. 1973, 1974, 1976). The region of maximum carburization is indicated by line A, and the penetration depth for the transition between single-phase austenite and a two-phase austenite plus carbide mixture is represented by line B. The variation of the carbon concentration at the surface of the steel with temperature is shown in the plane corresponding to zero penetration in the material.

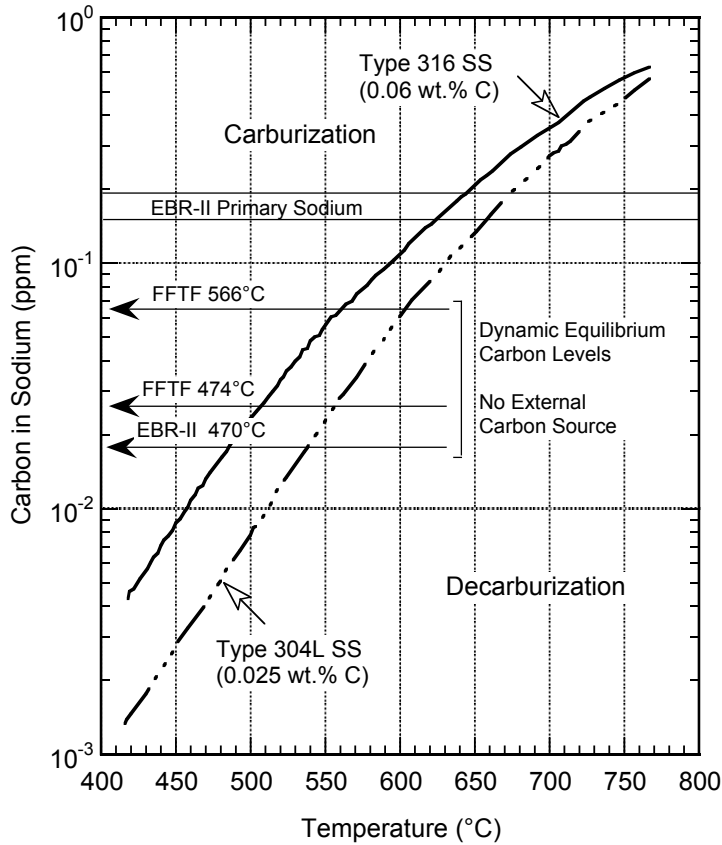


Figure 4.21. Dependence of carburization/decarburization in austenitic stainless steels on temperature and C content in sodium.

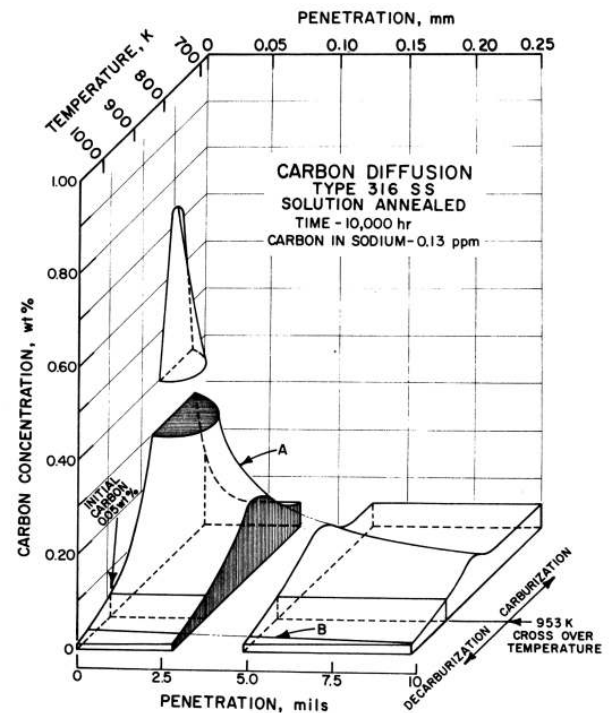
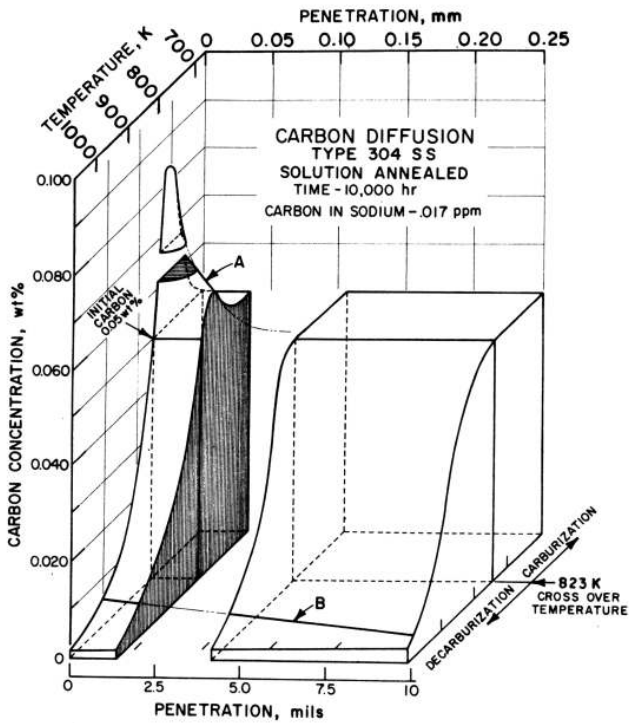


Figure 4.22. Effect of temperature on the carburization/decarburization of Type 304 SS and Type 316 SS.

In sodium loops the structural material acts as the source or sink for C, depending upon the temperature and material composition. In addition, routine maintenance operations and leaks in components (e.g., pumps) can result in ingress of carbonaceous material to the sodium directly or via the cover-gas system. From a knowledge of the ability of the system material to getter C and from the estimates of contamination rate for carbonaceous materials, it is possible to evaluate the steady-state C concentration in sodium and the overall C transport in the system. The relationship between the C contamination rate and the steady-state C concentration in the sodium for the FFTF and EBR-II primary sodium systems is given in Figure 4.23 (Snyder et al. 1976).

During 6 years of operation from 1973 the C concentration in the EBR-II primary sodium increased from 0.11 to 0.22 ppm, as determined from periodic equilibrations of steel foils in sodium (Natesan and Kassner 1973). The information in Figure 4.23 (Snyder et al. 1976) indicates that a C contamination rate of ≈ 250 to 300 g/y would result in such C levels in sodium. The low operating temperatures coupled with relatively minor contamination of the sodium by carbonaceous material have resulted in minimal composition changes in the austenitic steels in this circuit.

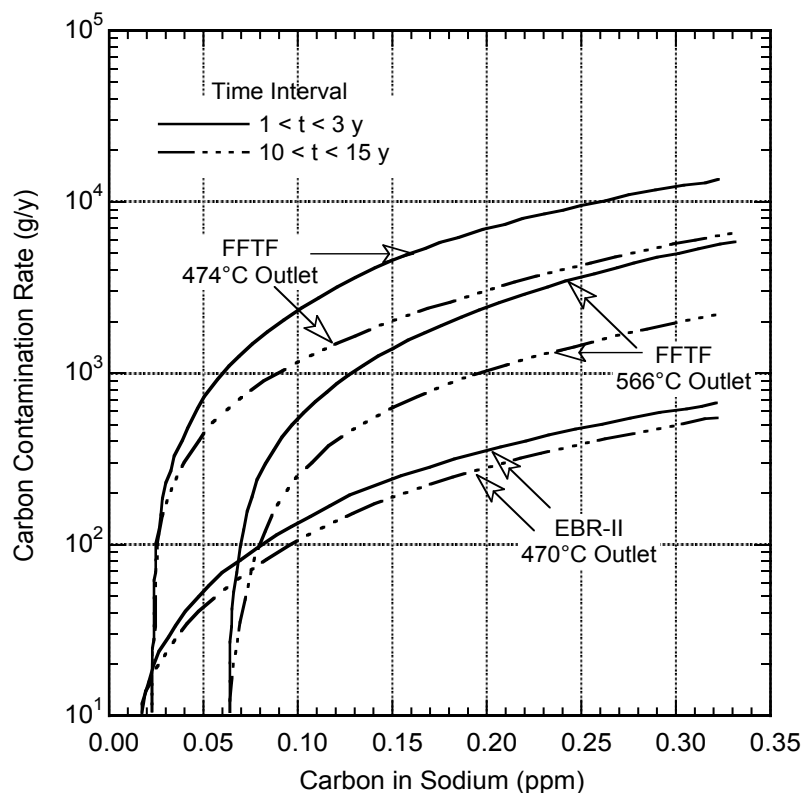


Figure 4.23. Relationship between carbon contamination rate in FFTF and EBR-II primary systems and steady-state carbon concentration in sodium (Snyder et al. 1976).

The transport of N in or out of austenitic stainless steels in sodium occurs in a similar manner to C transfer. Nitridation of austenitic stainless steels often occur below 535°C and denitridation occurs at higher temperatures (Atsumo et al. 1976, Shiels et al. 1971, Schrock et al. 1976).

Degradation in Mechanical Properties

Tensile Properties

The sodium environment itself has nearly no influence on tensile properties. Changes in tensile properties are largely dependent on the degree of carburization/decarburization that occurs during long-

term exposure to sodium. The influence of carburization/decarburization on the mechanical properties of austenitic SSs has been the subject of numerous investigations. Tensile data have been obtained from materials that were carburized in sodium to produce specific C-penetration depths. At temperatures between 400 and 800°C, the ultimate tensile elongation decreases with an increase in C concentration in the material (Kirschler et al. 1969, Thorley et al. 1970, Natesan et al. 1972, Kirschler and Andrews 1968, Thorley and Tyzack 1971, Natesan et al. 1975, Chopra and Natesan 1977, Natesan et al. 1978). Figures 4.24-4.26 show the variation in the ultimate strength, uniform elongation, and total elongation for Types 304 and 316 SS after exposure to a sodium environment at temperatures between 425 and 700°C. For these tests, the depth of C penetration in the specimens varied from 0.1 to 0.3 mm and the increase in average bulk C concentration of these specimens was up to 0.2 wt.% for Type 316 and 0.15 wt.% for Type 304 SS. The effect of sodium exposure on the tensile properties is greater at lower temperatures because of the greater pickup of C at these temperatures.

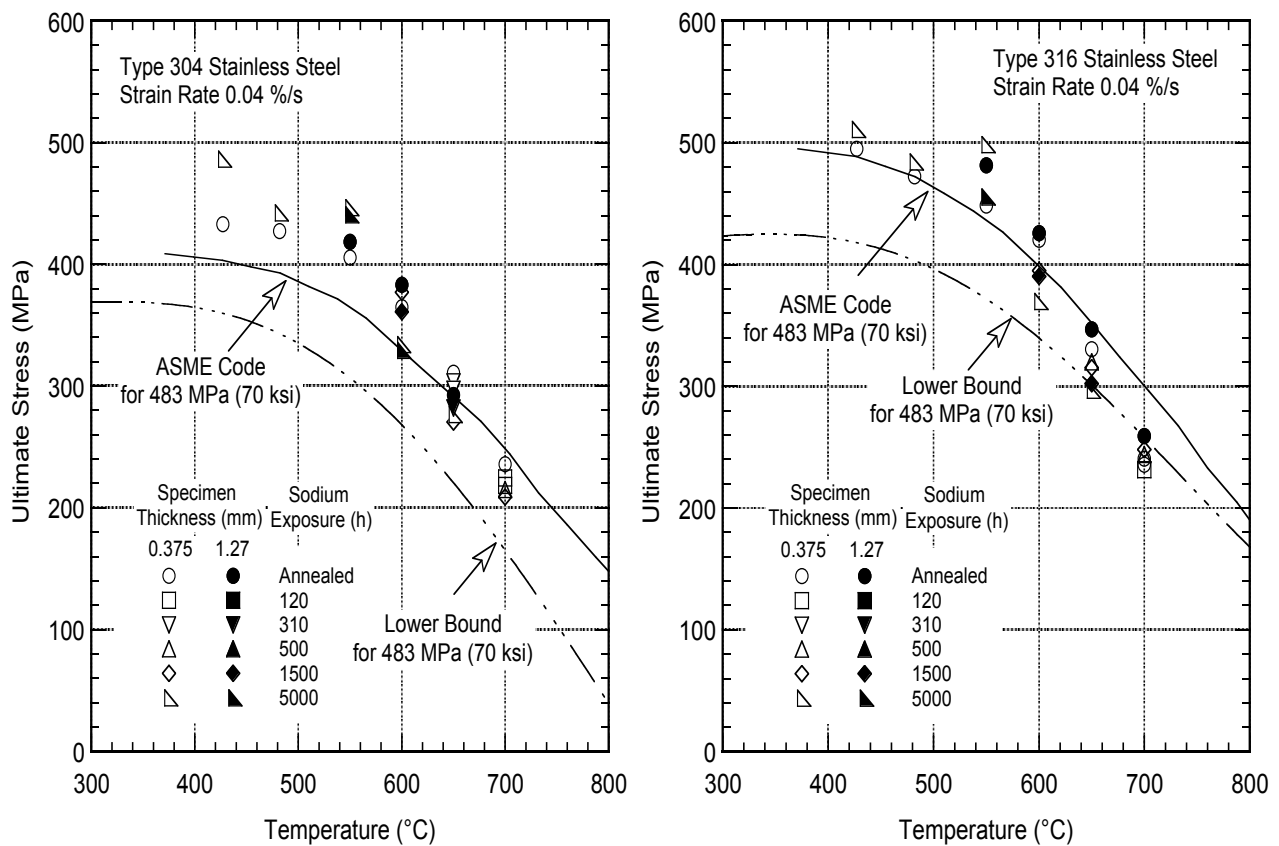


Figure 4.24. Effect of sodium exposure on the ultimate tensile strength of Types 304 and 316 SS.

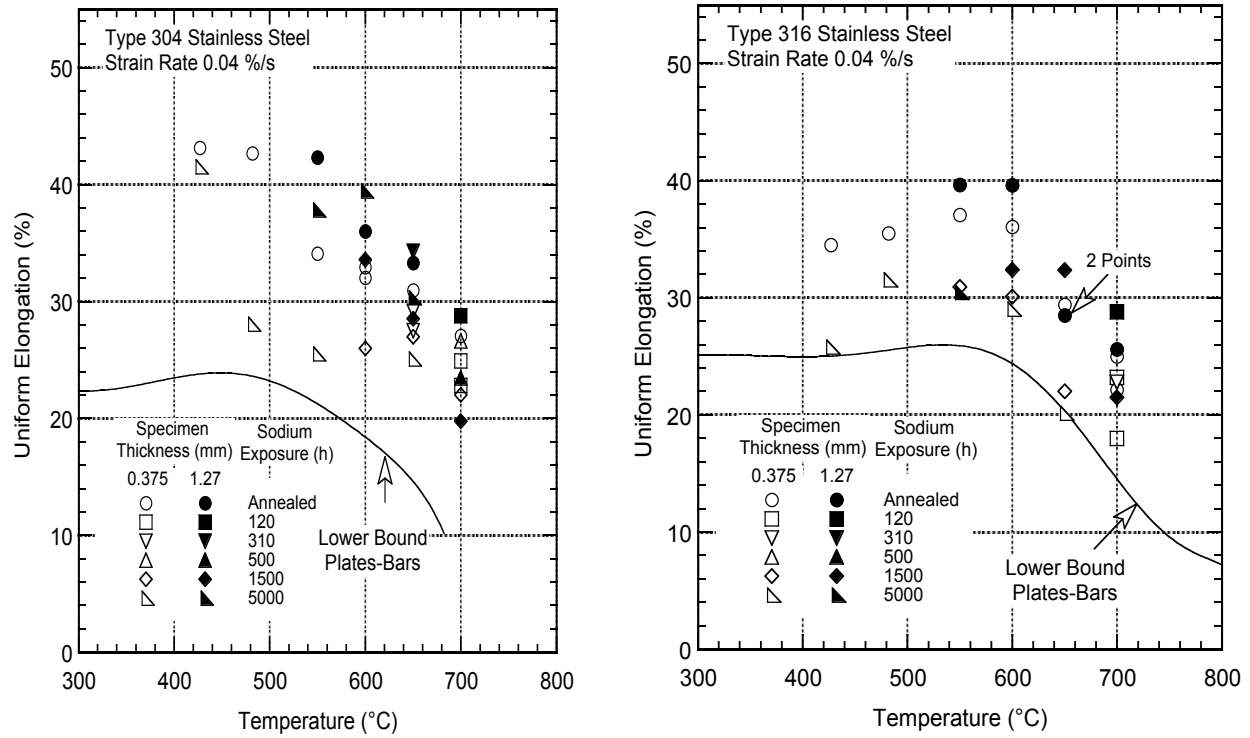


Figure 4.25. Effect of sodium exposure on the uniform elongation of Types 304 and 316 SS.

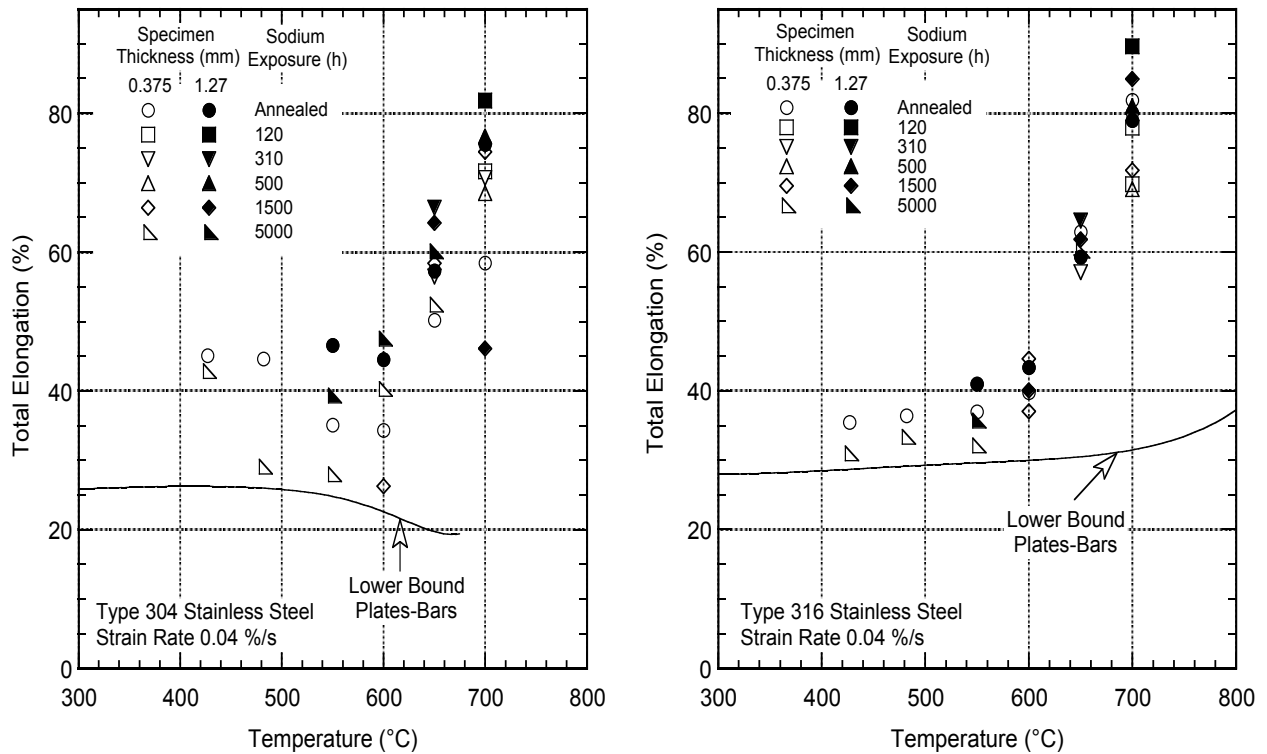


Figure 4.26. Effect of sodium exposure on the total elongation of Types 304 and 316 SS.

Creep Properties

Sodium exposure has nearly no influence on creep rupture properties in Type 316 SS. As shown in Figure 4.27 (Flagella et al. 1978, 1980, Natesan et al. 1977, 1978, Natesan 1983), creep rupture properties of 316 SS are unchanged even after 10,000 hours. The sodium effect was observed in sensitized 316 SS. It is worth mentioning that Type 316L(N) SS exhibited two stages of secondary creep during long-term creep tests (>6,000 h), due to sensitization occurring during the test.

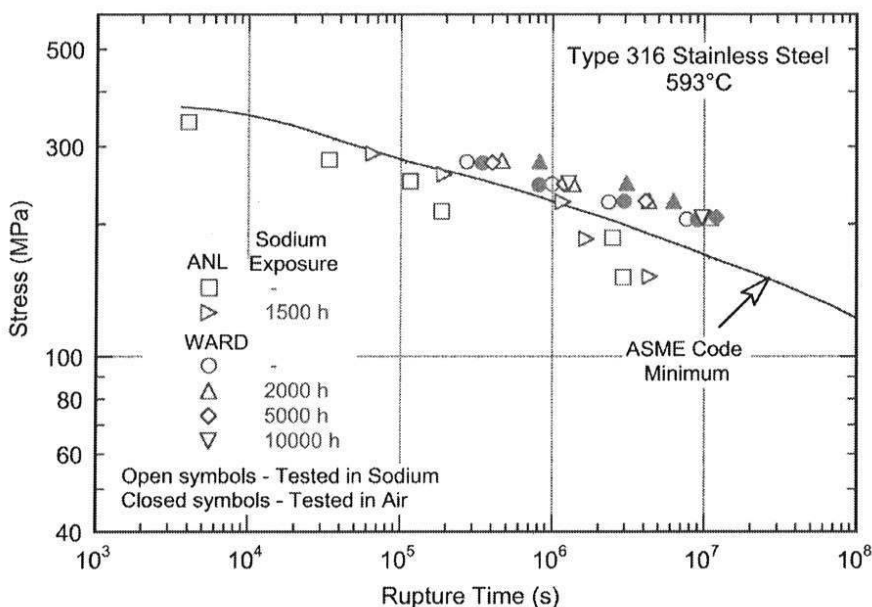


Figure 4.27. Effect of sodium exposure on creep rupture properties for Type 316 SS.

Carburization in austenitic stainless steels can lead to significant degradation in creep rupture strength. Carburization of the material in sodium (with 0.4 ppm carbon) at 550°C results in a significant reduction in rupture life and increase in the minimum creep rates of the sodium-exposed specimens than solution-annealed material. The carburized material shows no tertiary creep and exhibits an intergranular fracture mode; a predominantly ductile mode of fracture is observed for materials exposed to sodium and tested at temperatures between 600 and 700°C (Natesan 1983). Such degradation in creep properties is also observed for the material exposed to sodium at 550°C but tested at 600 and 650°C.

Figure 4.28 (Tas et al. 1976, Huthman et al. 1980, Natesan et al. 1976, 1977) shows the creep-rupture behavior of Type 304 SS tested at 550°C. The primary cause for the degradation seems to be significant nucleation of microcracks in the carburized regions of the sodium-exposed specimens that result in a reduction in the nucleation time of cracks. The surface C concentration for the specimen exposed at 550°C was greater than 1 wt.% compared to 0.30 and 0.05 wt.% for the specimens exposed at 600 and 700°C, respectively. The rupture life of the heavily carburized steel is an order of magnitude lower than that of the annealed material tested in air, argon, or sodium environments. Similar behavior is observed for carburized Type 316 SS. However, additional data in the temperature range of 450 to 600°C are required on the material, especially at a C level of 0.4 ppm which is anticipated to be an upper bound value in reactor sodium, to quantify the extent of degradation of creep properties in the material.

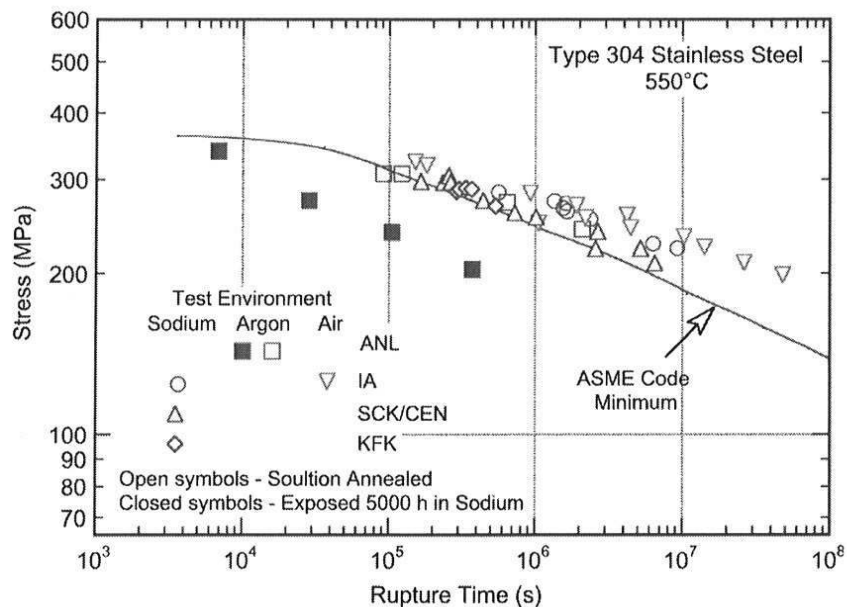


Figure 4.28. Effect of sodium exposure on creep rupture strength for Type 304 SS.

Fatigue and Creep-Fatigue

Evaluation of the fatigue and creep-fatigue behavior of materials for service in a sodium environment requires an understanding of the influence of the environment itself as well as the effects of compositional and microstructural changes that occur in the material during the long-term exposure to sodium. The available data indicate that both the environment and microstructural changes due to sodium exposure influence the low-cycle fatigue behavior of austenitic SSs (Smith et al. 1975, 1976, Zeman and Smith 1979, Chopra 1985, Flagella et al. 1978, Flagella and Kahrs 1976, Flagella 1983, Cowgill 1985, Husslage and Drenth 1980). In general, a low-oxygen sodium environment has a beneficial effect on the fatigue life of Types 304 and 316 SS. At temperatures between 480 and 700°C, the fatigue life of these steels in sodium is superior to that in air. The fatigue life of annealed, thermally aged, and sodium exposed Type 316 SS in air and sodium environments at $\approx 600^\circ\text{C}$ is shown in Figure 4.29. The best-fit air curve is also included in the figure for comparison. For the sodium exposure conditions used in these studies, the specimens developed a C concentration profile that varied from ≈ 0.4 wt.% at the surface to the initial concentration in the steels at a depth of 0.01-0.02 cm. The results indicate that moderate carburization of the steel has no effect on the fatigue life and the fatigue lives of sodium-exposed material are comparable to those of the annealed or thermally aged material. The difference between the ANL and WARD data is believed to be due to differences in the composition and initial heat treatment of the steels. For example, the ANL heat was a low-N heat tested in the mill-annealed condition. The unusually low fatigue life in air of the Type 316 SS investigated in the WARD study is not clear.

A similar behavior is observed for Type 304 SS. The fatigue life of annealed, thermally aged, and sodium exposed Type 304 SS in air and sodium environments at 550 and 593°C is shown in Figure 4.30. At both temperatures the fatigue life in sodium is superior to that in air. A moderate amount of carburization has little or no effect on fatigue life, e.g., the strain vs. life relationship for thermally aged or sodium exposed steel are identical.

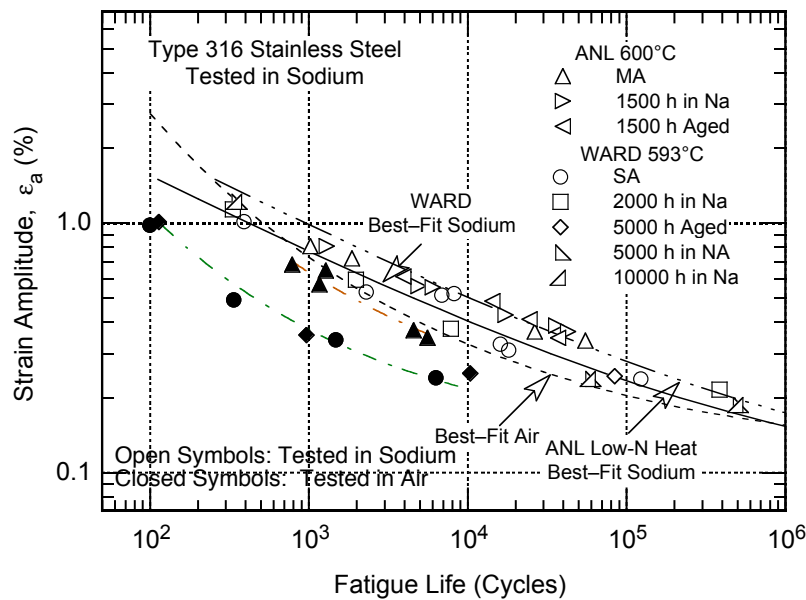


Figure 4.29. Fatigue strain-life relation for Type 316SS in air and in sodium environments.

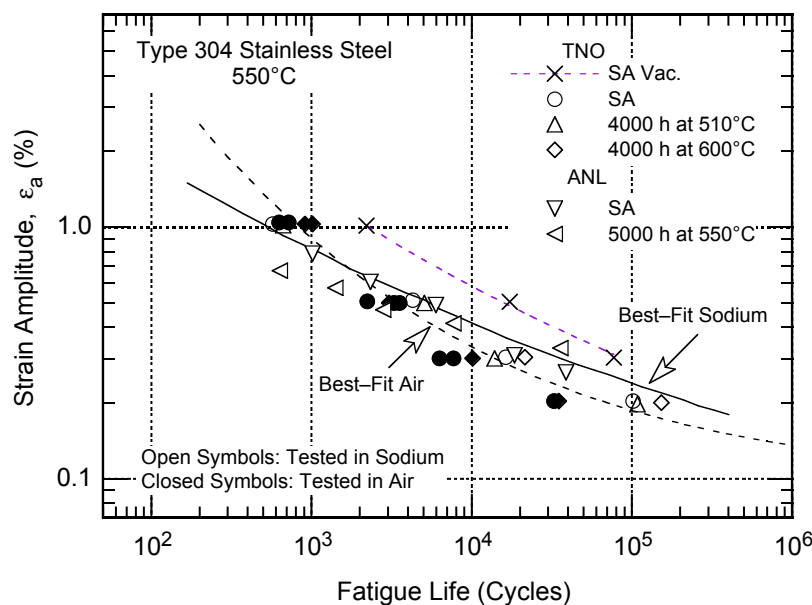


Figure 4.30. Fatigue strain-life relation for Type 304 SS in air and in sodium environments.

Metallographic evaluation of the fracture surface and the liquid/metal interface in the gauge region of the specimens indicates that environmental effects are virtually absent in a low-oxygen sodium environment. The specimens are completely free of oxide and any other corrosion product. On the other hand, fatigue tests in air at high temperatures show substantial oxidation that may influence cyclic deformation in several ways. For example, oxidation of the slip steps can prevent slip reversal, adsorption of nonmetallic elements at grain boundaries or slip bands may accelerate cracking, or strengthening of the surface due to oxide film can cause strain accumulation and enhanced cavitation.

In sodium, the specimen gauge surfaces show coarse slip lines and virtually no secondary cracks. Similar surface features have been observed for Type 304 SS tested in vacuum (Maiya 1981). In a chemically inert environment, such as sodium or vacuum, fatigue cracks probably initiate at the slip steps.

Oxidation of the slip steps in air will promote early crack initiation. Furthermore, studies on fatigue crack growth show that growth rates in sodium and vacuum are significantly lower than those in air (James and Knecht 1975). The differences in growth rates are attributed to more efficient slip reversal in the crack-tip region due to the absence of an oxide film on the crack surface. This behavior results in the diffuse nature of fatigue striations formed on the fracture surfaces of specimens tested in sodium. These results indicate the fatigue life in sodium is greater than that in air because of a longer period for crack initiation and low crack growth rates.

When a hold time is applied at the tensile side of loading, a significant reduction in fatigue life was observed. The creep-fatigue behavior of austenitic SSs in sodium has been investigated using a slow-fast sawtooth waveform or a triangular waveform with tensile-hold period. The results show significant reduction in fatigue life. A tensile-hold period leads to creep damage and reduces fatigue life, whereas compressive- or symmetric-hold periods have little or no effect. The creep damage during a tensile-hold time depends on the material grain size. The 50- μm grain size rod material is resistant to bulk cavitation; the larger grain size plate material shows extensive grain-boundary cavities.

The strain vs. life data for thermally aged Type 304 SS in sodium using a slow-fast sawtooth waveform or tensile hold periods is shown in Figure 4.31 (Chopra et al. 1982). As compared to continuous-cycle fatigue, the reduction in fatigue life is greater at lower strain amplitudes; i.e., fatigue life is a factor of ≈ 20 lower at strain amplitude of 0.25%, whereas life is a factor of ≈ 8 lower at strain amplitude of 0.5%. Although the continuous-cycle fatigue life in sodium is greater than that in air, life under creep-fatigue conditions (i.e., for the slow-fast or hold-time tests) is comparable to that in air. The slow-fast or hold-time tests in air under similar loading conditions result in a reduction in life by a factor of ≈ 6 . These results suggest that the creep-fatigue interaction may be greater in sodium than in air, particularly at low-strain amplitudes. It is probable that the slow-fast or hold-time strain sequence facilitates crack initiation, and the apparent larger effect on life under creep fatigue conditions is not due to creep damage but early crack initiation. On the other hand, a substantial portion of fatigue life for continuous-cycle fatigue is spent in initiating a crack, particularly at low-strain ranges.

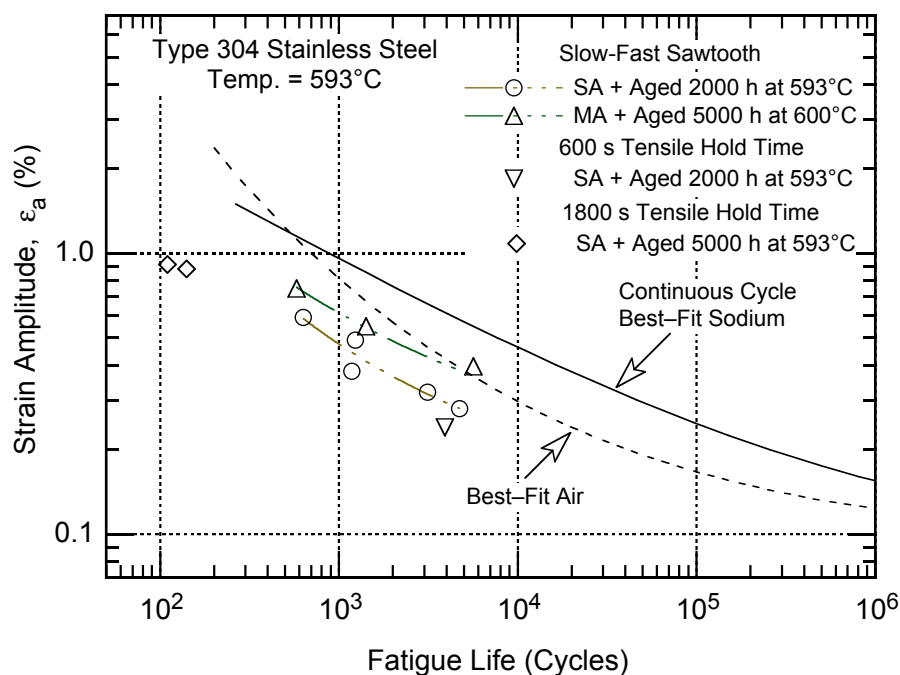


Figure 4.31. Effects of sodium on fatigue and creep-fatigue behavior of Type 304 SS.

The specimens tested under creep-fatigue conditions exhibit a predominantly intergranular fracture (Figure 4.32). The specimen gauge surfaces also showed some differences relative to those from continuous cycle tests; most of the grains showed coarse slip markings and deep grooves or cracks along some of the slip bands. Examination of the longitudinal section of the specimens tested under creep-fatigue conditions revealed several intergranular cracks and cavities in the bulk material away from the specimen surface (Figure 4.33). Bulk cavitation was greater in the large-grained plate material, and was not observed in the tests at low strain amplitudes. It is possible that at low strain amplitudes, cavities that form are too small to resolve.

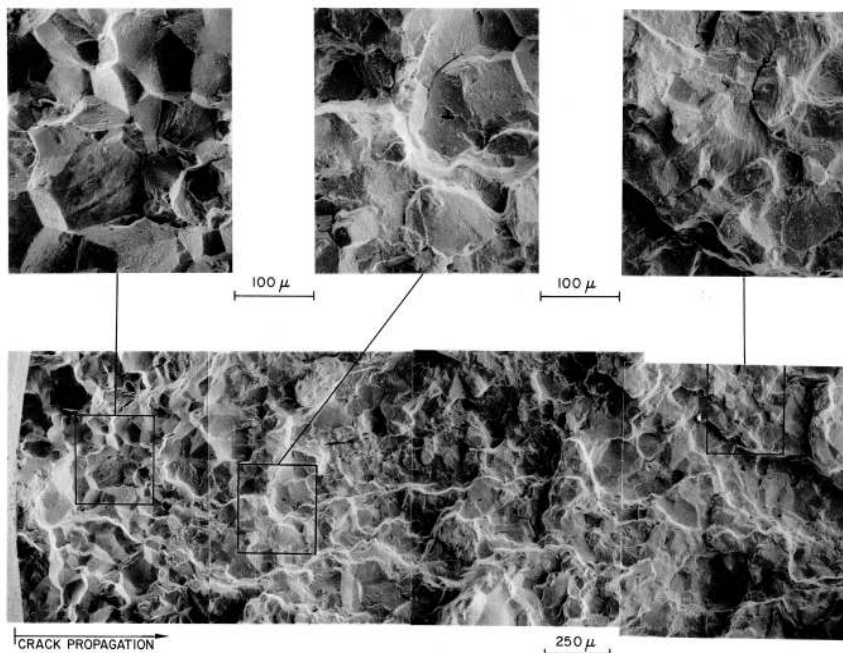


Figure 4.32. Micrographs of the fracture surface of thermally aged Type 304 SS tested in sodium at 593°C with a 600-sec hold period at peak tensile strain.

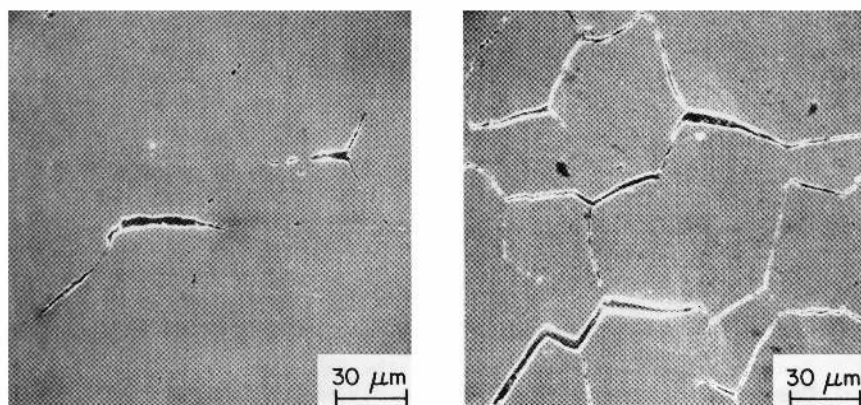


Figure 4.33. Grain boundary cracks and cavities in thermally aged Type 304 SS specimens tested in sodium at 593°C with an 1800-sec hold period at peak tensile strain.

Fatigue Crack Growth

The fatigue crack growth rates (shown in Figure 4.34) for Types 304 SS and 316 LN stainless steels in Na are considerably lower than in air at the same test temperature (James and Knecht 1975). Higher crack growth rates in air are attributed to the oxidation environment compared to an “inert” environment of sodium.

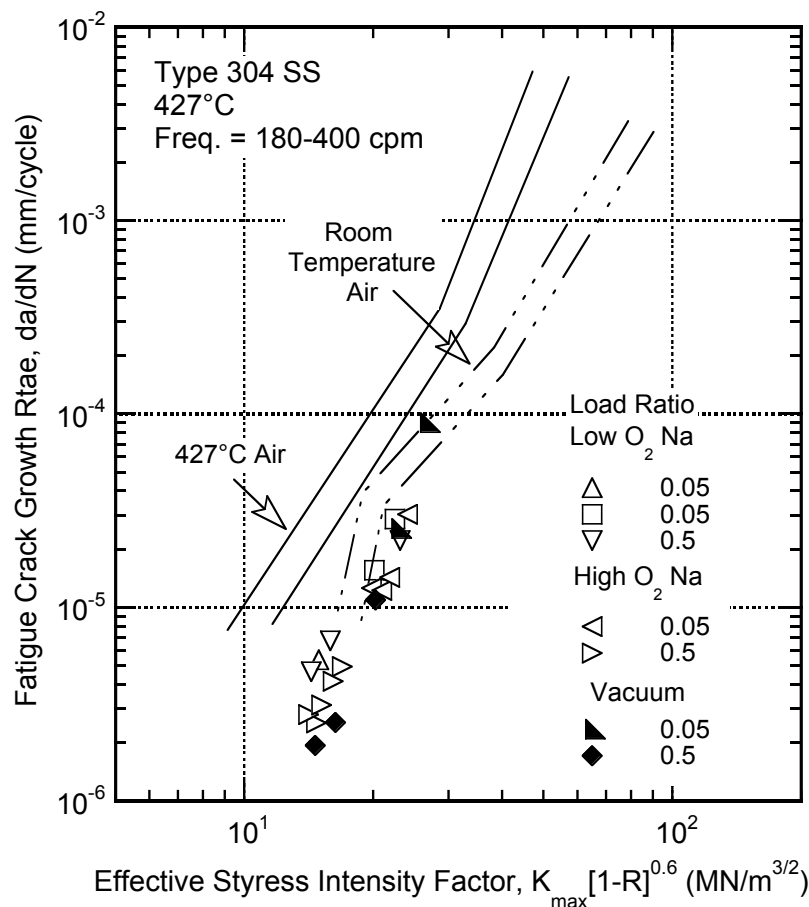


Figure 4.34. Fatigue crack growth rates of 304 SS tested in air, sodium and vacuum (James and Knecht 1975).

4.2.4 Effects of Neutron Irradiation

When exposed to neutron irradiation, structural metallic materials may experience degradation in the mechanical properties that are important to long-time operation of the reactor. Relative to irradiation effects on ARR materials, the structural components of interest are those in the reactor system: reactor vessel, vessel and deck support, guard vessel, and core support structure. Note that fuel cladding materials do not fall within the purview of this project because they do not fall within the domain of structural materials and are not considered by the ASME Code. The ASME Code does not deal directly with environmental issues, including those associated with effects of irradiation. To the extent that irradiation effects are mentioned at all in the ASME Code, there are notes to warn the user that irradiation effects should be considered. However, NRC does consider irradiation effects in its licensing process. In its review of PRISM, the NRC noted that extrapolation of stress allowables to 60 years from the current 34 years is a major issue. This aspect of a 60-year operating license is directly related to irradiation effects, since the effects of longer exposures on materials reliability in an irradiation environment needs consideration. In this regard, however, it is noteworthy that the NRC has approved license extensions to 60 years for more than 40 LWRs.

The NRC noted that effects of irradiation exposure [damage and displacements per atom (dpa) limits] are major issues, as are the absence of in-situ testing/exposure of specimens (e.g., a surveillance program). Another issue noted in that review, also associated with the increased design life, is that of modeling and predictive capability. This issue applies to irradiation effects as well as to material deformation. Thus, although the ASME Code does not include requirements for irradiation effects, the

NRC requires the designer to demonstrate that the structural components subjected to neutron irradiation will maintain adequate material properties to the end of the license period. In the case of LWR pressure vessels, for example, there are predictive correlations available with which one can demonstrate that the proposed material satisfies the guidelines provided. For high temperature components such guidelines do not exist, so a demonstration of adequacy for a given component will require an extensive experimental database and an accepted procedure with which to judge such adequacy.

Radiation damage can produce large changes in structural materials, depending on a variety of factors including temperature and the amount of exposure. Radiation hardening and embrittlement, irradiation-induced creep, volumetric swelling from void formation, high temperature helium embrittlement, and phase instabilities from radiation-induced precipitation are the major effects of concern. The dominant form of irradiation degradation is alloy specific and depends on reactor operating conditions. There are currently five materials (Types 304 and 316 stainless steel, Alloy 800H, 2¹/₄ Cr-1Mo, and 9Cr-1MoV) that are qualified for elevated temperature service in Subsection NH of Section III of the ASME Code. In past liquid-metal reactor research and development programs, the primary material classes investigated were 300 series and modified 300 series austenitic alloys, high nickel alloys (especially the gamma prime and gamma double-prime precipitate-strengthened alloys), and ferritic and ferritic-martensitic (F-M) alloys. Information has been liberally extracted from an unpublished report by Mansur et al. (2005) and presented in the following subsections.

The austenitic stainless steels offer a number of positive attributes for application in the ARR. There is a large database of experience with these alloys that covers a wide range of radiation dose, temperature, and loading conditions. They have a very mature industrial infrastructure, including fabrication, joining, and demonstrated compatibility in sodium. From the irradiation effects perspective, they have fair radiation resistance (those variants developed specifically for swelling resistance). However, stainless steel is known to experience several forms of irradiation-induced degradation (Ehrlich et al. 2004, Bloom et al. 2007, Klueh 2004, Busby et al. 2007, Busby and Leonard 2007, Maloy 2007, Lucas 1993, Garner 1994, Harries 1979). These include reduced uniform elongation for irradiation below $\approx 400^{\circ}\text{C}$, swelling above irradiation temperatures of $\approx 330^{\circ}\text{C}$, irradiation creep and He-embrittlement at even higher temperatures and high neutron fluences. Alloys not designed for resistance to swelling should not be used in applications where radiation exposure is greater than about 15 dpa. Those developed for swelling resistance can be used to about 100 dpa. Of course, volumetric swelling is temperature dependent with significant effects in the range of 350-600 $^{\circ}\text{C}$ and with peak swelling occurring at about 500 $^{\circ}\text{C}$; there is also some dependence on the dose rate. At temperatures below 300 $^{\circ}\text{C}$, irradiation-induced hardening and loss of ductility are factors, whereas at temperatures above $\approx 550^{\circ}\text{C}$ helium embrittlement is of concern.

The most important variable for effects of irradiation on physical and mechanical properties is the irradiation temperature, both in terms of which properties are changed and magnitude of the changes. Figure 4.35 shows microstructures for unirradiated material and for irradiated stainless steels at three different temperatures (Mansur and Bloom 1982). For a given dose and irradiation temperature, specific irradiation-induced defects are responsible for such changes in properties. Precipitates, voids, dislocation loops, and helium bubbles generally increase in size and decrease in concentration as irradiation temperature increases. Relative to irradiation-induced precipitates, the concentrations, sizes and compositions are different with respect to what would result from thermomechanical treatments without irradiation (Lee et al. 1981). At higher temperatures, equilibrium bubbles, which often occur on grain boundaries, are the main stable radiation produced defect.

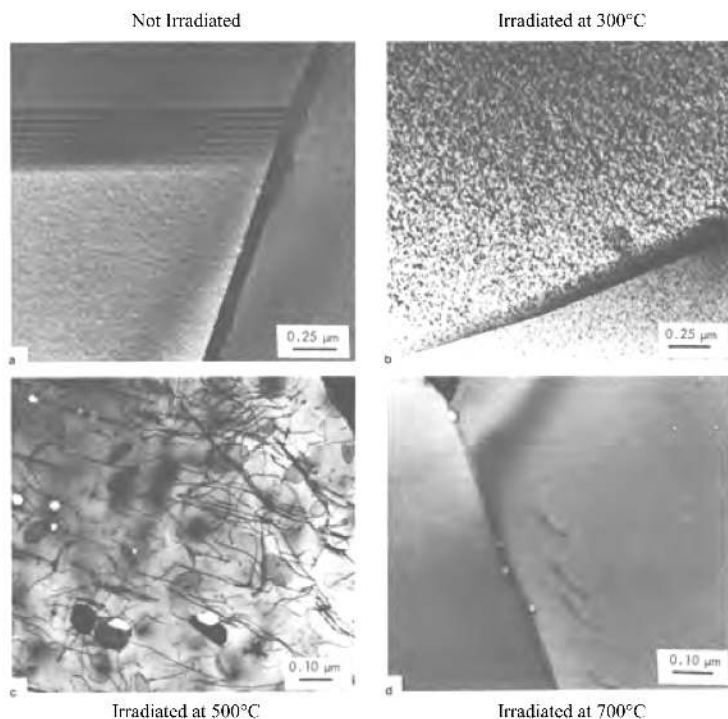


Figure 4.35. Defects produced in annealed 300 series stainless steel during neutron irradiation in a fast reactor, as observed by transmission electron microscopy (TEM): a) microstructure of material before irradiation, b) dislocation loops formed during irradiation at 300°C ($\approx 0.35 T_m$), c) dislocation loops, voids, dislocation networks and precipitates formed during irradiation at about 500°C ($\approx 0.47 T_m$), d) helium bubbles on a grain boundary formed during irradiation at about 700 °C ($\approx 0.59 T_m$). After Mansur and Bloom (1982).

For compositions similar to Types 316 and 304 there is by far the highest concentration of neutron and ion irradiation data available for any material, developed in This is because alloys in the composition range were being qualified for service in the cladding and duct program of the DOE for the LMFBR through extensive reactor irradiation experiments (Garner 1994), as well as to understand the basic physical mechanisms of swelling in the basic radiation effects program of the DOE (Mansur 1994). In addition, alloys in this composition range are of interest for other nuclear systems; e.g., 316LN stainless steel has been specified for the first wall of the International Thermonuclear Experimental Reactor (Tavassoli 2002), and has also been recommended for the spallation target container of the Spallation Neutron Source. Many reviews of swelling in stainless steels are available: Theory and modeling of swelling are developed and related to experimental observations (Mansur 1987). The wide range of variables that influence swelling is reviewed in (Rowcliffe and Grossbeck 1984, Maziasz 1993, Zinkle et al. 1993, Garner 1994).

In stainless steels, not designed to be swelling resistant, swelling can reach several percent at ten dpa and can reach tens of percent at doses in the range 40-50 dpa. The swelling at a given dose depends strongly on the major constituents of the particular alloy, solute and impurity content, thermomechanical pretreatment, irradiation temperature, dose rate, and other material or environmental factors. The onset of swelling, often referred to as the incubation dose, varies markedly for different alloys. Figure 4.36 shows a good example of this variability for various stainless steel fast reactor fuel cladding alloys irradiated in the EBR-II reactor at temperatures in the range 450 to 500°C (Makenas et al. 1982). In this figure the fast neutron fluence is plotted on the x-axis. It can be translated to dpa by the conversion $10^{23} \text{ n/cm}^2 \approx 50 \text{ dpa}$.

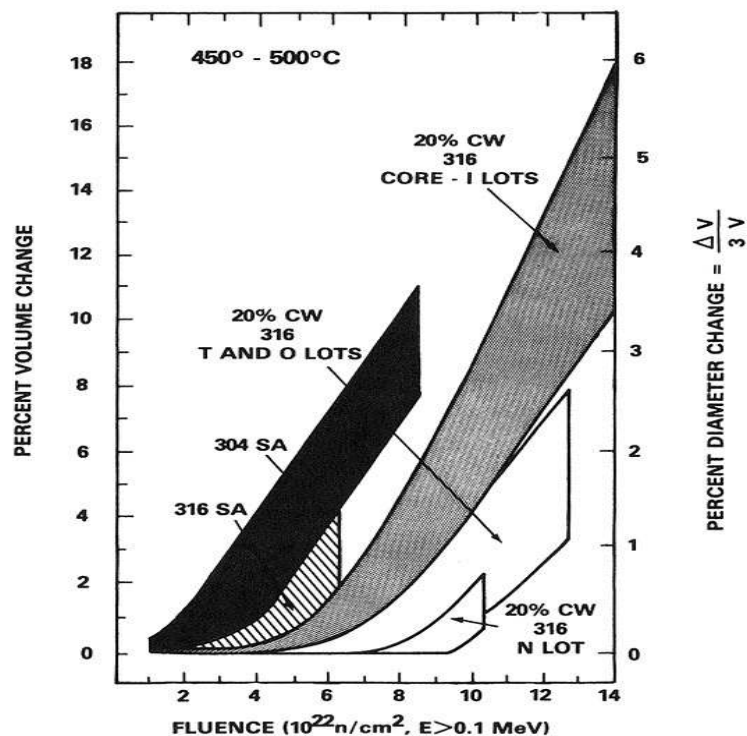


Figure 4.36. Fuel pin cladding swelling for several Type 304 and 316 stainless steels versus fast neutron fluence for irradiations in the EBR-II reactor at 450 to 500°C. After Makenas et al. (1982).

Based upon the initial experiences with the phenomena of void swelling and grain boundary embrittlement encountered in the 300 series stainless steels, a number of improved alloys were developed by the international community, for fast breeder reactor and fusion reactor applications. Many of these advanced alloys have been produced in a variety of product forms on a commercial scale. Within the family of advanced austenitic steels candidate compositions include: a) composition-restricted 316 stainless steels with nitrogen modifications such as the French breeder-reactor program 316 and the Japanese 316FR; b) 316-type microalloyed with Ti, B and P such as the Japanese PNC 316, and the US D9 alloys and HT-UPS alloys; and c) more highly alloyed versions such as the French 15Cr-15Ni-Ti and the 12Cr-25Ni-Ti alloys. Many of these materials have demonstrated swelling incubation regimes up to 130 dpa and many of them also exhibit superior creep strength relative to 316 stainless steel. Garner and Gelles (1990) assembled swelling data vs neutron fluence for 20% cold-worked stainless steel at irradiation temperatures from 400 to 650°C, as shown in Figure 4.37. They observed that the eventual swelling rate of 316 at all temperatures is $\approx 1\%/dpa$ and that the temperature dependence lies only in the duration of the transient regime (e.g., see plot for data at 400°C).

Irradiation creep is a time-dependent plastic deformation process driven by irradiation and by the presence of an applied stress. It occurs in excess of the well-known thermal creep seen at high temperatures, which is driven by thermal vacancy formation and diffusion as well as by other thermally activated processes. Irradiation creep exhibits different stress and temperature dependencies than thermal creep. For stainless steels, thermal creep is not of concern below about 550°C, but increases exponentially with temperature above that range. The exact borderline temperature depends on stress and can be lowered somewhat for very high stresses. However, irradiation creep occurs at all temperatures of interest and has lower temperature dependence than thermal creep--in some cases it appears to have little or no temperature dependence.

At very high temperatures irradiation creep can be ignored because it is insignificant compared to thermal creep. However, it can be a very important deformation mode at intermediate and low

temperatures, e.g., in the temperature regime of 330 to 600°C. Extensive data on irradiation creep from US and worldwide reactor irradiation programs are reviewed by Garner (1994). Observed temperature,

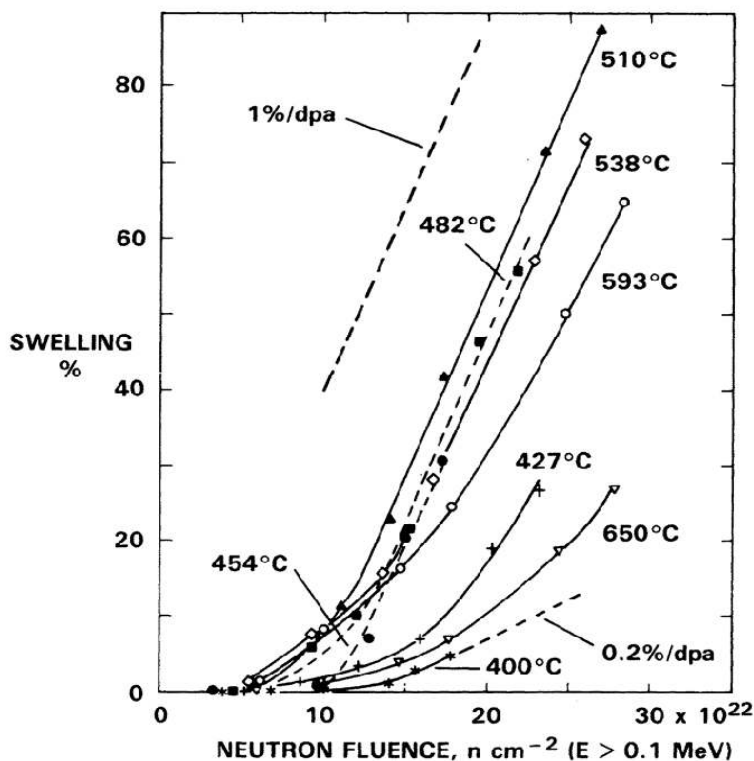


Figure 4.37. Swelling of 20% cold-worked 316 stainless steel vs. neutron fluence (>0.1 MeV) for irradiations in EBR-II. After Garner and Gelles (1990).

stress, dose rate, and other dependencies are compiled there. In the literature, the observed irradiation creep for steels has sometimes been characterized by an empirical coefficient $B = \Xi/\Phi$, giving the creep rate per unit displacement damage and per unit stress, where Ξ is the effective creep rate per unit dpa and Φ is the effective stress in MPa. To develop empirical correlations, sometimes this creep coefficient, rather than the creep rate itself, is plotted versus other parameters such as temperature or dose rate. Typical values for the irradiation creep compliance coefficient, B , for stainless steels with compositions near the Type 300 series specifications are of the order of several $\times 10^{-6}$ MPa⁻¹dpa⁻¹ (Uehira et al. 2000).

Figure 4.38 gives a convenient summary of creep rupture performance in the unirradiated condition for stainless steels together with other alloy systems, including ferritic/martensitic steels, high nickel superalloys, and refractory alloys (Tavassoli 2002). Figure 4.39 summarizes the stress-temperature design window for Type 316 stainless steel (Zinkle et al. 2002). This analysis is based on the extensive experimental database on tensile properties and thermal creep (Grossbeck et al. 1990, Tavassoli 2001) for stainless steel. The maximum stress limit at 423-823K is defined as 1/3 ultimate tensile strength, which is a more conservative design limit than 2/3 of the yield stress for stainless steel. The stress limit at high temperatures is defined as 2/3 of the creep rupture strength in this plot. To account for the influence of irradiation, a lower temperature limit is set at 1/3 T_m in order to avoid low-temperature radiation embrittlement. This operational window may be further adjusted by accounting for any potential corrosion effects. As mentioned earlier, they may also need to be adjusted for the effects of irradiation creep at intermediate temperatures.

In many different austenitic stainless steels, similar behavior is seen, even to the point of nearly identical saturation values of yield strength under given temperature and dose conditions. Although the trend of lowered ductility with increasing dose is also similar for the stainless steels, the numerical values

can vary somewhat more than the yield strength values. At low irradiation temperatures the hardening can be quite high, with the yield strength increasing by a factor of up to four. At higher temperatures the

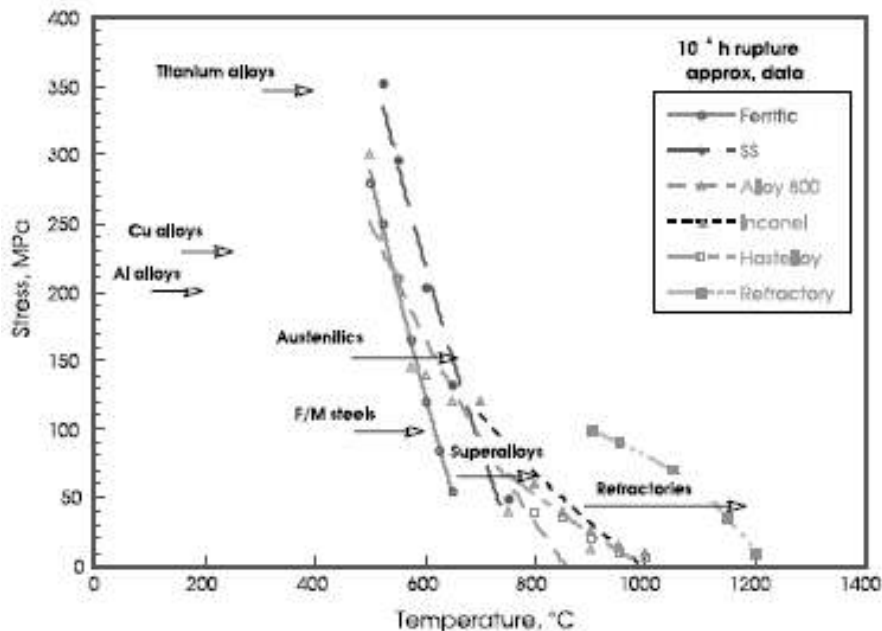


Figure 4.38. Approximate upper temperature limit of austenitic stainless steels compared to other structural materials based on 10^4 h creep-rupture time. After Tavassoli (2002).

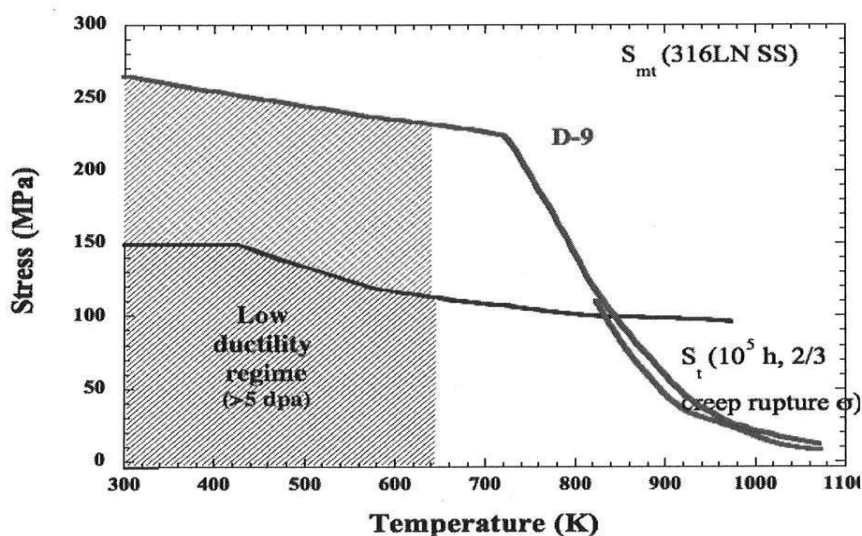


Figure 4.39. Temperature window based on the maximum design stresses versus temperature, which define the allowable operating limits for type 316 and D-9 stainless steel structural components. After Zinkle et al. (2002).

increase is lower. Figure 4.40 shows the yield strength as a function of temperature for Type 316 stainless steels and variants of this material, termed prime candidate alloys for fusion reactors, which have lower chromium and higher nickel than type 316 and are titanium stabilized (Pawel et al. 1996). It can be seen that the irradiated values are in the range 2-4 times higher than the unirradiated values and that hardening in the irradiated materials shows higher values near 300°C. Figure 4.41 shows data from Garner et al. (1981) for Type 316 stainless steel in both the annealed and 20% cold-worked conditions. At an irradiation temperature of 538°C, the yield strengths of the material in both conditions appears to stabilize at about 400 MPa and at about 2×10^{22} n/cm², with the cold worked material exhibiting softening and the annealed material hardening. In contrast, the results at 427°C indicate irradiation-induced hardening for both material conditions with yield strength stabilization occurring at about 4×10^{22} n/cm² and at somewhat less than 800 MPa. Assuming the same conversion as for the EBR-II, those fluences

convert to 10-20 dpa and show similar results to those in Figure 4.40. Such a high degree of hardening implies significant effect on degradation of fracture toughness.

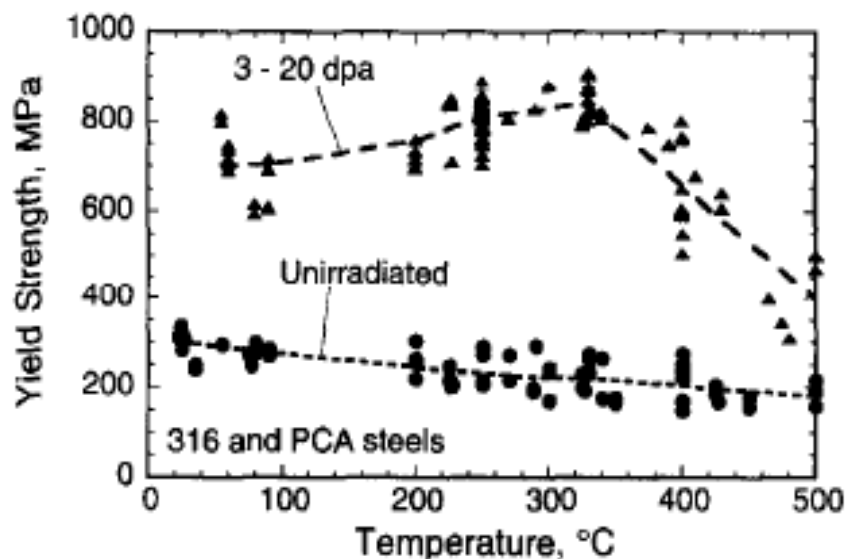


Figure 4.40. Yield strength as a function of temperature for several solution annealed type 316 and PCA materials irradiated in a variety of reactors. In each case, the irradiation temperature is equal to the test temperature. The neutron doses range from 3 to 20 dpa. After Pawel et al. (1996).

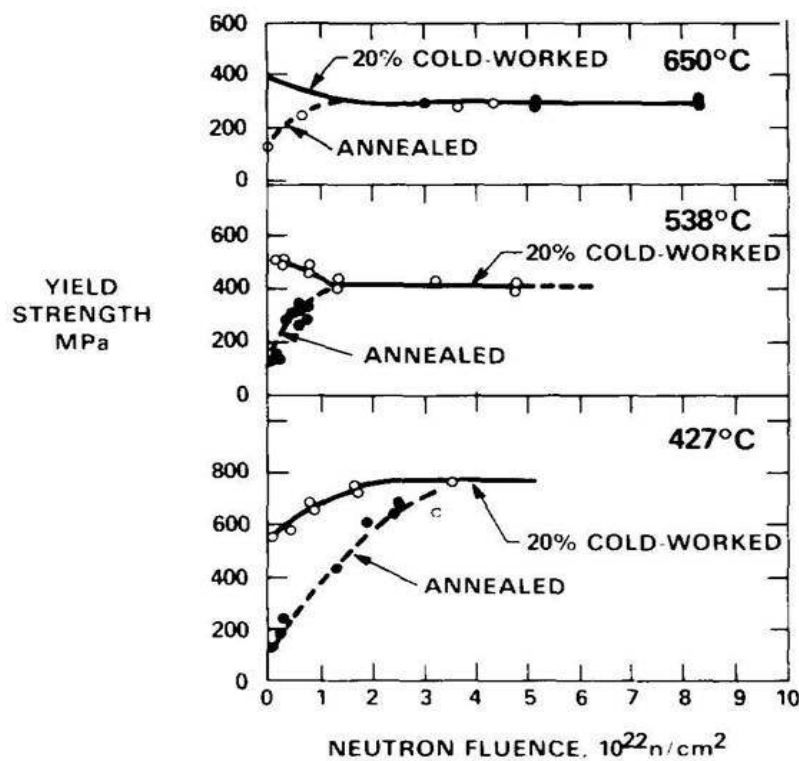


Figure 4.41. Yield strength as a function of fluence for AISI Type 316 stainless steel irradiated in the EBR-II reactor to demonstrate progression to steady state values. After Garner et al. (1981).

Mills (1986) reported results of tensile and fracture toughness testing with various stainless steel base and weld metals irradiated between 400 and 427°C and with all testing performed at 427°C. Irradiation exposures ranged from 1.5 to 28 dpa for the tensile tests and from 14-17 dpa for the fracture toughness tests. For annealed Type 316 stainless steel, yield strength increased from 165 MPa in the unirradiated condition to 544 and 644 MPa after exposures to 10 and 16 dpa, respectively. The yield strength value after 16 dpa is somewhat close to those reported by Garner et al. (1981) in Figure 4.41, but

the increase in yield strength with dpa exposure was much slower. The tensile results reported by Mills (1986) for Type 304 base metal and type 308 weld metal were similar to those of the type 316, even though the unirradiated yield strength of the 308 weld metal was 312 MPa. Figure 4.42 shows a comparison of the J-R curves for the two base metals and one weld metal in unirradiated and irradiated conditions for the data at 10-17 dpa (Mills 1986). As shown in that figure, the J-R curves have been significantly decreased by irradiation, as reflected both by the critical J-integral (J_c) and tearing modulus (T) results shown on the figure.

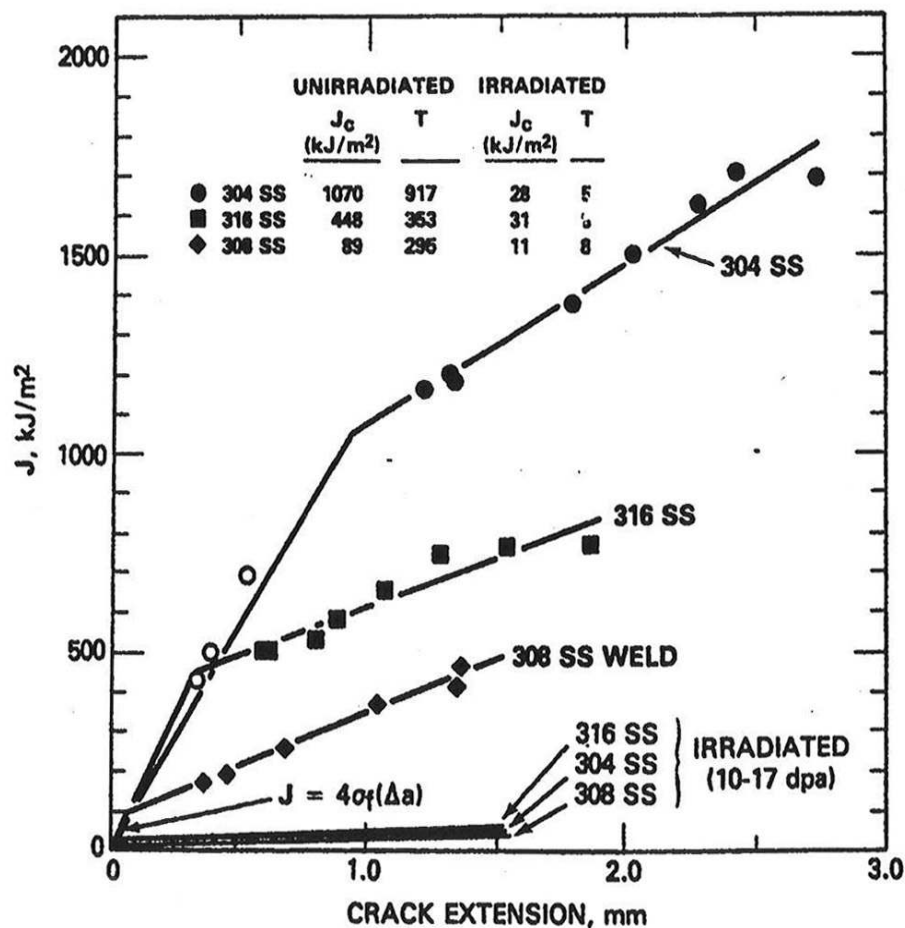


Figure 4.42. Comparison of J_R curves for unirradiated and irradiated 316 SS, 304SS and 308SS weld at 427°C. Note that stretch zone data points (denoted by open symbols) are in agreement with the blunting line for high strain-hardening materials. After Mills (1986).

Figure 4.47 shows the J-R curves for the irradiated materials only and shows somewhat higher toughness for the Type 316 stainless steel compared with the Type 304 and Type 308 weld metal. Moreover, inspection of the data in Figure 4.47 shows that the effects of irradiation were significantly less on Type 316 than in Type 304. Mills also compared his results with literature data, shown in Figure 4.48, including two data points for Inconel 600 and Incoloy 800. These stainless steel data show higher fracture toughness for base metal than weld metal in the post-irradiation condition.

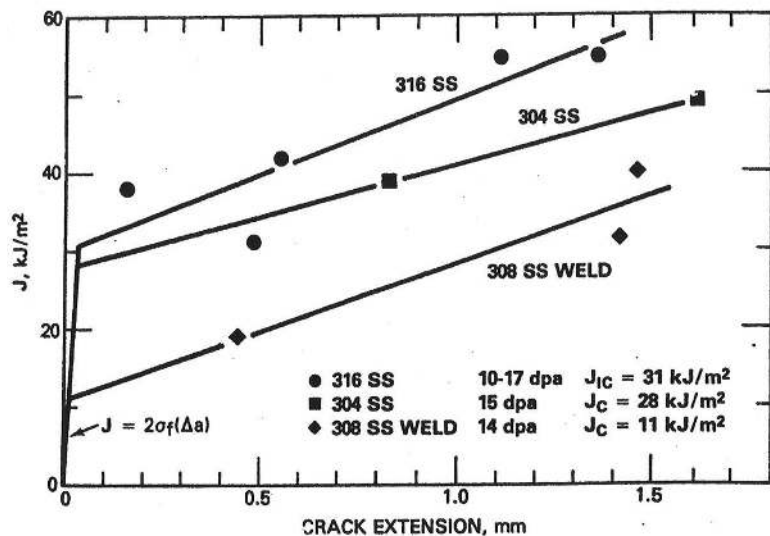


Figure 4.43. J_R curves for 316 SS, 304SS, and 308SS weld at 427°C. After Mills (1986).

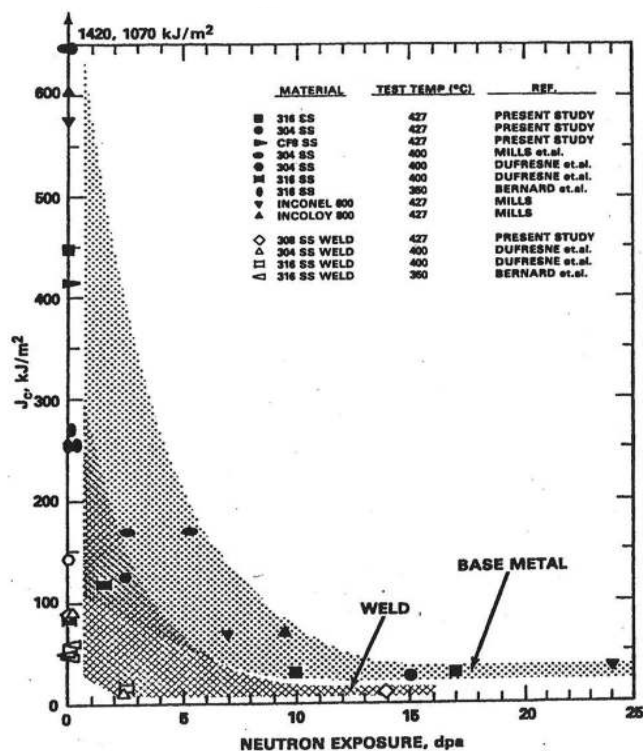


Figure 4.44. Summary of J_c fracture toughness behavior as a function of neutron exposure. After Mills (1986).

Other fracture toughness results for various stainless steels, both base metals and weld metals are shown in Figure 4.45 (Van Osch et al. 1998). The degradation of the normalized fracture toughness (normalized by dividing the toughness at 1 mm crack extension by J_{1mm} before irradiation), is plotted as a function of dose level together with various other austenitic plate and weld metal data. As stated by Van Osch et al. (1997), “Remarkably, it turns out that the degradation of fracture toughness by irradiation is similar for many materials, even when irradiated and tested at very different temperatures (range 350–725K).” Another comparison of fracture toughness data for various stainless steels is shown in Figure 4.46 (Chopra and Natesan 2007). This figure shows effects similar to those in Figure 4.44 from Mills, and includes the Mills data as well as more recent data from other sources. Note that the closed symbols in the left hand graph are for data in BWR water, while the open symbols are for data obtained in air.

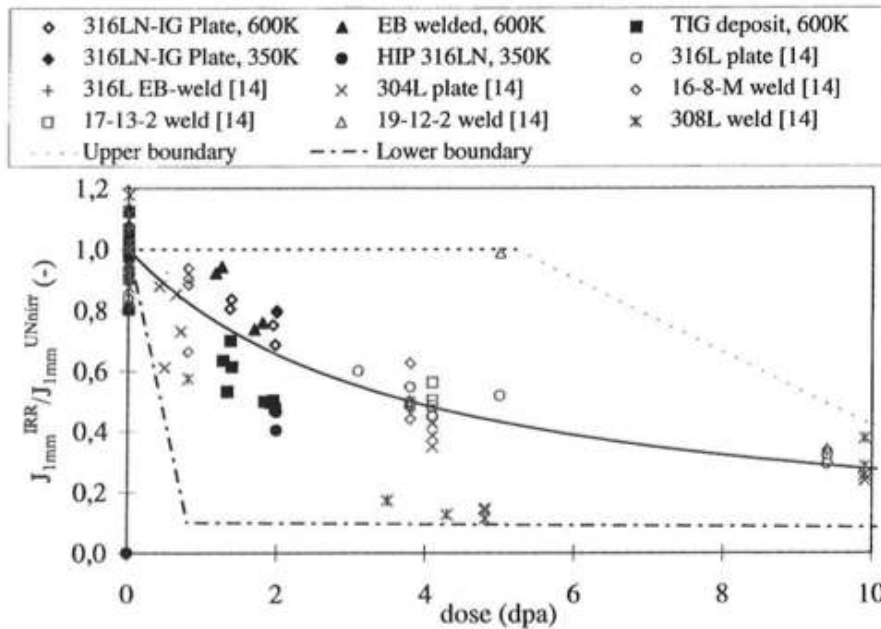


Figure 4.45. Irradiation degradation of fracture toughness austenitic stainless steels and weld metals. After Van Osch (1998).

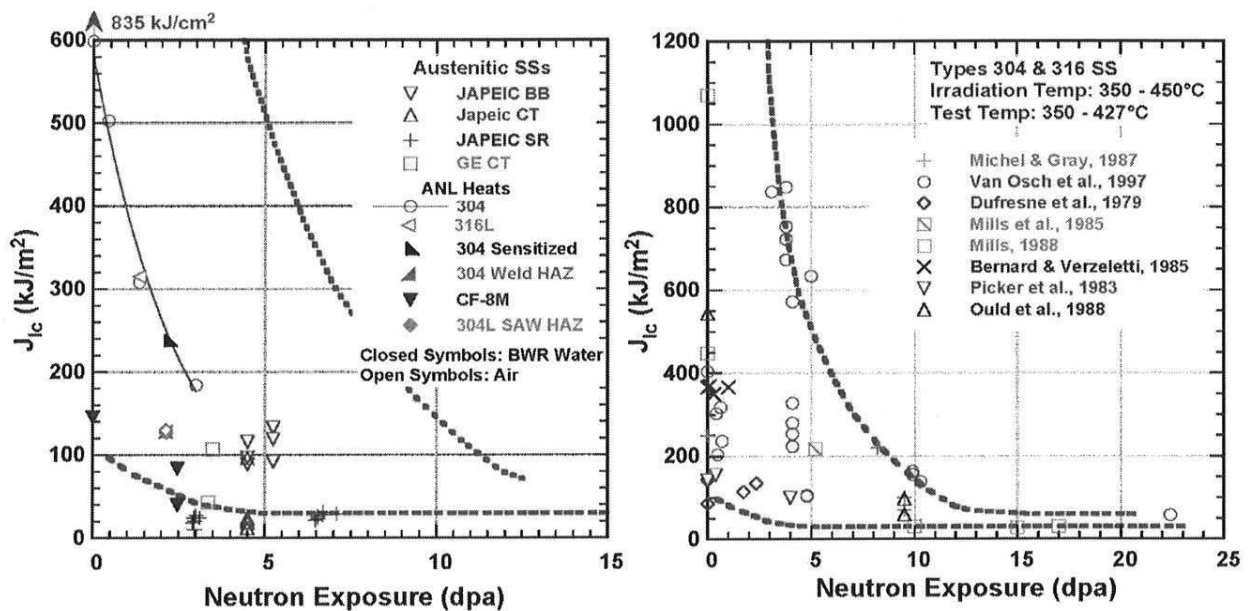


Figure 4.46. Fracture toughness, J_{1c} , vs. neutron exposure in dpa for a variety of austenitic stainless steel base metals, weld metals, and heat-affected zones. (Chopra and Natesan 2007).

In summary, radiation-induced swelling is of concern from ≈ 350 to 600°C , with peak swelling at $\approx 500^\circ\text{C}$ for high dose rates of $\approx 10^{-7}$ to 10^{-6} dpa/s, and at somewhat lower temperatures for lower dose rates. However, stainless steels designed for swelling are relatively resistant to ≈ 100 dpa. At temperatures below 300°C , irradiation-induced hardening and loss of ductility are factors, whereas at temperatures above $\approx 550^\circ\text{C}$ helium embrittlement is of concern. Irradiation creep is not a strong function of temperature, and at very high temperatures irradiation creep can be ignored because it is insignificant compared to thermal creep. However, it can be an important deformation mode at intermediate and low

temperatures, e.g., in the temperature regime of 330 to 600°C, applicable to the ARR operating temperature range. It is apparent that irradiation exposures of Types 304 and 316 stainless steels and Type 308 weld metal experience significant loss of fracture toughness at irradiation temperatures below 500°C and at dpa levels of about 5 dpa and higher.

Synergetic Effects of Sodium and Irradiation on Creep

Ukai et al. (2000) reported the data on Type 316 SS tested in-reactor in sodium over the temperature range from 605 to 750°C using MOTA of FFTF. It was found that in-reactor creep rate was significantly higher and creep rupture lives were shorter than those of the out-of-reactor tests, even though creep ductility was retained under irradiation. The Larson-Miller plots of in-air, in-sodium and in-reactor data shown in Figure 4.47, indicate that creep rupture strength is not affected by sodium exposure only when the LMP <16.5; significant effects of sodium occur above that value. Combined effects of sodium and irradiation cause a remarkable reduction in rupture strength throughout the LMP range.

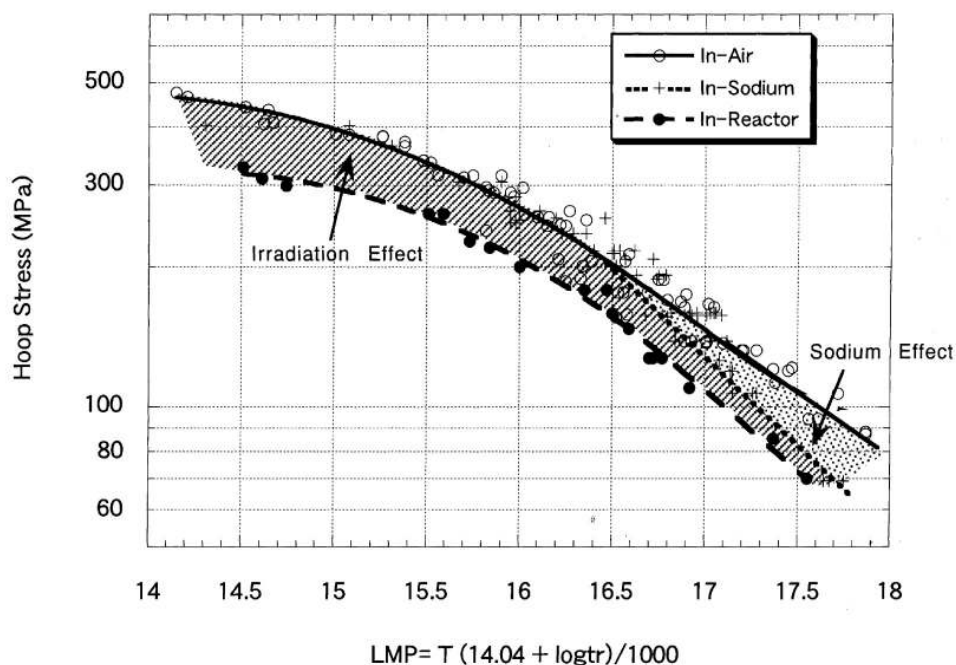


Figure 4.47. Effects of sodium and irradiation on creep rupture properties of 316SS. After Ukai et al. 2000.

4.2.5 316 FR and 316LN Stainless Steels

Type 316L(N) stainless steel is a modified version of conventional Type 316 SS with lower carbon and higher nitrogen content to improve high temperature performance and corrosion resistance. It offers good combination of tensile properties, toughness, creep properties, and enhanced resistance to sensitization and associated intergranular cracking relative to conventional 316 SS. There are various versions of 316L(N) depending on the country of the origin. 316L(N) has been used in several fast reactors in Europe, including Rapsodie, Phenix, and Superphenix (Tavassoli 1995). It has been qualified by the French design and construction rules for nuclear components (RCC-MR). 316FR is a Japanese version of 316L(N) developed for applications in reactor vessel and internals for the Japanese demonstration fast breeder reactor (JDFBR). 316FR has slightly lower nitrogen content than in the American grade, AISI 316L(N). Extensive research has been conducted on both 316L(N) and 316FR, and there is increased interest to include 316FR or 316L(N) in the ASME Subsection NH.

316LN-IG is an ITER grade 316LN with even lower nitrogen content than in 316FR. It is the main structural material for the ITER vacuum vessel and in-vessel components (Barabash et al. 2007). 316LN-IG has higher allowable stresses than typical 316LN due to an optimal combination of the alloying elements such as carbon, nitrogen, nickel, chromium, manganese and molybdenum, with a tight specification of their allowable composition range. A comprehensive database has been established on 316LN-IG, including heat-to-heat variations, the effect of product size, fracture toughness, effects of neutron irradiation, etc., and the data can be found in the ITER Materials Properties Handbook (MPH) (ITER MPH 2007). The design properties of 316LN-IG are included in the RCC-R Code. The main reasons for the selection of 316LN-IG are (Tavassoli 1995):

- High mechanical strength
- Good combination of strength and toughness
- Small heat variations
- Good resistance to stress corrosion cracking of both base metal and weld metal
- Resistance to hot cracking
- Less sensitive to irradiation hardening and irradiation embrittlement.

The chemical compositions of 316LN, 316LN-IG, and 316FR stainless steels are given in Table 4-11 (Asayama 2001, Tavassoli 1995, Brinkman 2001). Significant data base of tensile, creep, fatigue and creep-fatigue properties of 316FR and 316LN base metal and weld metal can be found in the RCC-MR, ITER MPH and open literature. There is also an extensive database on 316LN from fast reactor and fusion reactor materials program, though neutron irradiation data obtained in fusion materials program are mainly at lower temperatures. Data on sodium effects of 316LN and 316FR are limited. Here, we focus on several prominent issues, including heat variations and product form and size effects, creep and creep-fatigue properties and high temperature design rules, sodium effects, neutron irradiation effects and weldments, and compare 316LN and 316FR with conventional 316SS.

Table 4.11. Chemical composition of 316FR.

	C	Si	Mn	P	S	Ni	Cr	Mo	N	B
316	≤0.08	≤0.75	≤2.00	≤0.045	≤0.030	10-14	16-18	2-3	≤0.10	
AISI 316LN	≤0.03					10-14	16-18		0.18-0.25	
316LN-IG	0.015-0.03	0.50	1.6-2.0	0.025	0.005-0.010	12-12.5	17-18	2.3-2.7	0.06	0.002
316FR	0.01	0.52	0.86	0.024	0.004	10.59	16.58	2.14	0.08	0.003

Tensile Properties

Tavassoli (1995) summarizes the tensile properties of 316LN-IG of several heats and a wide range of product forms and sizes, and thermal aging effects on tensile properties. As shown in Figure 4.48, there is a large scatter of tensile stress data due to variation in alloy grade and product forms and sizes. Data of long-term thermal aging up to 50,000 h at 650°C fall within the scatter band.

Creep and Creep-Fatigue Properties and High Temperature Design Rules

Significant work has been carried out to evaluate the creep and creep-fatigue of 316FR in recent years in the Japan fast reactor programs. Figure 4.49 shows the stress-rupture data for 316FR and 316LN

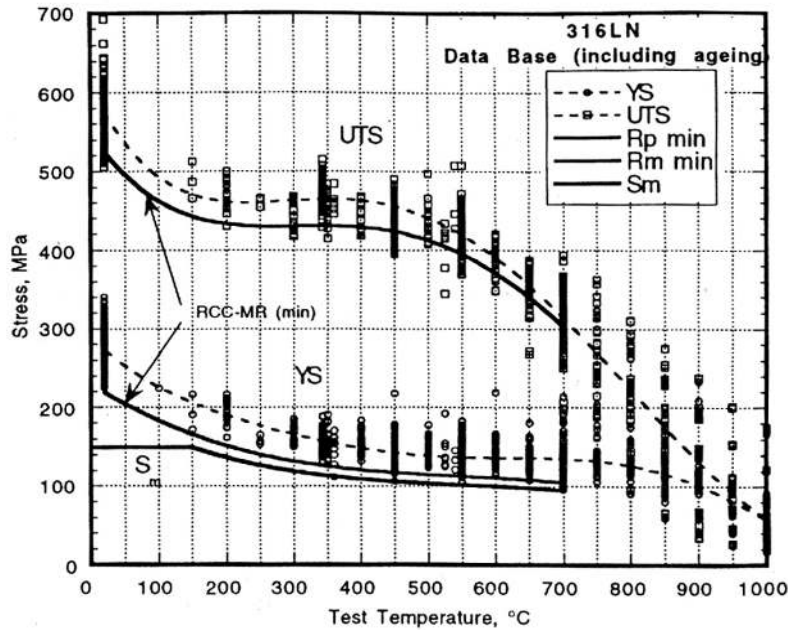


Figure 4.48. The yield stress and ultimate tensile stress of 316LN-IG for several heat variants and product forms and sizes (Tavassoli 1995).

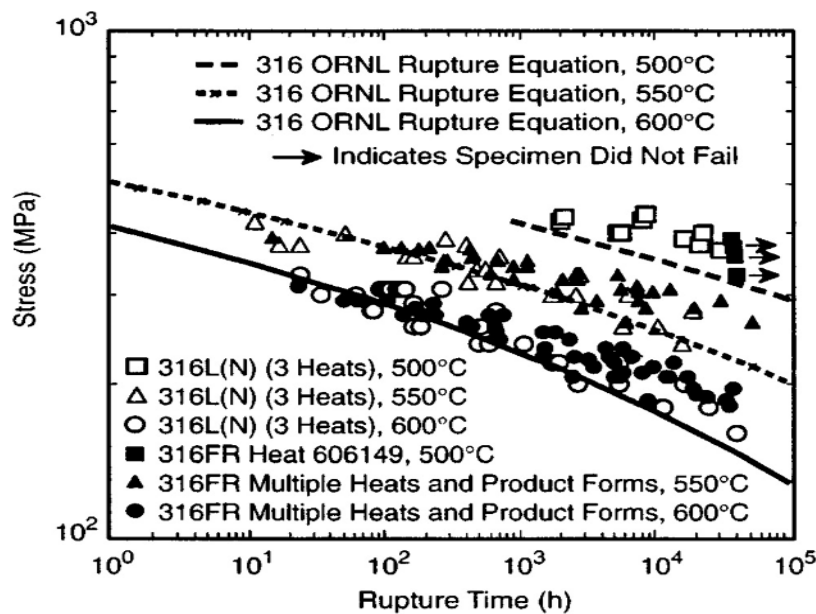


Figure 4.49. Stress-rupture data for 316FR, 316LN and 316 stainless steels (Brinkman 2001).

stainless steels tested at 500, 550 and 600°C (Brinkman 2001). The data set consist of data for several heats and various product forms (e.g. plate, forging and tubing). The creep rupture life of 316FR and 316LN are significantly longer than conventional 316SS particularly at lower stress levels. Improvement in creep ductility in 316FR was also observed.

Fatigue data of 316FR are shown in Figure 4.50, and compared with conventional 316SS (Brinkman 2001). Fatigue lives of 316FR and 316 are almost the same at 500-600°C. However, when hold time was applied to the cyclic loading, 316FR showed significantly improved creep-fatigue resistance over 316SS as shown in Figure 4.51 (Brinkman 2001). The improvements were more pronounced at longer hold time and at lower strain ranges. For both 316FR and 316 stainless steels, the fatigue life continuously decreases with increasing hold time at a given strain range level. Recent works

on creep-fatigue evaluation methods for 316FR showed that ductility exhaustion method may predict the creep-fatigue life for a wide range of strain ranges and hold time periods (Takahashi et al. 2008).

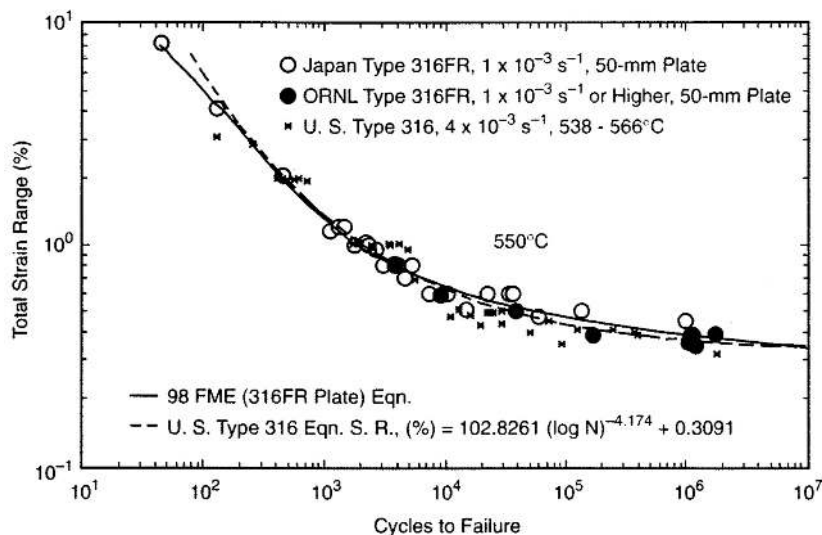


Figure 4.50. Fatigue data of 316FR and 316 stainless steels (Brinkman 2001).

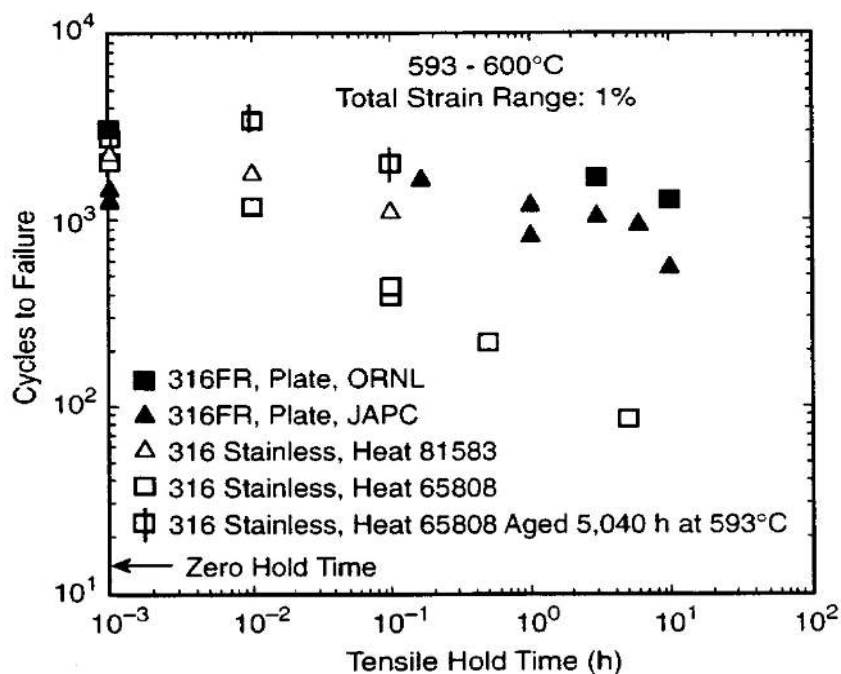


Figure 4.51. Creep-fatigue data for 316FR and 316 stainless steels (Brinkman 2001).

The effect of ratcheting on fatigue and creep-fatigue life was investigated on 316FR (Date et al. 2008, Isobe et al. 2008). It was found that tensile ratcheting significantly reduces the fatigue life at small strain ranges, while compressive ratcheting has no effect on the fatigue life.

316FR and 316LN Weldments

Significant progress has been made in recent years to evaluate the weld metals of 316LN and 316FR in the unirradiated and irradiated conditions. The ITER MPH has been extended to include weld metals of 316LN-IG, the RCC-MR has been used for data analysis and determination of allowables

(Tavassoli 2007). The ITER MPH includes the code recommendations and additional material property data such as neutron irradiation effects not covered by the RCC-MR. For weld joints, special attention was paid to weld condition, weld positions, weld sections, etc.

Creep rupture data of 316LN weldments at temperatures of 550-650°C reported by Mathew et al. (2005) showed that the base metal has the highest rupture strength, followed by the weld joint, and the weld metal has the lowest rupture strength, as shown in Figure 4.52 (Mathew et al. 2005). The weld strength reduction factors for 316LN weld joints recommended by the RCC-MR are 0.73 at 550°C, 0.70 at 600°C, and 0.63 at 650°C for a rupture time of 100,000 h. The strength reduction factors determined by using the experimental data of the strength of base metal and the strength of weld metal or weld joint are much higher than the RCC-MR values. The creep ductility of the weld metal and the weld joint is much lower than that of the base metal at high temperature (e.g. 600°C shown in Figure 4.57). The ductility loss during high temperature creep deformation was associated with the phase transformation of delta-ferrite in the weld metal. Transformation of delta-ferrite to sigma phase was slow at 550°C, while the entire delta-ferrite transformed to sigma phase in 300 hours at 650°C (Mathew et al. 2005, Asayama and Hasebe 2000).

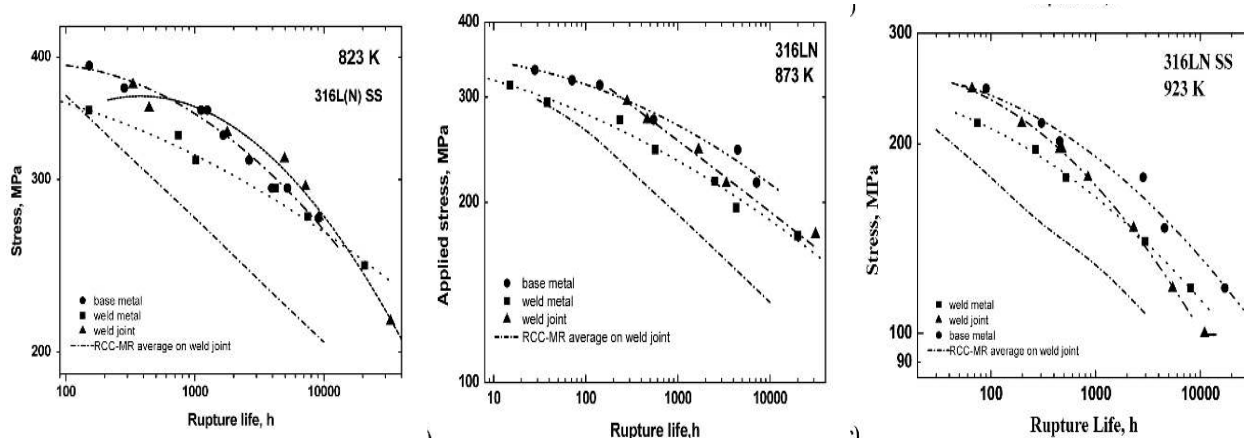


Figure 4.52. Stress rupture curves of base metal, weld metal and weld joint and RCC-MR curves at temperatures of 550, 600, 650°C (Mathew et al. 2005).

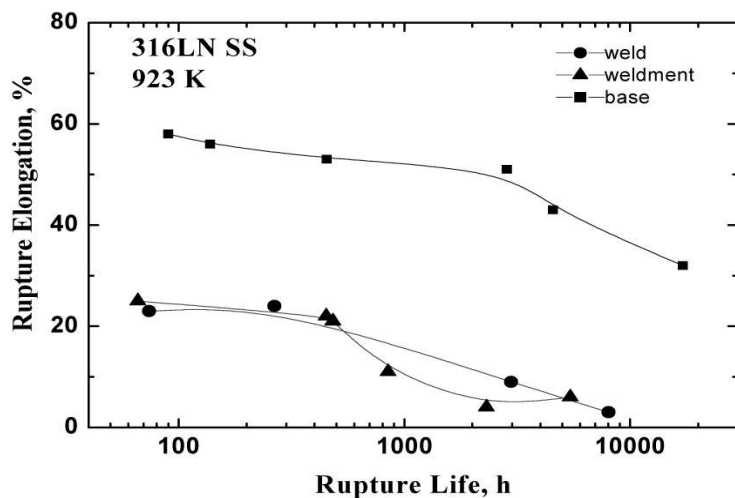


Figure 4.53. Change in rupture elongation with rupture life at 600°C in 316LN (Mathew et al. 2005).

Figure 4.54 compares the fatigue and creep-fatigue results of weld metal and base metal of 316FR tested at 550°C (Asayama 2000). The fatigue life of weld metal is nearly the same as that of the base metal. However, the creep-fatigue life of the weld joints is considerably lower than that of the base metal. The creep-fatigue damage in weld joints was suggested to be attributed to stress/strain concentration within a joint and the strength variations across the weld joint. A creep-fatigue evaluation method for 316FR weldments has been proposed.

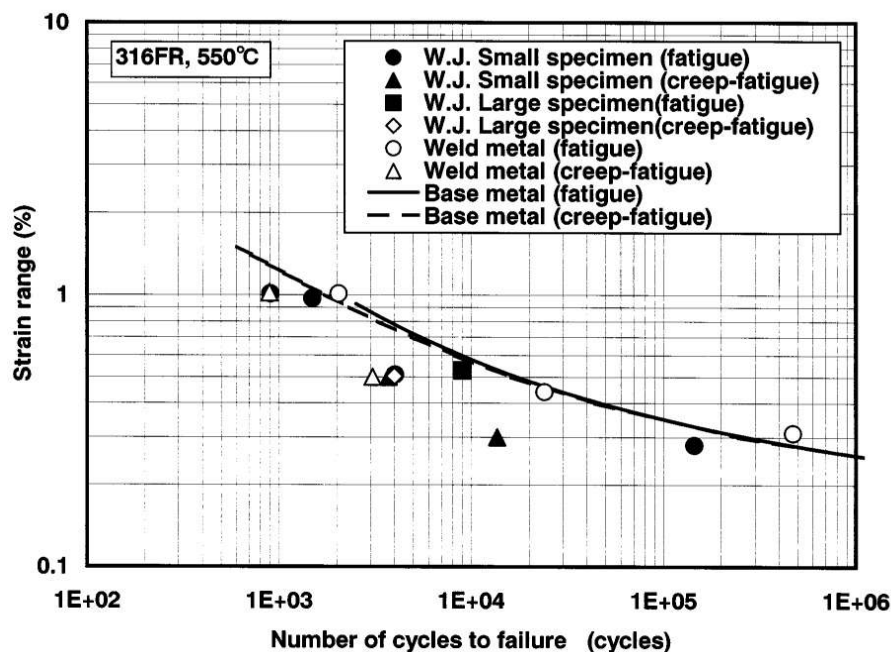


Figure 4.54. Fatigue and creep-fatigue results of weld metal and base metal for 316FR tested at 550°C (Asayama 2000).

Effects of Sodium Exposure

Studies on the effects of sodium exposure have been done primarily on 316FR by the Japanese fast reactor program (Asayama et al. 2001). They discussed the material degradation issues in sodium environment and the evaluation procedures to account for the sodium effects. It was found that corrosion mechanisms in sodium in 316FR are the same as in conventional 316 SS. No pitting corrosion, excoriation of surface grains, or grain boundary corrosion was observed. The corrosion rate was 3×10^{-7} m/yr at 550°C in sodium at the oxygen level of 1 ppm. Alloying element leaching (e.g. Cr, Ni, and Mn) occurred, leading to the formation of delta-ferrite surface layer. The thickness of the degraded surface layer is about 1×10^{-5} m, and almost kept constant over time.

Carburization is a concern in 316FR as the desired low carbon content and high nitrogen content give rise to improved creep properties and resistance to stress corrosion cracking and hot cracking. Carburization and loss of nitrogen in sodium environment can cause serious damage to mechanical performance of 316FR. At the operating temperatures at the ARR, 316FR tends to carburize. Carburization in 316FR was observed at 5000 h at 550°C, with the maximum carbon level of 0.05%. The carburization constant was an order of magnitude lower than that in conventional 316 SS (Ito et al. 1990). No significant loss of nitrogen was observed.

Furukawa et al. (1998) reported tensile data on 316FR pre-exposed to sodium, and creep, fatigue, and creep-fatigue results on 316FR in flowing sodium. It was found that tensile properties of 316FR were not affected by sodium exposure at 500-550°C for 5000 h. Creep rupture tests conducted at 550-600°C in

flowing sodium at the oxygen level of 1 ppm showed that creep rupture strength in sodium was slightly lower than that in air with predominant surface grain boundary cracking when the rupture time was between 1000 and 10,000 h; at the lower stress level and longer rupture time, sodium exposure had no influence on the creep rupture strength of 316FR, as shown in Figure 4.59 (Asayama et al. 2001).

Date reported the fatigue test results in sodium and in air, as shown in Figure 4.56 (Date et al. 2008). When tested in air, 316FR showed longer fatigue lives at lower strain ranges compared to 316SS. The fatigue life of 316FR in sodium is longer than that in air. The similar sodium effect on fatigue life was observed in 316SS.

The creep-fatigue data of 316FR in sodium are shown in Figure 4.57 (Date et al. 2008). It is seen that the beneficial effect of sodium exposure on the fatigue life is nearly diminished when only 1-hr hold time was applied during cyclic loading. Fracture mode changed from transgranular fracture under pure fatigue loading to intergranular fracture under creep-fatigue loading (see Figure 4.58). Furukawa et al. (1998) reported similar results for creep-fatigue in sodium. Creep-fatigue damage in sodium is more pronounced at lower strain ranges. Reduction in fatigue life also occurred under unsymmetric loading (slow-tension and fast-compression) in sodium compared to symmetric loading (fast-tension and fast-compression).

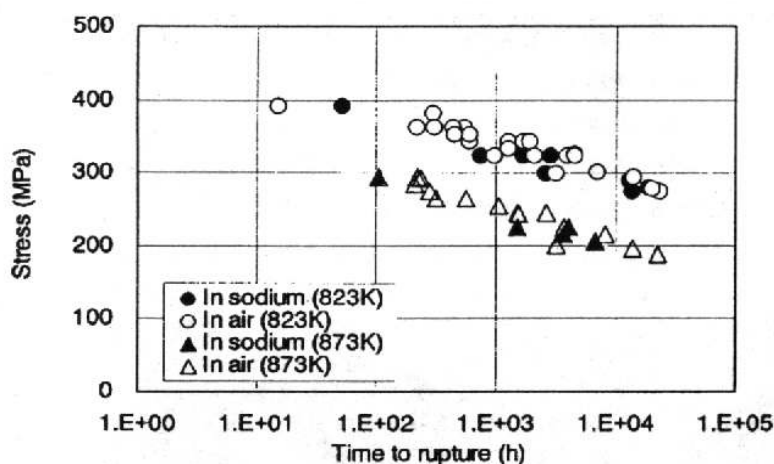


Figure 4.55. Creep rupture data of 316FR tested in sodium (Asayama et al. 2001).

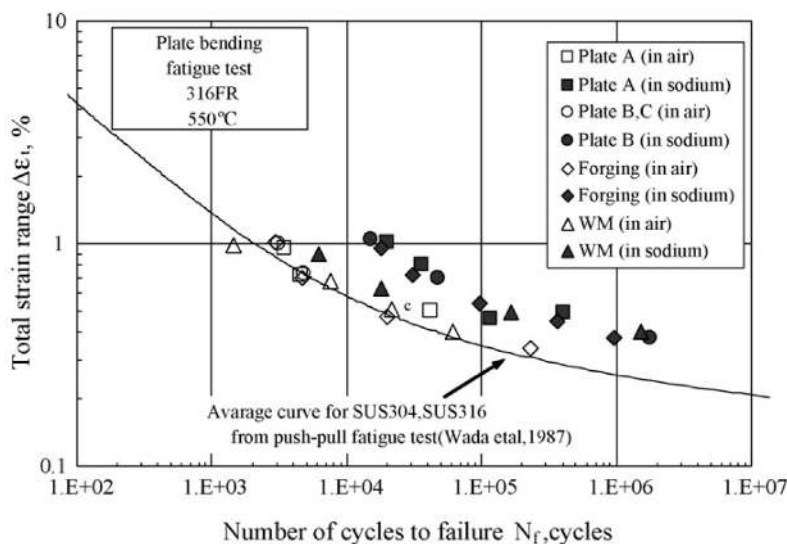


Figure 4.56. Fatigue data of 316FR tested at 550°C (Date et al. 2008).

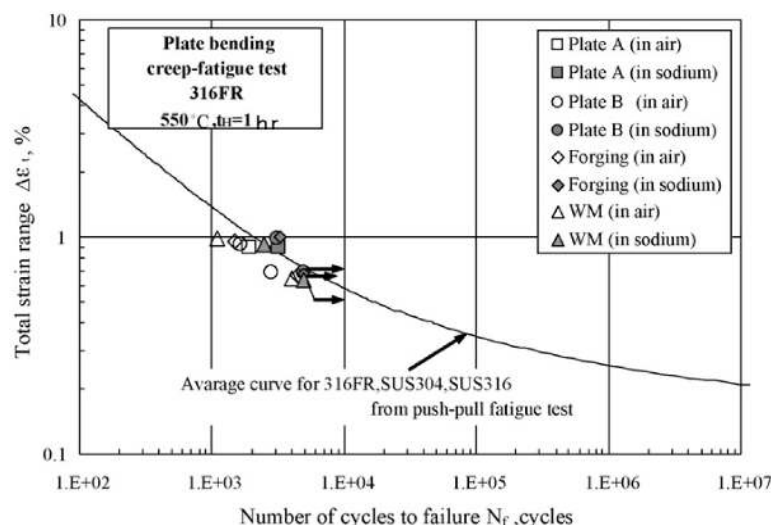


Figure 4.57. Creep-fatigue results in sodium for 316FR tested at 550°C with the hold time of 1 hr. (Date et al. 2008).

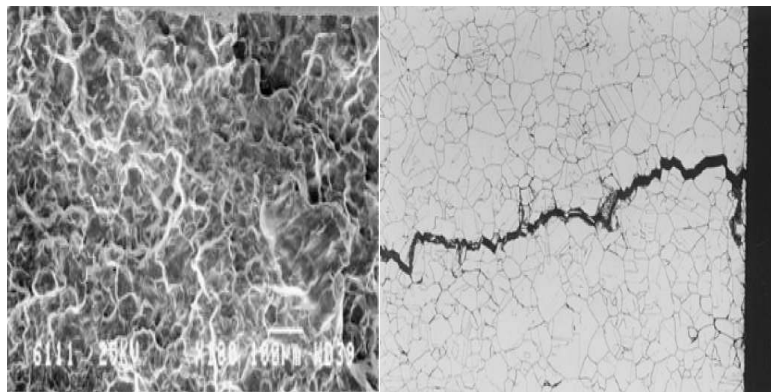


Figure 4.58. Intergranular fracture observed in 316FR under creep-fatigue loading at 500°C (Date et al. 2008).

Effects of Neutron Irradiation

There is an extensive database of the effects of neutron irradiation on 316LN-IG for the ITER structural applications (ITER MPH). The emphasis of the 316LN-IG research was placed on the lower irradiation temperature behavior due to the low operating temperature ($\leq 300^\circ\text{C}$) of 316LN-IG in the ITER components (Tavassoli 1995). Limited data of neutron-irradiated Japanese 316FR can be found in the open literature (Miyaji et al. 1999, Asayama et al. 2001).

Tavassoli (1995) summarized the irradiation effects on tensile properties of 316LN-IG. Tensile property data of 316LN-IG neutron-irradiated up to 400°C showed that the yield stress increased significantly below 1 dpa and saturated at ≈ 3 dpa. Irradiation hardening was accompanied by marked decrease in uniform elongation, total elongation and reduction in area. Irradiation hardening can be recovered when irradiation temperature increased to 550°C . Similar effects of neutron irradiation on tensile properties were observed in the weld metal. Since the yield stress and the ultimate tensile strength are not degraded by neutron irradiation, no design factors are necessary (Asayama et al. 2001).

Some reductions in impact properties and fracture toughness were observed at either low or high temperatures. At intermediate irradiation temperature of around 300°C , there is a concern of irradiation embrittlement in 316LN (Tavassoli 1995). There are insufficient data of tensile, impact, and fracture toughness data to clearly define the irradiation embrittlement issue in the intermediate temperature range.

Weld metal showed large scatter of fracture toughness data due to inconsistent weld qualities. The fracture toughness values of irradiated weld metal could fall below the lower bound of the unirradiated curve (Tavassoli 1995).

Miyaji et al. (1999) evaluated the creep properties of irradiated 316FR. The accumulated neutron fluence ($E > 0.1$ MeV) was in the range of 5×10^{22} to 5×10^{25} n/m². The post-irradiation creep properties decreased with reduced rupture life and ductility and increased creep rate. The reduction factors of rupture life and rupture ductility determined by experimental data are given in Figure 4.59 (Miyaji et al. 1999). Intergranular brittle fracture was observed in creep-ruptured irradiated 316FR. The creep life reduction factor and the steady-state creep rate factor were suggested to account for the irradiation effects (Asayama et al. 2001). It should be noted that there might be a significant discrepancy of data between post-irradiation creep tests and in-reactor creep tests.

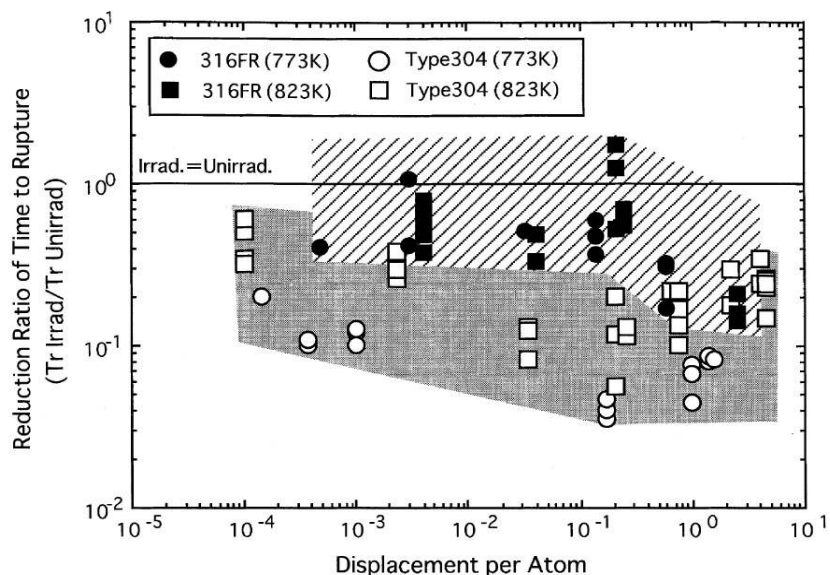


Figure 4.59. Reduction ratio of creep rupture life as a function of dpa in 316FR (Miyaji et al. 1999).

4.3 Low-Alloy and Ferritic-Martensitic Steels

4.3.1 2.25Cr-1Mo Steels

UNS K31835 steel, having a nominal composition of Fe-2.25Cr-1Mo-0.25V, is permitted for structural use under ASME specification SA-336 (Grade F22V), SA-182 (Grade F22V), and SA-541 (Grade 22V) in the ASME B&PV Code (ASME 2004). This steel is approved only for non-nuclear applications and has not been approved for use in ASME Section III for nuclear applications. SA-336 forging is the standard for construction of large pressure vessels. The composition of UNS K31835, identical for all three ASME specifications, has a composition of (in wt%): C 0.11-0.15, Ni 0.25, Cr 2.0-2.5, Mn 0.3-0.6, Mo 0.9-1.1, V 0.25-0.35, P 0.015, S 0.01 (max), Si 0.1 (max), and Nb 0.07 (max). UNS K31835 steel is a vanadium-modified 2.25Cr-1Mo steel and is extensively used in the fossil and petroleum industries. In addition to vanadium, the alloy also contains small amount of other elements such as boron, titanium, etc. Conventional 2.25Cr-1Mo steel (without vanadium addition) is the primary reactor pressure vessel candidate for the Japanese HTTR reactor, which operates at nominal temperature range of 400-440°C (Tachibana 2005).

Addition of vanadium offers increased tensile and creep rupture strengths, and increases hardenability when compared to conventional 2.25Cr-1Mo steel (ASM 1990). In addition, vanadium also

improves resistance to hydrogen attack, which is an important attribute for hydrogen reactors/petrochemical industries. The microstructure of 2.25Cr-1Mo-0.25V steel is typically bainitic, which offers better short-term creep resistance compared to ferrite-pearlite microstructures (ASM 1990). For long life service, creep strength is offered by the presence of various fine carbides of chromium, vanadium, molybdenum, etc. The stability of carbides increases in the following order of alloying elements: Cr, Mo, V, and Nb. The hardening (implies secondary hardening) resulting from these carbides increases with an increase in tempering temperature. Furthermore, low-chromium-vanadium modified steels such as 2.25Cr-1Mo-0.25V offer the fabricability and toughness of bainitic microstructures without special precautions that are needed for welding and heat treating 9 or 12Cr martensitic materials (Imgram et al. 1990). During heat treatment of thick sections (>300 mm), the objective is to avoid the formation of proeutectoid ferrite, which affects hardenability. Achievement of fully bainitic microstructures through the thickness is facilitated by the addition of small amounts of boron (Ishiguro et al. 1982, Klueh and Swindeman 1986). As per the ASME code (ASME 2004), all three grades of 2.25Cr-1Mo-0.25V steels are to be used in the normalized (at a minimum temperature of 899°C) and tempered (at a minimum temperature of 677°C) condition.

Mechanical Properties

Several studies (Ishiguro et al. 1982, Klueh and Swindeman 1986, Imgram et al. 1990, Prager 1998, Hucinska 2003, Tsuchida et al. 2004) have been performed on evaluating the mechanical properties and thermal stability of 2.25Cr-1Mo-0.25V steels. The study of Imgram et al. (1990) contains an exhaustive database on tensile and creep results on several heats obtained from different forging manufacturers. The vanadium content in different heats was in a range of 0.25-0.35 wt.%. The different heats of the alloy were in the form of 50.8-mm-thick plates, which were austenitized, air cooled, and tempered. The specimens for tensile testing were slowly cooled after tempering to simulate post-weld heat treatment of heavy wall vessel construction. Using ASME procedures, ratio trend curves for yield and tensile properties were established and are shown in Figure 4.60. The yield or tensile ratio is the ratio of yield or tensile strength at a given temperature to those at room temperature.

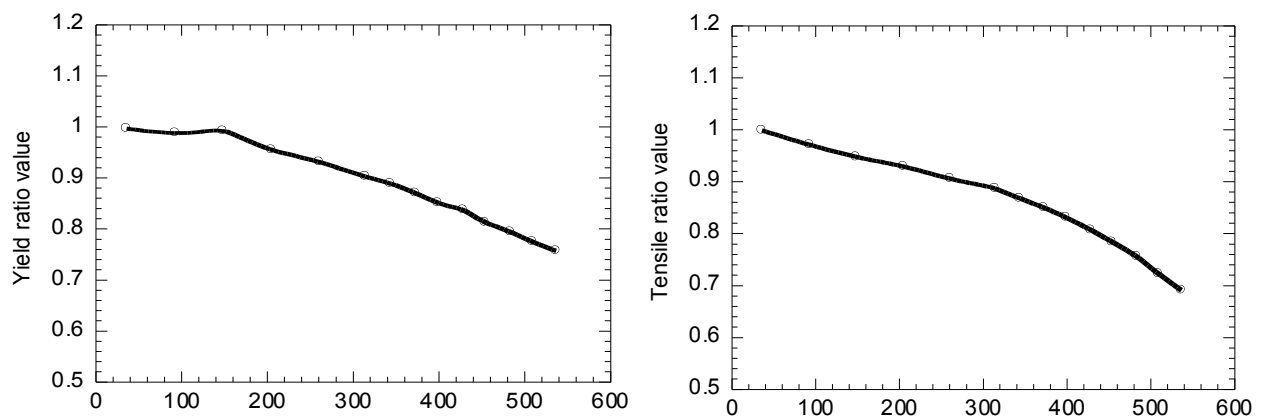


Figure 4.60. Ratio trend curves of YS and UTS ratio as a function of temperature (a) YS and (b) UTS (Imgram et al. 1990).

Ishiguro et al. (1982) evaluated the mechanical properties of several 2.25Cr-1Mo steels with varying amounts of V, B, and Ti. Table 4.12 summarizes the results of room temperature tensile and Charpy impact toughness properties of VB6 heat of 2.25Cr-1Mo-V steel at different simulated plate thicknesses that is obtained by a programmed cooling after austenitization. The chemical composition of the VB6 heat is 2.3Cr-0.97Mo-0.21V-0.0022B-0.022Ti with minor alloying additions of Si, Mn, Ni, Al,

P, S, N and trace elements As, Sb, and Sn. It can be seen that the tensile properties remain the same for all the thicknesses while the fracture appearance transition temperature (FATT) slightly increased over the range of plate thickness. Table 4.13 shows the effect of austenitizing temperature on the tensile and impact properties for a simulated 200-mm thick plate. As evident from the table, a higher austenitizing temperature results in higher yield and tensile strengths and higher impact transition temperature. At higher austenitizing temperature, a larger amount of vanadium in solution available for subsequent precipitation results in higher strength.

Table 4.12. Summary of tensile and impact test results for Heat VB6 simulating 100- to 400-mm thick, water quenched and tempered plates (Ishiguro et al. 1982).

Thickness (mm)	0.2% Proof stress (MPa)	Ultimate tensile strength (MPa)	Elongation (%)	Reduction of area (%)	FATT (°C)
100	529	625	26.5	80.4	-31
200	524	616	26.1	80.0	-17
300	535	622	25.4	80.2	-14
400	520	617	26.5	82.3	-7

Table 4.13. Effect of austenitizing temperature on tensile and impact properties for VB6 heat simulating 200-mm thick water quenched and tempered plates (Ishiguro et al. 1982).

Austenitizing temperature (°C)	0.2% Proof stress (MPa)	Ultimate tensile strength (MPa)	Elongation (%)	Reduction of area (%)	FATT (°C)
920	490	589	25.8	80.1	-20
950	524	616	26.1	80.0	-17
980	557	637	24.7	78.3	-6

Figure 4.61a shows a comparison of elevated temperature tensile properties of VB6 steel with those for the conventional 2.25Cr-1Mo steel. As evident in the figure, the VB6 steel has significantly higher yield and tensile strengths compared to those of conventional 2.25Cr-1Mo steel from room temperature to 650°C. The VB6 heat, in this case, was a 50 mm thick plate austenitized at 950°C for 5 h followed by programmed cooling to simulate the quarter thickness location of a 200-mm thick water quenched plates, and subsequently tempered at 690°C for 2 h. The conventional 2.25Cr-1Mo steel received the same heat treatment to that of VB6. In contrast to the above result, Klueh and Swindeman (1986) observed that a V-Ti-B modified 2.25Cr-1Mo steel had lower tensile strength than the conventional 2.25Cr-1Mo steel as illustrated in Figure 4.61b. The difference in the tensile behavior of conventional 2.25Cr-1Mo steel in the two studies (Ishiguro et al. 1982, Klueh and Swindeman 1986) is attributed to differences in microstructures, bainite+polygonal ferrite in Ishiguro et al. study and fully bainitic structure in the work of Klueh and Swindeman. Even in the fully bainitic microstructure, there was some evidence of lath structure with precipitates present on lath boundaries.

The creep behavior of conventional 2.25Cr-1Mo steel was lower than the bainitic vanadium modified 2.25Cr-1Mo steel in studies of both Ishiguro et al. (1982) and Klueh and Swindeman (1986). Figure 4.62(a-b) shows the respective stress vs. life curves. Figure 4.62b indicates that except at high stress low life region, creep resistance of the modified steel is better than the conventional steel in the temperature range 482-538°C. Figure 4.63 shows the scatter band in creep data of conventional steel vs. modified steels plotted as rupture strength vs. Larson Miller Parameter, clearly indicating the superior

creep properties of the modified steel. The superior creep strength was attributed to the higher room temperature strength and precipitation of fine carbides of vanadium and titanium (Ishiguro et al. 1982). Higher creep strength in the modified steel (due to precipitation of fine carbides of vanadium and titanium), containing a high dislocation density, was confirmed by Klueh and Swindeman (1986).

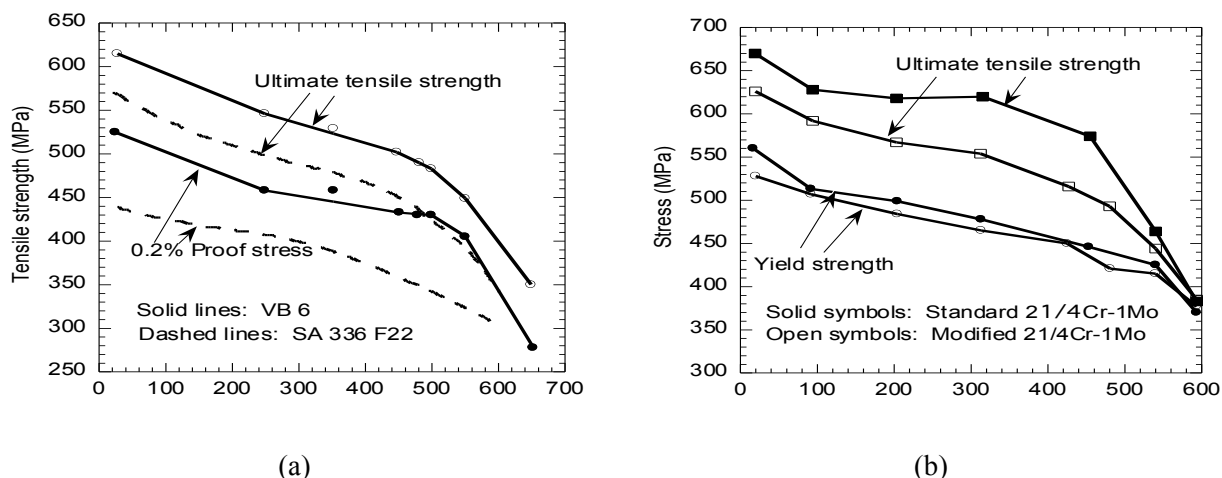


Figure 4.61. Tensile properties of (a) vanadium-modified 2.25Cr-1Mo (VB6) steel and (b) conventional 2.25Cr-1Mo steel (SA336-Grade F22). (Ishiguro et al. 1982, Klueh and Swindeman 1986).

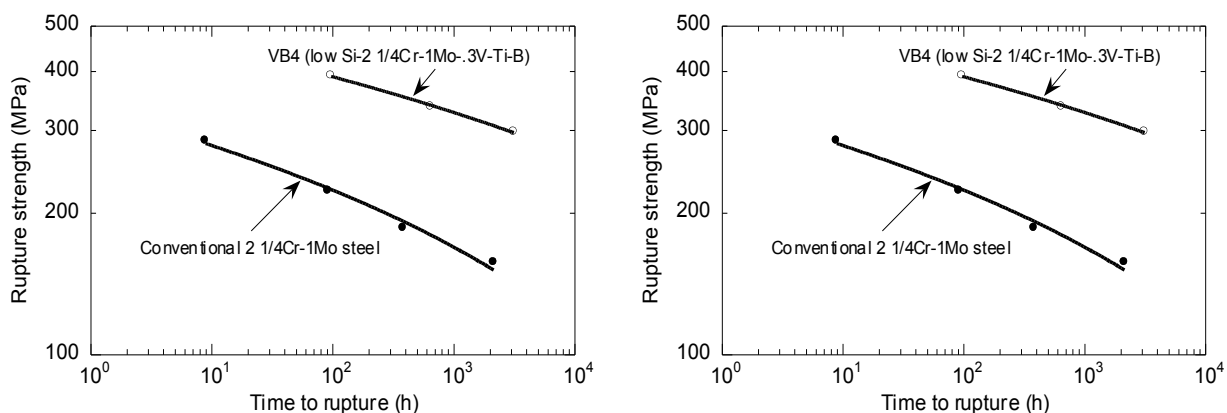


Figure 4.62. Comparison of creep rupture behavior of conventional vs. vanadium modified 2.25Cr-1Mo steel from two studies. (a) Ishiguro et al. (1982) and (b) Klueh and Swindeman (1986).

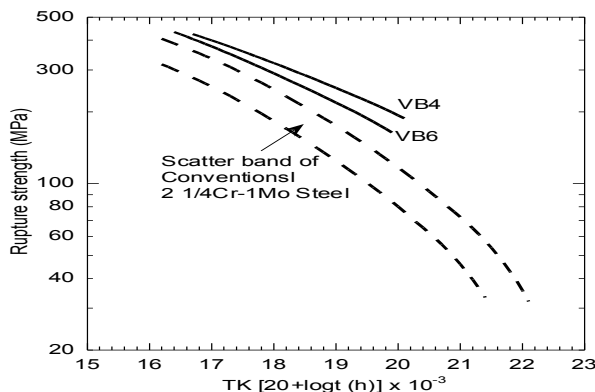


Figure 4.63. Creep rupture response of standard 2.25Cr-1Mo steel and modified 2.25Cr-1Mo-V steel (Ishiguro et al. 1982).

The creep rupture behavior of 2.25Cr-1Mo-0.25V steel of different heats, produced by various forging manufacturers, is shown in Figure 4.64 (Imgram et al. 1990). All five heats were furnished as

50.8 mm thick plate, austenitized by the manufacturers, air cooled and tempered. The final microstructure was bainitic in all heats. As evident in the figure and understandably so, the creep strength is higher at lower temperatures. The Larson-Miller Parameter curve for the steel is shown in Figure 4.65 (Prager 1998). Figure 4.66 shows a comparison of the creep strength of vanadium modified 2.25Cr-1Mo steel with a high chromium modified 9Cr-1Mo steel (Tsuchida et al. 2004). The heat treatment of the vanadium modified 2.25Cr-1Mo steel consisted of austenitization at 980°C, tempering at 730°C for 5h, which was followed by a simulated post-weld heat treatment at 705°C for either 6 or 30 h. The microstructure was tempered bainite with V, Mo and Cr precipitates in the matrix and some evidence of lath structure having globular M7C3 precipitates along grain and lath boundaries. As evident in the figure, the creep strength of this steel is comparable to modified 9Cr-1Mo up to ≈ 500 h in the temperature range of 450-600°C, but decreases at longer rupture life.

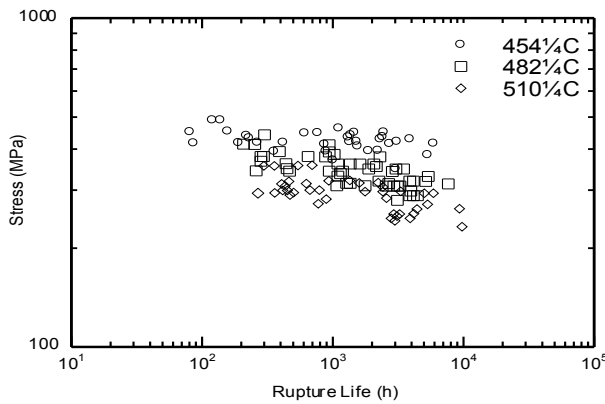


Figure 4.64. Creep rupture behavior of 2.25Cr-1Mo-0.25V steel at different temperatures. (Imgram 1990).

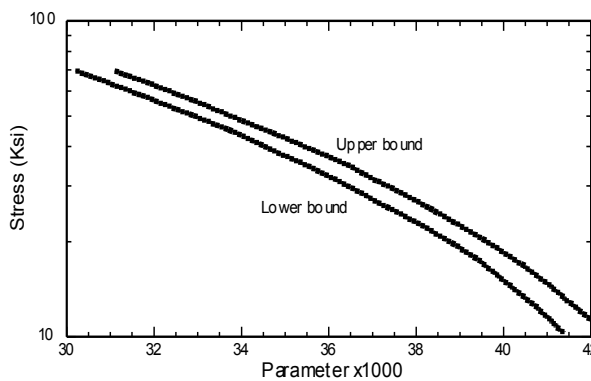


Figure 4.65. Larson-Miller Parameter plots for alloy 22V (Prager 1998).

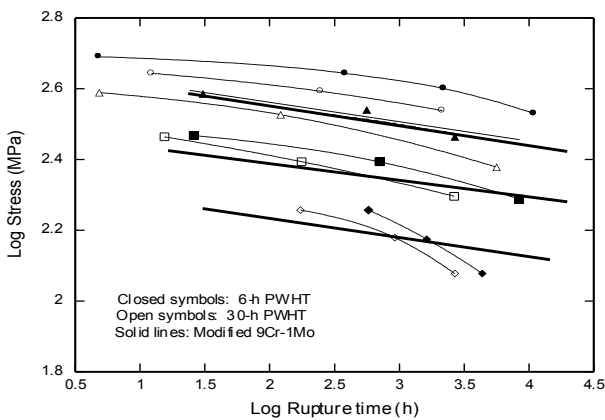


Figure 4.66. Comparison of creep data of 2.25Cr-1Mo-V steel with modified 9Cr-1Mo steel (Tsuchida et al. 2004).

Thermal Aging Effects on Mechanical Properties

Long term operation of reactor structural components like pressure vessels could cause a significant change in the material microstructure and may alter the mechanical performance due to thermal aging of the component. Temper embrittlement or temper aging embrittlement is a time and temperature dependent process that could occur due to thermal aging, thereby affecting component performance. The thermal stability of 2.25Cr-1Mo-0.25V steels has been evaluated by an isothermal exposure and by a step cooling method (Ishiguro et al. 1982, Prager 1998). The step cooling method is an accelerated aging technique to characterize thermal aging response and should be cautiously used in design.

Table 4.14 shows the transition temperature and its shift at an absorbed energy of 40 ft-lb for different heats (BM1, BM2 and BM4) of 2.25Cr-1Mo-0.25V and for the conventional 2.25Cr-1Mo steel (BM3). BM2 had a high phosphorus content (0.018 wt.%) and also contained small amounts of Sb, Sn and As. BM1 and BM4 had lower phosphorus contents and did not contain Sb, Sn or As. It is clear from the table that the modified steel with higher purity has lower impact properties before exposure and shows good toughness retention after thermal aging. BM2 has poor impact properties probably due to the presence of high concentration of phosphorus and other impurities. The results of the accelerated aging study by Ishiguro et al. (1982) are shown in Table 4.15. All three heats VB6, VB7 and VB8 had impurities P, Sn, Sb, and As, with the highest levels in VB8 and the lowest in VB6. As seen in Table 4.14, all three heats showed very little change in transition temperature after the step cooling. This is in contrast to the results in Table 4.14 (Prager 1998), which indicated poor impact properties for the steel with higher impurities.

Table 4.14. Charpy impact 40 ft-lb temperature after isothermal exposure at 482°C (Prager 1998)

Steel	Chemical composition	Isothermal exposure time at 482°C (900°F)								
		5,000 h			10,000 h			30,000 h		
		Tr ₄₀ (°C)	ΔTr ₄₀ (°C)	Tr ₄₀ +2ΔTr ₄₀ (°C)	Tr ₄₀ (°C)	ΔTr ₄₀ (°C)	Tr ₄₀ +2ΔTr ₄₀ (°C)	Tr ₄₀ (°C)	ΔTr ₄₀ (°C)	Tr ₄₀ +2ΔTr ₄₀ (°C)
BM1	V mod. -low. P	-60	-5	-70	-57	-2	-61	-55	0	-55
BM2	V mod. -high. P	54	47	148	56	58	181	75	68	211
BM4	V mod. -med. P	-31	-4	-39	-26	1	-24	-24	3	-18
BM3	Conventional	-37	-1	-39	-34	2	-30	-31	5	-21

Table 4.15. Charpy impact transition temperatures before and after step cooling (Ishiguro et al. 1982)

Sample No.	FATT ^a (°C)		Tr ₄₀ ^b (°C)		Absorbed energy ^c (J)	
	Before	After	Before	After	Before	After
VB6	-17	-23	-30	-36	274	272
VB7	+2	+5	-13	-18	274	272
VB8	+2	+10	-8	-4	269	269

^aTransition temperature at shear fracture of 50 percent.

^bTransition temperature at absorbed energy of 40 ft·lb.

^cAbsorbed energy at upper shelf temperature.

Ishiguro et al. (1982) attributed the low susceptibility to temper embrittlement, partly to the low Si content and partly to the presence of Ti and B. Although B and Ti were present in all the heats evaluated by Prager (1998), the Si contents were higher (0.07-0.11%) compared to a Si content of 0.02% in all the heats studied by Ishiguro et al. (1982). Furthermore, Prager (1998) studied the thermal aging behavior by a step cooling method and indicated that it was not a good method for such characterization. Clearly, more studies are needed to establish the effect of Si, Ti, B, V, and other impurities on thermal aging and resulting temper embrittlement of 2.25Cr-1Mo-0.25V steels.

Recently, Kim et al. (2006) studied the susceptibility to temper embrittlement of 2.25Cr-1Mo and 2.25Cr-1Mo-0.25V steel (V=0.29 wt.%) forgings of size 400 mm thick and 2.3 m inner diameter. In the vanadium modified steel, P= 0.006 wt.% while in the standard steel, P≈0.007 wt. %. Both the steels were subjected to a simulated post-weld heat treatment at 650-700°C. Both the steels had a tempered bainite structure. Charpy V-notch 54J transition temperature (vTr_{54}) and 50% shear fracture appearance transition temperature (FATT₅₀) were measured as a function of aging time up to a maximum of 50,000 h. The aging temperatures ranged from 430°C to 515°C. Figure 4.67 shows the variation of FATT and vTr_{54} with aging time at two different temperatures. It is evident from the figure that at both aging temperatures, the vanadium-modified steel has better resistance to temper embrittlement than the standard 2.25Cr-1Mo steel. This result also reinforces Prager's (1998) result (Table 4.14) that low-P in steel reduces susceptibility to temper embrittlement.

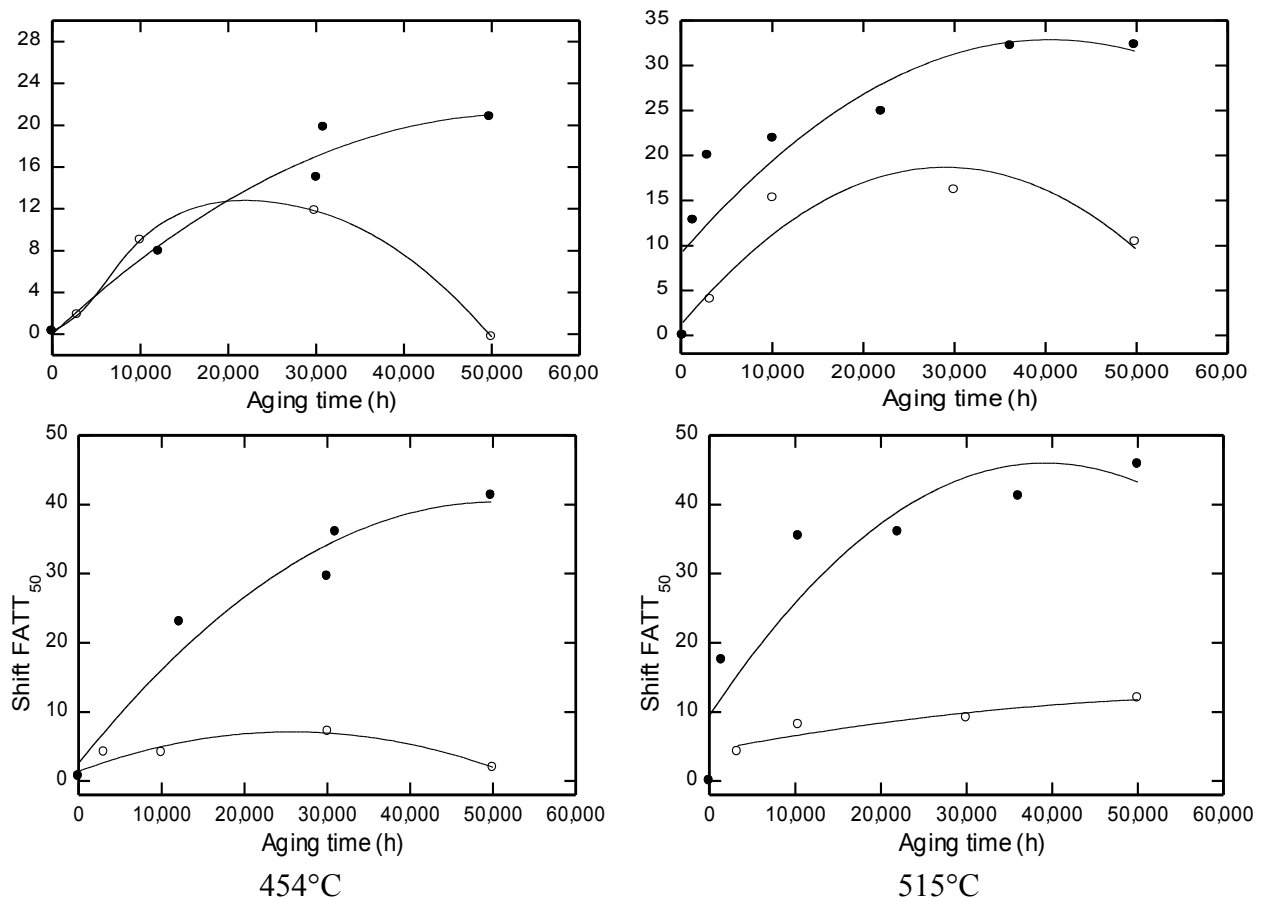


Figure 4.67. Average shift of fracture appearance transition temperature (FATT₅₀) and 54J transition temperature (vTr_{54}) by isothermal aging for 50,000 h of 2.25Cr-1Mo and 2.25Cr-1Mo-0.25V steels.

ASME Code Allowables

Conventional 2.25Cr-1Mo steel (without vanadium addition) is code approved under Section III of the ASME code for use up to 593°C service. On the other hand, 2.25Cr-1Mo-0.25V steel (UNS K31835) is approved only under Section VIII of the ASME Code for temperatures up to 482°C. Additional mechanical property data, especially in the areas of thermal aging, creep-fatigue, and sodium interactions for the 2.25Cr-1Mo-0.25V steel are needed for inclusion in Section III of the ASME code.

4.3.2 Mod.9Cr-1Mo (Grade 91) Steel

Mod.9Cr-1Mo (Grade 91) steel has significantly improved creep strength and corrosion resistance than 2.25Cr-1Mo. The alloy was co-developed by Combustion Engineering and the Oak Ridge National Laboratory (ORNL) in the late 1970s for steam generation applications for the liquid metal fast breeder reactors (Sikka et al. 1983). Grade 91 has been extensively used in the high-temperature components of fossil-fired power plants, steam generators of nuclear power plants, and petrochemical industries due to its good creep properties, low thermal expansion coefficient, good thermal conductivity, and virtual immunity to stress corrosion cracking in aqueous and chloride environments. Grade T91 was first approved for use in the ASME Section I in 1984. It was approved in 1993 in the AMSE Power Piping Code, B31.1 for seamless pipe in Specification SA-335 and plate in Specification SA-387. The chemical composition for Grade 91 in wt% is as follows: C 0.08-0.12, Si 0.2-0.5, Mn 0.3-0.6, Cr 8-9.5, Mo 0.5-1.05, Nb 0.06-0.1, Ni 0.4 max, N 0.03-0.07, Al 0.04 max, P 0.02 max, and S 0.01 max.

The high strength of Grade 91 relies on tempered martensitic microstructure stabilized by $M_{23}C_6$ carbides and a fine distribution of vanadium/niobium rich carbon-nitride (MX) precipitates. Molybdenum in the solution also contributes to the strength of Grade 91. The improved high temperature strength of Grade 91 allows construction of thinner-wall components, resulting in lower thermal stresses during transients and lower material costs. However, the superior properties of Grade 91 highly depend on the creation of an appropriate microstructure from fabrication and heat treatment and maintenance of the microstructure during service. Special consideration is required in handling Grade 91 steel.

Specifications

The specifications, product forms, types, grades, or classes of Grade 91 that are permitted in Subsection NH are listed in Table 4.16.

Table 4.16. Permitted product forms of Grade 91

Permitted Grade 91 for Subsection NH		
Spec. No.	Product Form	Types, Grades, or Classes
SA-182 [Note (1)]	Forgings	F91
SA-213	Seamless Tube	T91
SA-335	Seamless Pipe	P91
SA-387	Plate	91
Note: (1) This specification limits forging size to 4540 kg (10,000 lb).		

Baseline Mechanical Properties

Room Temperature Minimum Yield and Tensile Strengths

The specified minimum yield strength at room temperature for all the product forms, types, grades and classes given in Table 4.17 is 415 MPa (60 ksi).

The specified minimum tensile strength at room temperature for all the product forms, types, grades and classes given in Table 4.17 is 585 MPa (85 ksi).

Maximum Metal Temperature

The maximum metal temperature permitted by Subsection NH for Grade 91 is 649°C (1200°F).

Yield Strength at Temperature

The yield strength values at temperature, S_y , for all Grade 91 listed in Table 4.16, are tabulated in Section II, Part D, Table Y1 from room temperature to 538°C (1000°F) and in Subsection NH from 538 to 649°C. These are minimum expected values. These values are given in Table 4.17 and are also plotted in Figure 4.68.

Table 4.17. Yield strength, Grade 91

Temperature (°C)	S_y (MPa)	Source (2007 Edition)
30	414	Sec II
40	414	Sec II
65	394	Sec II
100	384	Sec II
125	380	Sec II
150	378	Sec II
175	378	Sec II
200	377	Sec II
225	377	Sec II
250	377	Sec II
275	377	Sec II
300	377	Sec II
325	375	Sec II
350	371	Sec II
375	366	Sec II
400	358	Sec II
425	348	Sec II
450	337	Sec II
475	322	Sec II
500	306	Sec II
525	288	Sec II
550	269	NH
575	243	NH
600	218	NH
625	193	NH
649	165	NH

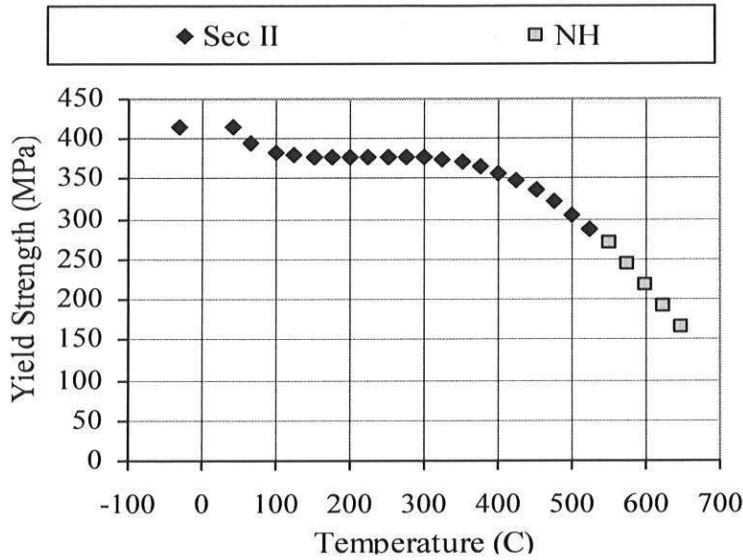


Figure 4.68. Yield strength, Grade 91.

Tensile Strength at Temperature

The values of tensile strength at temperature, S_u , for Grade 91 are tabulated in Section II, Part D, Table U, from room temperature to 538°C (1000°F), and in Subsection NH from above 538°C to 649°C (1200°F). These are average values. These values are given in Table 4.18. Tensile strength data for Grade 91 are also plotted in Figure 4.69.

Table 4.18. Tensile strength, Grade 91

Temperature (°C)	S_u (MPa)	Source
30	586	Sec II
40	586	Sec II
100	586	Sec II
150	586	Sec II
200	584	Sec II
250	582	Sec II
300	577	Sec II
325	570	Sec II
350	561	Sec II
375	549	Sec II
400	534	Sec II
425	516	Sec II
450	494	Sec II
475	469	Sec II
500	441	Sec II
525	410	Sec II
550	379	NH
575	341	NH
600	303	NH
625	265	NH
649	228	NH

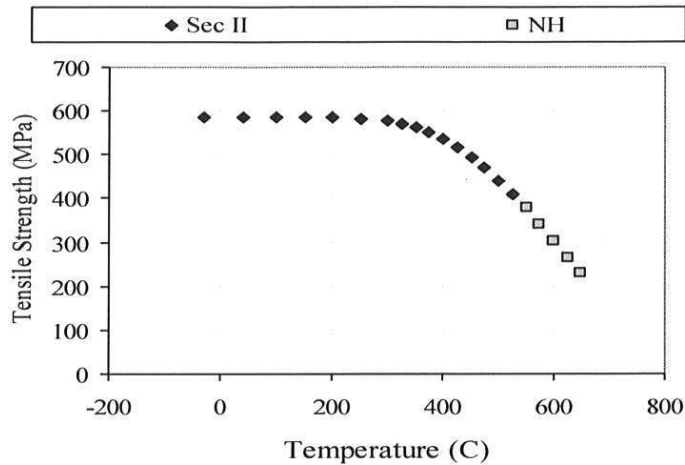


Figure 4.69. Tensile strength, Grade 91.

Modulus of Elasticity

Section II (2007 Edition), Table TM-1 lists the values of modulus of elasticity, E , for groups of materials. Per the chemical composition, the E values in Sec II, Table TM-1, Group E are applicable to Grade 91. These values are given in Table 4.19.

Table 4.19. Modulus of elasticity, Grade 91

Temperature (°C)	E (GPa)
25	213
100	208
150	205
200	201
250	198
300	195
350	191
400	187
450	183
500	179
550	174
600	168
650	161

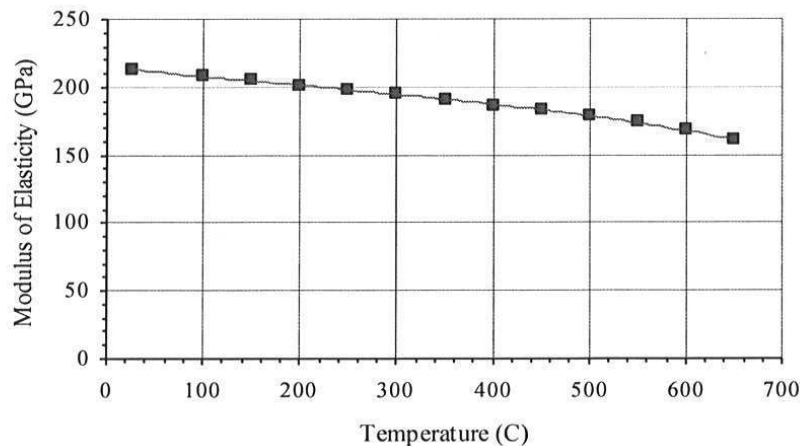


Figure 4.70 Modulus of elasticity (average), Grade 91.

A polynomial fit to the values of E , shown in Figure 4.70, is expressed in the form

$$E = \sum_{n=0}^3 a_n T^n, \quad 25^\circ\text{C} \leq T \leq 649^\circ\text{C}$$

where E is given in GPa and the temperature T is in $^\circ\text{C}$. The polynomial coefficients are given in Table 4.20. Note that these E values are best estimate (average) values.

Table 4.20. Polynomial coefficients for E , Grade 91

n	Coefficient a_n
0	2.1513281E+02
1	-7.8658587E-02
2	7.1105335E-05
3	-1.1908162E-07

Thermal Creep Strain

A thermal creep strain-time relation for Grade 91 was developed by Swindeman (1999). This relation forms the basis for generating the isochronous stress-strain curves for Grade 91 in Subsection NH. Since the isochronous stress-strain curves are limited to 2% strain, the creep strain-time relation was limited to modeling primary and secondary creep as the tertiary creep often began at 2% strain. The creep strain is given in the form:

$$e_c = a_0 t^{1/3} + \dot{e}_m t$$

where

- e_c creep strain (%)
- a_0 primary creep strain constant ($\% / \text{h}^{1/3}$)
- t time (h)
- \dot{e}_m minimum creep rate ($\%/h$)

and

$$\dot{e}_m = CS^n \exp(VS) \exp(-Q/T)$$

$$a_0 = DS \exp(V_0 S) \exp(-Q_0/T)$$

with T is temperature in K, and S is applied stress in MPa. The material parameters are in Table 4.21.

Table 4.21. Material parameters for creep strain, Grade 91

Parameter	Value	Unit	Applicable temp (°C)
D [Note(1)]	5450000	$\% / h^{1/3} / MPa$	538 to 649
D [Note(1)]	847000	$\% / h^{1/3} / MPa$	427 to 482
Q_0	23260	K	538 to 649
Q_0	25330	K	427 to 538
V_0	0.023	1/MPa	427 to 649
C	2.25E+22	$\% / h / MPa^5$	427 to 649
n	5	dimensionless	427 to 649
V	0.038	1/MPa	427 to 649
Q	77280	K	427 to 649

Note (1): Linear interpolation between 482 and 538°C

Some examples of the creep curves generated from these equations are shown in Figure 4.71.

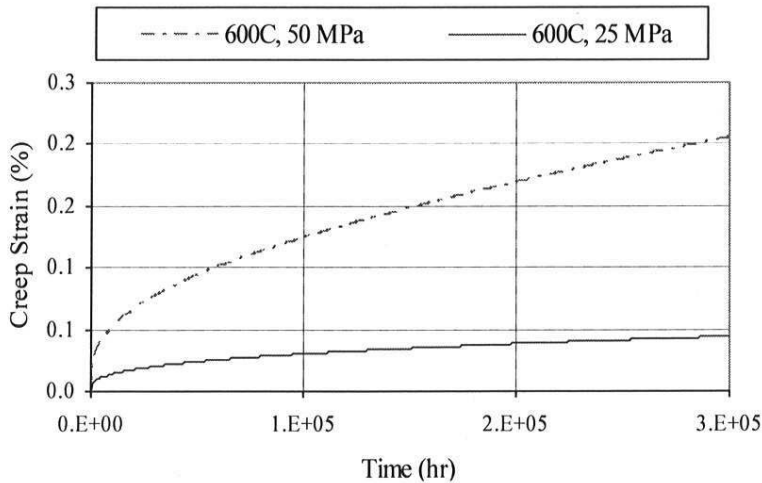


Figure 4.71. Example of creep curves, Grade 91.

Fatigue

The fatigue design curve for Grade 91 at the temperatures of 538°C (1000°F) is given in Subsection NH. The design fatigue strain range is given in Table 4.22. The cycle strain rate is 4×10^{-3} m/m/s.

Table 4.22. Design fatigue strain range, Grade 91

Nd, number of cycles	Strain range (m/m) at temperature, 538°C (1000°F)
1×10^1	0.028
2×10^1	0.019
4×10^1	0.0138
1×10^2	0.0095
2×10^2	0.0075
4×10^2	0.0062

Nd, number of cycles	Strain range (m/m) at temperature, 538°C (1000°F)
1x10 ³	0.005
2x10 ³	0.0044
4x10 ³	0.0039
1x10 ⁴	0.0029
2x10 ⁴	0.0024
4x10 ⁴	0.0021
1x10 ⁵	0.0019
2x10 ⁵	0.00176
4x10 ⁵	0.0017
1x10 ⁶	0.00163
2x10 ⁶	0.0155
4x10 ⁶	0.00148
1x10 ⁷	0.0014
2x10 ⁷	0.00132
4x10 ⁷	0.00125
1x10 ⁸	0.0012

A plot of the design fatigue curve is shown in Figure 4.72.

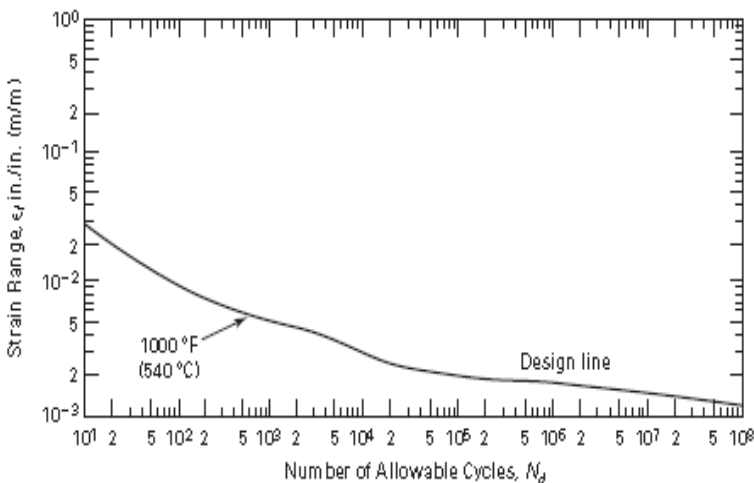


Figure 4.72. Design fatigue curves, Grade 91.

Creep-Fatigue Interaction

Creep-fatigue tests show that the fatigue life of Grade 91 is reduced with hold times. Figure 4.73 shows the creep-fatigue data for Grade 91 at 600°C assembled by Asayama and Tachibana (2007). Test data from continuous cycling, tensile hold, and compressive hold are included. Some tests were carried out in vacuum while the bulk of the data were from air tests. Generally for Grade 91, compressive hold is more damaging, i.e., more reduction in fatigue life, than tensile hold.

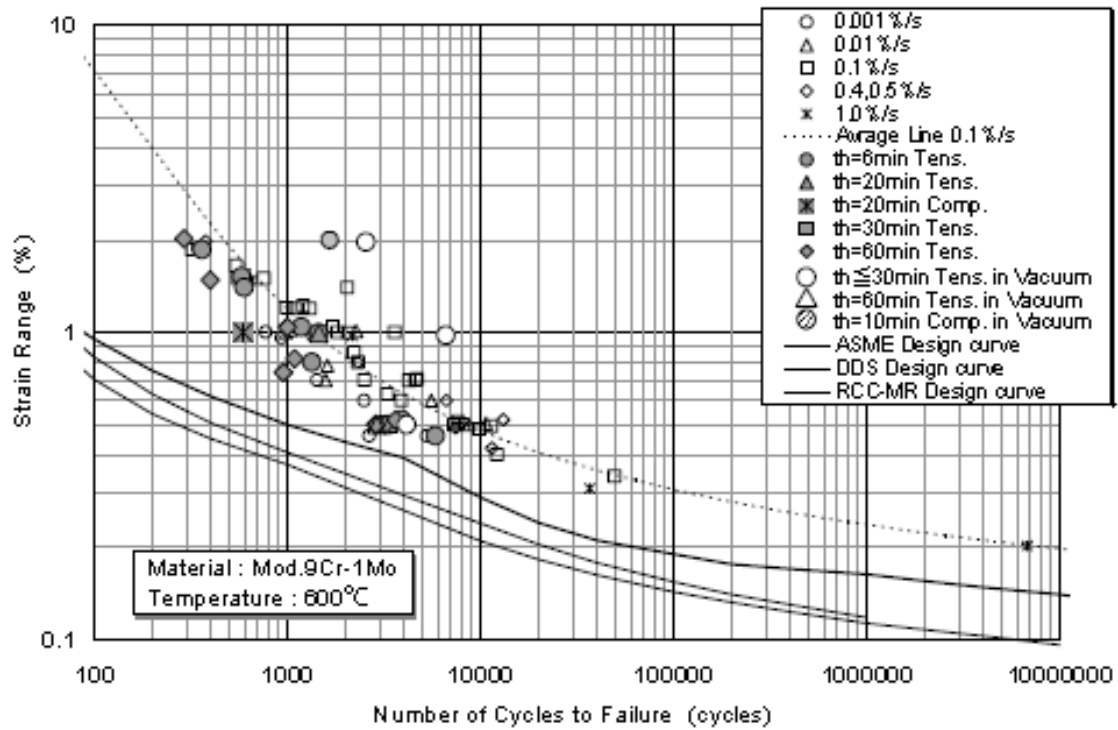


Figure 4.73. Creep-fatigue data for Grade 91 at 600°C (Asayama and Tachibana 2007).

Subsection NH employs a very restrictive creep-fatigue interaction criterion, as shown in Figure 4.74, for designing against creep-fatigue failure of Grade 91.

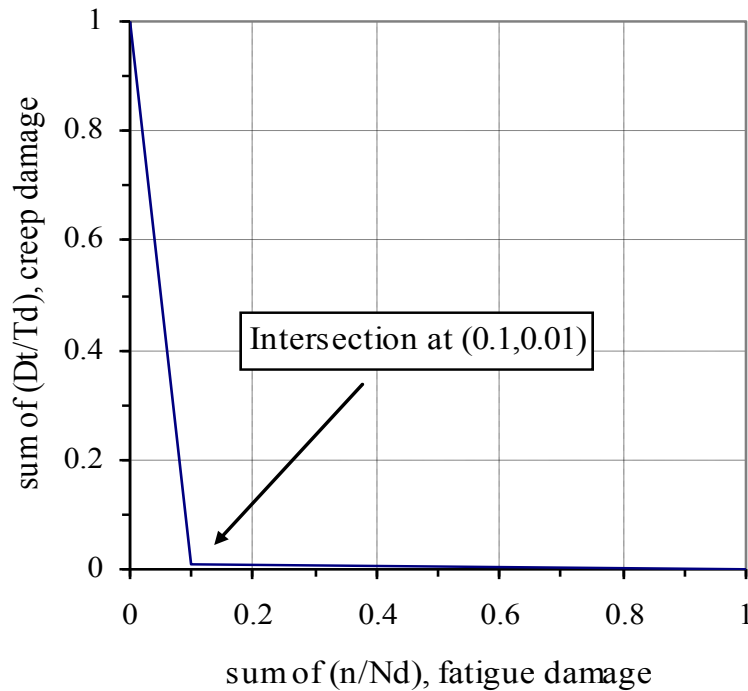


Figure 4.74. Subsection NH creep-fatigue interaction diagram, Grade 91.

ASME Code Allowables

Design Condition Allowable Stress

The values of the design condition allowable stress S_0 for Grade 91 are tabulated in Subsection NH and they are shown in Table 4.23.

Table 4.23. S_0 – Design condition allowable stress intensity for design condition calculations, Grade 91

Temperature (°C)	S_0 (MPa)
371	184
400	178
425	172
450	165
475	154
500	133
525	117
550	102
575	81
600	62
625	46
649	30

Operating Condition Allowable Stress

The values of the operating condition allowable stress S_{mt} for Grade 91 are tabulated in Subsection NH and they are shown in Table 4.24. The maximum time is 300,000 hours.

Table 4.24. S_{mt} – Operating condition allowable stress intensity values for Grade 91

T (°C)	1 h	10 h	30 h	1E2 h	3E2 h	1E3 h	3E3 h	1E4 h	3E4 h	1E5 h	3E5 h
371	184	184	184	184	184	184	184	184	184	184	184
400	179	179	179	179	179	179	179	179	179	179	179
425	172	172	172	172	172	172	172	172	172	172	172
450	165	165	165	165	165	165	165	165	165	165	165
475	156	156	156	156	156	156	156	156	156	156	154
500	147	147	147	147	147	147	147	147	147	138	131
525	136	136	136	136	136	136	136	132	126	115	106
550	125	125	125	125	125	125	121	111	102	93	85
575	114	114	114	114	114	108	99	90	81	73	66
600	101	101	101	101	97	86	80	71	63	54	48
625	88	88	88	86	78	70	63	54	44	36	30
649	77	77	77	70	63	54	45	37	30	23	17

The operating condition allowable stresses are also shown in Figure 4.80. The S_{mt} value for each time and temperature condition is given as the smaller of the time independent primary stress S_m and the time dependent primary stress S_t shown in Figure 4.75.

Time Dependent Primary Stress

The values of time dependent primary stress, S_t for Grade 91, are tabulated in Subsection NH and they are shown in Table 4.25. They are also presented graphically in Figure 4.76. The maximum time is 300,000 hours.

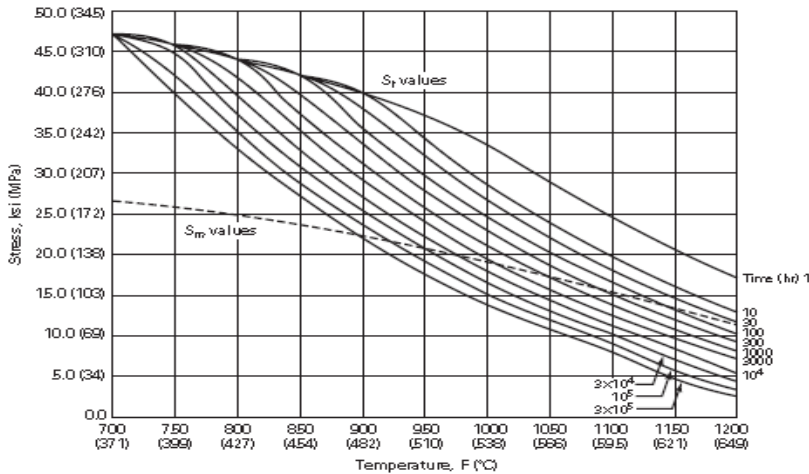


Figure 4.75. S_{mt} for Grade 91.

Table 4.25. S_t – Time dependent allowable stress intensity values for Grade 91

T (°C)	1 h	10 h	30 h	1E2 h	3E2 h	1E3 h	3E3 h	1E4 h	3E4 h	1E5 h	3E5 h
371	326	326	326	326	326	326	326	326	326	326	326
400	317	317	317	317	317	317	316	316	307	290	275
425	307	307	307	307	307	307	292	276	262	246	232
450	294	294	294	294	279	264	249	234	220	206	193
475	275	275	271	256	241	225	211	197	184	171	160
500	262	249	235	219	205	191	178	165	153	141	131
525	242	214	200	185	172	163	148	136	126	115	106
550	217	182	170	156	144	132	119	111	102	93	85
575	189	154	142	130	119	108	99	90	81	73	66
600	164	126	115	107	97	86	79	71	63	54	48
625	139	106	96	86	78	70	62	54	44	36	30
649	118	88	79	70	63	54	48	37	30	23	17

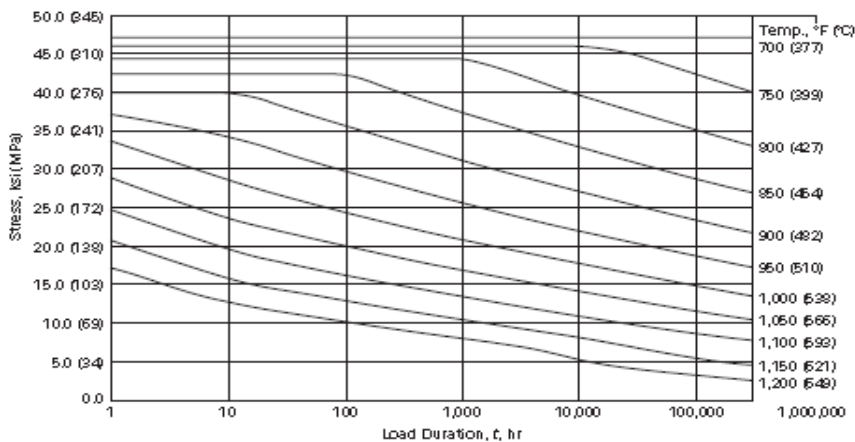


Figure 4.76. S_t -Time dependent primary stress for Grade 91.

Stress-to-Rupture

The values of stress-to-rupture, S_r , for Grade 91 are tabulated in Subsection NH and are shown in Table 4.26. They are also presented graphically in Figure 4.77. The maximum time is 300,000 hours. These are minimum expected values. The values in the table or the graphs in the figure are used to determine the creep rupture time for given stress and temperature in carrying out design calculations.

Table 4.26. S_r - Expected minimum stress-to-rupture values for Grade 91

T (°C)	10 h	30 h	1E2 h	3E2 h	1E3 h	3E3 h	1E4 h	3E4 h	1E5 h	3E5 h
371	490	490	490	490	490	490	490	490	490	490
399	476	476	476	476	476	476	476	464	438	415
427	459	459	459	459	459	435	410	387	363	342
454	437	437	437	412	386	363	340	319	299	280
482	412	393	367	345	321	301	280	261	243	226
510	353	330	307	286	265	247	228	212	194	180
538	295	275	254	235	216	200	183	169	154	141
566	245	227	208	191	174	160	145	132	119	108
593	201	185	168	154	139	126	113	102	90	81
621	163	149	134	121	108	97	85	70	57	46
649	131	118	105	94	82	72	55	45	34	26

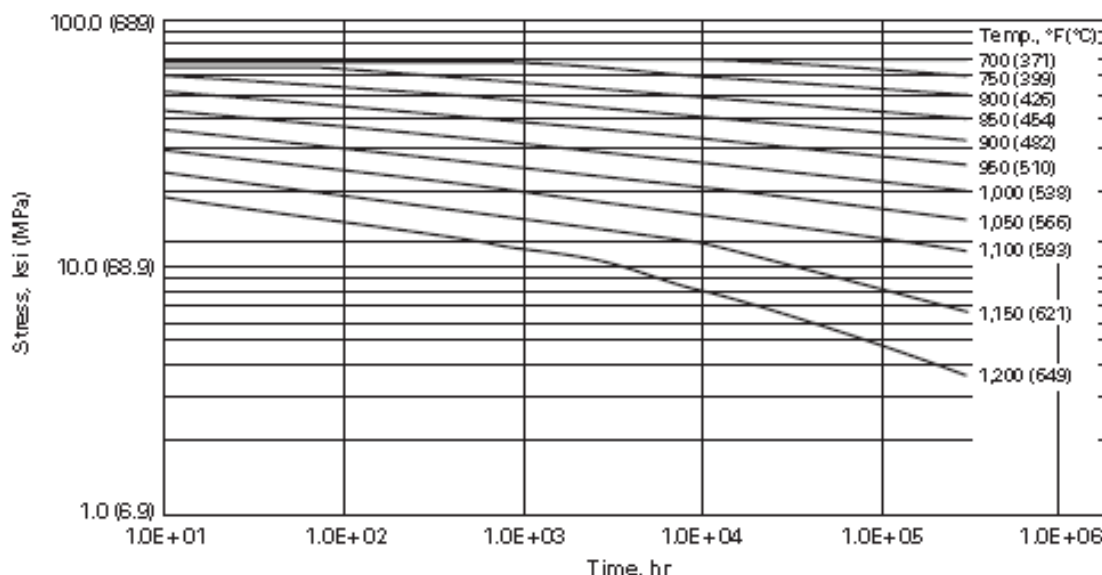


Figure 4.77. Minimum expected stress-to-rupture for Grade 91.

4.3.3 Effects of Long-term Thermal Aging

As part of the development of modified 9Cr-1MoV during the 1970s and 1980s, a substantial amount of thermal aging experiments were performed. The report by DiStefano, et al. (1986) includes much of that data and some of those results are reproduced for this report. Additional sources of information are the monograph by Klueh and Harries (2001) and a report by Blass et al. (1991). Figure 4.78 (a) and (b) (DiStefano, et al. 1986) show the effects of thermal aging of Grade 91 steel for 25,000 h at a wide range of temperatures. As the caption states, thermal aging has minimal effect on room temperature yield strength of modified 9Cr-1Mo steel for aging temperatures up to 600°C, while results

of testing at the aging temperature show different behavior for two different heats, with the results for one heat being essentially on the minimum curve. Similar effects were observed for ultimate tensile strength and tensile ductility.

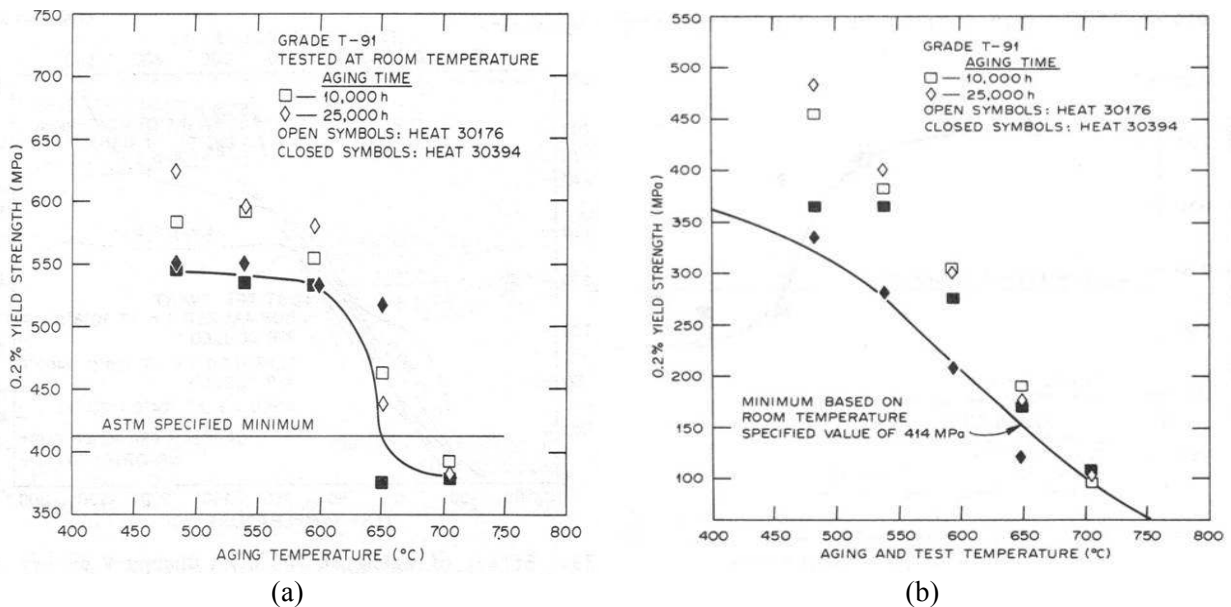


Figure 4.78. Thermal aging for 25,000 h has (a) minimal effect on room temperature yield strength of modified 9Cr-1Mo steel for aging temperatures to 600°C, and (b) testing at the aging temperature for two different heats.

Figure 4.79 shows effects of 5,000-h thermal aging on the yield and ultimate tensile strengths at four different temperatures, the same amount of time for which irradiation experiments were conducted with the same heat of material. The irradiations were performed in EBR-II to 10-12 dpa. The results for strength and for tensile ductility (not shown) indicate that 5,000 h at the irradiation temperature had no effect on the tensile properties of Grade 91 steel at the four different irradiation/aging temperatures (Klueh and Vitek 1985).

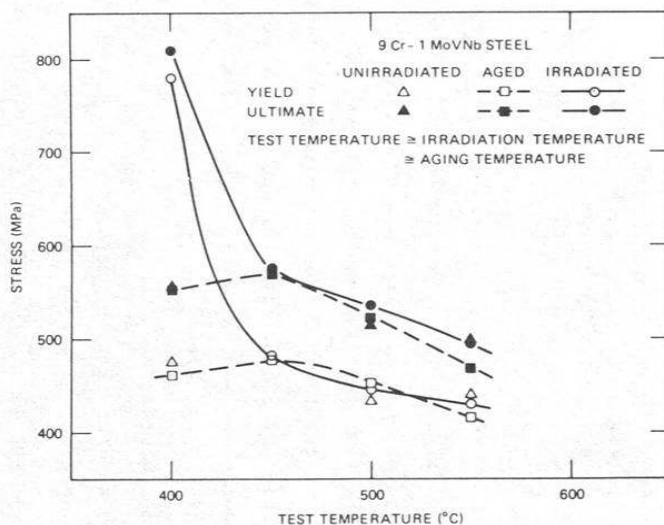


Figure 4.79. Effects of aging for 5,000 h at 400, 450, 500, and 550°C or irradiation in EBR-II to 10 to 12 dpa at different temperatures on 0.2% yield strength and ultimate tensile strength. (Klueh and Vitek 1985).

Figure 4.80 shows the effects of thermal aging for 25,000 h at three different temperatures (DiStefano, et al. 1986). The time-to-rupture data are shown and compared with the average curve for the

material in the unaged condition. The data show a minimal effect of thermal aging on the creep-rupture life for Grade 91 steel even after 25,000 h at 649°C. Figure 4.81 from Blass et al. (1991) shows a similar effect for aging at 593 and 649°C for 75,000 h and testing at the aging temperature.

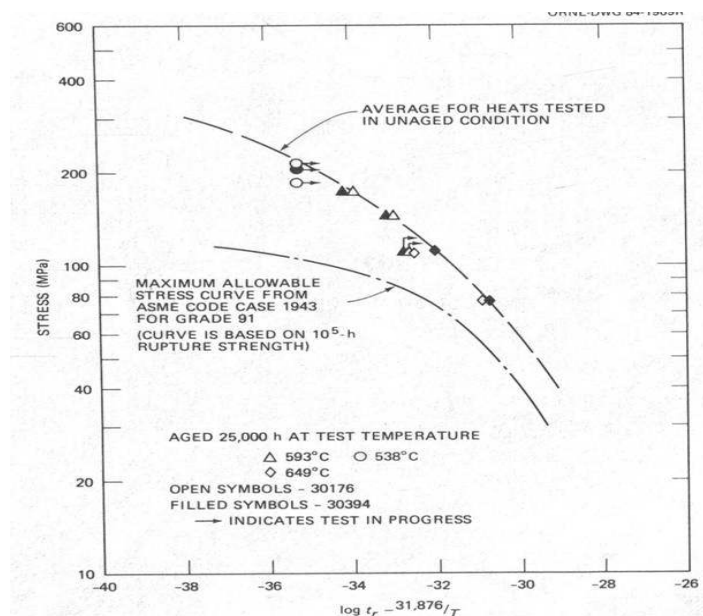


Figure 4.80. Effect of aging for 25,000 h on creep-rupture life of modified 9Cr-1Mo steel. (DiStefano et al. 1986).

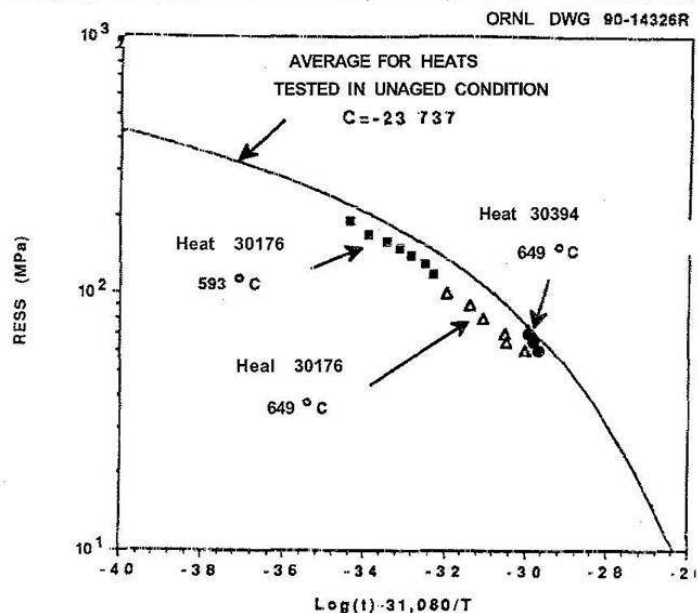


Figure 4.81. Comparison of average rupture behavior for unaged modified 9Cr-1Mo steel with rupture data for two heats aged for 75,000 h prior to testing at the aging temperature. (Blass et al. 1991).

Regarding effects of thermal aging on toughness, the report by DiStefano et al. (1986) provides a series of CVN impact results for Grade 91 steel aged for times up to 25,000 h at temperatures from 482 to 704°C. Figure 4.82 shows the CVN results for aging at 482°C. The ductile-brittle transition temperature shift is about 60°C for that aging temperature, while the shift was about 75°C for aging at 538 and 593°C. For aging at 649 and 704°C, the CVN curves tend to shift to lower temperatures indicating a beneficial effect on the CVN toughness. Regarding other aging studies on grade 91 steel, Klueh and Harries (2001) report results of aging from <450 to 704°C and state that the maximum embrittlement is produced by aging at 538°C for 25,000 h, with transition temperature shift of about 70°C. Figure 4.83 shows effects of aging temperature and time on the CVN ductile-brittle transition temperature shift and the upper-shelf

energy for Grade 91 steel containing 0.40 wt.% Si. Those results confirm that the maximum degradation in toughness from thermal aging occurs from 500-550°C.

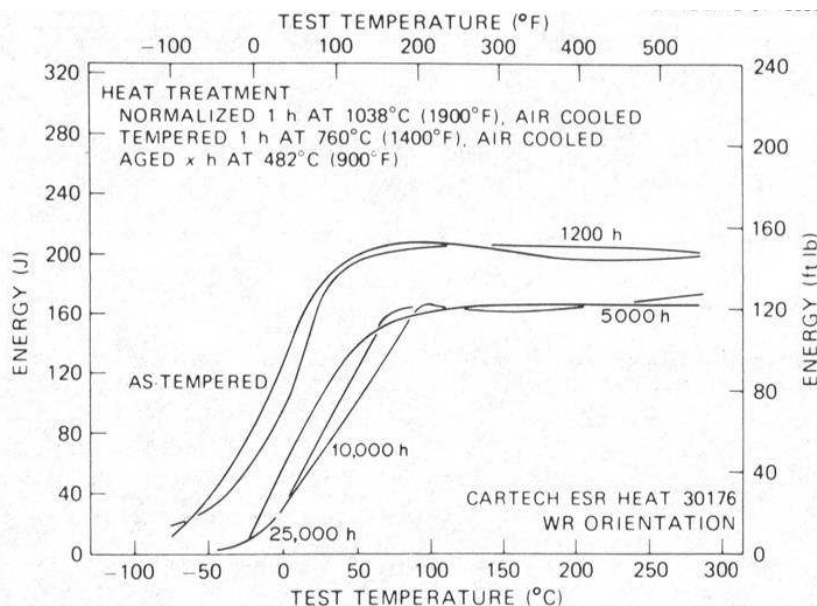


Figure 4.82. Effect of aging at 482°C on Charpy-V energy of 27-mm thick commercially-processed modified 9Cr-1Mo steel plate, CarTech ESR 30176 (DiStefano et al. 1986).

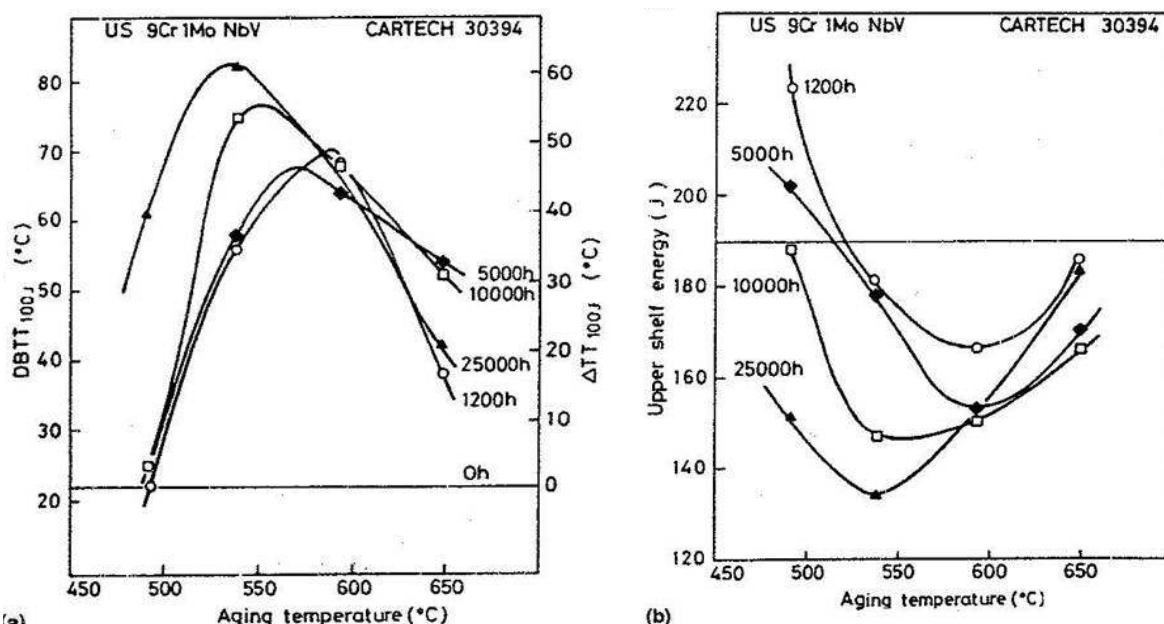


Figure 4.83. Effect of aging temperature and time on the CVN impact DBTT and USE of Grade 91 steel (Klueh and Harries 2001).

Thermal Aging Effect on Code Allowables

The yield and tensile strength reduction factors for Grade 91 are given in Subsection NH. The yield strength reduction factor is one (1) for all temperatures from 371 to 649°C and times up to 300,000 hours. The tensile strength reduction factor is temperature and time dependent and they are shown in Table 4.27.

Table 4.27. Tensile Strength Reduction Factor due to Aging, Grade 91

T (°C)	1 h	10 h	30 h	1E2 h	3E2 h	1E3 h	3E3 h	1E4 h	3E4 h	1E5 h	3E5 h
371	1.00	1.00	1.00	1.00	1.00	1.00	1.00	1.00	1.00	1.00	1.00
400	1.00	1.00	1.00	1.00	1.00	1.00	1.00	1.00	1.00	1.00	1.00
425	1.00	1.00	1.00	1.00	1.00	1.00	1.00	1.00	1.00	1.00	1.00
450	1.00	1.00	1.00	1.00	1.00	1.00	1.00	1.00	1.00	1.00	1.00
475	1.00	1.00	1.00	1.00	1.00	1.00	1.00	1.00	1.00	1.00	0.98
500	1.00	1.00	1.00	1.00	1.00	1.00	1.00	1.00	1.00	0.97	0.97
525	1.00	1.00	1.00	1.00	1.00	1.00	1.00	1.00	1.00	0.94	0.91
550	1.00	1.00	1.00	1.00	1.00	1.00	1.00	1.00	0.94	0.92	0.89
575	1.00	1.00	1.00	1.00	1.00	1.00	1.00	0.95	0.92	0.88	0.83
600	1.00	1.00	1.00	1.00	1.00	1.00	0.96	0.92	0.89	0.85	0.84
625	1.00	1.00	1.00	1.00	1.00	0.97	0.94	0.90	0.87	0.83	0.81
649	1.00	1.00	1.00	1.00	0.98	0.94	0.91	0.87	0.84	0.81	0.78

To account for the effect of long-time elevated temperature service for Grade 91, the S_{mt} values of Table should be redefined as the smaller of

- S_{mt} value from Table 4.24
- $1/3 \times$ specified minimum tensile strength at room temperature \times tensile strength reduction factor of Table 4.10
- $1/3 \times$ tensile strength at temperature of Table 4.18 \times tensile strength reduction factor of Table 4.10
- $2/3 \times$ specified minimum yield strength at room temperature
- $2/3 \times$ yield strength at temperature of Table 4.18

4.3.4 Effects of Sodium Exposure

Sodium Corrosion and Carburization/Decarburization

Mechanisms that contribute to sodium corrosion damage in structural alloys include dissolution of alloy constituents, mass transfer, and interstitial effects. Mass loss and wall thinning, selective leaching of alloying elements and formation of surface ferrite layers, carburization and decarburization, and nitridation and denitridation can occur in liquid sodium, depending on the chemistry and service temperature, and time. These corrosion processes can lead to microstructural changes and degradation of mechanical properties of the structural components. The corrosion processes depend on various factors including material composition, thermo-mechanical treatment, thermal stability of the material microstructure, exposure temperature and time, impurity contents in sodium, sodium velocity, dissimilar materials in contact with sodium, etc.

Corrosion studies of ferritic steels have been focused on 2.25Cr-1Mo steel over the temperature range from 450 to 650°C. Selective leaching of alloying elements occurs in ferritic steels as well. Absorption of Ni, dissolution of Cr, and resultant increase in Fe in the surface was observed in ferritic steels exposed to liquid sodium (Suzuki and Mutoh 1987). Similar to austenitic stainless steels, the corrosion rate of ferritic steels is primarily determined by temperature, oxygen content in sodium and sodium velocity, as shown in Figure 4.84.

The corrosion rate of 2.25Cr-1Mo steel exhibits a power-law relation with oxygen concentration. The corrosion rate increases with increasing sodium velocity up to ≈ 7 m/s, above which the rate is independent of sodium velocity. The accurate dependence of the corrosion rate on the sodium velocity

cannot be determined due to lack of experimental data. Under similar sodium conditions, the corrosion rate of 2.25Cr-1Mo is higher than that of austenitic stainless steels.

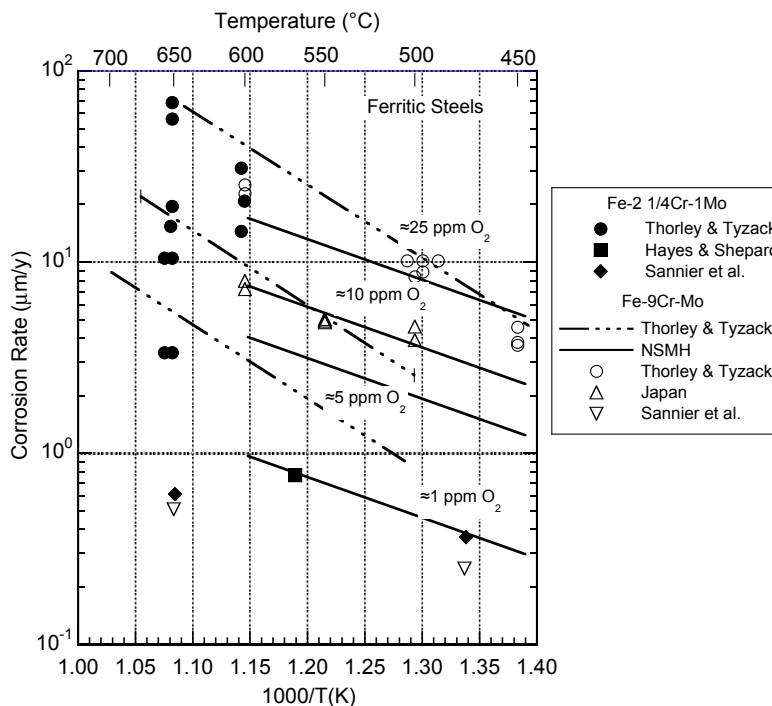


Figure 4.84. Corrosion rates of ferritic steels in flowing sodium (Atsumo et al. 1976, Tyzack and Thorley 1978, Sannier et al. 1971, Hayes and Shepard 1958).

A limited number of studies have been performed on high Cr steels. There are insufficient data to determine the corrosion rate of 9Cr-Mo steels in sodium. In general, 9Cr-Mo steels have lower corrosion rates than 2.25Cr-1Mo steels. Unlike 2.25Cr-1Mo steels, 9Cr-Mo steels showed internal oxidation and surface-oxide formation when exposed to liquid sodium, and the oxidation behavior depends on both the oxygen level and velocity of sodium. More work is needed to understand the corrosion behavior of high Cr ferritic/martensitic steels.

Low-alloy Fe-2.25Cr-1Mo ferritic steel has been favored for use in the construction of sodium heated steam generators on the basis of its high thermal conductivity, established fabrication techniques, and cost. A major concern for this application is the susceptibility of the steel to decarburization when exposed to high-temperature flowing sodium (Natesan et al. 1976, Krankota and Armijo 1974, Matsumoto et al. 1976). The C loss from the material leads to a significant reduction in elevated-temperature mechanical strength (Krankota and Armijo 1973, Sponseller et al. 1973). Furthermore, in sodium systems that contain austenitic and ferritic components, decarburization of the ferritic material can lead to carburization of the austenitic Ss (Atsumo et al. 1976, Besson et al. 1976, Krankota and Challenger 1976).

Ferritic/martensitic steels with higher Cr content, e.g., 9 wt%Cr with 1-2 wt%Mo, have been proposed for both steam evaporator and superheater units to minimize the extent of C transfer in bimetallic sodium heat-transport systems. The high-Cr steels provide a greater resistance to C transfer (Chopra et al. 1976, Menken et al. 1978) and possess adequate elevated-temperature mechanical properties. The carburization/decarburization behavior of these steels can be ascertained from the relationship between equilibrium C concentration and C activity in steel, shown in Figures 4.90 and 4.91 for normalized Fe-2.25Cr-1Mo and normalized and tempered Fe-9Cr-Mo, respectively (Natesan et al. 1976, Chopra et al. 1981). The results show that the variation in the C concentration in steel with C

activity is fairly insensitive to temperature. At temperatures between ≈ 500 and 700°C , the equilibrium C concentration for 2.25Cr-1Mo steel can be expressed as a function of C activity (a_c) by the relation:

$$\ln(C_{2.25\text{Cr-1Mo}})(\text{wt}\%) = -1.12 + 0.61 \ln(a_c)$$

and for 9Cr-1Mo steel with the equation of

$$\ln(C_{9\text{Cr-1Mo}})(\text{wt}\%) = 0.61(a_c)^{0.14} + 10.5(a_c)^{2.2}$$

The equilibrium relationships indicate that, at a C concentration in sodium of 0.05 ppm at 550°C (which corresponds to a C activity of 0.017 in sodium), the Fe-2.25Cr-1Mo and Fe-9Cr-Mo steels would contain ≈ 0.027 and 0.092 wt% C, respectively. The microstructure as well as the composition of the steel plays an important role in the carburization/decarburization behavior. For example, stabilizing elements such as Nb and V in Fe-9Cr-Mo steel (e.g., EM-12 steel) increase the equilibrium C concentration in the steel for a given C activity of the sodium, as shown in Figures 4.85 and 4.86.

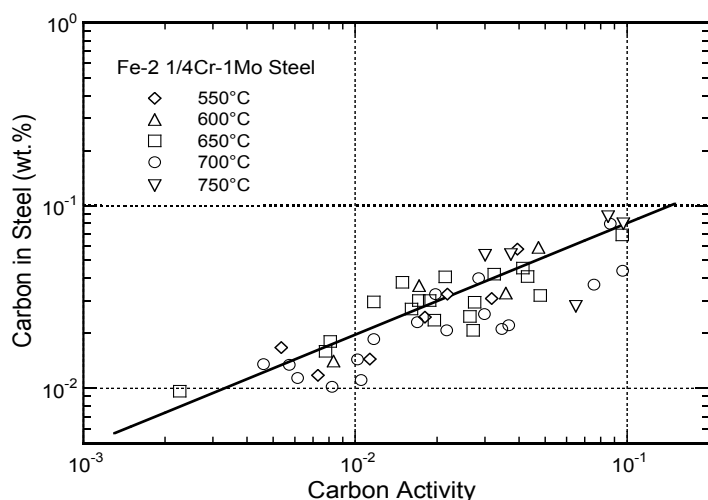


Figure 4.85. Carbon activity – concentration relationship for Fe-2.25Cr-1Mo steel at temperatures of 550 - 750°C (Natesan et al. 1976).

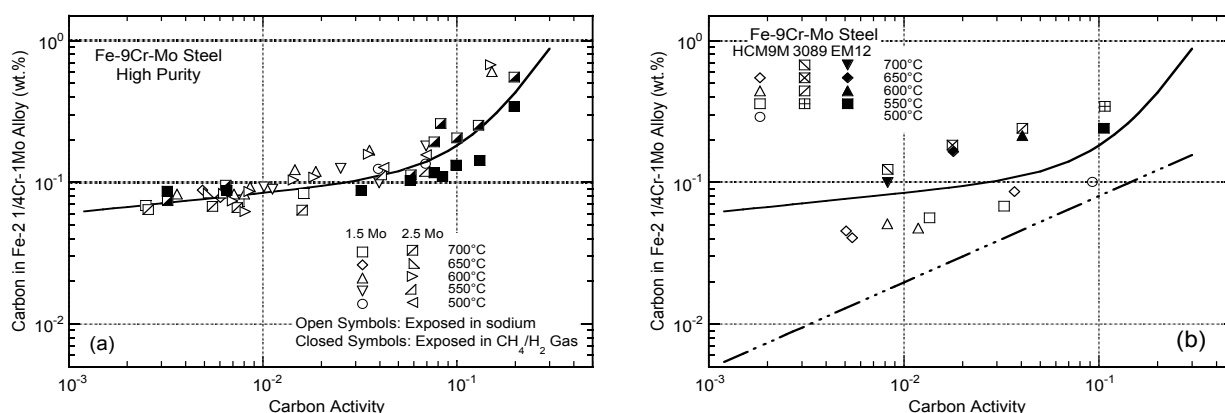


Figure 4.86. Carbon activity – concentration relationship for Fe-9Cr-1Mo steel at temperatures of 550 - 700°C (a) high purity, and (b) commercial purity steels (Chopra et al. 1981).

Numerous investigators have studied the kinetics of carburization/decarburization of ferritic steels in static and dynamic sodium. The extent of carburization/decarburization (expressed in terms of C loss

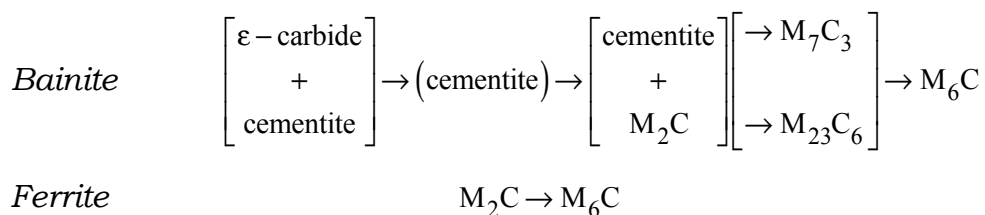
per unit surface area of the steel (M_t) is a function of temperature and sodium-exposure time, t , as defined by the parabolic relationship

$$M_t = 0.5a\rho\Delta c = Kt^{0.5}$$

where a is the radius of the specimen, ρ the density of the steel, Δc the change in the average C concentration in the specimen at time t , and the carburization/decarburization rate constant, K , has an exponential dependence on reciprocal absolute temperature. Krankota and Armijo (1974) have analyzed the available data on decarburization of Fe-2.25Cr-1Mo steel in sodium and obtained “best fit” and “upper limit” curves for the decarburization rate constant. Figure 4.87 shows the upper limit curve as well as some of the more recent data on the decarburization of Fe-2.25Cr-1Mo steel. The scatter in the results arises from differences in the C-activity gradients between the steel and the sodium, which are produced by different initial C contents in the steel and/or the C content of the sodium. In principle, the data used to calculate the decarburization rate constant can be normalized with respect to these factors, from knowledge of the C concentration vs. C activity relationship shown in Figure 4.86 and the C activity in sodium. However, at temperatures above 475°C, the initial heat treatment of Fe-2.25Cr-1Mo (e.g., normalized and tempered, annealed, or isothermally annealed) influences the carbide structure and consequently the decarburization kinetics. Also, in many investigations, the concentration of C in sodium was not determined experimentally.

The influence of heat treatment on the decarburization rate constant can be seen in Figure 4.87. The values for the normalized and tempered material lie well below the upper limit curve, whereas the rate constants for the normalized or annealed material lie above or along the upper limit curve. Differences observed in the rates of decarburization between normalized and normalized-tempered material result from variations in the C activity in steel that occur due to the different microstructures and carbide phases which evolve during the initial heat treatment. When exposed to high-temperature sodium, the material undergoes microstructural changes due to thermal aging and interstitial element transfer. The initial structure and subsequent changes in microstructure are also important in the kinetics of decarburization.

The carbide phases present in normalized steel are primarily M_7C_3 and $M_{23}C_6$ with a small amount of M_2C carbide whereas the normalized and tempered steel contains mostly $M_{23}C_6$ and M_6C carbides. Thermal aging of the material at temperatures between 550 and 700°C leads to the formation of M_6C carbide according to the sequence:



When the Fe-2.25Cr-1Mo steel is exposed to sodium at high temperatures, C loss from the material accelerates the formation of M_6C . The M_6C carbides are considered to be resistant to decomposition because of their relatively stable thermodynamic state in contrast to $M_{23}C_6$ and M_7C_3 . Consequently, the decarburization rate of normalized steel would be higher than that of normalized and tempered steel. The normalized steel will decarburize to a certain C level at each temperature corresponding to a stable carbide structure. Any additional decarburization will be slow because the decarburization rate will be controlled by the dissolution rate of the carbide phases in the ferrite matrix.

A decrease in the decarburization rate constant with time has been observed in isothermally annealed Fe-2.25Cr-1Mo steel after prolonged sodium exposure (Spalaris et al. 1978).

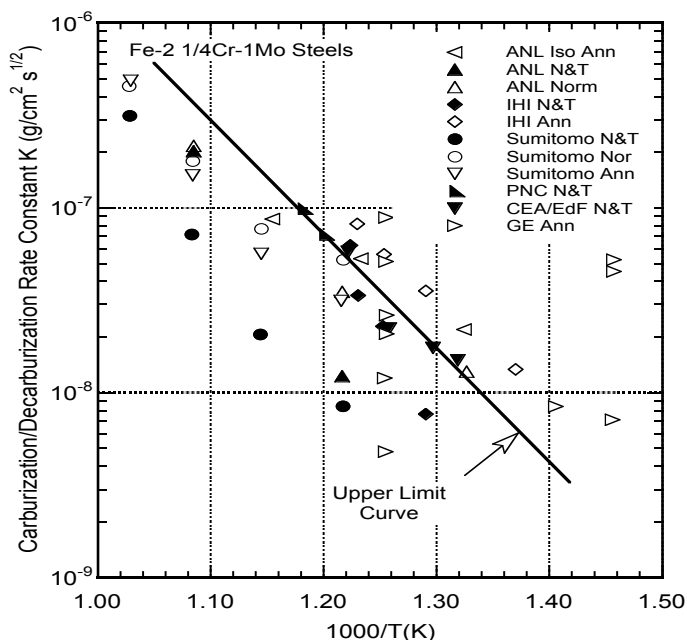


Figure 4.87. Temperature dependence of decarburization rate constant for Fe-2.25Cr-1Mo steel in sodium.

The studies on the C-transfer behavior of Fe-9Cr-Mo steels in sodium show that these steels can either carburize or decarburize depending on the C activity in sodium (Chopra et al. 1976, Menken et al. 1978, Chopra et al. 1981). The temperature dependence of the rate constant is shown in Figure 4.88. The results show that in the temperature range from 500 to 650°C the carburization/ decarburization rate constant varies between $\approx 1 \times 10^{-8}$ and $2.3 \times 10^{-8} \text{ g/cm}^2 \text{ s}^{1/2}$. Similar values for the rate constant were reported by Menken et al. (1978) at 500 and 600°C.

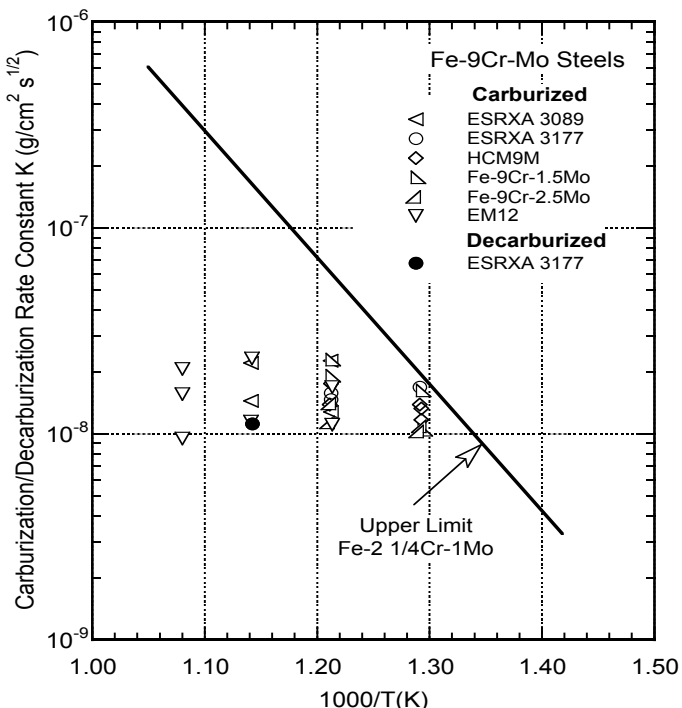


Figure 4.88. Temperature dependence of decarburization/carburization rate constants for 9Cr-1Mo steels in sodium (Chopra et al. 1981).

The carburization/decarburization behavior of higher-Cr ferritic steels is also very sensitive to the microstructure obtained during the initial heat treatment. Studies on the stability of carbide phases in various Cr-Mo steels show that the most stable carbides in Fe-9Cr-1 to 2Mo steels are $M_{23}C_6$ and M_6C . The relative amounts of $M_{23}C_6$ and M_6C depend on the atom ratio of Mo:C in the steel, i.e., M_6C coexists with $M_{23}C_6$ if the Mo:C atom ratio in the matrix is between 1.0 and 3.3, and M_6C is the only carbide when Mo:C is >3.3 . Analyses of carbides extracted from several Fe-9Cr-Mo steels revealed that the M_2X phase (a metal carbide/nitride phase), which forms during the initial heat treatment, is also present in these steels. This phase is metastable at high temperatures and eventually transforms to $M_{23}C_6$ or M_6C carbides with time. The Fe-9Cr-Mo steels that decarburize to very low carbon concentrations when exposed to sodium with low C activity either contain M_2X phase or have M_6C as the only stable carbide (Chopra et al. 1981). Formation of M_2X phase and the subsequent decarburization of the material can be prevented by limiting the N concentration of the steel to <0.04 wt.%. The relative amount of M_6C in Fe-9Cr-Mo steels can be reduced by keeping the Mo:C atomic ratio ≤ 3.3 .

The information on the kinetics of decarburization of Fe-2.25Cr-1Mo steel in a sodium environment can be used to calculate the average C concentrations of a typical steam-generator tube (initial C content of 0.12 wt% and 3.68 mm wall thickness) as a function of service temperature after a 30-y period. The results are presented in Figure 4.89 along with the approximate temperature ranges for the steam generators in the EBR-II, Phenix, and Super Phenix plants. Figure 4.90 is a plot of C loss from the steel after 30-y operation as a function of tube-wall thickness and temperature. The amount of C loss is greater for tubes with thinner wall sections, and increases with temperature.

The transport of N into and out of ferritic steels in a sodium environment can occur independent of C migration (Atsumo et al. 1976, Chopra et al. 1976). No N loss in 9Cr-Mo steels was observed below 550°C in sodium. Above 550°C , loss of N increases with increasing temperature and exposure time.

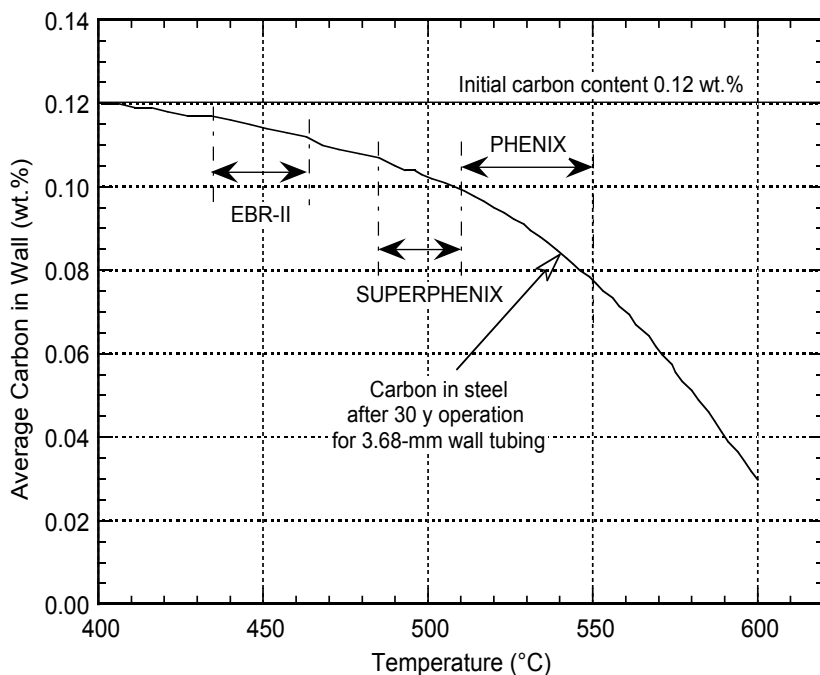


Figure 4.89. Calculated average C concentration in 2.25Cr-1Mo steel tubing as a function of temperature after 30 y exposure to a sodium environment.

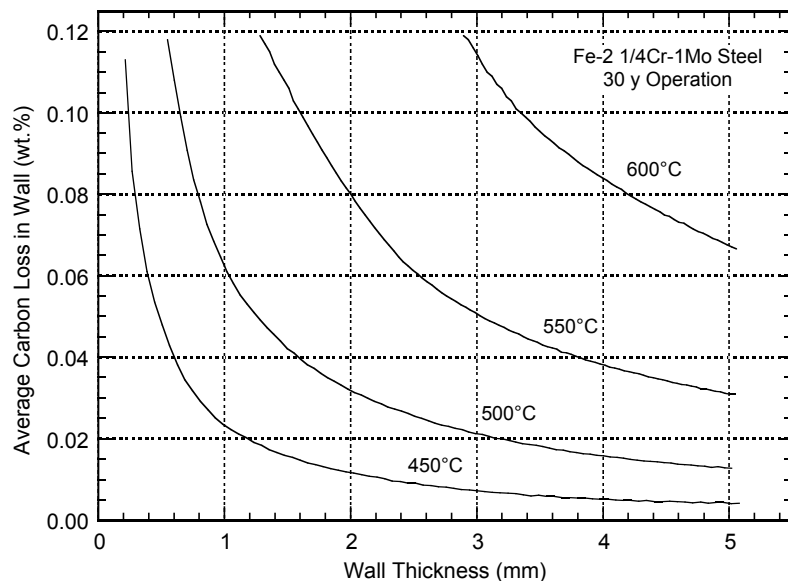


Figure 4.90. Average carbon loss as a function of tube wall thickness and temperature for 2.25Cr-1Mo steel after 30-y exposure to a sodium environment.

Degradation in Mechanical Properties

Tensile Properties

The loss of C from Fe-2.25Cr-1Mo steel in a sodium environment leads to a reduction in tensile strength. For components with intermediate section thicknesses (e.g., pipe), the decrease in strength is proportional to the depth of the decarburized layer. Maximum reduction will occur in thin sections, e.g., superheater and evaporator tubes. Therefore, for design of components with thin and intermediate section thicknesses, it is essential to establish long-term environmental effects and modify the allowable design stresses to ensure satisfactory performance of components over the expected service life.

Ideally, the effect of sodium environment on the mechanical behavior of structural materials should be evaluated from mechanical property data on material with specific depths of decarburized or carburized layer, which were established under known conditions, e.g., time, temperature and sodium purity. However, the current assessment of the change in mechanical behavior of Fe-2.25Cr-1Mo steel due to decarburization in a sodium environment is primarily based on the mechanical-property data obtained from steels with low initial bulk C contents (Sponseller et al. 1973, Klueh 1973, Apblett and Matejic 1973, Smith 1953, Zeisloft et al. 1973). These data are in a good agreement with results obtained from specimens that were decarburized in sodium to different bulk C contents. The tensile and yield strengths of Fe-2.25Cr-1Mo steel with different C contents is shown in Figure 4.91. The results indicate that the strength of steels with >0.03 wt% C is generally above the minimum recommended. Steels with less than 0.03 wt% C exhibit poor tensile and yield strengths.

The tensile and yield strengths of specimens that were exposed to elevated-temperature sodium are given in Figure 4.92. Decarburization of the specimens causes a reduction in tensile strength. Studies on the influence of thermal aging on the tensile properties of Fe-2.25Cr-1Mo steel show significant decrease in the tensile strength of this steel (Shiels et al. 1971, Borgstedt et al. 1973, Schrock et al. 1976). Consequently, to establish the effect of a sodium environment on the mechanical properties, it is important to evaluate the influence of thermal aging as well as decarburization. Figure 4.93 shows the change in mechanical strength of decarburized Fe-2.25Cr-1Mo steel as a function of bulk C content. The control data shown in this figure refer to specimens that were thermally aged in an inert atmosphere for

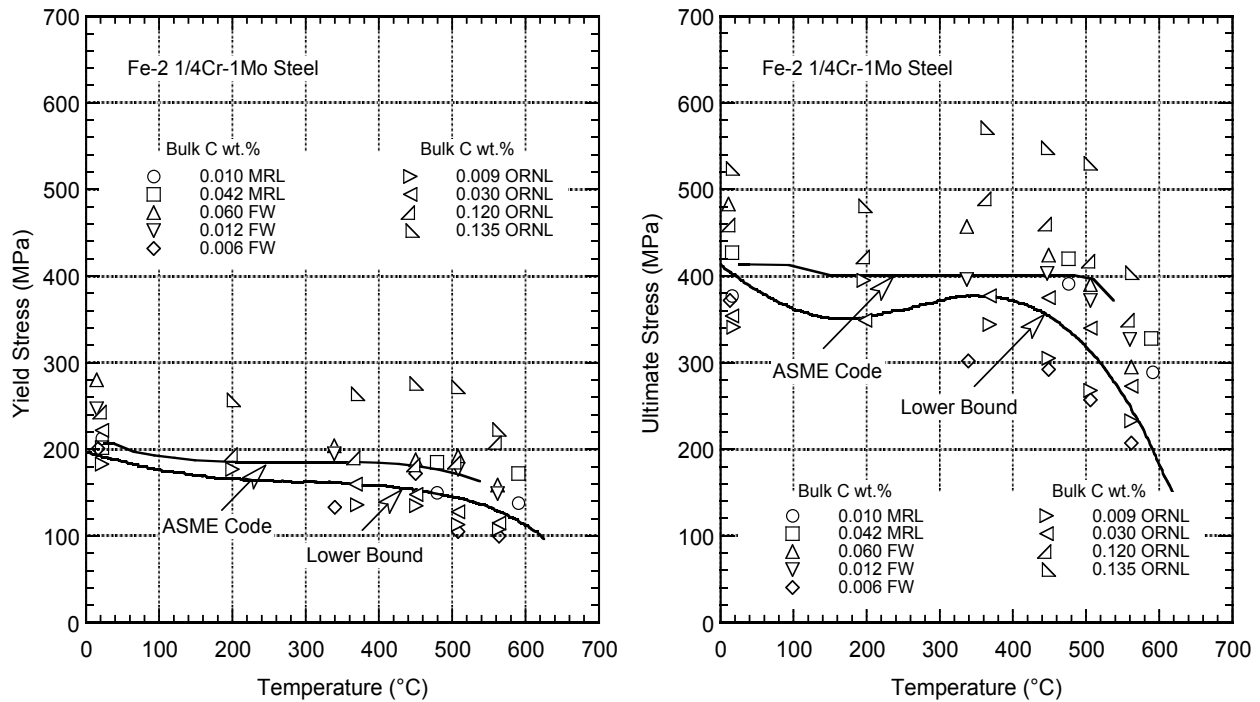


Figure 4.91. Yield and tensile strengths for 2.25Cr-1Mo steels containing different bulk carbon concentrations (Sponseller et al. 1973, Klueh 1973, Aplett and Matejic 1973, Smith 1953, Zeisloft et al. 1973).

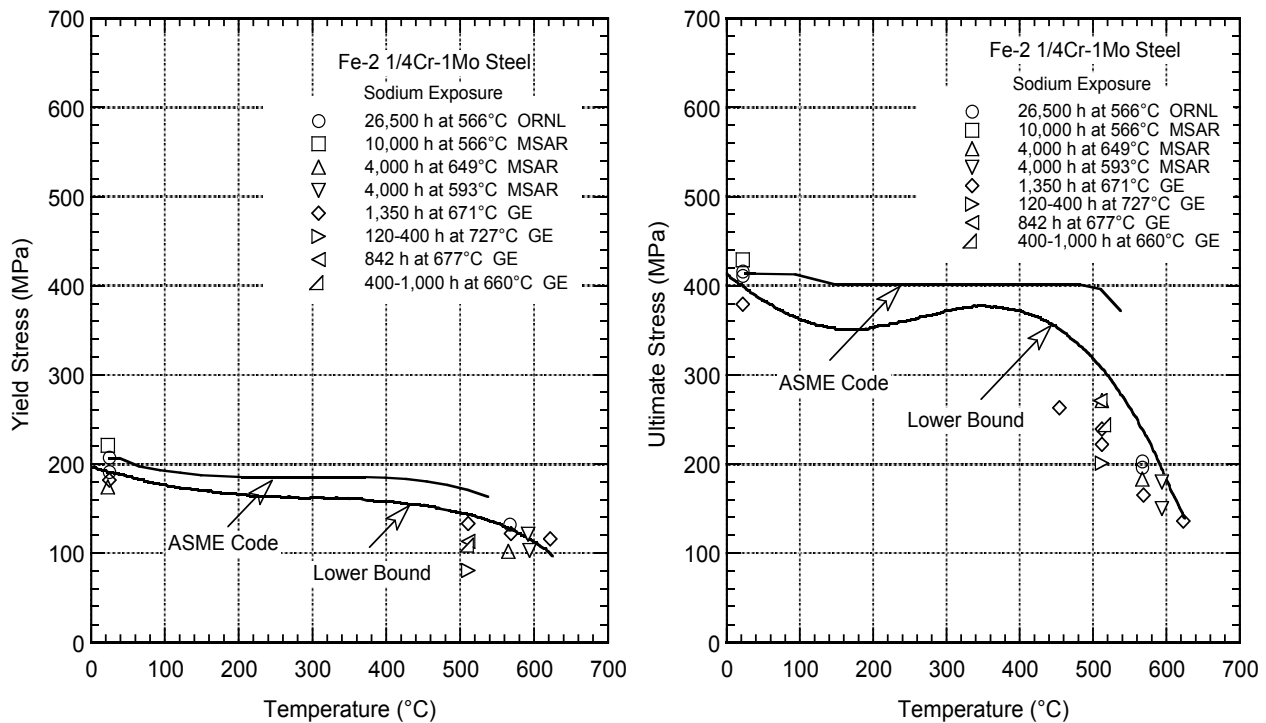


Figure 4.92. Yield and tensile strengths for 2.25Cr-1Mo steels after decarburization in sodium (Klueh 1976, 1977, Hiltz et al. 1972, Licina and Roy 1982, Pizzo and Hampton 1980, Wozadlo et al. 1980, Licina and Roy 1984, Chopra 1985, Yuhara and Atsumo 1978).

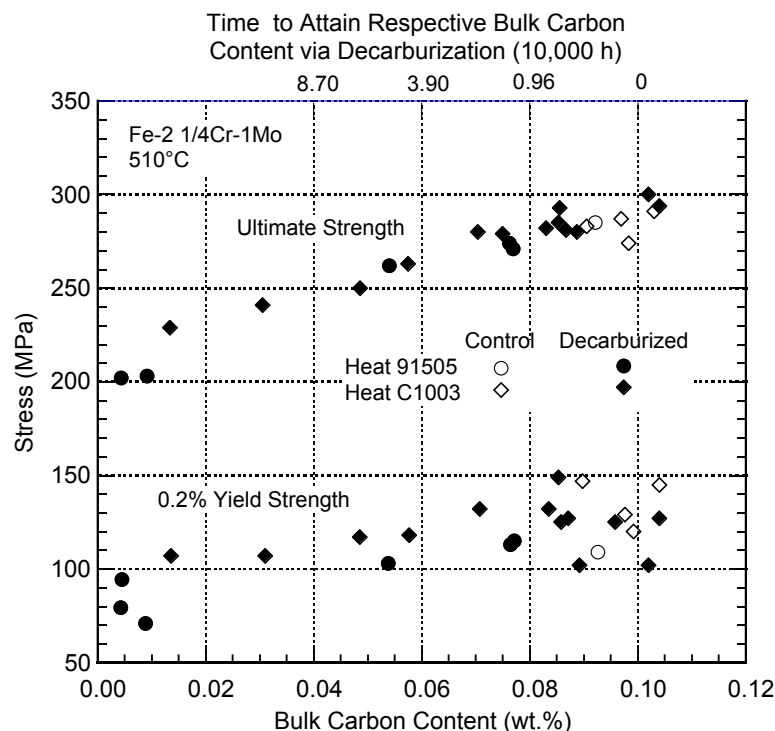


Figure 4.93. Tensile strength of decarburized 2.25Cr-1Mo steel as a function of bulk carbon concentration (Program for the Development of Design Data LMFBR Steam Generator Materials 1978).

identical time and temperature conditions. Decarburization progressively reduces the tensile and yield strengths of the steel. The data can be used to estimate the time-dependent reduction in tensile strength due to decarburization of the steel in a sodium environment. Based on the decarburization kinetics shown in Figure 4.87, the total C loss for superheater tubing (3-mm thick) during a design life of 10^5 h at 510°C is approximately 0.025 wt%. This represents a strength reduction of $\approx 10\%$.

Data on the effects of carburization/decarburization and the sodium environment itself on the mechanical properties of Fe-9Cr-Mo ferritic steels are sparse. The average and minimum values of tensile yield and ultimate strength for various normalized and tempered Fe-9Cr-Mo steels tested in air are shown in Figure 4.94. As discussed above, under typical temperature and sodium-purity conditions for liquid metal fast breeder reactors, the Fe-9Cr-Mo steels tend to carburize. The long-term effects of sodium environment on the tensile properties of the Japanese modified Fe-9Cr-Mo steel have been determined from data on thermally aged and sodium-exposed materials with different bulk C contents (Ito et al. 1992). In spite of the presence of a thin carburized layer, no difference in tensile properties was observed between the sodium-exposed and thermally aged materials containing 0.08-0.14 wt.% C.

Ito et al. (1992) exposed Fe-9Cr-1Mo steels for $\approx 10,000$ h in a sodium environment. Based on the results they estimated that the average bulk C content of the tubes to be 0.10-0.15 wt% relative to an initial C content of 0.10 wt% in Fe-9Cr-1Mo steel steam generator tubes in liquid metal fast breeder reactors after $\approx 200,000$ h operation at 505°C in sodium containing 0.01-0.10 wppm C. Based on the limited data, it may be concluded that a sodium environment is not likely to have a significant effect on the tensile properties of Fe-9Cr-Mo steels at temperatures below 550°C .

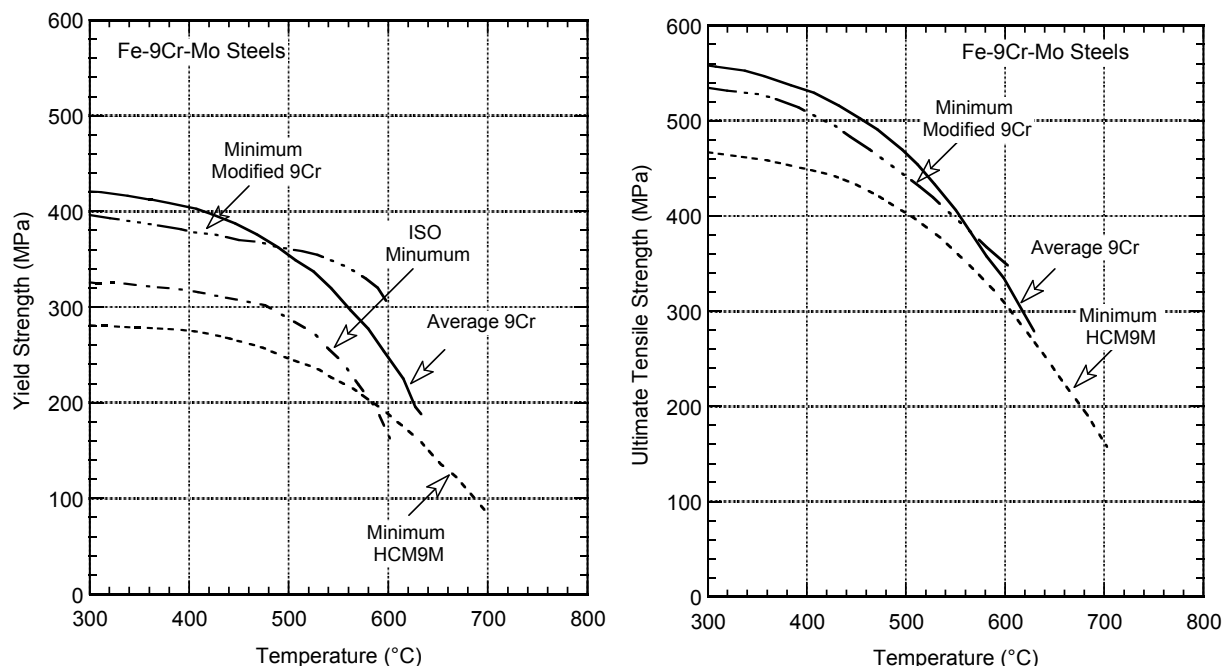


Figure 4.94. Change in yield and ultimate tensile strengths of 9Cr-Mo steels with temperature (Wood et al. 1978, Sikka 1984, Yukitoshi et al. 1978, Smith 1975).

Creep Properties

Little information is available on the creep rupture properties of ferritic/martensitic steels exposed to high temperature sodium. For 2.25Cr-1Mo steel, a loss of creep rupture strength in sodium has been suggested to be mainly due to decarburization in the material. A direct correlation between reduction in creep rupture strength and decarburization in sodium has been developed, as shown in Figure 4.95. A reduction of 10% of the creep rupture strength was estimated for a service life of 100,000 h in sodium at 510°C. The loss in bulk C content and the change in creep-rupture strength at different temperatures are plotted in Figure 4.96 as a function of section or wall thickness of a component. The results show that the 105-h creep-rupture strength ratio for material with wall thicknesses >3 mm is >0.9.

Data on the effect of sodium environment on the creep properties of Fe-9Cr-Mo steels are also very limited (Wood 1978, Charnock et al. 1978, Ito et al. 1992, Wood et al. 1977, Asayama et al. 2001). A study by Asayama et al. (2001) on 9Cr-Mo steel indicated that the creep rupture strength was not affected by pre-exposure in sodium at 500 and 550°C for 5,000 hours, as shown in Figure 4.97. The data for sodium exposed are comparable to those of thermally aged specimens (Ito et al. 1992).

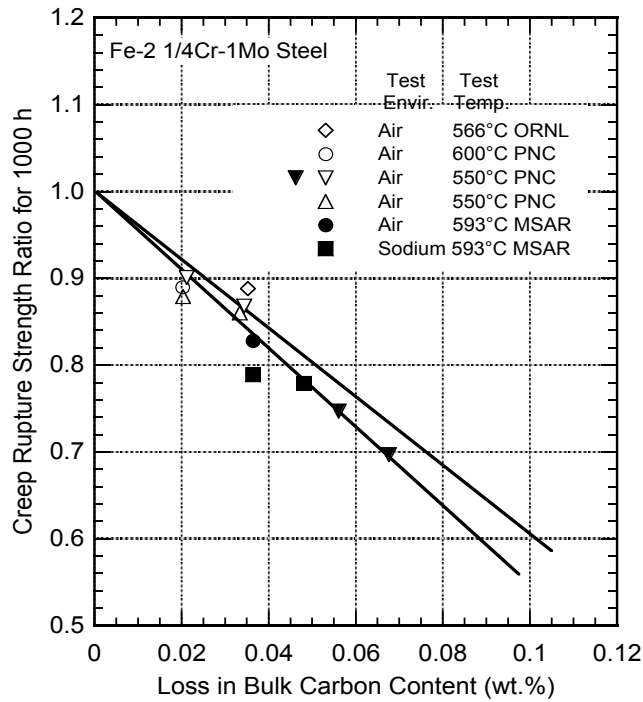


Figure 4.95. Relation between C loss from sodium-induced decarburization and reduction in creep rupture strength for 2.25Cr-1Mo (Kluh 1977, Yuhara and Atsumo 1978, Andrews and Kirschler 1966).

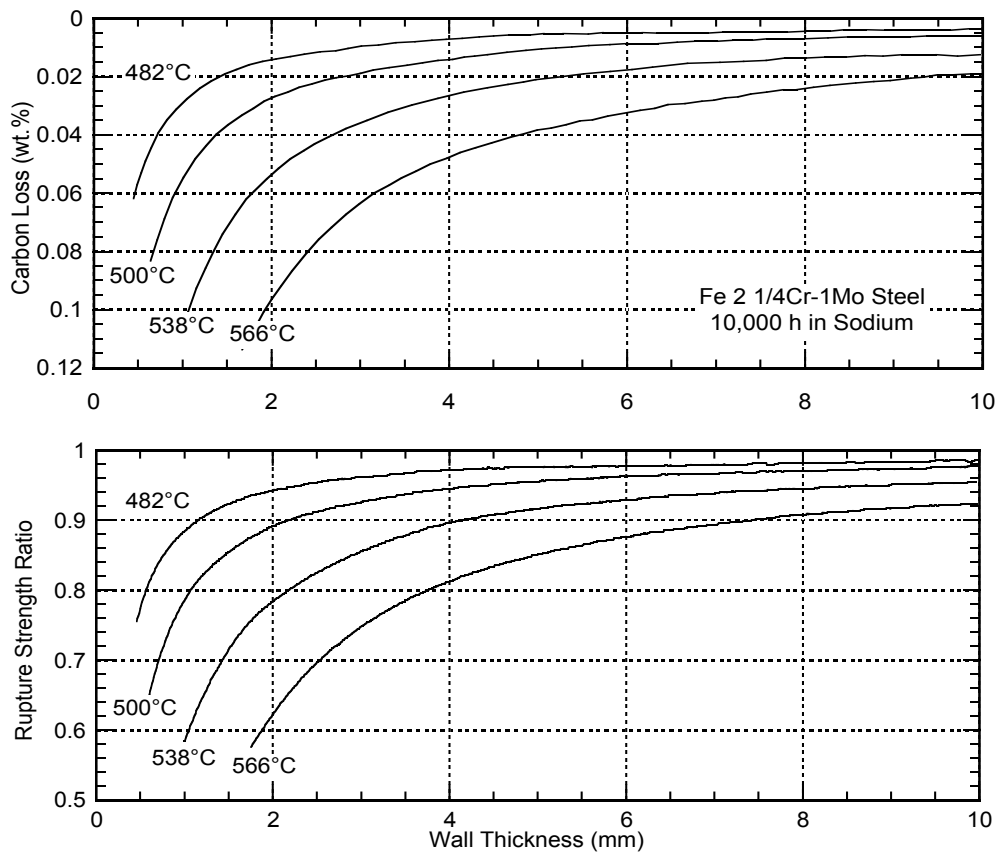


Figure 4.96. Change in carbon concentration and creep-rupture strength for 2.25Cr-1Mo steel, as a function of wall thickness.

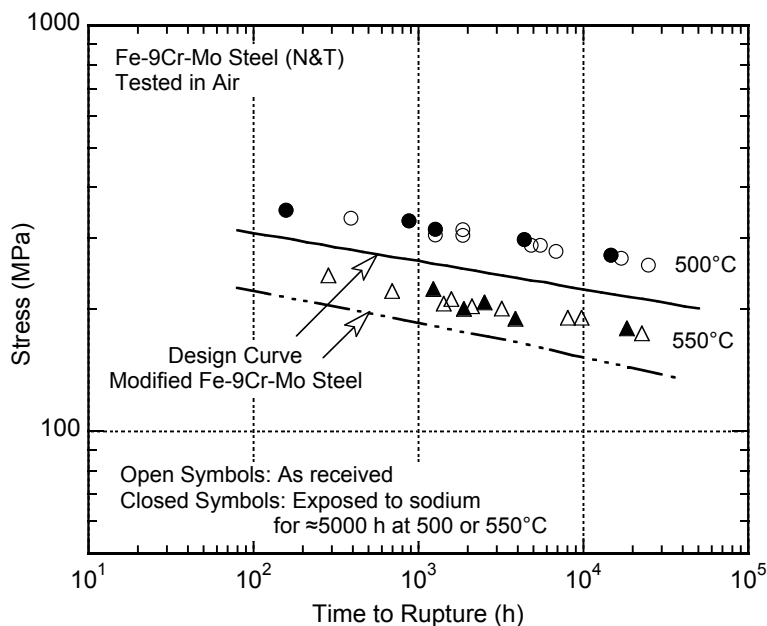


Figure 4.97. Creep rupture data for 9Cr-Mo steels in air and in sodium (Asayama et al. 2001).

Fatigue and Creep-Fatigue

In contrast to the tensile and creep properties, where the variation in mechanical strength is primarily due to decarburization rather than the sodium environment per se, the fatigue life of Fe-2.25Cr-1Mo steel tested in sodium is greater by a factor of 3 to 10 than when tested in air (Andrews and Kirschler 1966, Chopra 1981). The absence of surface oxidation in a sodium environment increases the fatigue life of the material. In oxidizing environments such as air or steam, the oxide scale that forms on the surface of the test specimen can influence the crack initiation process. However, the partial pressure of oxygen in a liquid-sodium environment is much lower than that of other test environments and, therefore, surface oxidation effects are less likely to influence fatigue life in liquid sodium. Consequently, for a given fatigue life, the allowable design strain of a component for service in a sodium environment is at least 25% higher than that in air. These results are applicable for low-oxygen sodium of normal purity, i.e., sodium containing ≈ 0.05 to 0.4 ppm carbon and ≈ 1 ppm oxygen.

Fatigue data for isothermally annealed Fe-2.25Cr-1Mo steel show a unique plastic strain life relationship which is independent of temperature between 482 and 593°C and strain rate in the range of 4.0-0.004 %/s (Tomkins 1976). Similarly, irrespective of the temperature and material condition, the plastic strain life behavior of thermally aged and sodium-exposed material is represented by a single relationship (the effect of strain rate on the fatigue life of thermally aged and sodium exposed material has not been investigated). The plastic strain amplitude vs. fatigue life data are shown in Figure 4.103 for isothermally annealed Fe-2.25Cr-1Mo steel in sodium. Similar data for thermally aged and sodium-exposed steels are shown in Figure 4.99. The fatigue life of isothermally annealed steel in helium are also included in Figure 4.98, and the best-fit strain vs. life curves in air (Ellis et al. 1975, Booker et al. 1979, Brinkman et al. 1980) are included in both figures for comparison. The variation in the total strain-life behavior for different temperatures and material conditions arises from the changes in the cyclic stress strain behavior as a function of temperature, strain rate, and material condition. The influence of sodium environment on the fatigue life of Fe-2.25Cr-1Mo steel at temperatures of 482 and 538°C is shown in Figure 4.100.

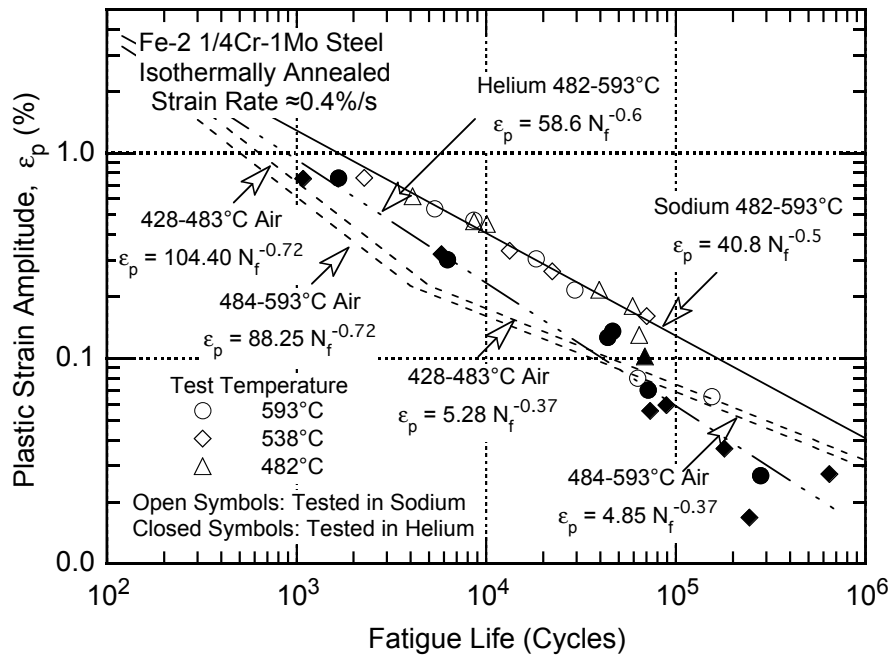


Figure 4.98. Plastic strain amplitude vs. fatigue life data for isothermally annealed 2.25Cr-1Mo steel in sodium (Andrews and Kirschler 1966, Chopra et al. 1981, Ellis et al. 1975, Booker et al. 1979, Brinkman et al. 1980).

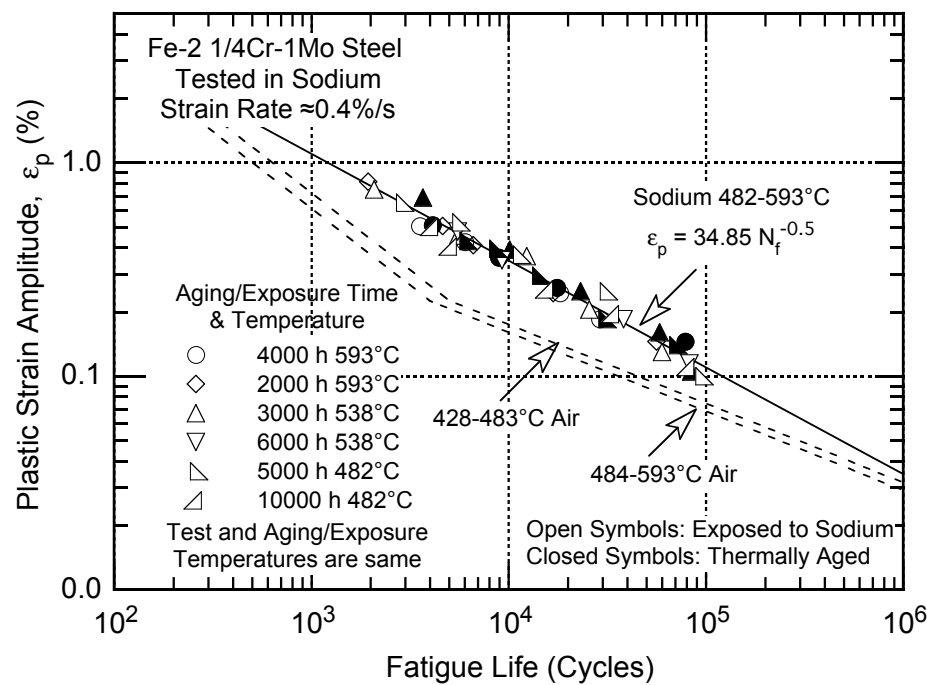


Figure 4.99. Plastic strain amplitude vs. fatigue life data for thermally aged and sodium exposed 2.25Cr-1Mo steel in sodium (Chopra et al. 1981, Ellis et al. 1975, Booker et al. 1979, Brinkman et al. 1980).

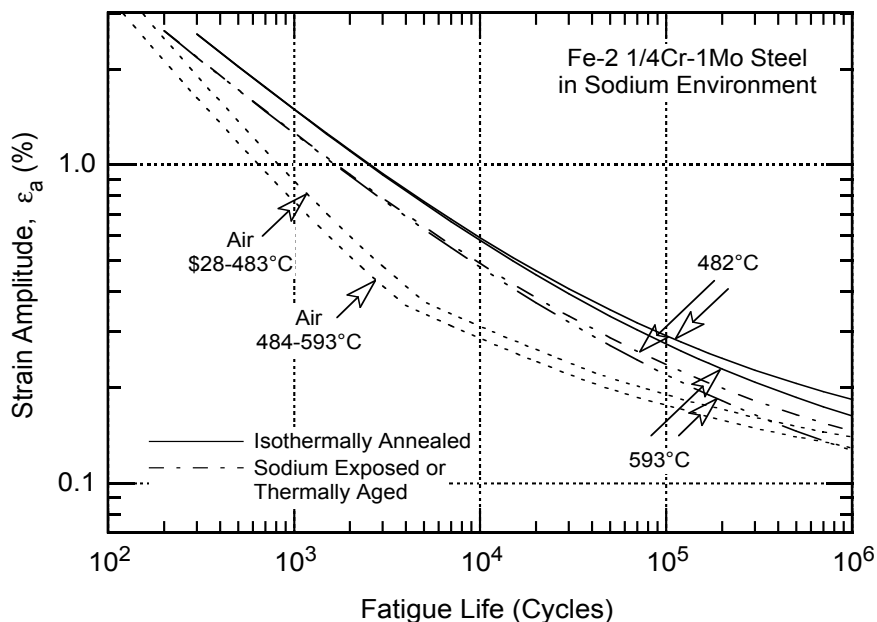


Figure 4.100. Fatigue strain-life curves for 2.25Cr-1Mo steel in sodium at 482 and 593°C (Brinkman et al. 1980).

The creep-fatigue interaction for Fe-2.25Cr-1Mo steel has also been investigated in a sodium environment using a triangular waveform with hold periods at peak tensile and/or compressive strain, as well as a slow/fast sawtooth waveform in which strain rates during the tensile and compressive half of the fatigue cycle differed by a factor of 100 (Brinkman et al. 1980). The results indicate a significantly different creep-fatigue behavior than that observed in air. In sodium, a tensile-hold period or a slow/fast sawtooth waveform reduces fatigue life whereas a compressive hold period or a fast/slow waveform has no effect.

The reduction in life is strongly dependent on temperature, i.e., for a given loading condition, fatigue life is a factor of ≈ 4 lower at 593°C, and a factor of ≈ 2 lower at 538°C, and is affected very little at 482°C. Metallographic examination of the test specimens reveals that the tensile-hold period or a slow tensile half of the loading cycle leads to creep damage of the material, i.e., bulk cavitation (Figure 4.101) and intergranular cracks (Figure 4.102) at the surface. Such creep damage is not observed for the fast/slow or slow/slow tests (i.e., constant strain rate of 0.004%/s). This behavior indicates that the bulk damage in Fe-2.25Cr-1Mo steel occurs only under tensile creep conditions. For symmetric hold periods or slow strain rate tests, the cavities that form during the tensile half of the fatigue cycle either anneal out during the compressive cycle or do not grow to sufficient size to cause bulk damage.

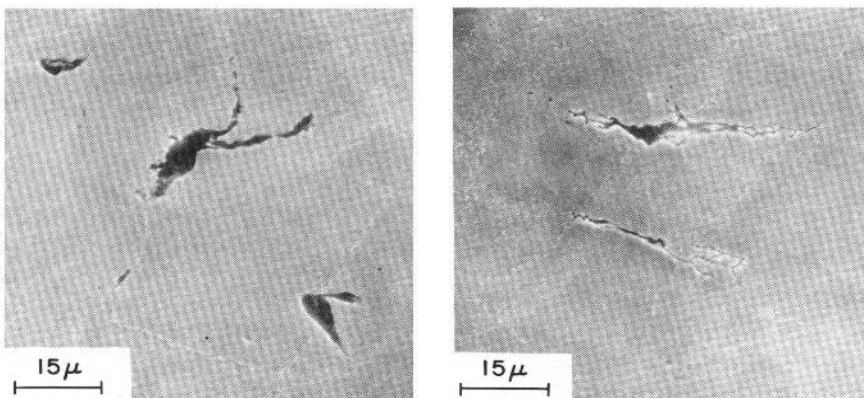


Figure 4.101. Micrographs showing cavities in sodium-exposed 2.25Cr-1Mo steel tested in sodium at 538°C with a slow-fast strain rate (Chopra 1981).

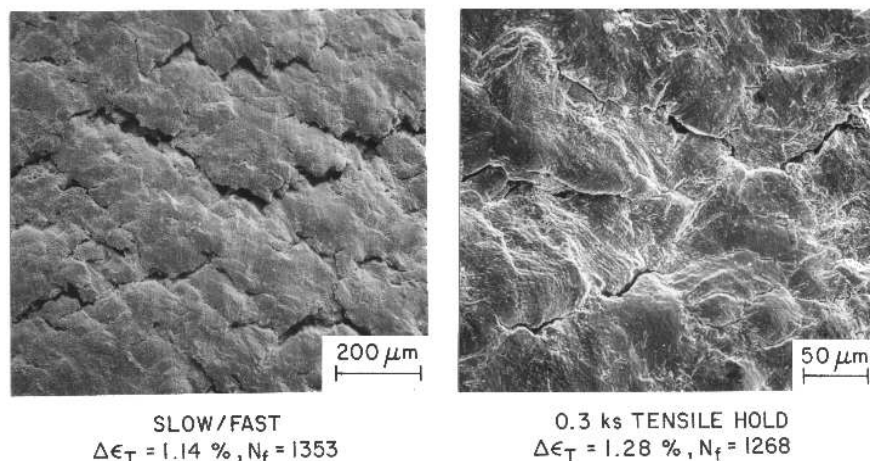


Figure 4.102. Micrographs of the gauge surfaces of sodium-exposed 2.25Cr-1Mo steel tested in sodium at 593°C (Chopra 1981).

The creep-fatigue behavior for Fe-2.25Cr-1Mo steel in a sodium environment is very different than that in air, where compressive hold time was found to be more damaging than tensile hold time at low (<1%) strain ranges (Ellis et al. 1975, Booker et al. 1979, Brinkman et al. 1980). As mentioned above, surface oxidation effects are absent in a low-oxygen sodium environment, whereas in air, oxidation effects may completely dominate fatigue life such that the creep-fatigue interaction is negligible. For example, the reduction in fatigue life for compressive hold time tests in air has been attributed to cracking of the surface oxide, which reduces the period for crack initiation (Brinkman et al. 1980). The oxide scale that forms during the compressive hold period is subjected only to tensile strains and may crack easily. On the other hand, oxide developed during tensile hold period is subjected only to compressive strains and therefore does not crack readily. In a helium environment, where environmental interactions are less pronounced, tensile hold periods are observed to be more damaging than compressive hold periods.

The creep-fatigue behavior of Fe-2.25Cr-1Mo steel in sodium is best represented by the damage-rate approach for predicting fatigue life (Majumdar and Maiya 1980). However, the data are rather limited and additional information is needed to establish the long-term creep-fatigue behavior of this steel in a sodium environment and to determine the influence of thermal aging and decarburization on creep-fatigue interactions.

The fatigue life of ferritic steels, in general, is better in sodium than in air. The fatigue strain vs. life data for normalized and tempered Fe-9Cr-Mo steel in air (Wood 1979, Sanderson and Jacques 1984, Mannan et al. 2005) and sodium (Asayama et al. 2001, Chopra 2007) environments are shown in Figure 4.103. Fatigue life in sodium is a factor of 3-10 longer than in air. Also, moderate carburization after exposure to sodium has little or no effect on the fatigue life of these steels at 538°C. A beneficial effect on fatigue life is also observed in a helium environment; the fatigue life in helium is 10% higher than that in air (Wood et al. 1977). These results are consistent with the data on Fe-2.25Cr-1Mo steel in sodium. The partial pressure of oxygen in a liquid-sodium environment is much lower than that of other test environments and, therefore, surface oxidation effects do not influence fatigue life in sodium. In oxidizing environments such as air or steam, the oxide scale that forms on the surface of the test specimen can influence the process of crack initiation. Additional data on the effect of sodium environment on the mechanical behavior of Fe-9Cr-Mo steels are needed to establish the performance limits for components fabricated from this material.

The creep fatigue life of Mod. 9Cr-1Mo under tensile hold in the sodium environment is similar to that in the atmospheric tests with the same condition; a compressive hold has nearly no effect on the

fatigue life in sodium (see Figure 4.104). It is suggested that internal creep damage is predominant under creep-fatigue loading, and the creep damage under the compressive stress is insignificant (Shoichi et al. 2001).

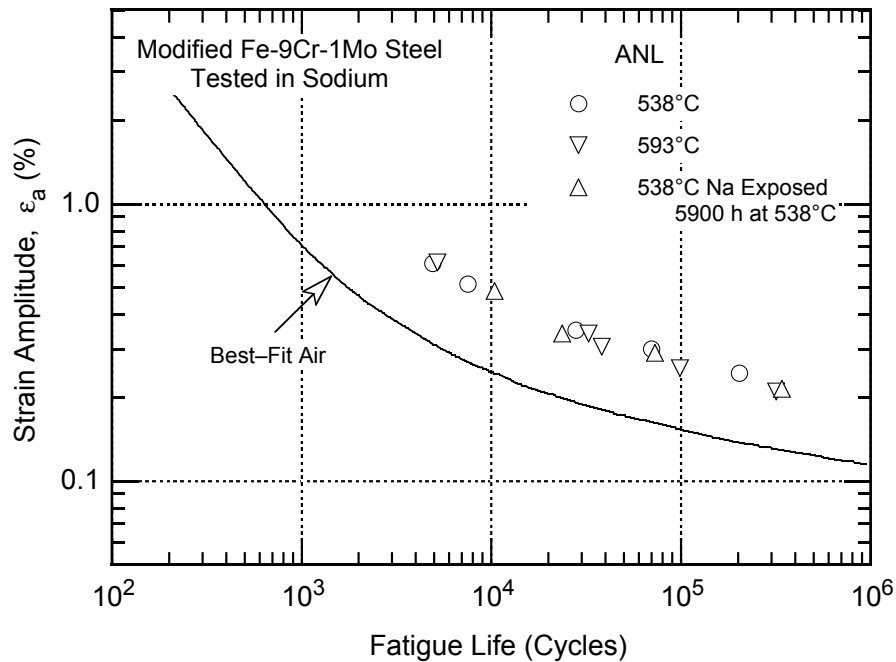


Figure 4.103. Effect of sodium environment on fatigue life of mod.9Cr-1Mo.

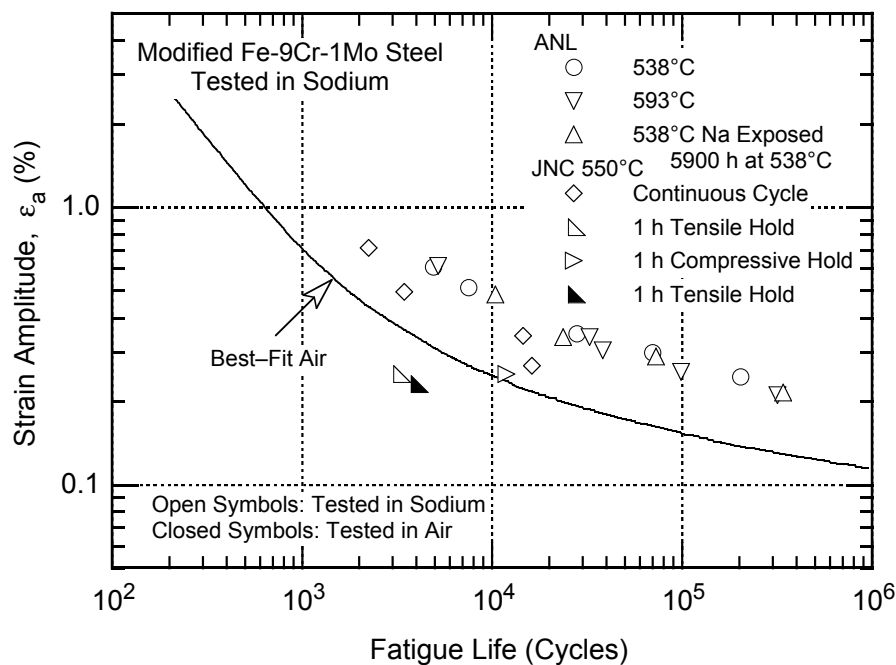


Figure 4.104. Effects of sodium on fatigue and creep-fatigue behavior of mod. 9Cr-1Mo steel.

Fatigue Crack Growth

The fatigue crack growth rate of 2.25Cr-1Mo in a flowing sodium environment at 427°C was found to be about five times lower than that in air under the same test conditions (Figure 4.105).

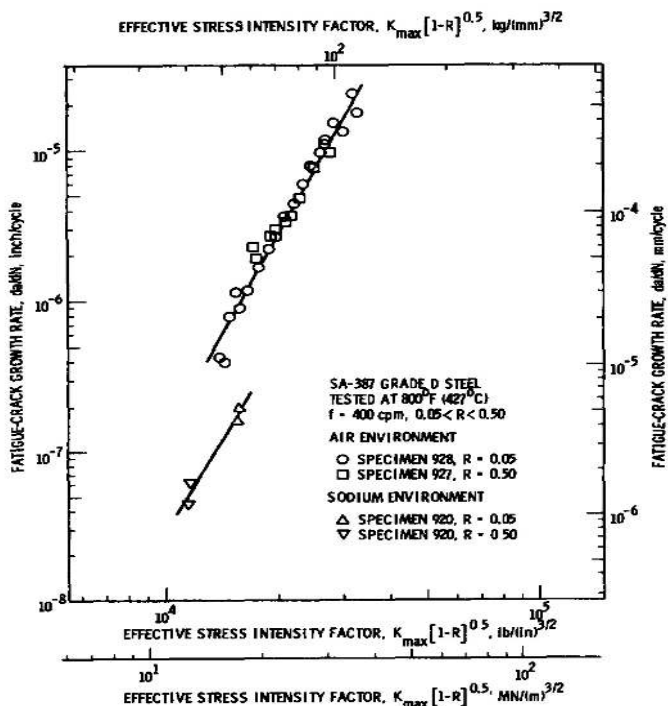


Figure 4.105. Fatigue crack growth rate of 2.25Cr-1Mo steel tested in air and sodium at 427°C (James 1976).

4.3.5 Effects of Neutron Irradiation

The F-M alloys (e.g., HT-9 and 9Cr-1MoV) exhibit significantly greater swelling resistance than the austenitic stainless steels, with HT-9 having demonstrated no swelling in the core of FFTF to a dose level of about 200 dpa. For such high doses, however, further work is needed to examine other helium effects. For irradiation temperatures below $\approx 400^\circ\text{C}$, however, radiation embrittlement is an issue. Although radiation hardening is not a concern at temperatures $>450^\circ\text{C}$, very long-term combined thermal and radiation-driven processes may lead to changes in mechanical behavior. One example is that of thermal creep possibly affected by low dose irradiation. Moreover, long-term thermal exposure, accelerated by very low fluxes of point defects at low dose rates, may lead to microstructural and phase changes that affect mechanical properties. Possible examples are strain aging due to segregation of carbon and nitrogen, temper embrittlement due to segregation of solutes such as phosphorus to grain boundaries, and formation of precipitates and solute-defect clusters that cause hardening. For these steels, irradiation creep is not an issue at low doses, but can be at higher doses. For the ABR operating temperature of $\sim 500^\circ\text{C}$, and with these materials being in the creep regime, the effect of irradiation will be a significant issue from the standpoint of licensing of a new plant with a design life of 60 years.

During the LMFBR Program, it was realized that the F-M steels also offered better resistance to liquid metal embrittlement from fission products, higher thermal conductivity and lower thermal coefficient of thermal expansion. Moreover, towards the end of that program, the relatively newer modified 9Cr-1Mo steel (modified with vanadium and niobium and designated grade 91) began receiving increased attention because it offered improved fracture resistance, higher creep rupture strength, and improved long-term phase stability than the older HT-9 alloy. Since that time, evolution of the F-M steels has resulted in development of steels with operating capability (for inclusion within the ASME Code) to 650°C . This evolutionary history of the alloy, physical metallurgy, and mechanical properties, are described in a monograph by Klueh and Harries (2001) and in a review paper by Klueh and Nelson (2007). Additional details on the microstructural features responsible for improved high temperature performance of T91 are available in (Jones et al. 1991).

Radiation effects in F-M steels can be summarized by noting the principal modes that degrade the material performance and the irradiation temperature regimes in which they occur:

- a) Low temperature radiation hardening and loss of ductility. Radiation hardening (increase in yield strength) occurs due to formation of point defect clusters and loops at temperatures up to 400-425°C, resulting in flow localization and loss of uniform strain. Radiation embrittlement occurs because the crack tip stress is raised above the critical stress required for cleavage fracture resulting in an increase in the ductile-brittle transition temperature.
- b) Irradiation creep, which is relatively independent of temperature (as with the stainless steels), occurs at irradiation temperatures to about 480-500°C; above that temperature thermal creep dominates deformation behavior.
- c) Void swelling in F-M steels occurs in the temperature regime of 300-600°C, is dependent on dose, and is strongly dependent on temperature and dose rate. As would be expected, transmutation-produced helium and hydrogen have a significant influence on void swelling.
- d) Phase instabilities can occur in the range 250-650°C by radiation-induced segregation of solute atoms to sinks, and by radiation-enhanced diffusion. These phase instabilities, depending on the primary driving source, are dependent on temperature, dose, and dose rate.
- e) Non-hardening embrittlement occurs at temperatures of 450-650°C, which is higher than the hardening regime, and can lead to intergranular fracture due to weakening of grain boundaries from segregation and phase instabilities. Grain boundary decohesion can also occur from helium and hydrogen at the grain boundaries.

Following the ending of the LMFBR Program, most of the developmental effort and data base establishment for nuclear applications of F-M steels has come from various national and international programs to develop damage resistant, low activation F-M steels for fusion applications. Further work (Rensman et al. 2002, Rensman et al. 2005, Shiba et al. 1996, Schneider et al. 2003, Jitsukawa et al. 2002) provides relevant results, while a comprehensive set of irradiation data and phenomenological empirical-fitting models are presented by Yamamoto et al. (2006). Figure 4.106 reproduces generic model predictions for radiation hardening of F-M steels, measured in tests at the irradiation temperature, and shows the general form of the dose and temperature dependence of radiation hardening. In summary, radiation hardening in FM steels can be described by a saturating function of $\sqrt{\text{dpa}}$ with a saturation hardening $\Delta\sigma_{ys}$ and a saturation dose parameter dpa_0 . The modeling, shown in Figure 4.106, predicts a maximum yield stress increase of ≈ 490 MPa at $\approx 300^\circ\text{C}$ which then decreases rapidly at higher temperatures with softening observed for irradiation temperatures above $\approx 400^\circ\text{C}$.

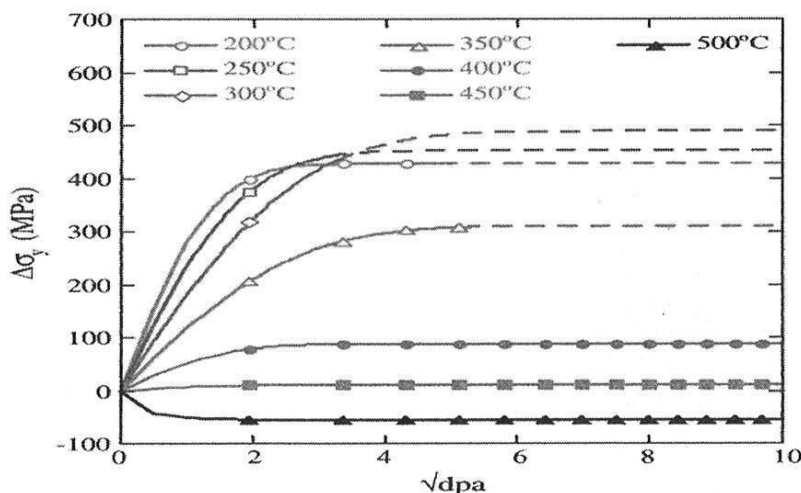


Figure 4.106. Model predictions for the dose dependence of $\Delta\sigma_y$ for various irradiation temperatures.

An extensive database was compiled on the hardening-induced embrittlement of the FM steels (Yamamoto et al. 2006), and the shifts in Charpy transition temperature ΔT_c , were analyzed as a function of irradiation temperature and dpa for the F82H, 9Cr-1Mo and 9Cr-W alloy classes. The results of fitting $\Delta T_c = k_c \sqrt{\text{dpa}}$ for F82H and for the 9Cr-1Mo FM steels are shown in Figure 4.107. The values of the slope k_c are higher for F82H in each temperature range and there is a positive slope for F82H even for the irradiation temperatures above the hardening regime (450-592°C).

Analyses of all the data showed differences in radiation hardening behavior among the various alloys. It was observed that the Charpy shift coefficient for F82H is 0.38°C/MPa compared to 0.58°C/MPa for the fracture toughness shift, indicating that the sub-sized Charpy specimen used in the experiments provides a non-conservative estimate of embrittlement due to radiation hardening.

Regarding 9Cr-1MoV (grade 91) steel specifically, Figure 4.108 shows Charpy impact toughness results for both 9Cr-1MoV and HT-9 base metals in the unirradiated condition and following irradiation to 13 dpa at various temperatures in EBR-II (Hu and Gelles 1986, 1987). As the figures show, the HT-9 steel exhibits a radiation-induced shift at all temperatures to 550°C, while the 9Cr-1MoV exhibits virtually no significant shifts at and above 450°C. Hardness measurements showed much higher hardness of the HT-9 at all temperatures (Hu and Gelles 1986, 1987).

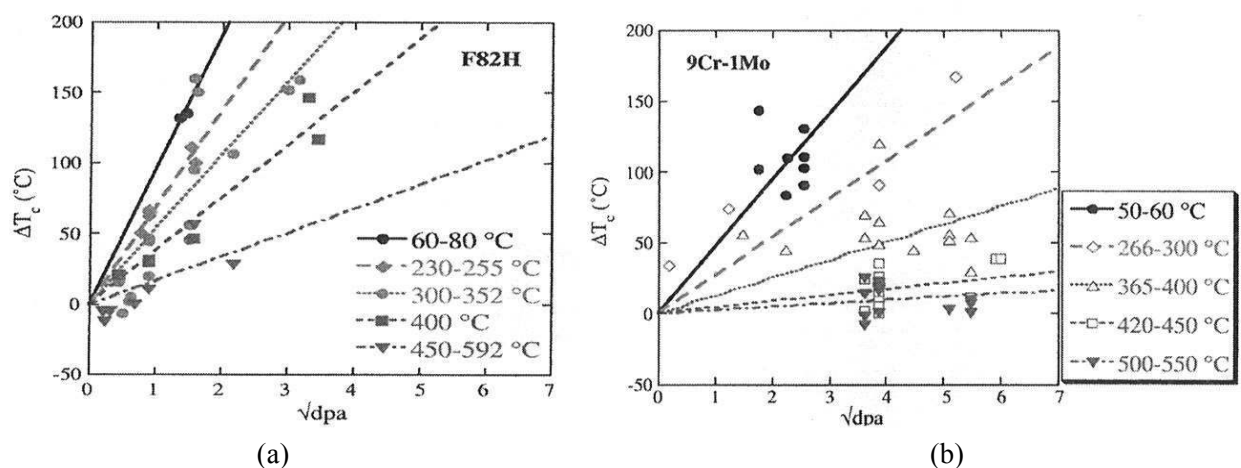


Figure 4.107. Temperature shifts for (a) F82H and (b) 9cr-1Mo steels, fitted to $\sqrt{\text{dpa}}$ dependence for a range of irradiation temperatures.

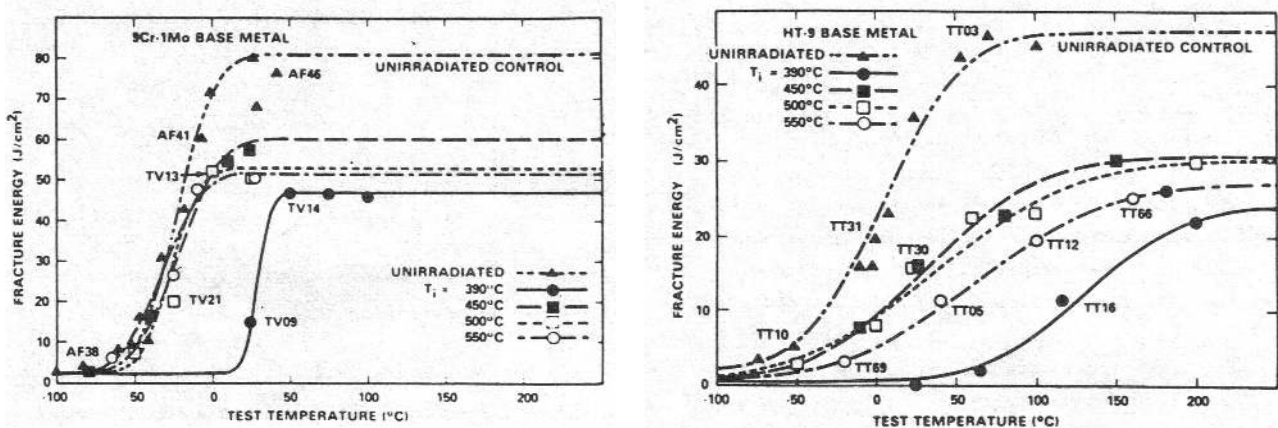


Figure 4.108. Effects of irradiation temperature on DBTT and USE for T-91 and HT-9 irradiated to 13 dpa in EBR-II (Hu and Gelles 1986).

For irradiation to higher doses, Figure 4.109 shows yield and ultimate strength results for both HT-9 and Grade 91 steels irradiated at temperatures from 400 to 550°C and to a dose of about 25 dpa (Lauritzen et al. 1984). The results show considerably higher strength for the HT-9 alloy, although the strengths are about the same in the unirradiated condition up to about 600°C. Thus, the HT-9 alloy exhibits greater radiation-induced hardening than the Grade 91 steel and, as shown in Figure 4.109, this greater hardening is reflected in greater embrittlement as measured by Charpy impact tests. In related work, Klueh and Vitek (1985) conducted experiments to evaluate the potential effects of thermal aging on the hardening of the Grade 91 steel during irradiation exposures. Thermal aging for the same time (5,000 h) as the irradiation exposures at 10 or 12 dpa showed no effects of thermal aging. Thus, the observations of radiation-induced hardening from 400 to 550°C do not seem to be influenced by thermal aging.

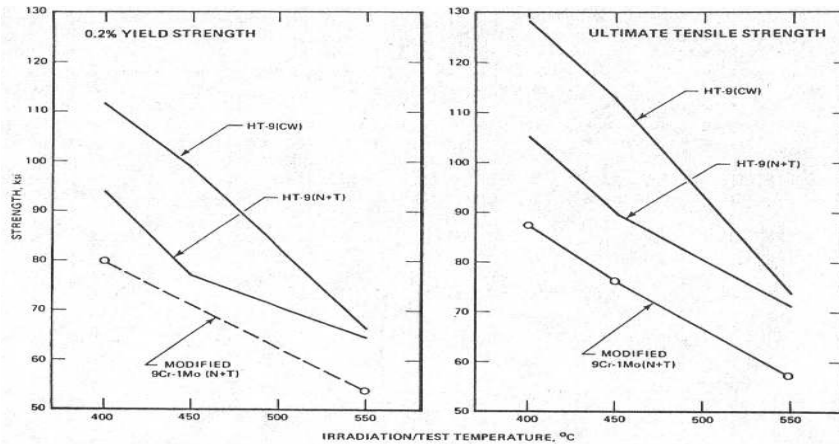


Figure 4.109. Yield and ultimate tensile strengths of T-91 and HT-9 after irradiation to ≈ 25 dpa in EBR-II at 400, 450, and 550°C. Test temperature was the same as the irradiation temperature for each specimen (Lauritzen et al. 1984).

At even higher doses, Figure 4.110 (Klueh and Harries 2001) shows fracture toughness J_{Ic} and tearing modulus (T) data for grade 91 steel irradiated at three dose levels from about 13 to 105 dpa at about 420°C and to the low dose at 520°C. At the highest temperatures, the J_{Ic} values decreased about 50% relative to the unirradiated values, while the tearing modulus decreased by more than a factor of two. The J_{Ic} values do not appear to decrease with increasing dose, although the amount of data is small with which to make a definitive judgment. It is clear from the data discussed in the review of Klueh and Harries (2001) that the effects of irradiation on the ductile fracture toughness of F-M steels is quite varied and deserves considerable attention.

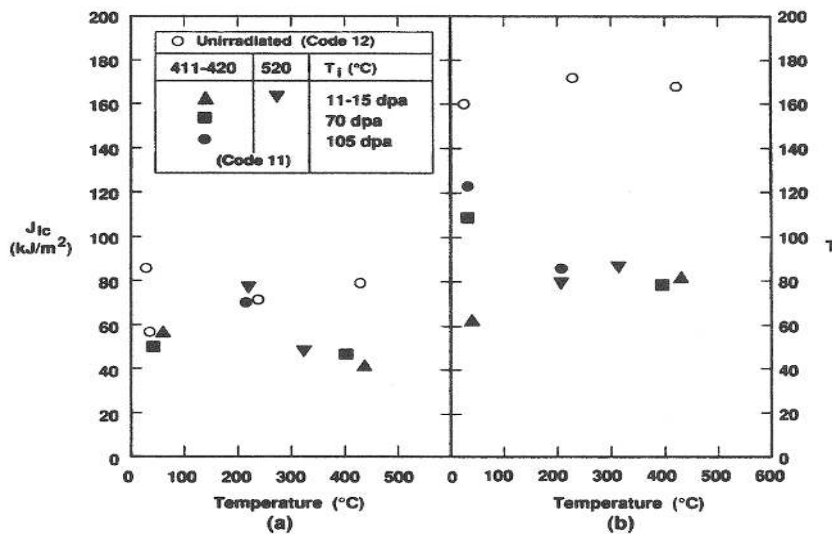


Figure 4.110. The (a) fracture toughness and (b) tearing modulus of modified 9Cr-1Mo steel irradiated in FFTF to doses as high as 105 dpa, and tested at temperatures from room to about 425°C.

As stated earlier, a major advantage of the F-M steels relative to stainless steels is their superior resistance to swelling. The schematic drawing in Figure 4.111 shows the relative swelling behavior of six commercial heats of F-M steels and various heats of Type 316 stainless steel (Klueh and Harries 2001). At very high dpa levels, Table 4.28 shows swelling data for many different ferritic steels at doses of about 200 dpa. Only one of the steels exhibited swelling greater than 3% (Gelles 2008).

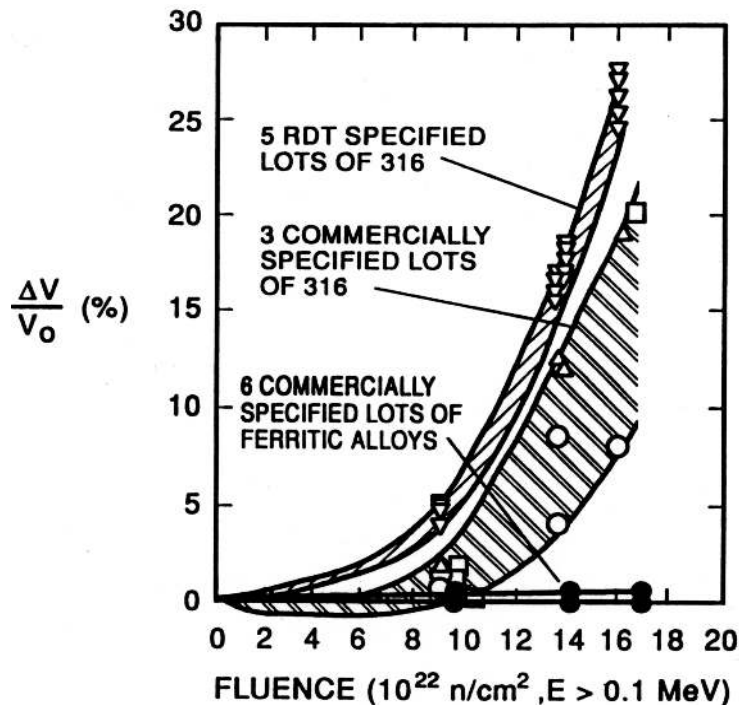


Figure 4.111. Swelling behavior of six commercial heats of ferritic/martensitic steels compared to Type 316 stainless steel after irradiation in EBR-II at 420°C to ≈ 80 dpa (Gelles 2008).

Table 4.28. Swelling of a series of reduced-activation ferritic/martensitic steels and conventional 9Cr-1MoVNb and 12Cr-1MoVW steels.

Alloy	Fluence, dpa	Swelling
2Cr-0.5V	203.2	1.11
2Cr-1V	203.5	1.3
2Cr-1.5V	204	1.52
9Cr-0.5V	204.8	0.54
9Cr-1V-1Mn	205.7	2.2
9Cr-0.5V-3Mn	206	4.66
12Cr-1V-6.5Mn	208.8	1.43
9Cr-1W-2Mn	204.4	5.04
12Cr-1W-6.5Mn	206.9	-0.77
9Cr-1MoVNb	204.5	1.76
12Cr-1MoVWa	204.5	0.09
12Cr-1MoVWb	204.5	1.02

Figure 4.112 shows a summary by Spencer and Garner (2000) of an extensive database on swelling behavior of Fe-Cr ternary alloys by Gelles (1995 and 1996). For alloys irradiated in EBR-II in the range of 400-454°C and for doses to 130 dpa, an incubation regime to about 30-40 dpa is followed by

a steady state regime with a linear swelling rate of $\approx 0.2\%$ /dpa. This compares to the previously stated rate for austenitic stainless steels of about 1% /dpa.

Relative to irradiation creep, Alamo et al. (2007) recently summarized the irradiation creep behavior of the reduced activation F-M steels Eurofer and 9Cr2W1TaV together with 9Cr-1Mo during irradiation at $\approx 325^\circ\text{C}$ for doses up to $\approx 65\text{dpa}$ and with stresses of 150 and 220 MPa. All three steels behaved in similar fashion, (Figure 4.112) with an average creep coefficient of $\approx 0.7 \times 10^{-6} \text{MPa}^{-1} \cdot \text{dpa}^{-1}$.

Regarding radiation-induced segregation (RIS), the possible mechanisms in bcc alloys has been discussed by Faulkner et al. (1998) while Little (1993) has published a review of experimental observations of RIS in F-M steels. From the limited data available for these steels, the indications are that RIS temperature dependence is approximately the same as that for void swelling.

Regarding non-hardening embrittlement, the monograph by Klueh and Harries (2001) includes a comprehensive review of the topic. They point out that such embrittlement can be minimized through compositional modifications, such as reduction in the concentration of specific impurity elements to very low levels, which can eliminate the formation of brittle Laves phases.

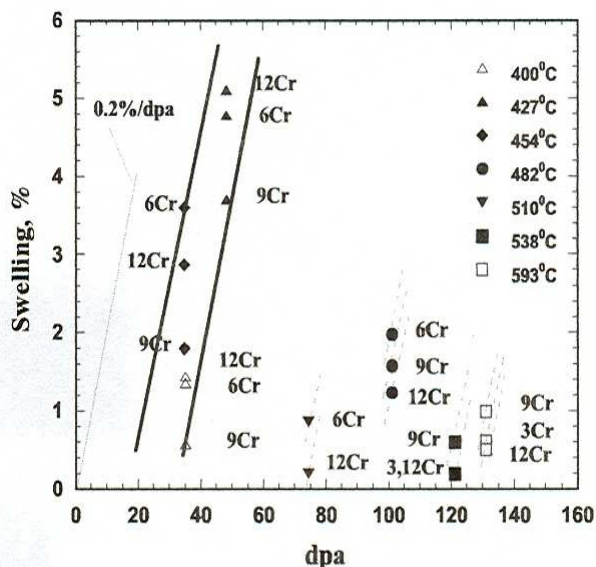


Figure 4.112. Swelling of Fe-Cr alloys irradiated in EBR-II to doses up to 130 dpa over temperatures in the range 400-650°C. After a short incubation regime a steady state swelling rate of $\sim 0.2\%$ /dpa- is established in the 400-454°C range; a transition from incubation regime to steady state swelling is probably underway at the higher temperatures (Spencer and Garner 2000).

4.3.6 Weldments

Weldments of high-strength, high-Cr ferritic/martensitic steels are generally considered more problematic than weldments of austenitic stainless steels and low-strength, low-Cr ferritic steels. It is often required to pre-heat before welding to avoid cracking, and post-weld heat treatments are mandatory. However, there is significant experience in welding Grade 91 steel, and satisfactory welds can be obtained with great care. Welding of P91 can be accomplished with gas tungsten arc welding (GTAW), gas metal arc welding (GMAW), submerged arc welding (SAW), shielded metal arc welding (SMAW), and flux cored arc welding (FCAW) processes. Table 4.29 summarizes the weld metal specifications for welding P91.

Welding parameters play an essential role in the performance of weldments, as the performance of high-Cr ferritic/martensitic steels depends entirely on precise precipitation microstructure. A typical heating and cooling cycle for welding P91 is shown in Figure 4.113 (EPRI 2002). Pre-heat, interpass and post-weld heat treatments are important steps and need to be very well controlled to ensure creep

resistance and sufficient toughness. Post-weld heat treatment is regarded as the foremost important factor in producing satisfactory P91 weldments.

Table 4.29. P91 weld metal specifications.

Process	Specification, A/SFA	Classification
SMAW	A 5.5	E90XX-B9
SAW	A5.23	EB9+flux
GTAW/GMAW	A5.28	ER90S-B9
FCAW	5.29	E91T1-B9

It is known that P91 weldments have good resistance to creep cracking. However, Type IV cracking in the HAZ is often observed in Grade 91 components, leading to premature failure of the components, and it has been regarded as the life-limiting factor in the use of mod.9Cr-1Mo steel in power plants. Figure 4.120 shows a Type IV failure of a superheater tube made from Grade 91 that was in service only for four years in a fossil-fired boiler. The tube failure was caused by improper intercritical heat treatment during fabrication (Henry 2005).

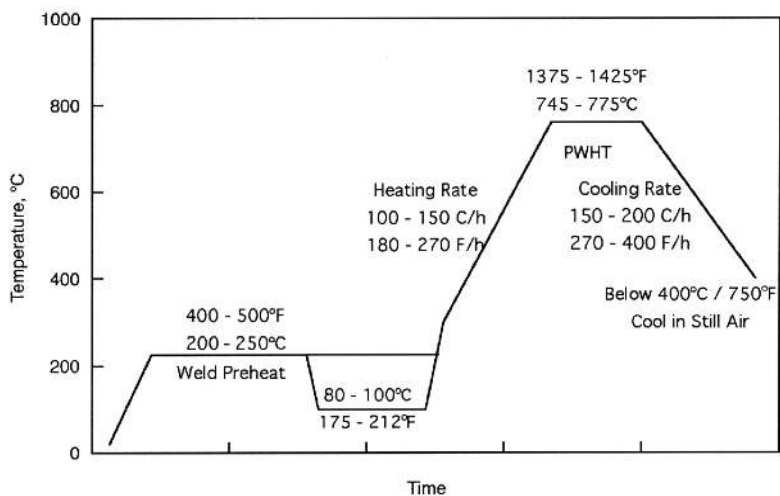


Figure 4.113. Typical thermal cycles for welding P91 (EPRI 2002).

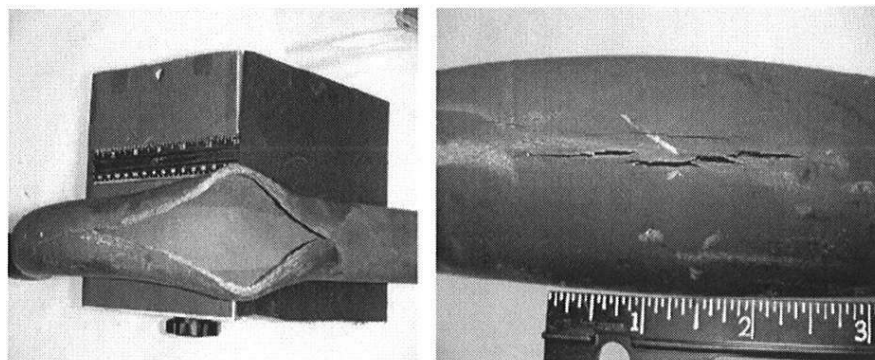


Figure 4.114. Type IV failure in a superheater tube after four years of service in a conventional fossil-fired boiler (Henry 2005).

As shown schematically in Figure 4.115 (Vlasak et al. 2005), weld cracking can be categorized into four types depending on the location of a crack in the weld. Type IV cracking occurs in the fine-grained and inter-critical region of the HAZ close to the base metal. The weld thermal cycle generates an inhomogeneous microstructure in the HAZ, resulted in marked difference in mechanical strength across

the weld joint. Figure 4.116 shows a schematic view of the microstructure developed in the HAZ as a function of peak temperature during welding (Francis et al. 2006). The coarse grain HAZ (CGHAZ) is next to the fusion boundary where the temperature is above A_{c3} . Significant grain growth occurs due to dissolution of carbides. The fine grain HAZ (FGHAZ) experiences lower temperature than the CGHAZ but still higher than A_{c3} . Incomplete dissolution of carbides limits austenitic grain growth. The inter-critical region (ICHAZ) where the temperature is between A_{c3} and A_{c1} , has both newly-formed austenitic and tempered martensite at high temperature, and tempered and untempered martensite after cooling. The over-tempered region next to the unaffected base metal undergoes further tempering during the heating cycle. The different types of microstructure formed across the weld joint results in the hardness gradients, as shown in Figure 4.117 (EPRI 2002). The HAZ shows the lowest hardness, and this “soft zone” offers the least performance.

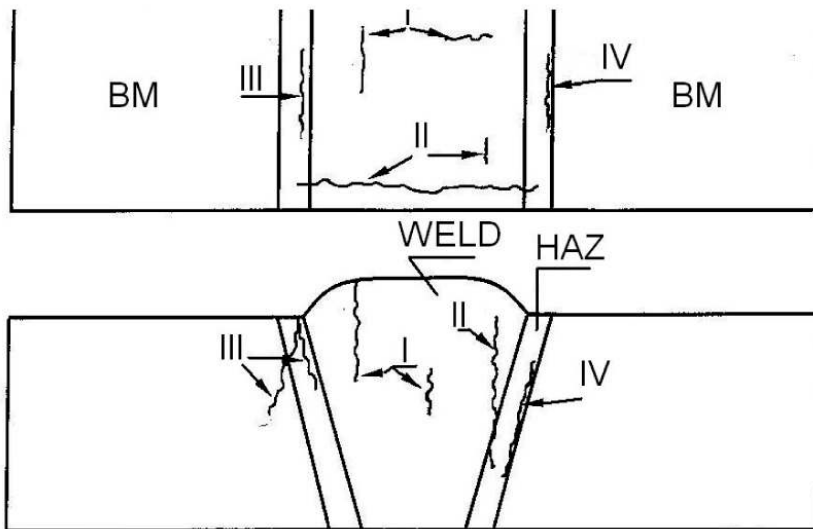


Figure 4.115. Different types of cracking in a weld (Vlasak et al. 2005).

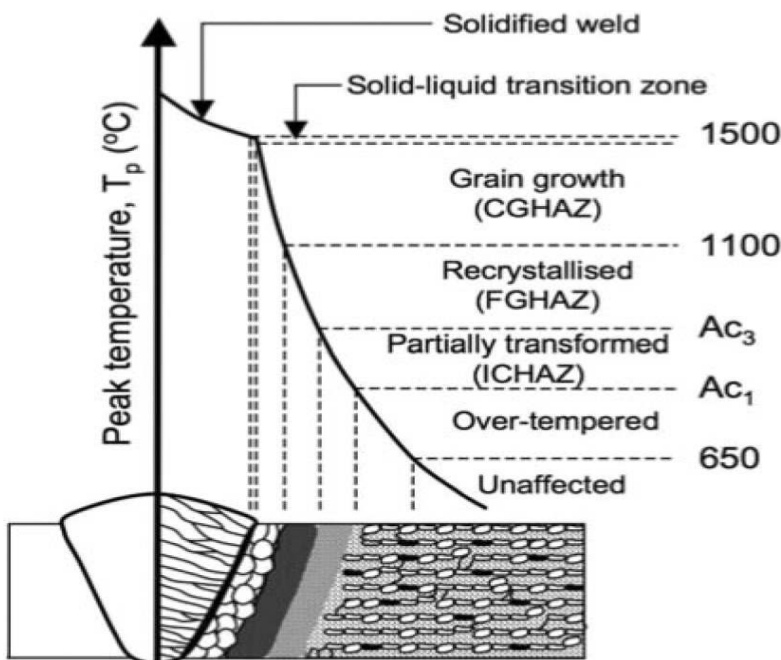


Figure 4.116. Schematic view of microstructure developed in the HAZ in a weld (Francis et al. 2006).

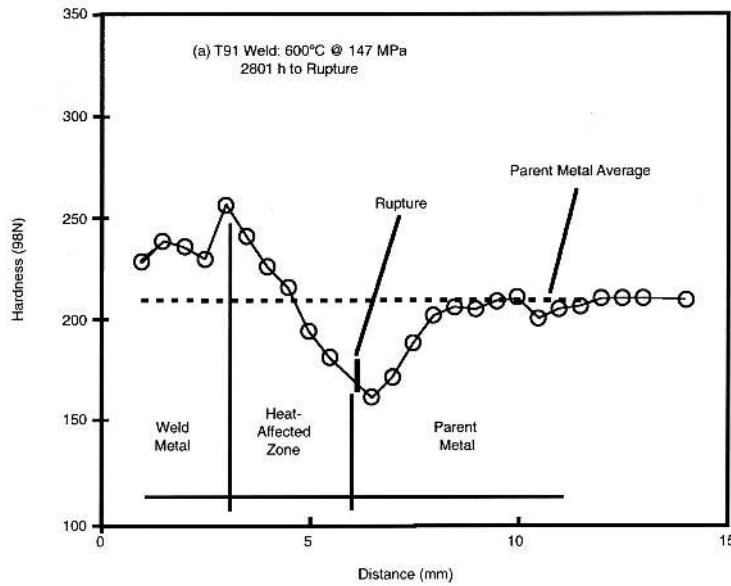


Figure 4.117. Hardness changes across the weld of Grade 91 (EPRI 2002).

In an HAZ of a weld joint, each unique microstructural region is surrounded by regions having different creep strength. The flow, in the low creep strength region, is restricted by the surrounding regions with greater creep resistance. A complex multi-axial stress condition develops across the weld joint because of the mechanical constraint from the creep strength inhomogeneity. A high strain concentration in the soft inter-critical region of the HAZ has been predicted and validated in Grade 91 welded pipe by Eggeler et al. (1994). This multi-axial state of stress developed across the weld joint during creep testing is widely reported and accepted to be the main cause of the preferential creep cavitation in the soft inter-critical region of the HAZ, leading to brittle Type IV failure in Grade 91 weld joint (Abe et al. 2007).

Type IV creep fracture significantly reduces the creep life of welded joints of ferritic steels at elevated temperature and low-stress conditions. Figure 4.118 shows the creep rupture strength of welded joints is lower than that of base metal (Masuyama 2005). The creep rupture strength loss in welded joints becomes more significant with increasing temperature, especially above 600°C.

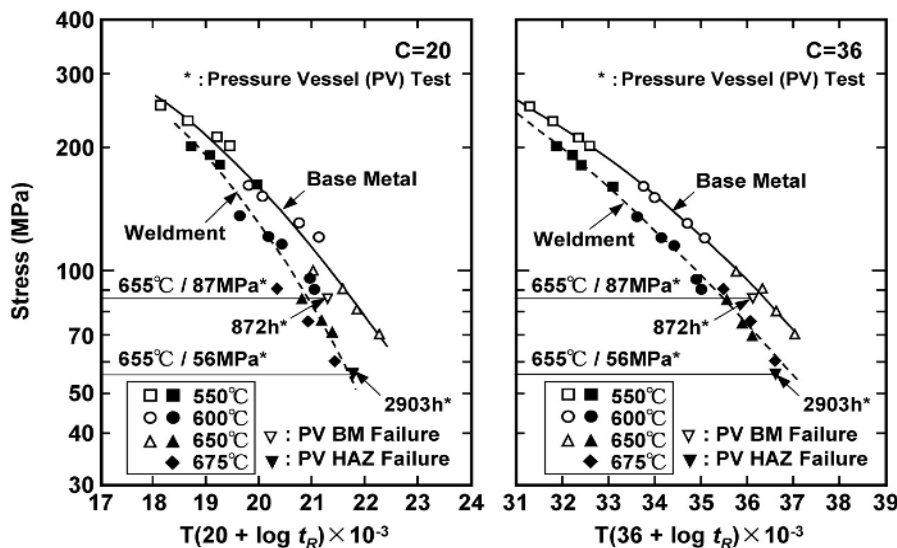


Figure 4.118. Comparison of creep rupture strength of base metal and weld metal for Grade 91 (Masuyama 2005).

The addition of about 100 ppm boron combined with minimized nitrogen as low as 10-20 ppm suppresses the Type IV fracture in HAZ at low stresses and improves the long-term creep rupture strength of welded joints. The suppression of fine-grained microstructure in HAZ is a main reason for the suppression of Type IV fracture. The welded joints are fractured in the fine-grained HAZ at low stresses, indicating Type IV fracture. Reducing the width of HAZ by EB welding is effective for the extension of creep life of welded joints, but the brittle Type IV fracture takes place at low stresses. Multi-axial stress condition in fine-grained HAZ with lower creep strength, resulting from mechanical constraint effect by the surrounding weld metal and base metal with higher creep strength, is essential for the formation of creep voids and brittle Type IV fracture in fine-grained HAZ (Abe et al. 2007).

Three measures have been proposed to improve the Type IV cracking resistance (Laha et al. 2007). The first is heat treatment to eliminate/minimize the strength heterogeneity across the weld joint by renormalizing the component after welding. In actual practice, renormalizing of components such as, long pipe is impractical and uneconomical. An alternative is called half-tempering treatment. The material to be welded is in the under-tempered condition. However, under-tempered regions of the base metal may be present in the long pipes, which is disadvantageous. The second is modification of the welding technique. An increase in width of the HAZ is expected to reduce the stress triaxiality so that the soft intercritical region of the HAZ deforms with less constraint to minimize the type IV cracking tendency. The width of the HAZ can be increased by changing preheat and heat-input during welding. The third is adjustment of composition. The resistance against intercritical softening of the steel can be improved by increasing the strength of the steel with the addition of solid solution hardening elements such as W and Co and also by microalloying the steel with boron.

Dissimilar metal welding is often required for superheaters and pipes in conventional power plant boilers. Transition joints have to accommodate significant differences in physical, chemical, and mechanical properties and may operate at temperatures within creep range of ferritic steels. Dissimilar metal weld joints between Grade 91 and austenitic steel are of concern due to the difference in thermal expansion coefficients, carbon migration, and creep strength across the weld interface. Transition joint between P91 and nickel-based weld metal is often needed. The difference in thermal expansion coefficients between Grade 91 and austenitic stainless steels can lead to fatigue cracking during plant operation. The nickel-based weld metals have intermediate values of thermal expansion coefficient, and will reduce the thermal fatigue stress across the weld joint. The major issue with dissimilar metal welds between high-strength Grade 91 and lower-strength steels such as P22 is the carbon transfer from P22 to P91 due to higher stability of carbon in high-Cr steels. Decarburization on the P22 side of the interface leads to lower strength and susceptibility to cracking.

The ASME Subsection NH (2007 Edition) specifies the stress rupture factors for Grade 91 welded with SFA-5.28 ER90S-B9, SFA-5.5 E90XX-B9, and SFA-5.23 EB9 in Table 1-14.10 E-1, and they are given in Table 4.30. The adequacy of the weld reduction factors has been of concern, particularly for long-term performance of Grade 91 weldments. A number of publications have shown that the cross weld rupture strength of 9Cr ferritic/martensitic steels fall much below that of the base metal. One example is given in Figure 4.119 that shows the rupture strength of the cross weld specimens showing Type IV cracking in E911, an European version of 9Cr ferritic steel (Shibli 2002). A recent study has shown that the weld strength reduction factor for E911 could be as high as 40% when Type IV cracking occurs. Data Extrapolation to 100,000 h gives a reduction factor of 50% (Allen and Fleming 2000). It is also recognized that the weld strength reduction factor in high-Cr ferritic steels is affected by a number of parameters, including base metal, weld metal, thermal-mechanical treatment, loading condition, temperature, and test duration, etc. (Schubert 2005).

Table 4.30. Stress rupture factors for Grade 91 weldments

Temperature, °C	Ratio
425	1.0
450	0.95
475	0.93
500	0.92
525	0.91
550	0.89
575	0.87
600	0.84
625	0.80
650	0.76

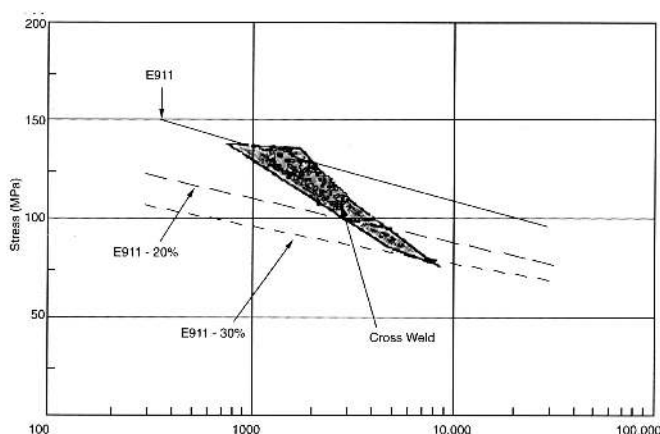


Figure 4.131. Comparison of rupture strength between cross welds and base metal for E911 (Shibli 2002).

Knowledge of weldment performance in sodium environment and welding of irradiated metals is lacking.

4.3.7 Industrial Experience

The survey conducted by EPRI has showed that there are 43 applications of Grade 91 in the U.S. and Canada for headers, tubes and pipes in the boilers (EPRI 2002). It has also been used for heavy-section components and for thin-section tubing worldwide in power plants. Tubes after 143,000 h of operations have been removed to gauge the service performance. Metallurgical analysis indicated typical microstructural evolution and minimal loss in tensile and creep strength, which are consistent with the data obtained in long-term thermal studies.

There is limited in-plant experience of long-term performance, especially with thick section components such as headers and steam pipework. Limited experience with Grade 91 shows that the long-term performance of Grade 91 components needs careful investigation (EPRI 2002). There have been some surprising reports of premature failures of P91 piping weldments and T91 tubing in plants. Cohn et al. (2005) compiled several cases of premature failures of Grade 91 fossil power components. Creep or creep-fatigue failure of superheat outlet tubes has been reported due to over-tempering during tubing fabrication. A finned heat recovery steam generator tube cracked due to short-term overheating. There is also a case that T91 tubes in a superheat had throughwall leaks and substantial swelling due to long-term creep rupture. Other failure cases were due to improper fabrication, low creep strength of weldments, etc.

5. NEW ADVANCED ALLOYS for ARR

5.1 Selection of Candidate Advanced Alloys

The development of advanced materials and design methodologies for high temperature components is the major challenge for advancing reactor technology. Development of new advanced materials requires a proper and thorough assessment of all possible classes of alloys and selection of the most promising ones for further development. Besides currently available commercial materials discussed above, there are more advanced materials that can be brought to the level of maturity required for application in advanced reactors. Some of these are summarized below.

In the Cr-Mo class of alloys, NF616 (Fe-9Cr-1.8W-0.5Mo-0.06N-0.004B-0.1C) and HCM12A (Fe-12Cr-1.8W-1Cu-0.5Mo-0.07N-0.1C) offer significantly higher creep rupture strength at 600°C compared with HT-9 and mod.9Cr-1Mo alloys. The maximum use temperature (for long-time operation) for the advanced alloys is reported as 620°C compared to 565°C for HT-9 and 593°C for mod.9Cr-1Mo. However, scarce data are available on sodium and neutron irradiation effects for either of these advanced F-M steels and they are not qualified for use by the ASME Code.

Another potential F-M alloy is a dispersion-strengthened 9Cr steel (9.5Cr-3Co-1Ni-0.6Mo-0.3Ti-0.07C) that offers superior elevated temperature strength and impact toughness compared to conventional 9-12Cr steels. These superior properties are the result of a high number density of nano-size TiC precipitates in the microstructure. A major advantage of this alloy relative to oxide-dispersion strengthened (ODS) steels is that it is produced by conventional steel processing techniques. Such a processing of modified 9Cr-1Mo led to over an order-of-magnitude increase in creep-rupture life. However, the composition of this high-strength dispersion strengthened steel has not been optimized for nuclear applications (with 3 wt% Co), but it may be possible to produce reduced-activation compositions using a similar processing technique.

There are also nanostructured ferritic alloys (NFAs) that offer room temperature yield strengths of 1200 MPa and higher. One of these, MA957, has been commercially produced for more than 20 years and exhibited good radiation damage tolerance (based on ion irradiation data to ≈ 100 dpa) at relatively high temperatures. However, the database is not as mature as needed, needs demonstration of joining and industrial scale-up, and the alloy is not ASME Code qualified. Beyond that commercial material, more advanced NFAs are under development, such as the 12YWT and 14YWT alloys that feature a high number density of nano-clusters resulting in improved high temperature strength, including creep performance. These developmental alloys require a significant amount of additional data before application in nuclear structural components, but their offerings of very high strength indicate their potential. In the non-metallic materials, the primary candidate is silicon carbide/silicon carbide (SiC/SiC) composites. Silicon carbide offers good radiation resistance, thermal resistance, thermo-chemical stability, low activation and low decay heat, and low gas permeability. The SiC/SiC composites also offer relatively good strength and fracture toughness, with the possibility for tailoring the strength and thermal properties for specific applications. To enable SiC/SiC as a viable candidate for nuclear applications, additional data on compatibility and irradiation effects are needed; these include irradiated strength beyond 1000°C and 15 dpa, irradiation creep, void swelling at temperatures above 1000°C, environmental effects under irradiation, and additional understanding regarding the physical processes of radiation damage mechanisms in the material. These needs are precursors to the efforts needed for ASME Code qualification such as design procedures, development of test standards, and development of databases with which qualification can be achieved.

A recent structural materials assessment has identified four advanced materials for further development in support of ARR. These include two ferritic-martensitic steels, NF616 and NF616 with special heat treatment and two austenitic stainless steels, HT-UPS (High-Temperature Ultrafine Precipitate-Strengthened) steel and NF-709. As discussed before, NF616 is a variant of Mod. 9Cr-1Mo and offers considerably higher strength and improved creep resistance than the traditional HT-9 used in liquid metal reactors. Further improvements of NF616 may be achieved through minor compositional changes and microstructure refinement by special thermo-mechanical treatments. HT-UPS is Fe-15Cr-15Ni austenitic steel containing nanometer-sized Ti+Nb+V carbide precipitates. The carbides remain stable and provide increased creep resistance and irradiation tolerance over traditional 316 stainless steels. NF709 is another advanced austenitic alloy strengthened by solid solution and Nb nano-carbides and exhibit exceptionally high strength and creep resistance. All these four steels offer considerable improvements in strength and creep resistance over the more mature steels and yet maintain other critical properties at a similar level, which may enable improved economics, increased safety margins, and increased design limits.

In the following section, the baseline mechanical property data and effects of thermal aging, sodium environment, and neutron irradiation on these mechanical properties will be summarized. The mechanical properties and environmental effects (high temperature, sodium and neutron irradiation) of weldments will also be addressed. Based on the existing database, the needs for code qualification and licensing of advanced alloys are discussed.

5.2 NF616 (Grade 92)

NF616 is a variation of Grade 91 with improved high temperature strength and thermal creep resistance. It was developed by Nippon Steel Corporation for boiler piping and tubing applications in advanced power plants. The chemical compositions of NF616 are given in Table 5.1. The higher creep strength was achieved by replacing Mo with W for solid solution strengthening and addition of B to stabilize $M_{23}C_6$ precipitates and subgrain structure. NF616 represents (Table 5.2) the third generation of ferritic/martensitic steels for power-generation industries (Klueh 2005). The creep strength of NF616 was increased by 10-20% in 100,000 h at 600°C compared with Grade 91 (Haarmann et al. 2002). NF616 has been included in the ASTM/ASME standards under the designation P92 with SA213 for tubes, SA335 for pipes, SA-182 for forgings, and SA-369 for forged pipes. The sub-grain structure produced by the martensitic transformation and the precipitation of carbides, nitrides and carbonitrides are decisive microstructural features. As the applications of NF616 in power plants are at temperatures $\approx 600^\circ\text{C}$, a majority of experiments have been done around 600-650°C.

Table 5.1. Chemical requirements for Grade 92

C	0.07-0.13
Si	0.50 max
Mn	0.30-0.60
P	0.020 max
S	0.010 max
Cr	8.50-9.50
Mo	0.30-0.60
V	0.15-0.25
W	1.50-2.00
Nb	0.04-0.09
Ni	0.40
N	0.030-0.070
B	0.001-0.006
Ti	0.01 max
Zr	0.01 max

Table 5.2. Evolution of ferritic/martensitic steels (Klueh 2005).

Generation	Years	Steel modification	10 ⁵ h Rupture strength, 600 °C (MPa)	Steels	Max use temperature (°C)
0	1940–1960		40	T22, T9	520–538
1	1960–1970	Addition of Mo, Nb, V to simple Cr–Mo steels	60	EM12, HCM9M, HT9, HT91	565
2	1970–1985	Optimization of C, Nb, V, N	100	HCM12, T91, HCM2S	593
3	1985–1995	Partial substitution of W for Mo and add Cu, B	140	NF616, E911, HCM12A	620
4	Future	Increase W and add Co	180	NF12, SAVE12	650

5.2.1 Base Metal Properties

Physical Properties

Physical properties, e.g. thermal expansion coefficient, thermal conductivity and Young’s modulus, are important parameters particularly to the design and operation of thick-section components in power plants. The linear thermal expansion coefficient, thermal conductivity, and Young’s modulus for NF616 are shown in Figures 5.1-5.3, respectively. Comparisons with T91 and several other common steel materials are also given (Mimura et al. 1994). The Young’s modulus of NF616 can be expressed as a function of temperatures by the following equation:

$$E (T \text{ in } ^\circ\text{C}) (\text{GPa}) = -1 \times 10^{-4} T^2 - 0.0182 T + 215.5$$

The room-temperature modulus is 215 GPa. In general, the physical properties of NF616 are quite similar to those of Grade 91.

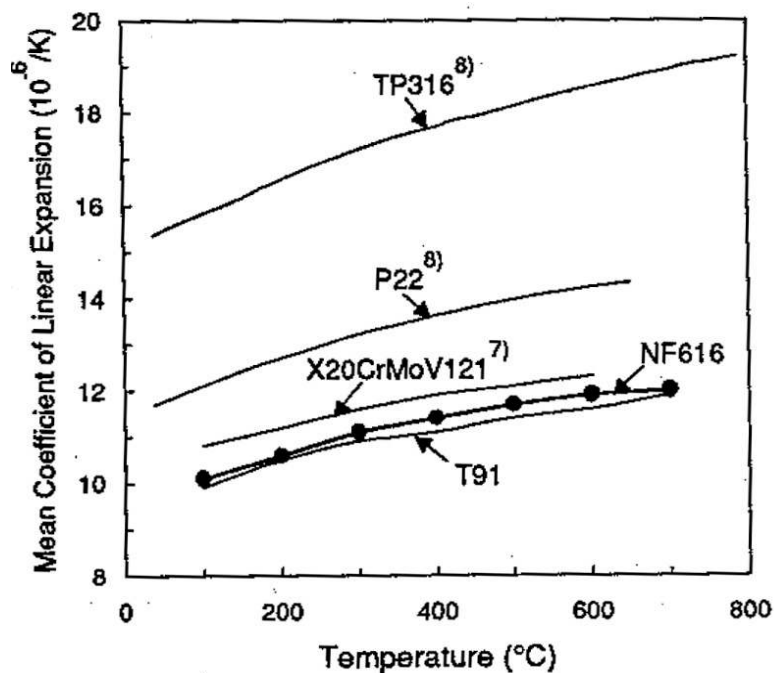


Figure 5.1. Linear thermal expansion coefficient for NF616 (Mimura et al. 1994).

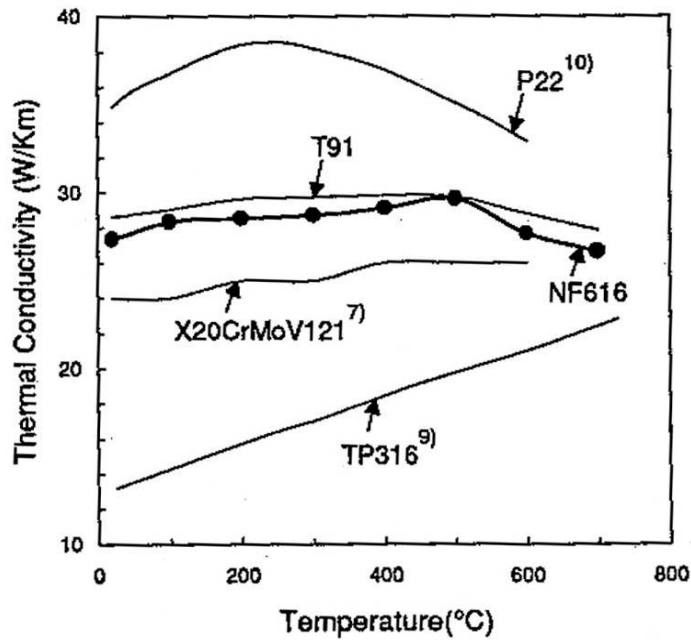


Figure 5.2. Thermal conductivity of NF616 (Mimura et al. 1994).

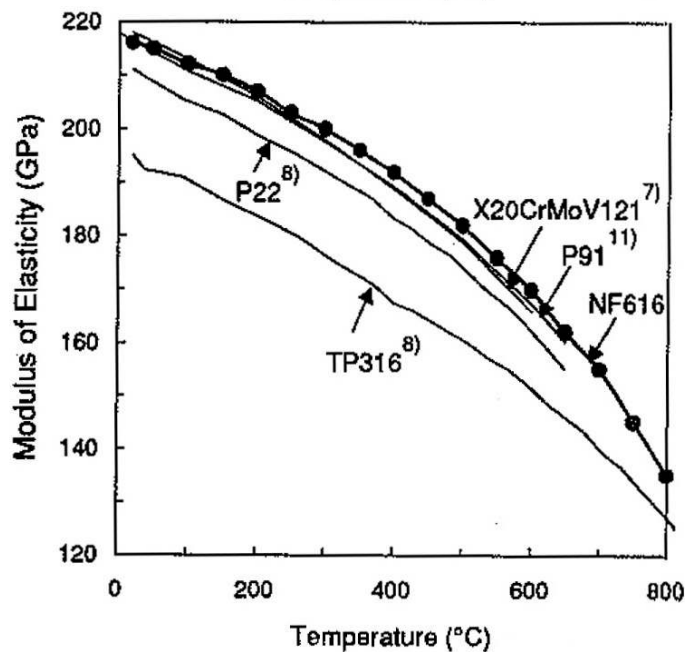


Figure 5.3. Young's modulus as a function of temperature for NF616 (Mimura et al. 1994).

Mechanical Properties

Tensile Properties:

The tensile properties, i.e. the yield stress, tensile strength, elongation and reduction of area are given in Figure 5.4 as a function of temperatures (Mimura et al. 1994). NF616 has sufficiently ductility over a wide range of temperature, with a minimum of $\approx 14\%$ at 400°C.

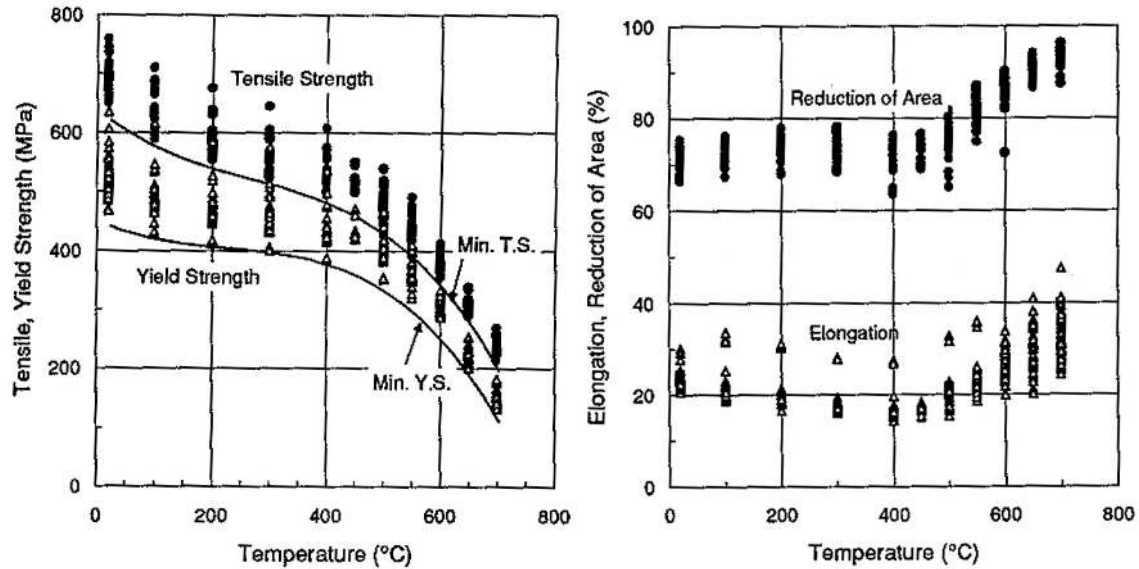


Figure 5.4. Tensile properties of NF616 as a function of temperature (Mimura et al. 1994).

Creep Properties

There is a large database of creep rupture data on NF616 produced in Japan and Europe. Creep rupture tests up to 100,000 h have been conducted. In the database of the European Creep Collaborative Committee (ECCC) program, 48 heats of NF616 have been tested and 851 data points have been obtained covering the temperature range of 550-750°C (ECCC data sheet 2005). The stress-rupture plot for NF616 reported by Nippon Steel Corporation is shown in Figure 5.5 along with the comparison with Mod.9Cr-1Mo (Nippon Steel). The creep rupture ductility plot is given in Figure 5.6. Compared with Grade 91, the creep rupture strength was increased significantly at temperatures of 550-750°C. The difference in rupture strength is more pronounced at higher temperatures. The creep rupture ductility of NF616 dropped faster than that of Grade 91.

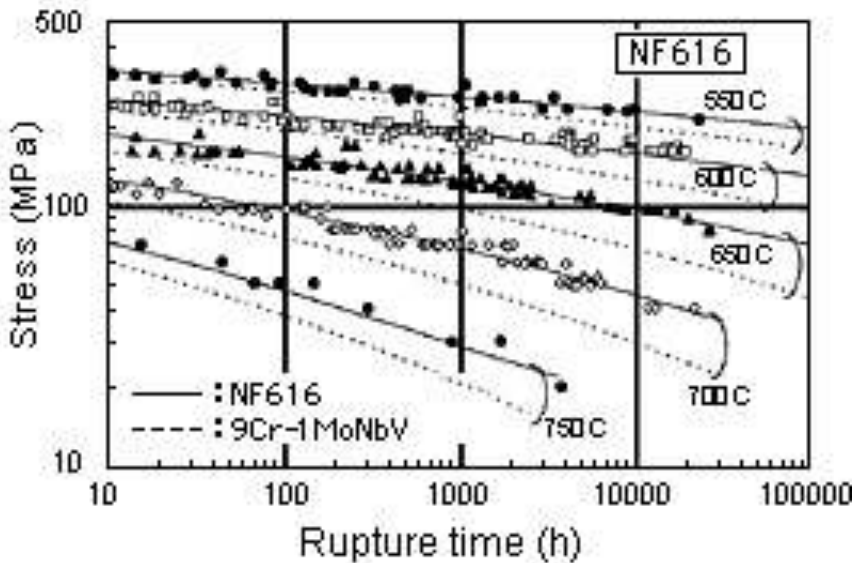


Figure 5.5. Creep stress-rupture plot for NF616 (Nippon Steel).

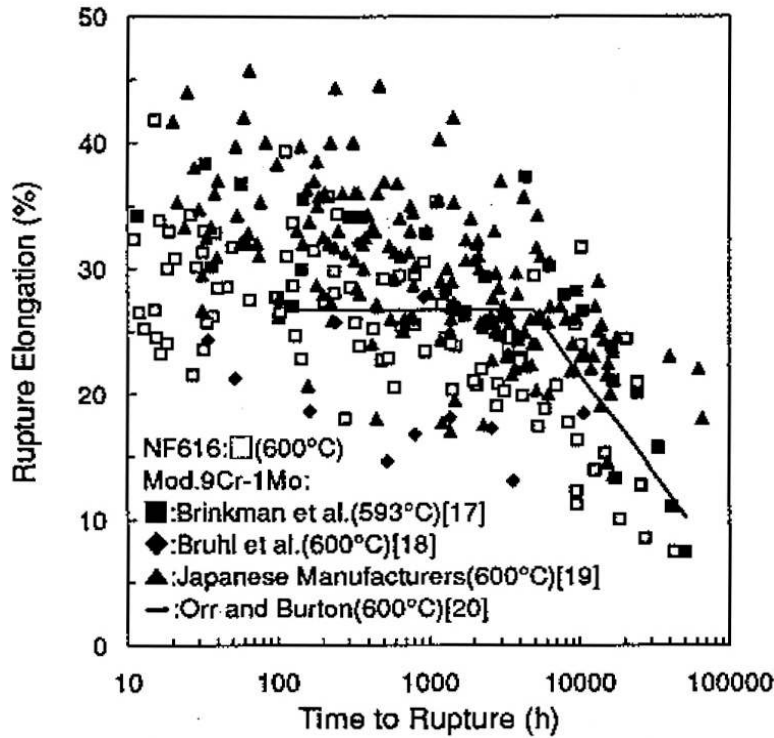


Figure 5.6. Creep rupture elongation for NF616 at 600°C (Mimura et al. 1994).

It should be mentioned that extra caution should be taken when dealing with an extrapolation of long-term creep strength in NF616. It was noted that large deviations and less conservative values were found when comparing 100,000 h test data with the assessed curves at 600 and 650°C (Bendick 2005). As the mechanical performance of NF616 is highly dependent on the microstructure, the changes in microstructure with service exposure can have significant effect on the material's strength. The creep rupture strength cannot be described by a single formula for the whole temperature and time range. The steady-state creep rates of NF616 were also measured over the temperature range of 550 and 750°C, and compilation of creep data is shown in Figure 5.7 (Hattestrand et al. 1998, Ennis et al. 1997, NIMS 2002, Mimura et al. 1994, Sawada et al. 2001).

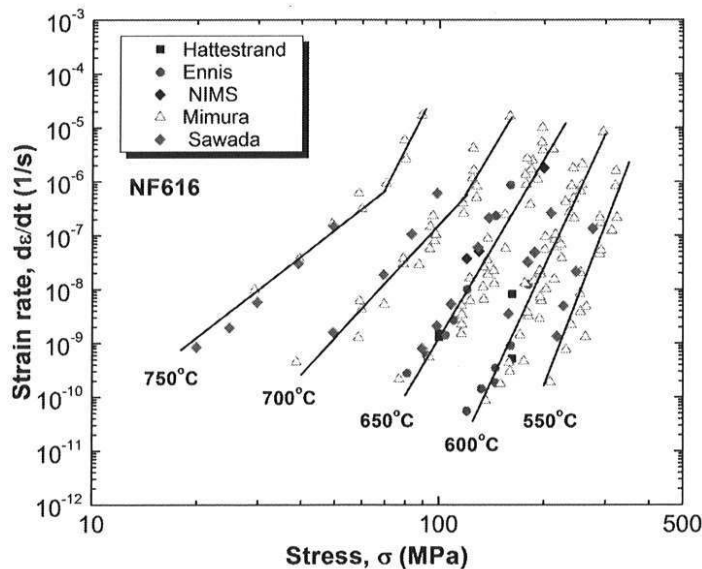


Figure 5.7. Steady state creep rate for NF616 at several temperatures.

Fatigue and Creep-Fatigue

A comprehensive database on fatigue properties for NF616 was produced by National Institute for Materials Science, Japan. Materials tested were in the plate form with a thickness of 30 mm. The heat treatment condition was 1060°C/1h air cool and 770°C/2 h air cool with room-temperature yield stress of 816 MPa and elongation of 18%. Fatigue tests were carried out in the fully reversed strain control with a strain rate of 10^{-3} s^{-1} over a temperature range from 20 to 700°C. The fatigue data are summarized in Figure 5.8 (NIMS 2002). The fatigue life of NF616 was significantly reduced at temperatures above 400°C, especially in the high-cycle fatigue region. Significant cyclic softening was observed at all test temperatures and strain ranges, similar to that in Grade 91. Cyclic stress-strain behavior at temperatures between 20 and 700°C were also determined.

A significant effect of strain rate on the fatigue life was observed in NF616 tested at 650°C, as shown in Figure 5.9. The fatigue life was reduced when it was tested at a slower strain rate (0.001 /s) compared with the fatigue life obtained at a strain rate of 0.01 /s.

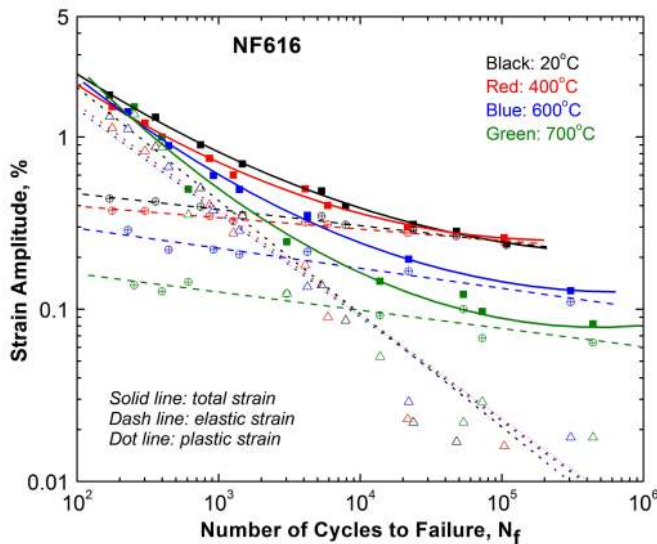


Figure 5.8. Fatigue strain-life relations for NF616.

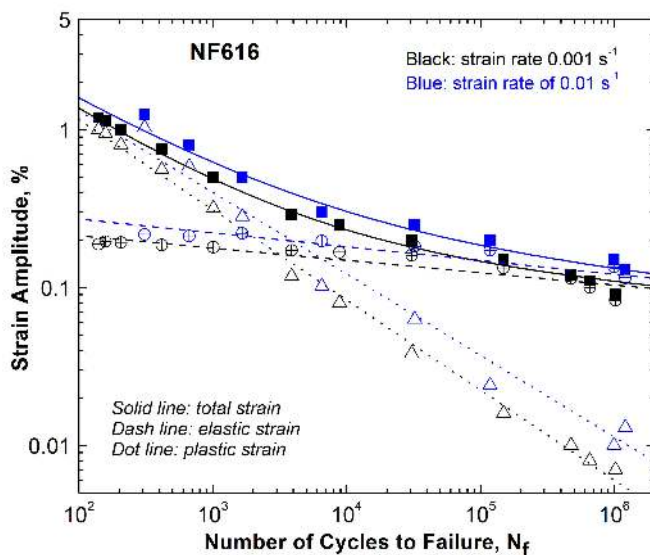


Figure 5.9. Effect of strain rate on the fatigue life of NF616 at 650°C.

5.2.2 Effects of Long-term Thermal Aging

As the high temperature strength and creep resistance of NF616 is highly dependent on the appropriate microstructure developed in the as-received material, microstructure stability during long-term service is an important subject in its applications. The strengthening mechanisms come from the high dislocation density inside the martensite laths, precipitates of carbides, nitrides, and carbonitrides, and solid solution strengthening of W and Mo. In the as-received condition, the microstructure of NF616 consists of tempered martensite with dislocation density of 10^{14} - 10^{15} m^{-2} ; M_{23}C_6 particles precipitate preferentially on prior austenite grain boundaries and subgrain boundaries and retard the subgrain growth; MX(Nb,V) type precipitates lie inside the subgrains, giving rising to significant precipitation hardening (Ennis and Czyska-Filemonowicz 2002).

During prolonged exposure at high temperatures, dislocation density will decrease, and well-developed subgrains with low dislocation density will form. Rapid reduction in dislocation density and an increase in subgrain width was observed in NF616 in the first 3000 h at 600 and 650°C with a 75% decrease in dislocation density compared with as-received material, as shown in Figure 5.10 (Ennis and Czyska-Filemonowicz 2002).

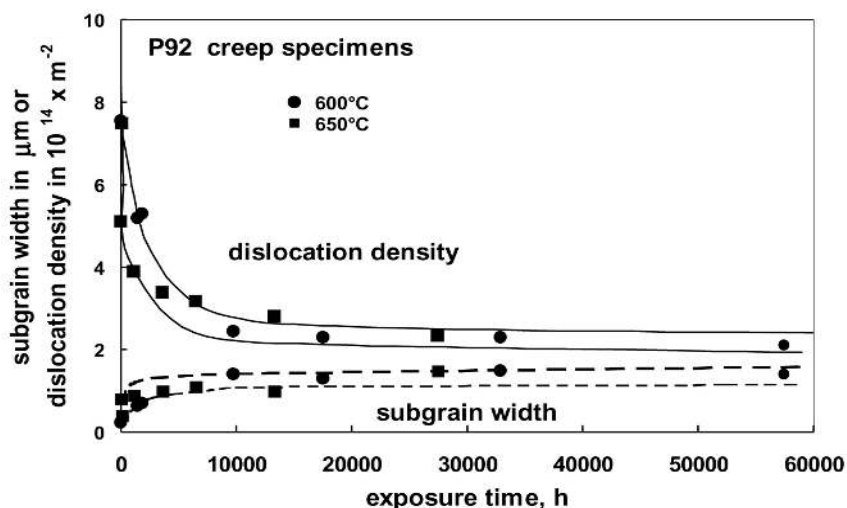


Figure 5.10. Changes in dislocation density and subgrain width during thermal exposure at 600 and 650°C in NF616 (Ennis and Czyska-Filemonowicz 2002).

The other important microstructural changes during aging are the size, morphology and distribution of carbide, nitride and carbonitride precipitates as well as the chemical composition of precipitates and matrix. MX carbonitrides show high stability against coarsening at 600°C (see Figure 5.11), while M_{23}C_6 particles coarsened to $\approx 20\%$ at 600°C and $\approx 70\%$ at 650°C after 26,000 h (Hattestrand and Andren 2001). Coarsening of M_{23}C_6 particles is accelerated by the creep strain (and stress), while the effect of stress on coarsening of MX precipitates is insignificant (Hattersrand and Andren 2001, Eggeler 1987, Schaffernak et al. 1998).

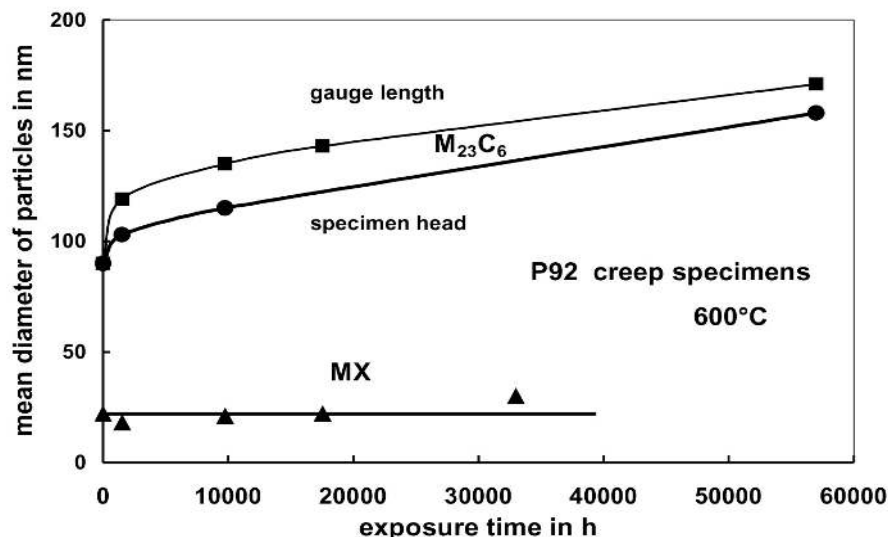


Figure 5.11. Size change of precipitate particles as a function of exposure time at 600°C in NF616 (Hattestrand and Andren 2001).

The most significant precipitation phenomenon during aging in NF616 is the formation of intermetallic Laves phase $[(Fe,Cr)_2(Mo,W)]$. Laves phase does not exist in the as-received material. Long-term thermal exposure at 600°C will lead to nucleation and growth of Laves phase in the matrix (Hald 2005). Laves phase particles were observed after 1000 h aging at temperatures of 600°C and above (Mimura 90). Significant coarsening of Laves phase occurs at 650°C (see Figure 5.12). Large differences are found between the Laves phase precipitation in Grade 91 and Grade 92. In Grade 91, the Laves phase particles grow to very large size during an extended growth phase up to $\approx 30,000$ h. After an initial growth phase of $\approx 10,000$ h the Laves phase particles in P92 are more stable against coarsening than in Grade 91. The difference in Laves phase behavior is explained by the lower solubility of the Mo Laves phase compared with W Laves phase (Hald 2005). Laves phase precipitates can also be affected by creep deformation. The number density of Laves phase precipitates formed during creep was found to be higher than that formed during isothermal aging (Hattestrand and Andren 2001) though no significant difference in particle size was measured in aged and crept specimens (Korcakova et al 2001). With increasing aging time the precipitation of the Laves phase removes Mo and W from the solid solution and the strengthening of the matrix is decreased (Hattestrand et al. 1998).

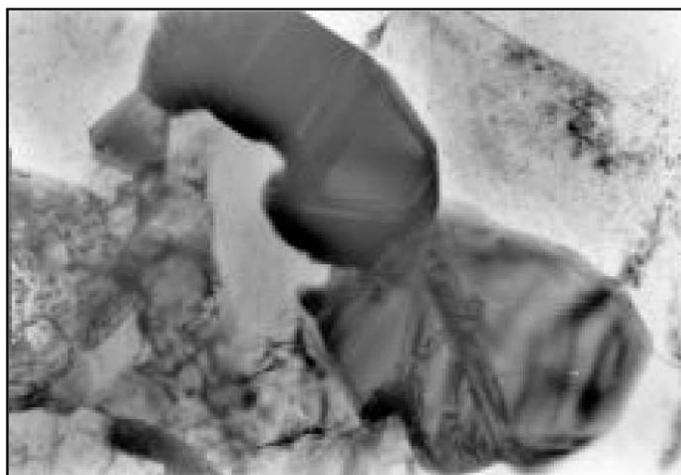


Figure 5.12. Laves phase formed after creep deformation for 27500 h at 650°C in NF616 (Hald 2005).

There have been different views on the effect of Laves phase formation on the mechanical performance of NF616. Hattestrand and Andren (2001) suggested that the Laves phase could improve creep strength if the coarsening does not occur too fast. However, the presence of large Laves phase particles ($>\approx 0.5 \mu\text{m}$) is generally considered to be deleterious.

Aging embrittlement due to Laves phase precipitation is a concern in the structural applications of NF616. The Charpy impact energy at 0°C decreased with increasing aging time up to 3,000 h and then saturated (Mimura et al. 1990). The Charpy impact tests on NF616 tubes unexposed and exposed up to 13,763 h at 600°C showed the decrease in the upper shelf energy and the shift of DBTT to higher temperatures as a result of thermal exposure, while the impact energy was still sufficiently high, $>50 \text{ J/cm}^2$ at 0°C . The effect of aging on tensile properties is insignificant (Mimura et al. 1990).

5.2.3 Effects of Sodium Exposure

No data on the effects of sodium exposure have been found for NF616.

5.2.4 Effects of Neutron Irradiation

Only two irradiation experiments have been performed on NF616, and both experiments were carried out in the high flux reactor (HFR) in Petten, Netherlands. The first irradiation experiment was to evaluate the irradiation hardening and embrittlement of various ferritic/martensitic 9-12% steels including mod. 9Cr-1Mo, HT9, MANET type steel, HCM12A and NF616 (Horsten et al. 2000). The target irradiation temperatures were 70 and 300°C with irradiation doses in the range of 1.5 to 2.5 dpa. NF616 was in the plate form, and was normalized at $1070^\circ\text{C}/1\text{h}$ and tempered at $780^\circ\text{C}/1\text{h}$, resulting in fully tempered martensitic structure with a grain size of $40 \mu\text{m}$ and a hardness of 300 HV. Post-irradiation examination on the NF616 included tensile property measurements, fracture toughness testing and Charpy impact testing.

Tensile properties indicated that the yield stress of unirradiated NF616 (750 MPa) was significantly higher than that of mod. 9Cr-1Mo and irradiation-induced hardening in NF616 was less or comparable to that in mod. 9Cr-1Mo steel, depending on the heat treatment. The accompanied ductility loss of irradiated NF616 was also smaller than in mod. 9Cr-1Mo steel with similar hardening. The increase in the yield stress in NF616 was about 250 MPa and the decrease in total elongation was $\approx 4.3\%$ after irradiation at 300°C and 2.5 dpa. The 10-12% Cr steels such as HT9 showed apparent higher hardening and ductility loss than the 9% Cr steels. The constant amplitude of irradiation hardening over a range of test temperatures in mod. 9Cr-1Mo indicates athermal hardening at the irradiation temperature of 300°C and the dose of 2.5 dpa.

The fracture toughness, K_Q for both unirradiated and irradiated NF616 was lower than that for mod. 9Cr-1Mo. The K_Q of NF616 irradiated at $300^\circ\text{C}/2.5 \text{ dpa}$ was less than $40 \text{ MPa}\sqrt{\text{m}}$ at room temperature. NF616 showed brittle fracture even at room temperature in unirradiated condition. The Charpy impact data of NF616 showed that neutron irradiation caused a significant increase in the DBTT and decrease in the upper shelf energy (USE). The DBTT of NF616 was shifted from -41°C prior to irradiation to 249°C after irradiation to 300°C and 2.5 dpa. The USE dropped from 7.3J to 4.5J under the same conditions. Compared with mod. 9Cr-1Mo irradiated in the same experiment, NF616 had inferior Charpy impact properties both before and after irradiation.

The second irradiation experiment on NF616 was also carried out at the irradiation temperature of 300°C but to a higher dose (10 dpa) (Rensman 2002). Only Charpy impact tests were performed on irradiated specimens. The Charpy impact data of NF616 irradiated to $300^\circ\text{C}/10 \text{ dpa}$ were nearly the same

as one irradiated to 300°C/2.5 dpa, which implies that the irradiation damage in NF616 was already saturated at 2.5 dpa.

Figure 5.13 compares the Charpy impact properties of three F-M steels: the first generation F-M steel, HT9 (12Cr-1MoVW) which has been used in liquid metal fast breeder reactors, the second generation F-M steel, mod. 9Cr-1Mo (9Cr-1MoVNb), and the third generation F-M steel, NF616 (Klueh and Alexander 1992, Vitek et al. 1986). The Charpy impact curves in the unirradiated condition and after neutron irradiation at 300°C were included for the three steels. It is evident that NF616 is more prone to embrittlement than other two steels both before and after irradiation. NF616 showed a higher DBTT and a lower USE than HT9 and mod. 9Cr-1Mo steel, even without irradiation. The Charpy toughness of unirradiated HT9 was slightly lower than that of unirradiated mod. 9Cr-1Mo. After neutron irradiation at 300°C, all three F-M steels exhibited significant shifts in the DBTT and reduction in the USE. The shift in the DBTT was much higher for NF616 than other two F-M steels, so as the reduction in the USE. The shift in the DBTT for HT9 was similar to mod. 9Cr-1Mo, though a larger decrease in the USE was observed in HT9. Literature has shown that mod. 9Cr-1Mo has a shift in the DBTT about half as large as HT9 when irradiation temperatures were at 365-420°C (Klueh and Alexander 1994).

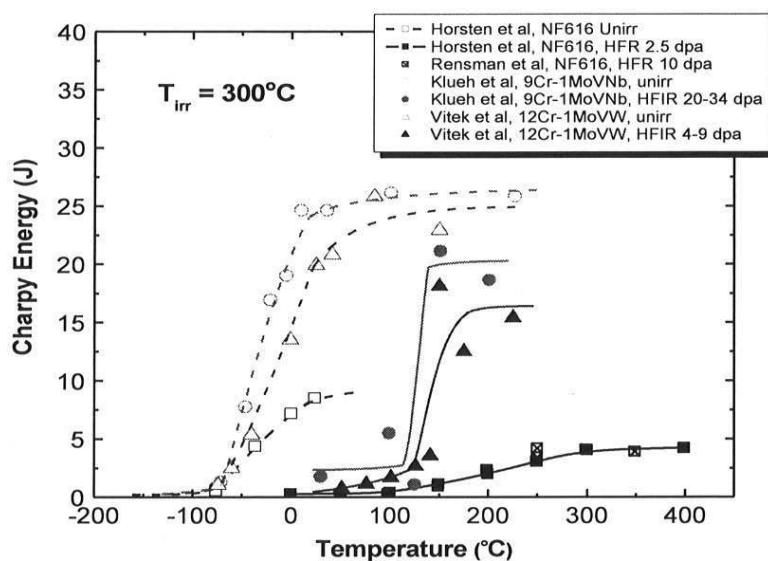


Figure 5.13. Comparison of Charpy impact curves for 12Cr-1MoVW (HT9), 9Cr-1MoVNb (mod. 9Cr-1Mo) and 9Cr-1.8W-0.5MoVNb (NF616) in the unirradiated condition and after irradiation at 300°C.

5.2.5 Weldments

The common welding processes for Grade 92 include GTAW, SMAW, FCAW, and SAW. Welding consumables for Grade 92 have not been specified. Filler metals are formulated to provide weld deposits similar in composition and performance as the base metal. Though there has been ample industrial experience and a significant database on the base metal of Grade 92, the properties of weldments, Type IV cracking, and restoration of HAZs have not been fully examined and understood. Like Grade 91, dealing with the HAZ in Grade 92 may be the most challenging task.

As observed in other ferritic/martensitic steel weld joints, Type IV cracking is frequently observed in weld joints of NF616. Figure 5.14 shows that NF616 exhibits softening behavior similar to Grade 91 (Sugiura et al. 2007). The creep rupture life of the HAZ is shorter, and crack growth rate is faster than those of base metal of NF616 (Kim et al. 2008). The creep rupture fracture occurred in the inter-critical HAZ region, which indicates Type IV failure. Multi-axial stress condition in fine-grained HAZ with lower creep strength, resulting from mechanical constrain effect by the surrounding weld metal

and base metal with higher creep strength, is essential for the formation of creep voids and brittle Type IV fracture in the fine-grained HAZ.

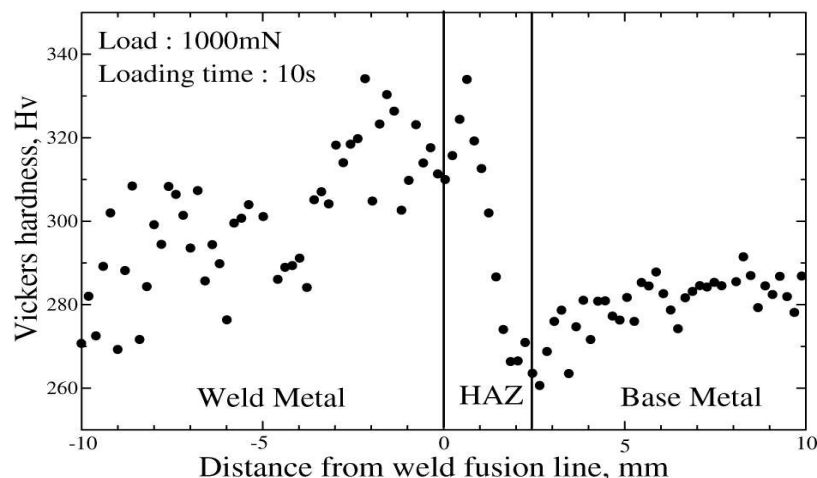


Figure 5.14. Hardness variation across a weld joint of NF616 (Sugiura et al. 2007).

Significant degradation of creep rupture strength in P92 welded joints is shown in Figure 5.15 (Masuyama 2005). The degradation of creep rupture strength became more serious with increasing test duration. The Impact energy at room temperature dropped significantly, from 72J in the PWHT to 12J after 3,000 h aging. Further aging to 9,000 h did not have more damage on the Impact toughness (Vyrostkova et al. 2007). In weld metal of Grade 92, the Laves phase reached the size of $\sim 0.6 \mu\text{m}$ after 1000 h aging, and $\approx 1.5 \mu\text{m}$ after 9000 h at 625°C . There are indications that the fine-grained HAZ is particularly susceptible to the formation of Cr-rich Z-phase, $\text{Cr}(\text{V},\text{Nb})\text{N}$ at the expense of MX precipitates during creep deformation (Francis et al. 2006).

Pre-heat and interpass temperatures are critical to weldment cracking. Great care should also be taken regarding heat input during welding to ensure the creep resistance and the required toughness values, and to eliminate hot cracking. Post-weld heat treatment is mandatory for NF616. The ASME code case 2179-6 states that the PWHT temperature should be in the range of 730 to 800°C . If any portion of the component is heated to a temperature greater than 800°C during the manufacturing, the component must be re-austenitized and re-tempered, or that portion of the component heated above 800°C including the HAZ created by the local heating must be replaced, or must be removed, re-austenitized and re-tempered and then replaced in the component, or otherwise lower allowable stresses are to be used.

Electron-beam welding has shown to be effective in reducing the width of the HAZ and to improve the creep rupture strength of welded joints. However, the brittle Type IV cracks appear even in the EBW joints at low stresses. Additions of boron between 90 and 130 ppm may be able to eliminate the fine-grained HAZ and suppress Type IV cracking (Francis et al. 2006).

Dissimilar metal weldments between P92 and austenitic stainless steels have been produced by diffusion welding by hot isostatic pressing (HIP). Nickel alloys are often used as filler metals. The thermal expansion coefficient of the filler material ($\approx 14 \times 10^{-6} \text{ K}^{-1}$) lies between that of austenitic stainless steel ($\approx 18 \times 10^{-6} \text{ K}^{-1}$) and that of ferritic-martensitic steels ($\approx 11 \times 10^{-6} \text{ K}^{-1}$) so that the thermal stresses induced by heating cycles can be spread over the whole weldment (Buchkremer 1999).

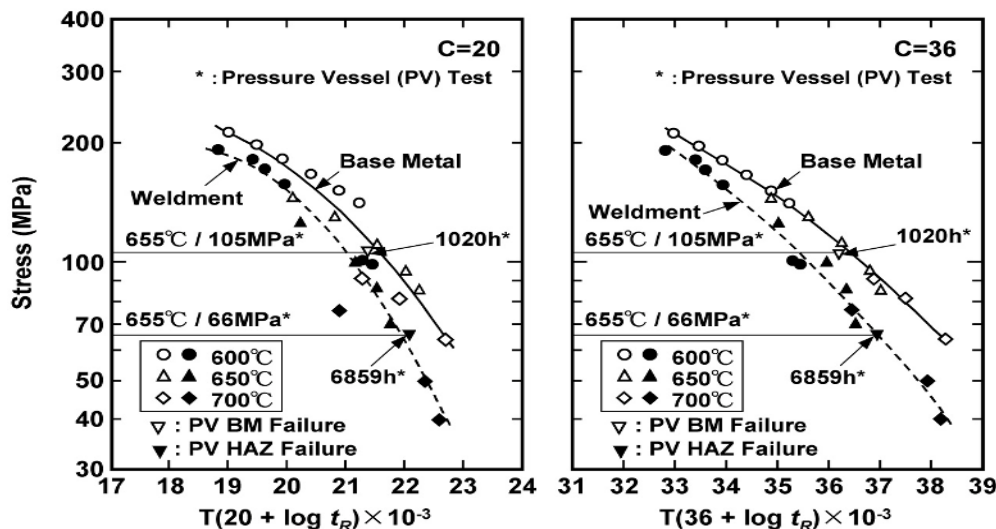


Figure 5.15. Creep stress rupture plots for the base metal and welds of Grade 92 (Masuyama 2005).

5.2.6 ASME Code Acceptance

NF616 has been included in the ASME Code Section I and Section VIII, Division 1 with the code case of 2179. The minimum mechanical properties requirements are specified for seamless tubes, pipes and forgings, and are given in Table 5.3. Specification is given in Table 5.4. The maximum allowable stresses for tubes and pipes are shown in Figure 5.16.

Table 5.3. Mechanical Property Requirements for Grade 92.

Yield strength, min. (MPa)	441
Tensile strength, min. (MPa)	620
Elongation, min. (%)	20

Table 5.4. Specification for Grade 92.

Forgings	SA-182
Forged pipe	SA-369
Pipe	SA-335
Tube	SA-213

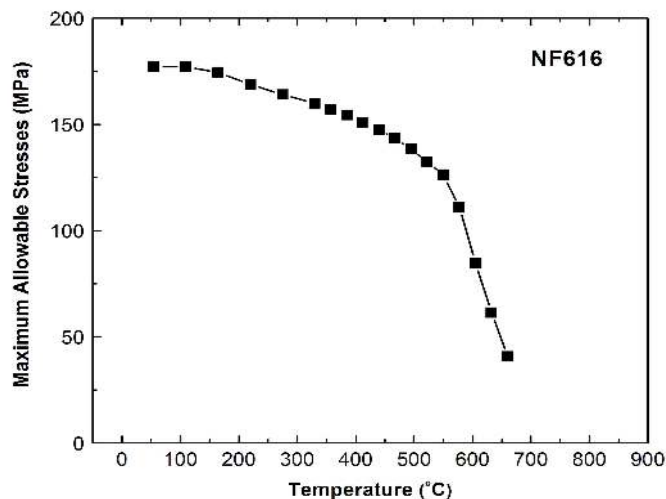


Figure 5.16. Maximum allowable stresses for NF616.

5.2.7 Industrial Experience

P92 has been used primarily in Japan, Denmark, and Germany. The applications of P92 in European power stations are summarized in Table 5.5 (EPRI 2002).

Table 5.5. Usage of P92 in European Power Stations (EPRI 2002)

Power Station	Size (mm)	Component	Steam Condition	Installation Date
Vestkraft (Unit 3)	ID 240 x39	Straight pipe main steam	560°C/25 MPa	1996
Nordjyllands-vaerket	ID 160x45	Header	582°C/29 MPa	1996
GK Kiel	ID 480x28	Header	545°C/5.3 MPa	1997
Wesrfalen	ID 159x27	Steam loop	650°C/18 MPa	1998

5.3 NF616 + TMT

“NF616+TMT” refers to NF616 with special thermo-mechanical treatment to achieve better high temperature strength and creep properties. No data has been reported on “NF616+TMT” in the US. Initial attempts have been made to improve creep resistance by heat treatment by researchers in England (Yescas and Morris 2005). An alternative heat treatment was investigated besides the ASTM Standard heat treatment (the solution temperature is at 1050-1070°C and tempering at 730 to 800°C). The alternative heat treatment consisted of solution treatment at a higher temperature (1150°C) followed by double tempering at a lower temperature (660°C). Significant improvements in rupture life were obtained in the specimens with the alternative heat treatment. The rupture life in the alternatively heat treated alloy was 17,235 h at 172 MPa and 17,144 h at 156 MPa vs. 2,722 h at 172 MPa and 8,222 h at 156 MPa in the conventionally heat treated alloy at 600°C. The alternative heat treatment produced a considerably larger prior austenite grain size, and a finer dispersion of MX particles than found in the alloy with conventional heat treatment, and a much higher hardness. This preliminary work has demonstrated the possibility of improving creep resistance with a novel heat treatment. A more extensive and systematic test program was suggested to fully explore this approach. The concept was also successfully demonstrated in a mod.9Cr-1Mo, where the high temperature strength and creep resistant in the “mod.9Cr-1Mo + TMT” were higher than in the alloy without the TMT treatment (Alinger et al. 2002).

5.4 NF709

NF709 (Fe-20Cr-25Ni-1.5Mo-Nb,B,N) is a commercial heat- and corrosion- resistant austenitic stainless steel developed by Nippon Steel Corporation in Japan for boiler tubing applications. The chemical compositions of NF709 are given in Table 5.6. The high strength of NF709 is achieved by controlling the carbon content to 0.07–0.10% and precipitation strengthening by NbC and CrNbN (Z phase). NF709 also shows good fabrication properties and weldability. It is regarded as one of the best austenitic steels for elevated temperature applications among commercially available austenitic alloy classes. The NF709 alloy provides strength nearly double that for conventional 304 and 316 stainless steels at ABR relevant temperatures (Busby et al. 2008). While the cost for this alloy has been estimated at approximately 2-4 times that for 304 SS (and 1.5 to 3 times that for 316 SS), many fossil plants have found that the improved performance outweighs the initial cost, and is still far below the cost for superalloys at comparable strengths.

A similar variant of NF709, AL20-25+NbTM, has been developed in the U.S. by Allegheny-Ludlum as flat-rolled sheets and foils tailored for high-temperature compact heat exchanger and gas-turbine recuperator applications (Maziasz et al. 2007). The Fe-20Cr-25Ni austenitic stainless alloy was also a predominant material in the British advanced gas-cooler reactor program (Waddington and Speight 1979).

Table 5.6. Chemical requirements for NF709

C	0.10 max
Mn	1.50 max
P	0.030 max
S	0.030 max
Si	1.00 max
Ni	23.0 – 26.0
Cr	19.5 – 23.0
Mo	1.0 – 2.0
N	0.10 – 0.25
Nb	0.10 – 0.40
Ti	0.20 max
B	0.002 – 0.010

5.4.1 Base Metal Properties

Nippon Steel has developed a large database on the creep rupture properties of NF709 over the temperature range of 600 to 950°C up to 40,000 h. Figure 5.17 shows the creep rupture plot for NF709 (Nippon Steel). No other mechanical property data of NF709 are available in the open literature.

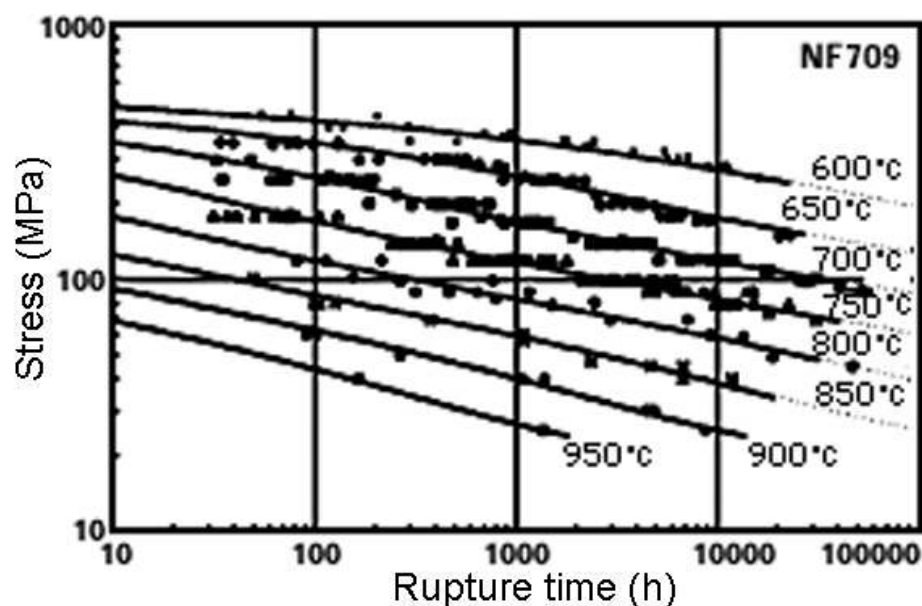


Figure 5.17. Creep rupture plot for NF709 (Nippon Steel).

5.4.2 Effects of Long-term Thermal Aging

The evolution of its microstructure during aging at elevated temperatures is of considerable interest. It is important to understand that if new phases will form that would be detrimental to creep properties and that could invalidate the extrapolations of short-term creep test data. Sourmail and Bhadeshia (2005) studied the microstructure stability in NF709 during aging at 750 and 800°C for 10,000h. The findings are summarized in Table 5.7. In the as-received condition, nitrides and carbides, NbN, TiN, and (Nb,Ti)C were observed. During aging at 750 and 800°C, NbN dissolved, $M_{23}C_6$ formed at grain boundaries and twin boundaries, along with other new phases, e.g. Z-phase (CrNbN) and Cr_3Ni_2SiX . The size of Z-phase precipitate remained ≈ 50 -100 nm long, the sizes of $M_{23}C_6$ and Cr_3Ni_2SiX

are in the range of 0.5–1 μm. TiN and (Nb,Ti)C tended to coarsen, but there was no significant change in number density. The effect of long-term aging on mechanical behavior is unclear at this stage.

Table 5.7. Summary of precipitates observed in NF709 aged at 750 and 800°C

Time (h)	0	200	2500	5000	10000
NF709	NbN	M ₂₃ C ₆ (+)	M ₂₃ C ₆ (+)	M ₂₃ C ₆ (+)	M ₂₃ C ₆ (+)
	TiN	Z-phase(+)	Cr ₃ Ni ₂ SiN(+)	Cr ₃ Ni ₂ SiN(+)	Cr ₃ Ni ₂ SiN(+)
	(Nb,Ti)C	NbN(-)	Z-phase(+)	Z-phase(+)	Z-phase(+)
		TiN	TiN	TiN	TiN
		(Nb,Ti)C	NbN(-)	NbN(-)	NbN(-)
			(Nb,Ti)C	(Nb,Ti)C	(Nb,Ti)C

Note: (+) indicates the formation of a new phase; (-) means phase dissolution.

5.4.3 Effects of Sodium Exposure

There has been no data and no experience on the sodium effects in NF709.

5.4.4 Effect of Neutron Irradiation

No neutron irradiation data can be found on NF709 or AL20-25+Nb. Some neutron irradiation data are available on 20Cr-25Ni based alloys due to the interest in British SGR fuel cladding applications. Madden and Callen (1983) examined the microstructural evolution of Ti-stabilized 20Cr-25Ni steel after irradiation to doses of 2.5×10^{24} n/m² (fast) and 5.0×10^{24} n/m² (thermal) at 510°C in the PLUTO reactor at Harwell. No significant irradiation damage was observed under these irradiation conditions. No helium bubbles were observed at a helium concentration of 4-5 appm. Helium embrittlement was not considered as an issue. Ashworth et al. (1992) studied irradiation-induced segregation in 20Cr-25Ni-Nb based model austenitic alloys by 1 MeV electron irradiation in a High Voltage Electron Microscope (HVEM) between 250 and 500°C to doses ranging from 0.6 to 7.2 dpa. Depletion of Cr, Fe and Mo enrichment of Ni and Si at grain boundaries were observed.

5.4.5 ASME Code Acceptance

NF709 has received ASME Code Approval with the ASME Code Case of 2581. The minimum tensile property requirements are given in Table 5.8. The maximum allowable stresses are shown in Figure 5.18. The maximum design temperature for NF709 is 815°C.

Table 5.8. Mechanical Property Requirements for NF709.

Yield strength, min. (MPa)	270
Tensile strength, min. (MPa)	640
Elongation, min. (%)	30

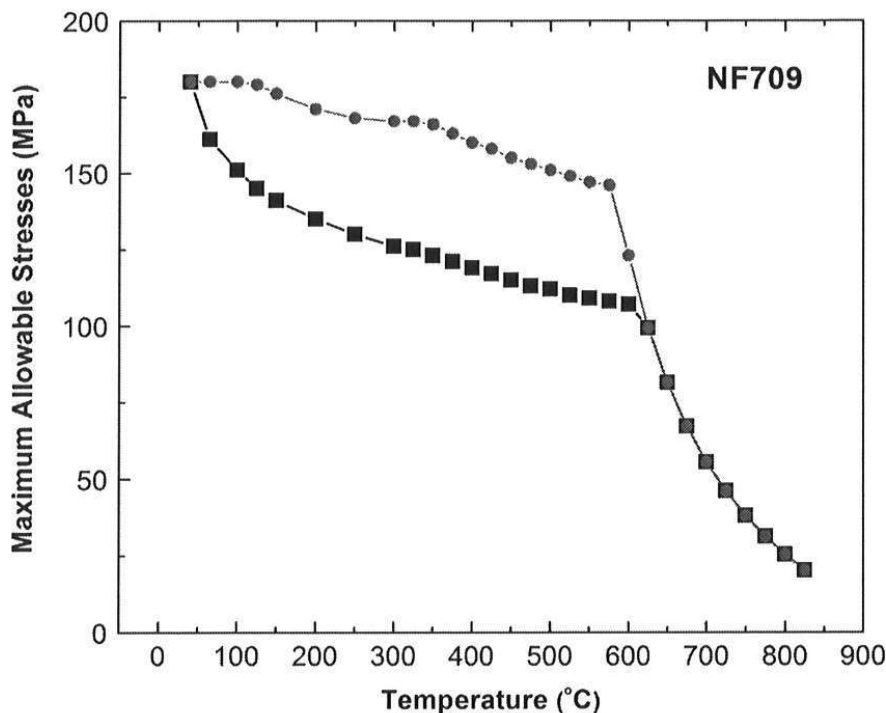


Figure 5.18 Maximum Allowable Stresses for NF709.

5.5 HT-UPS

The HT-UPS (high-temperature, ultrafine precipitation-strengthened) 14Cr-16Ni austenitic stainless steels were developed at Oak Ridge National Laboratory in the late 1980's to improve the combination of resistance to radiation-induced swelling and grain boundary helium embrittlement, and resistance to thermal creep-rupture for the U.S. Fusion Reactor Materials program (Maziasz 1989). The HT-UPS alloy is a 14Cr-16Ni-2.5Mo-2Mn-0.3Si-0.3Ti austenitic stainless steel modified with a combination of V+Nb+B+P to form stable nano-scale precipitates for high-temperature strengthening. The chemical composition of HT-UPS is similar to D9I (15Cr-15Ni-2Mo-2Mn-0.75Si-0.25Ti+B,P) austenitic stainless steel that was developed for improved irradiation resistance for the U.S. Fast Breeder Reactor Materials program (Busby et al. 2008). Both HT-UPS and D9I showed remarkably improved resistance to radiation-induced void swelling relative to type 316 and the standard D9 steels.

Only available data on HT-UPS are creep rupture data produced at Oak Ridge National Laboratory, and reported by Swindeman and Mazasz (1990). The data were replotted by Yamamoto et al. (2007) to compare with newly modified HT-UPS for improved corrosion resistance, which is shown in Figure 5.19. The creep rupture strength of the HT-UPS steels is significantly higher than other classes of austenitic stainless steels, comparable to nickel alloy, Alloy 617. Compared with Type 316 SS, the HT-UPS alloy, it has more than double the creep rupture strength at 700°C.

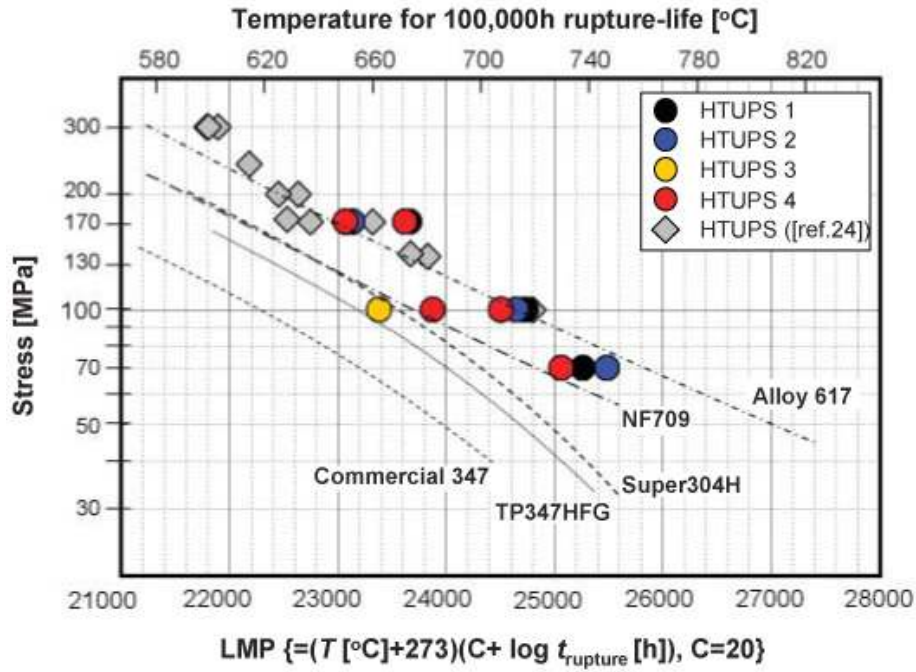


Figure 5.19. Creep rupture strength of HT-UPS (Yamamoto et al. 2007).

6. HIGH TEMPERATURE DESIGN METHODOLOGY

6.1 Creep-Fatigue Design Rules

The creep-fatigue damage could be a serious problem for piping operating at elevated temperatures. For a design to be acceptable, creep and fatigue damage must satisfy the following when using inelastic analysis:

$$\sum_{j=1}^p \left(\frac{n}{N_d} \right)_j + \int_0^t \frac{dt}{T_d} \leq D$$

where D is the total creep-fatigue damage due to n fatigue cycles of type j and time interval dt , N_d is the allowable cycles for cycles of type j and T_d is the allowable stress rupture time (function of effective stress and temperature) during time interval dt . The allowable fatigue cycles are given as functions of total effective strain range and temperature in Appendix T. The strain ranges must be augmented by an appropriate stress concentration factor if the design point is at a notch. If detailed inelastic finite element analysis is conducted, the notch effect should already be included in the analysis. The bilinear creep-fatigue envelope $D \leq 1$ is given for each material in Appendix T. Piping systems must be assessed for thermal expansion elastic follow up if elastic analysis is used.

Creep-fatigue design of welds in piping requires special attention. The analysis for strains and creep-fatigue interactions at welds has to include the stress and strain concentration factors corresponding to the worst surface geometry expected for the actual weld. In the vicinity of a weld, creep-fatigue evaluation should be made with reduced values of the allowable design cycles, N_d and allowable time duration T_d . The N_d value should be reduced by a factor of 2 compared to the parent material and the T_d value should be reduced by multiplying the stress rupture time for the parent material by a material-dependent weld strength reduction factor given in the code. These safety factors must be applied on top of the K' factor that is normally applied in the creep-fatigue design of the parent materials. Details about the creep-fatigue design rules are discussed below.

6.1.1 Background on Design Rules Development

The treatment of creep-fatigue interaction in Subsection NH had undergone a long history of development, starting with various code cases, and in particular Code Case N-49 which was the forerunner of Subsection NH. It was recognized very early on that creep-fatigue damage is a very severe structural failure mode under elevated temperature service and it was one of the main concerns of the ASME Subgroup on Elevated Temperature Design (Jetter 2008).

In 1969, Brinkman (1969) had conducted a literature review for the Creep-Fatigue Task Force of SG-ETD on the effects of parameters such as testing frequency, testing technique, strain range, wave shape, etc., and the effects of hold time, on creep-fatigue life. It was communicated to the Subgroup that failure under combined creep and fatigue could be predicted by combining fatigue usage and fractional creep damage in an interaction diagram, as suggested by Wood (1966). In 1970, the Creep-Fatigue Task Force recommended to the Subgroup the use of the linear damage summation, with a time fraction evaluation of creep damage, to address creep-fatigue failure:

$$\underbrace{\sum_i \alpha \left(\frac{N}{N_d} \right)_i}_{\text{Cyclic Damage}} + \underbrace{\sum_i \beta \left(\frac{t}{t_r} \right)_i}_{\text{Time Fraction}} \leq K$$

Here α and β are correlation constants, N the number of cycles, N_d the number of continuous cycles to failure, t the service time, and t_r the creep rupture time. The parameter K represents a nonlinear equation in the creep-fatigue interaction diagram in the form of

$$\log_{10} \left(\frac{t}{t_r} \right) + 4.25 \left[\left(\frac{N}{N_d} \right)^2 + 0.257 \left(\frac{N}{N_d} \right) \right] = 0$$

There were considerable discussions of what phenomena should be accounted for by various terms in the equation. It was decided that for inelastic analysis the cyclic damage is computed from fatigue damage due to continuous cycling with rate-independent plasticity, and the time fraction term encompasses all time-dependent creep damage. However, for elastic analysis, the reduction in fatigue life due to strain-controlled hold time induced creep damage is included in the cyclic damage term (Campbell 1971, Jetter 1976).

Such an approach was adopted as the Code procedure until 1990 when it was replaced in Code Case N-47 by the approach of Severd (1991), where for elastic analysis, all time dependent creep damage is accounted for in the time-fraction term and the cyclic damage term does not involve creep damage. The creep-fatigue failure criterion takes the form:

$$\underbrace{\sum_i \left(\frac{N}{N_d} \right)_i}_{\text{Cyclic Damage}} + \underbrace{\sum_i \left(\frac{t}{t_r} \right)_i}_{\text{Time Fraction}} \leq D$$

where D is represented as a bi-linear curve in the creep-fatigue interaction diagram. Methodology is provided in the Severd approach to account for the effect of plasticity and creep on the stress level used to determine the time fraction. For Code design allowable life calculation, a safety factor ($1/K'$) is used to increase the stress level that enters the stress-rupture curve. Margins are also introduced to the values of N_d and t_r when they are determined from continuous cycling data and creep rupture data, respectively.

6.1.2 Eddystone Impact

Jetter (2005) reported that in 1983, leaks and failures were found in the main steam line pressure parts of the Eddystone Unit No. 1. These 316SS pressure parts were operated at pressures to 5000 psig and temperatures to 649°C (1200°F). Widespread, nearly through-wall cracking was observed after about 130,500 hours. Crack initiation would have to occur much earlier. Failure investigation and evaluation were conducted by DeLong et al. (1988). An evaluation using the Code Case N-47 criteria was also carried out by Corum (1987). Similar effort was made by Bate (1988) in the UK where the ductility exhaustion method developed in the UK was compared with the Code Case N-47 criteria, using the reference Von Mises effective stress and the proposed multiaxial equivalent stress proposed by Huddleston. Additional structural tests were performed by Corum and Sartory (1985) to provide benchmark data. All of these evaluations led to the conclusion that the Code rules at the time were not adequately conservative and the

safety margin was increased by lowering the K' factor from 0.9 to 0.67. Thus the design stress that enters the stress-rupture curve to determine the rupture time t_r was increased from 1.1X to 1.5X.

6.1.3 Other Approaches Considered

According to Jetter (2005), due to the problems associated with Eddystone, the Subgroup had kept open an agenda item on improvements to creep-fatigue evaluation procedures. Some of the other approaches presented to Subgroup are captured below. Presentation based on the work of Wareing et al. (1985) provided the rationale for the UK ductility exhaustion approach and compared test results with time fraction approach. It was suggested that ductility exhaustion provided a better correlation. Also presented was the description of Bestwick and Clayton (1985) of the ductility exhaustion evaluation procedures.

Sartory (1987) presented the results of an assessment of the Code Case N-47 linear damage approach based on thermal shock tests of cylinders. It was found that the Code allowable life predictions were conservative and the best estimate predictions without safety factors were unconservative. Bass (1987) presented a comparison of ductility exhaustion and time fraction creep damage evaluation using data on 316SS. Bass concluded that the scatter of the results from the two approaches was comparable, but the creep-fatigue interaction diagram associated with ductility exhaustion correlated better with the test results used in the study.

Takahashi (1987) presented the results of a 1987 EPRI/CRIEPI joint study in which the linear damage fraction rule was compared to a number of other approaches (except ductility exhaustion). The results showed that best agreement was obtained with the damage rate approach developed by Majumdar (1990). But the approach required many more types of tests than the linear damage fraction approach.

Majumdar (1990) presented the results on the thermomechanical fatigue of 304SS. Figures 6.1 and 6.2 show that the Code Case N-47 approach was non-conservative without the Code safety factors. The degree of non-conservatism increases as the strain rate and strain range decreases.

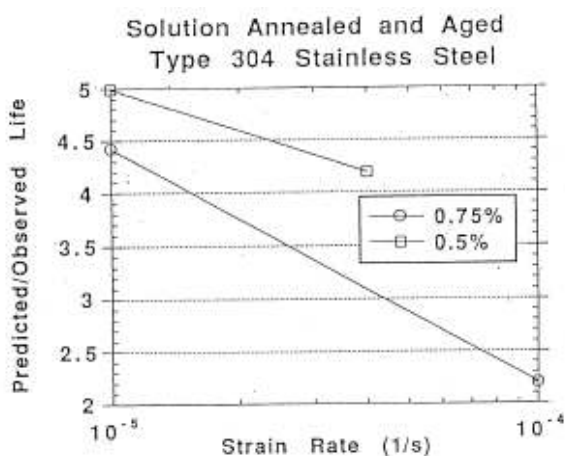


Figure 6.1. Best estimate predictions at strain ranges of 0.5% and 0.75%, Majumdar (1990).

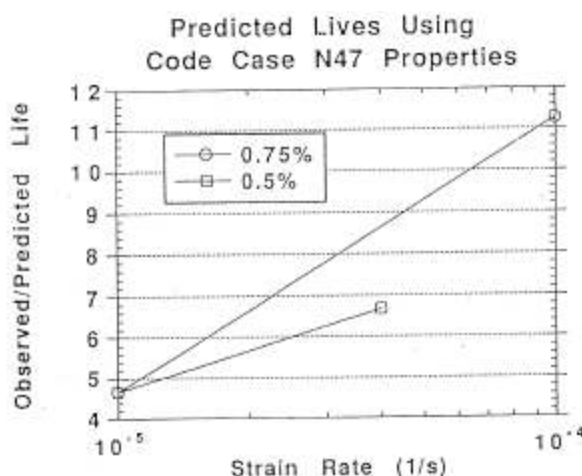


Figure 6.2. Predictions using Code safety margins at strain ranges of 0.5% and 0.75%, Majumdar (1990).

Corum (1991) presented the results from a JAPC-USDOE Study on Mod 9Cr 1Mo (Grade 91). It was shown that using a cyclic creep rupture curve instead of a monotonic rupture curve improved the time

fraction linear damage correlation, shown in Figures 6.3 and 6.4. However, the creep-fatigue damage correlation seemed to improve by use of the ductility exhaustion approach as shown by Figure 6.5.

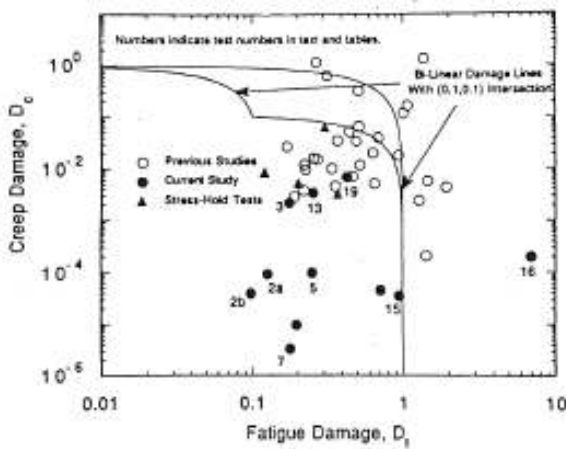


Figure 6.3. Creep-fatigue diagram calculated using monotonic rupture curves, showing very low apparent creep damage values as cyclic softening is not taken into account, Corum (1991).

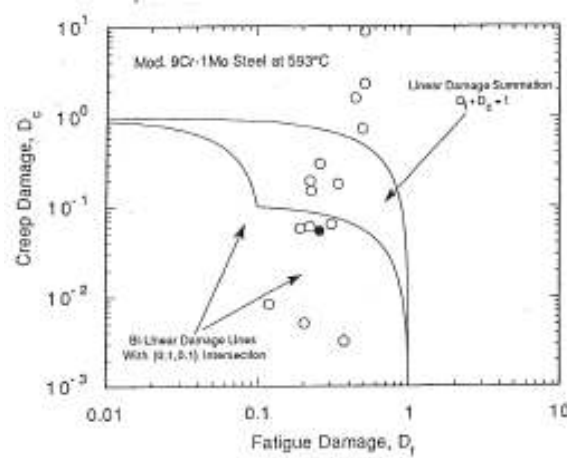


Figure 6.4. Creep-fatigue damage diagram calculated using cyclic rupture curve, showing increased creep damage, Corum (1991).

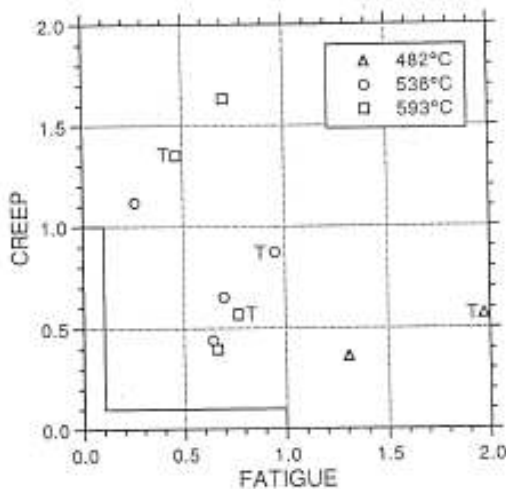


Figure 6.5 Creep-fatigue damage diagram calculated using ductility exhaustion, Corum (1991).

Smith (1989) presented the development and rationale for the UK strain based creep-fatigue procedure. The data was the same as Wareing (1985). Fatigue damage was based on crack growth and creep damage was based on ductility exhaustion. The creep damage evaluation was based on inelastic analysis and required separate evaluation during steady states and transients.

Majumdar (1993) presented an assessment of the UK ductility exhaustion method as applied to 304SS data. It was concluded that ductility exhaustion predicted fatigue life within a factor of two for low strain ranges but became non-conservative at higher ranges. The time fraction approach was non-conservative for tensile holds with increasing non-conservatism as the strain range decreased. The time fraction approach became highly conservative when the Code safety factors were used.

Taguchi (1995) presented further work on methods for dealing with the effect of cyclic softening and cyclic creep rupture on Mod 9Cr 1Mo creep-fatigue. Two methods were considered, (i) the approach modified by creep properties after cyclic softening, and (ii) the Japanese DDS approach wherein the stress relaxation behavior was analytically evaluated. Figure 6.6 compares predicted and observed life of the DDS approach using cyclic and monotonic stress-strain relations. It was concluded that the analytical DDS approach using the time fraction rule with a monotonic stress-strain relation is applicable to Mod 9Cr 1Mo.

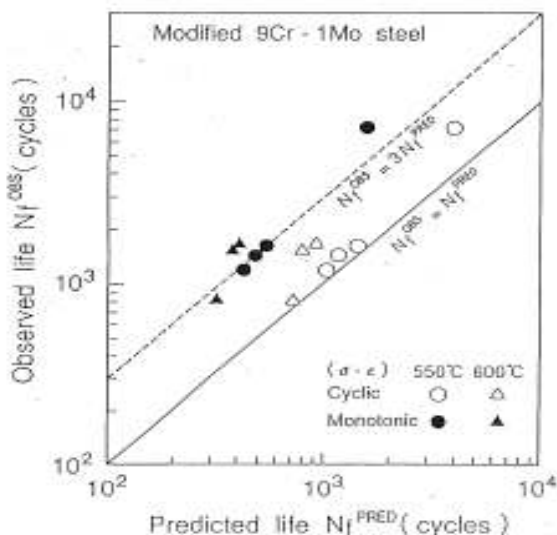


Figure 6.6. Life predictions using DDS approach, Taguchi (1995)

The above summary indicate that there had been many comparative evaluations of the time fraction and ductility exhaustion approaches to creep-fatigue evaluation. Both approaches showed considerable scatter. Generally the time fraction approach led to non-conservative results without Code safety factors, increasingly so as strain range and strain rate were decreased. However, the time fraction method was shown repeatedly to be conservative with Code safety factors. The ductility exhaustion approach was shown to have less scatter in some situations and was more conservative at low strain ranges and strain rates.

The overall conclusion was that the time fraction approach had the advantage that it was conceptually straight forward, drew on existing data (fatigue and creep-rupture), and was fairly readily implementable. The alternate approaches did not demonstrate a clear superiority in correlating experimental data, required additional new testing, and were more difficult to implement in design rules. The time fraction approach has been retained in the creep-fatigue Code rules to this day.

6.1.4 DOE/ASME Materials Project

A three-year collaboration between DOE and ASME was established in 2006 that addressed topics in support of an industrial stakeholder's application for licensing of a Generation IV nuclear reactor. Parts of Tasks 3 and 5 focused on the creep-fatigue procedure, within the time-fraction framework of Subsection NH. The overlaps of these two tasks were intended to bring different international perspective on Subsection NH.

Task 3

The objective of Part II of Task 3 (Riou 2007) was to compare the Subsection NH and RCC-MR creep-fatigue procedures for Grade 91, to explore the extent to which data for Grade 91 presently available in Subsection NH and RCC-MR are thought to be validated, to recommend improvements to existing Subsection NH creep-fatigue procedure for Grade 91, and to define a test program to validate the improved creep-fatigue procedure for Grade 91.

The major conclusion was that the Subsection NH creep-fatigue procedure for Grade 91 is very conservative. Other findings for Grade 91 include:

- For the test conditions studied the Subsection NH design approach (with $K' = 0.67$) was not executable as steps were encountered that led to excursion outside the bounds of the curves and tables in Subsection NH
- For the best-estimate approach with $K' = 1$ the life prediction is very conservative as compared with experimental results
- The values of the predicted stresses at the beginning of hold times are far too high
- The predicted amount of stress relaxation using the isochronous stress-strain curves is overly conservative (the amount of stress relaxation is too small as compared with the experimental results)
- The creep-fatigue damage envelope is very conservative for Grade 91 (bi-linear damage lines with (0.1, 0.01) intersection)

The following recommendations for Grade 91 were made:

- Modify the procedure for calculating the stress at the beginning of the hold time by accounting for cyclic softening and symmetrization effects for Grade 91
- Provide additional creep-strain laws in Subsection NH
- Provide guidance in Subsection NH to address elastic follow-up effects
- Change the K' factor from 0.67 to 0.9 for the elastic analysis route in the Subsection NH procedure, as employed in RCC-MR
- Change the intersection point in the creep-fatigue damage envelope from (0.1, 0.01) to (0.3, 0.3), as employed in RCC-MR for Grade 91
- Tests where environment plays a role (tests with hold time in compression) should not be included in the investigation of true creep-fatigue interaction

An extensive creep-fatigue and fatigue-relaxation test program on Grade 91 was proposed. Test programs that are relevant to ABR contain the following elements:

- Tests at 500°C (932°F) or 525°C (977°F) for comparison with data at 550°C (1022°F)
- Extension of the database at 550°C (1022°F) with tests with longer hold times
- Characterization of cyclically softened material and comparison with thermally aged material
- Tests after post-weld heat treatment and comparison with data from as-received material
- Screening tests on cross-weld specimens

Task 5

Part of the object of Task 5 (Asayama and Tachibana 2007) was to collect creep, creep-fatigue and fatigue (when available) data for Grade 91 in air, vacuum, and sodium environment, and to evaluate creep-fatigue procedures from Subsection NH, RCC-MR, and the Japanese high temperature design code.

Grade 91 data were collected from the Japan Atomic Energy Agency (JAEA), Electric Power Research Institute (EPRI), Oak Ridge National Laboratory (ORNL), Central Research Institute of Power Industry in Japan (CRIEPI), National Institute of Material Science in Japan (NIMS). They included 205 creep data, 281 fatigue data, and 78 creep-fatigue data. Product forms included plates, forgings and pipes. Most of the data were originally obtained for application to fast breeder reactors and the temperature range was limited to 400°C (752°F) to 649°C (1200°F).

These data were analyzed from the perspective of:

- General trend and sodium environmental effect for the creep properties
- General trend, effect of thermal aging, effect of environment, and stress-strain relationship for the fatigue properties
- Reduction of creep-fatigue life due to strain hold, and effect of strain hold period for creep-fatigue properties

Comparison of the creep-fatigue procedures from Subsection NH, RCC-MR and the Japanese high temperature design code was made, with emphasis on:

- Method of determination of strain range
- Initial stress of stress relaxation
- Stress relaxation behavior, and
- Formulation of creep damage

These creep-fatigue procedures were then applied to the collected data. Specific focus was given to:

- Determination of the initial stress of stress relaxation
- Description of stress relaxation behavior during the strain hold period
- Creep-fatigue damage diagram

The creep-fatigue evaluations were performed both with and without safety factors employed by each code. The major conclusion was that the creep-fatigue evaluation procedure of Subsection NH is overly conservative for Grade 91.

Other recommendations for Grade 91 include:

- Incorporate one of the following in the creep-fatigue procedure of Subsection NH
 - a. cyclic stress-strain curve
 - b. creep-strain law in conjunction with the strain hardening law
 - c. a combination of a. and b. from above
- Change the current intersection point of (0.1, 0.01) in the creep-fatigue damage envelope of Subsection NH to (0.3, 0.3)

Recommendations in the following areas were also made:

- Long-term material testing
- Evaluation method for welded joints
- Extrapolation of experimental data to the design regime
- Structural testing for validation

Task 10

Task 10 (Asayama 2008) is a new task in Phase II of the DOE/ASME Materials Project that was started in April, 2008. This task will complete in March, 2009. The background on initiating this new task is as follows.

The design analysis rules in Subsection NH were developed during the decades ending in the late 1980's. Since then there have been notable advances in computing technology that permit evaluation methodologies not previously considered. There have also been advances in the understanding of elevated temperature material behavior and failure mechanisms. Also, as shown by the results from Tasks 3 and 5 of the DOE/ASME Materials Project, the current methodologies for evaluating creep-fatigue interaction have a number of deficiencies.

The scope of Task 10 is summarized below:

- Review creep-fatigue methodologies, including damage-based, strain-based, and methods not involving separate accounting of creep and fatigue damage in various design codes
- Assess procedures and relevant literatures
- Assess the potential of deploying these methods in Subsection NH either to remove excessive conservatism or to resolve NH issues identified in the final report of Task 2 on NRC concerns
- Provide rationale and propose implementation strategies for these methods, where applicable
- Propose methods to address the effects of aging, surface conditions, and geometric discontinuity
- Recommend requisite requirements for codification, including data generation, data extrapolation strategies, and feature testing to validate methods

6.1.5 Creep-Fatigue Code Rule Improvement

Creep-fatigue is a very significant structural failure mode for components in elevated temperature service. It is vital that creep-fatigue design life can be predicted conservatively and with confidence. It is also important that the creep-fatigue Code rules do not lead to an overly conservative design such that the construction of the component is not feasible or economically viable.

There have been many efforts since the 1960s that aimed towards such goals. As evidenced by the latest development of the DOE/ASME Materials Project, the effort is still continuing. The results from Tasks 3 and 5 of the DOE/ASME Materials Project highlight the need to account for different material response in developing creep-fatigue procedures. The Code rules that were originally developed for austenitic stainless steels, which exhibit cyclic hardening behavior, do not apply without modifications to Cr-Mo steels that cyclically soften. Results to be obtained from the ongoing work in Task 10 should point the way to a possible overhaul of the creep-fatigue design rules that were established since the 1980's.

As the efforts from the DOE/ASME Materials Project principally concentrate on methods development, it is important to have the right data to validate/qualify any proposed procedure improvement. Most of the creep, fatigue and creep-fatigue test data were developed from smooth uniaxial specimens, with some small amount of data from structural tests. Testing in the following areas for both base metals and weldments is greatly needed to aid the development, validation and qualification of any improved creep-fatigue procedures.

- Uniaxial tests to support material model development – as demonstrated in Tasks 3 and 5, incorrect modeling of the creep and stress relaxation response significantly impacts the accuracy of the creep-fatigue procedure
- Creep-fatigue tests with long hold time and small strain range – to establish whether or not creep-fatigue damage will be saturated
- Appropriate creep-fatigue test data for loading sequence evaluations
- Multiaxial creep-fatigue tests – to provide data to qualify the treatment of multiaxial stress and strain states in the creep-fatigue design rules

- Structural tests – to provide data to qualify the treatment of structural discontinuities and the general non-uniform stress and strain states in the creep-fatigue design rules

The current approach in establishing creep-fatigue design rules is, by and large, empirical; relying on data correlation. Such an engineering approach often times proves to be successful when it is supported by a robust database and does not involve significant data extrapolation. But creep, fatigue and creep-fatigue are time dependent processes and components are designed to operate under these conditions for very long time. By necessity, shorter-term accelerated data are relied upon for correlation and extrapolation. Thus, establishing confidence in the creep-fatigue design rules based on such extrapolations is very important in ascertain the structural integrity of the design and for regulatory acceptance.

There has been much effort in the study of creep-fatigue mechanism from the materials science perspective (Raj 1985, Argon 1982). There were also innovative studies of creep-fatigue mechanism by in-situ SEM observations during creep-fatigue tests, Arai et al. (1996), Yamamoto and Ogata (2000). Detailed numerical studies of creep-fatigue interaction, with some details of the damage mechanisms incorporated, have also been reported, Nielsen and Tvergaard (1998). More efforts along these lines to establish a fundamental understanding of the creep-fatigue mechanisms, in parallel with the engineering approach development, are required. This will provide the basis to establish the range of validity for the extrapolation employed in the engineering approach. In addition, such understanding might suggest approaches to develop alloys that enhance the creep-fatigue resistance.

6.2 Weldment Design Methodology

It is well recognized that lack of validated weldment design criteria is a significant issue for advanced reactors. Weldments are often the critical locations in the design of high temperature components, due to their lower strength and metallurgical variations. Weldment safety evaluation was one of the nine areas of concerns that were identified by the NRC in the license review of the CRBRP project. Weldment cracking was regarded as the foremost-unresolved structural integrity issue, particularly in components that are subjected to repeated thermal transient loadings. The factors that needed considerations in the NRC review included (NUREG-0968):

- Crack initiation in the HAZ of the weldment exposed to cyclic sodium temperatures at the inside surface
- Effects of material property variations in the weld on creep-fatigue and creep-rupture damage
- Effects of time rate, cyclic rate, and hold-time effects on propagation of long shallow cracks in the HAZ of the weldment
- Enhanced creep in the remaining uncracked wall thickness caused by residual stresses and thermal cycling
- Stability of the remaining uncracked wall ligament for operation in the creep regime

A confirmatory program between the NRC and the CRBR project was established to address these issues, and to quantify the safety margins of weldments in service at elevated temperatures. The basic elements of the program were:

- Evaluate potential for premature crack initiation at weldments due to thermal fatigue, residual stresses, and damage caused by the welding process.
- Confirm adequacy of creep-rupture and creep-fatigue damage evaluation procedures at weldments.
- Assess growth behavior of cracks in the HAZ of weldments.

- Evaluate consequences of enhanced creep in uncracked ligaments.
- Assess stability of uncracked ligaments for creep conditions.
- Define effects of long-term elevated temperature service on crack initiation.
- Evaluate effects of loading sequence on creep-fatigue behavior.

Some R&D efforts have been made to develop and validate the weldment design methodology despite of the discontinuation of the CRBR project. Some strength reduction factors have been included in Subsection NH to account for limited ductility of welds at elevated temperatures and the potential for high strain concentrations (both metallurgical and geometric) in the HAZ. Creep rupture strength factors are given as a function of temperature and time. The primary time and temperature dependent stress limit S_t is defined to be less than or equal to $2/3 S_r$, where S_r is the expected minimum creep rupture strength of the base metal. At weldments, the allowable stress limit S_t is specified to be the lower of the tabulated values for the base metal or $0.8S_rR$, where R is the weld strength reduction factor, which is defined as the ratio of the uniaxial weld metal creep rupture strength to uniaxial base metal creep rupture strength. The creep-fatigue evaluation of welds utilizes reduced values of the allowable fatigue life with one-half the design life of the base metal and reduced allowable creep rupture life determined by multiplying the base metal rupture life by the weld strength reduction factors. Inelastic strains accumulated in the weld region cannot exceed one-half the strain values allowed for the base material.

The adequacy of the ASME Code weldment structural design requirements has been a concern and is being reviewed. The design rules for weldments do not take into account the effects of joint design, welding process, post weld heat treatment, multiaxial stress redistribution, etc. Improvements of weldment design methodology are being addressed for GenIV Very High Temperature Systems. Improved weldment design rules and criteria should also be developed for the service environments of ARRs and 60-year design life. Particular attention should be paid to ferritic/martensitic steels that have shown premature Type IV cracking in the HAZ of welded joints. Type IV cracking in the HAZ of the weld can be a life-limiting failure mechanism. Data extrapolation to long-term service live suggests that the strength reduction factor could reach alarmingly high values, e.g. 50%. Reduction in creep strength due to Type IV cracking needs consideration in design rules. As the cracking behavior depends on several factors including chemical composition, heat treatment and the stress state, there has been no satisfactory method that allows for the estimation of Type IV cracking-limited creep rupture life.

Weld residual stresses has not been considered in the Subsection NH. The Subsection NH assumes that the initial weld would be ductile, and that subsequent cyclic loading would reduce residual stresses. The effect of weld residual stresses on the creep performance should also take into account its effect on the microstructural evolution in the HAZ and Type IV failure.

6.3 Notch Weakening Effect

Notched tensile tests are often conducted on materials suspected of being embrittled, e.g., irradiated material. The presence of a notch creates not only a stress concentration, but depending on the ductility and strain hardening properties of the material, it can also create a zone of triaxial stress field at the notch tip with high hydrostatic stress. High hydrostatic stresses generally tend to reduce the ductility of a material. Thus, in relatively brittle materials, the presence of a notch tends to weaken the material (i.e., reduce load carrying capability) by early initiation of crack and fracture. However, if the material has sufficient ductility, the presence of a notch can also increase the load carrying capacity and lead to notch strengthening.

An extreme form of notch weakening occurs in a material, such as irradiated stainless steel, which loses its strain hardening capability with irradiation. In such materials, plastic strain at the notch

tip fails to homogenize and the material fails by a "sliding off" mechanism, as shown in the figure below, leading to a phenomenon known as flow localization. Such a material may retain high local ductility, but becomes highly notch sensitive.

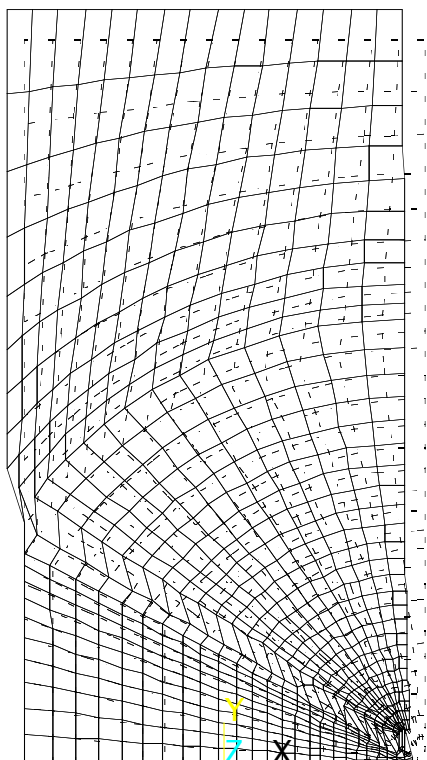


Figure 6.7. Failure of a notched tensile test specimen by flow localization.

6.4 Inelastic Design Procedures for Piping

The design rules for Class 1 piping are contained in NH-3600, which take precedence if there is a conflict with the rules in NH-3200. The dimensional standards for pipe fittings control the minimum wall thickness, but do not establish the maximum wall thickness, which will have to be imposed by the designer when significant thermal transients must be considered. Piping design must consider forces and moments resulting from thermal expansion and contraction and the restraining effects of hangers, supports and other localized loadings. It must include dynamic loading effects due to earthquake, vibration and provide for dynamic effects of any contained fluid.

The minimum thickness of piping should be derived from Design Loading analysis (NH-3222). The design of pipe bends shall satisfy the analysis requirements of NH-3200 and consider secondary deformations and irregularities inherent to the bending process (like ovality, wrinkling, surface irregularity).

Until special rules for piping components are developed for elevated temperature service, the analysis must demonstrate (by analysis or experiment) that the component fully complies with the requirements of NH-3200. Primary and secondary stress indices from Subsection NB may be used to determine stress intensities in satisfying the limits on load-controlled stresses and strain limits and creep-fatigue limits using elastic analysis or simplified elastic analysis. Analytical methods, such as, finite element analysis may be used to provide detailed stress distribution. Piping supports shall be designed

with applicable rules of Subsection NF, except for the stress analysis, which shall be in accordance with NH-3200.

When thermal and mechanical loadings are sufficiently severe to produce yielding and/or when creep processes are active, inelastic design analyses are required. Rules and limits given in Appendix T for buckling, creep ratcheting and creep fatigue assume that inelastic analyses will be carried out. This requires analysis of combined time-independent plastic and time-dependent creep behavior capable of predicting stresses, strains and deformations as functions of time. The constitutive equations must reflect features such as cyclic hardening or softening, primary creep and creep strain hardening and softening (due to reverse loading) and the effect of prior creep on subsequent plastic deformation and vice versa. Many of these properties for advanced alloys are not currently available. Particularly, classical separation of inelastic behavior into plasticity and creep does not represent the true material behavior of a material like 9Cr-1Mo-V.

6.5 Thermal Striping Design Methodology

Mixing of sodium streams at different temperatures creates thermal striping, which can potentially lead to serious cracking problems in LMRs. The mixing causes thermal fluctuations due to cyclic oscillations of the temperature distribution in the mixing region. The resulting cyclic thermal stresses in the structure can lead to cracking due to high cycle fatigue. Such cracking has been observed in the expansion tank and in the tee-junction of the secondary loop of the French Phoenix reactor. The striping frequency is generally reported to vary between 0.1-1 Hz.

The basic problem in thermal striping is one of high cycle fatigue crack initiation and growth driven by cyclic thermal stresses. To evaluate the high cycle fatigue initiation life, a detailed thermo-mechanical analysis of the fluid/structure is needed to obtain an accurate estimate of the mechanical strain range, i.e., total strain range minus the purely thermal expansion/contraction strain range at the critical location. Both the heat transfer and the stress analyses are generally conducted with a finite element program using either elastic or elastic-plastic analysis. If operating at high temperatures, creep effects must also be taken into account. Special attention must be paid to any weld that may be near the thermal striping region. The basic procedure for evaluating crack initiation life is given in the ASME Code, Section III, Subsection NB (low temperature) and NH (high temperature).

Striping may also lead to rapid growth of pre-existing flaws (or flaws initiated by striping) in the striping area, particularly if the structure includes a weld. Currently, the ASME Code, Section III does not require crack growth analysis in design. However, such analyses are conducted as part of defect management in many components of existing reactors using procedures given in Section XI. The basic requirement for such an analysis is the determination of the stress intensity factor range due to thermal striping, which is the driving force for the growth of the crack. The material property data needed to estimate crack growth life is a set of crack growth rate per cycle (da/dN) vs. stress intensity factor range (DK) curves as functions of temperature.

6.6 Buckling

The buckling rules of Subsection NB do not consider the potential deleterious effect of creep due to long term loading at elevated temperatures. Load factors for load-controlled and strain-controlled time-independent and time-dependent buckling are given in Appendix T. A design factor for purely strain controlled time-dependent buckling is not required because such loadings relax by creep. The effect of initial imperfection can be significant for buckling and if significant imperfections are present initially,

their enhancement due to creep should be considered at elevated temperatures. These effects should be included in satisfying the ratcheting strain limits.

6.7 Ratcheting Design Rules

Appendix T requires that the accumulated inelastic strain shall not exceed the following values:

- (a) strain averaged through thickness, 1%
- (b) strain at the surface due to an equivalent linear distribution of strain through the thickness, 2%
- (c) local strains at any point, 5%.

The above limits apply to the maximum positive (tensile) value of the three principal strains. When computing average or linear distribution of strain, the strains must be averaged or linearized on a component level and then combined to determine the principal strains. Because of the potential for limited ductility of weld metals at elevated temperature, these strain limits should be reduced by a factor of two for all welds. If detailed inelastic analyses are not carried out, Appendix T gives alternative methods for satisfying the above strain limits by using simplified inelastic analyses.

Under certain combination of a steady primary stress and cyclic secondary stress, there is a possibility that the structure will experience large distortions due to progressive accumulation of incremental plastic strains per cycle. For example, in a reactor vessel or piping, the coolant pressure generates steady primary stress and the cyclic secondary stress may be created by transient thermal stresses. The problem may be exacerbated at high temperatures where creep can be a factor. Section III of the ASME code has design rules to prevent the occurrence of ratcheting in structures operating either at low temperatures (Subsection NB) or at high temperatures (Subsection NH). Similar rules are also included in the French Code RCC-MR.

Elastic Analysis

Low temperature

To prevent the occurrence of progressive deformation with elastic analysis, either of the following two methods may be used:

- a) $3 S_m$ rule

$$P_L + P_b + Q \leq 3S_m$$

where $P_L + P_b$ is the sum of steady primary membrane and bending stress intensities and Q is the secondary stress intensity range. In the " $3 S_m$ rule", the limit is placed at a level that ensures shakedown to elastic action after a few repetitions of the stress cycle, except in regions containing significant local structural discontinuities or local thermal stresses. The last two factors are considered only in the performance of fatigue evaluation.

- b) Bree- diagram rule

The "Bree diagram rule" is adopted in the ASME Code Section III, Division 1 Subsection NB and Subsection NH (T-1330, test B1) to ensure that the axisymmetric structure behaves in the domain E, S1, S2 or P of the Bree diagram (Figure 6.8), corresponding to elasticity, shakedown or cyclic plasticity, without ratcheting (R1 and R2). In Figure 6.8, X is the primary stress intensity and Y is the secondary stress range intensity, both normalized by the yield strength of the material.

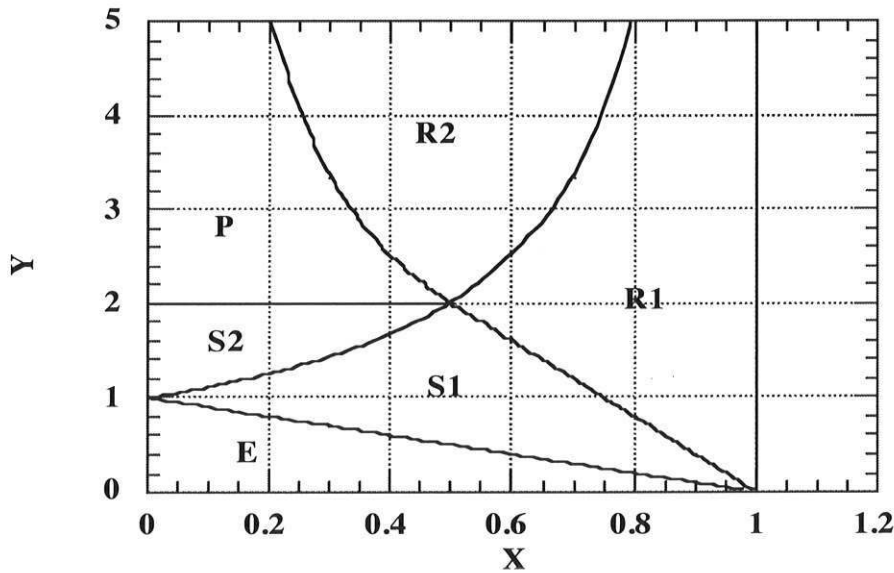


Figure 6.8. Bree diagram.

The efficiency diagram of RCC-MR has been developed on the basis of tests on a large variety of specimen geometry and loading, including non-axisymmetrical ones, as well as different materials (ferritic steel, austenitic steel, cooper, lead, etc.) and tests temperatures (from room to creep temperatures). The objective of the efficiency diagram approach is to combine the primary and secondary stress intensities into an effective stress intensity, which is then treated as a primary stress. An effective stress (P_1) is defined by the efficiency index (ν) and the secondary ratio (SR):

$$P_1 = \frac{P_m}{\nu}$$

$$SR = \frac{Q}{P_m}$$

where P_m is the primary membrane stress intensity, Q is the secondary stress range intensity and ν is given as follows:

$$\nu(SR) = \begin{cases} 1 & \text{for } SR \leq 0.46 \\ 1.093 - 0.926SR^2 / (1 + SR)^2 & \text{for } 0.46 \leq SR \leq 4 \\ 1 / \sqrt{SR} & \text{for } 4 \leq SR \end{cases}$$

To prevent ratcheting, P_1 has to be limited as a primary stress. Requiring $P_1 \leq S_m$ would ensure the same safety margin with and without progressive deformation. However, in RCC-MR, the safety margin has been reduced for the case of ratcheting deformation by limiting P_1 to $1.2 S_m$ ($\sim S_y$ for austenitic stainless steels), which leads to the following

$$\frac{P_m}{P_1} = v(SR) \geq \frac{P_m}{1.2S_m}$$

Similar rules are also provided in RCC-MR for limiting the primary membrane plus bending stress intensity.

High temperature

Both ASME Code, Section III, Subsection NH and the French RCC-MR Code contain high-temperature ratcheting rules, which are to be used when significant creep strain can occur in the structure. A brief summary of the rules is presented here to show that, as in the low-temperature case, the two sets of rules also lead to similar allowable stresses and strains for the high-temperature case.

There are more choices (tests) available in the ASME Code than in RCC-MR for meeting the strain limits using either elastic analysis or simplified inelastic analysis. The simple elastic analysis rule of RCC-MR is virtually identical to Test No. A-3 of the ASME Code. The main difference between the two codes is in the simplified inelastic analysis rules, which are based on the Bree diagram for the ASME Code and on the efficiency diagram for RCC-MR. Both approaches define an effective stress on the basis of the applied steady primary stress and cyclic secondary stress. It can be shown that the general shape and variation of the constant effective stress contour plots of the ASME Code and RCC-MR are similar when plotted in the Bree diagram coordinates, i.e., steady primary stress and cyclic secondary stress parameters.

The ASME Code allowables are based on limiting the accumulated creep strain to 1% (0.5% for welds) whereas the RCC-MR allowables are based on limiting the usage fraction defined in terms of accumulated creep strain as well as creep rupture time and onset of tertiary creep. By imposing the low-temperature ratcheting limits in addition to the high-temperature ratcheting limits, RCC-MR effectively does not allow structures to operate in the ratcheting regime (R₁ and R₂ of the Bree diagram). Although the ASME Code allows structures to operate in the ratcheting regimes and gives additional formulas for calculating the ratcheting strains when they do so, these rules apply strictly to axisymmetric structures under axisymmetric loading.

The ASME Code Subsection NH (T-1310) sets the following limits for the maximum accumulated inelastic (i.e., plastic plus creep) strains:

- (a) strains averaged through thickness, 1%;
- (b) strains at the surface due to an equivalent linear distribution of strain through thickness, 2%;
- (c) local strains at any point, 5%.

The above limits apply to the maximum positive value of the three principal strains and the limits are reduced by factor of 2 for welds. The inelastic strain limits in RCC-MR (RB 3261.2.1.2) are similar to (a) and (b) with the exception that 1% and 2% are replaced by allowable material-dependent ductility D_{\max} and $2D_{\max}$, respectively. In RCC-MR, there is no limit comparable to (c) above.

In both the ASME Code and RCC-MR, it is implicitly recognized that conducting detailed inelastic analysis for structures operating in the creep range can be complex and may be unwarranted in the face of uncertainties in constitutive equations, material properties, etc. Therefore, both codes provide a number of alternative rules that can be satisfied using either elastic analysis or simplified inelastic

analysis and give the designers the option for detailed inelastic analysis for the few cases where elastic (or simplified inelastic) analysis rules cannot be satisfied.

6.8 Flaw Assessment Procedures

6.8.1 Background

A number of safety concerns was raised by NRC and ACRS during the licensing process of the Clinch River Bleeder Reactor and the safety evaluation of the Power Reactor Innovative Small Module liquid-metal reactor. One of the concerns is related to early initiation and growth of creep crack in the heat-affected zone. Historically, ASME Code has covered crack growth issues in Section XI as part of in-service inspection. However, NRC has indicated that creep embrittlement and creep cracking of weldments need to be considered in design of high temperature components. Because of the importance of potential elevated temperature cracking of weldments, NRC wanted the designer to account for potential creep strain concentrations due to metallurgical notch effects.

The lack of a quantitative methodology for evaluating the potential for creep and creep-fatigue crack growth in structural discontinuities and weldments was identified by NRC as an NH shortcoming. Subsection NH does provide a number of design factors and procedures to ensure that elevated temperature weldments and stress risers will perform satisfactorily but it does not provide for a quantitative assessment of crack growth at elevated temperature. Although desirable for design, such a methodology is even more needed for evaluation of potential cracks and crack growth detected during in-service inspection.

6.8.2 R5 Procedure

R5 is an assessment guideline for the high temperature response of structures under creep and creep-fatigue loadings. The flaw assessment procedure in R5 permits the estimation of the remaining safe life of a structure which is subject to creep-fatigue loading and which contains a crack. Procedure for determining the amount of crack growth over a given operating period is also provided. The interaction between fatigue crack growth (which occurs during load changes) and crack growth during dwell (constant load) periods due to creep mechanisms is accounted for in the procedure. Screening tests are provided to demonstrate the insignificance of creep and/or fatigue loading, and their interaction. Flaw assessment procedure is invoked only if it fails to pass the screening criteria.

The estimation of creep rupture time in the presence of a pre-existing flaw is based on the use of the reference stress and the creep rupture data when the load is predominately primary. The reference stress in this case would be dependent additionally on the flaw size through the limit load. When the creep damage is due to cyclic relaxation or the relaxation of weld residual stress, ductility exhaustion methods are used.

The creep crack growth rate is correlated to the fracture mechanics parameters C^* or K (the stress intensity factor). However, during the transient period following initial loading, when initial elastic-plastic strains and creep strains are comparable, a time dependent fracture mechanics parameter $C(t)$ is used instead to characterize creep crack growth. The C^* and $C(t)$ parameters can be obtained from inelastic finite element analysis of the flawed structure. Simplified methods to conservatively estimate these parameters using the reference stress are provided in R5 to avoid the time-consuming inelastic finite element analysis of a structure with a flaw.

A procedure to assess the growth of a pre-existing flaw due to creep-fatigue loading is provided. However, the approach is restricted to loadings such that the uncracked body satisfies the condition of global shakedown. This relaxed shakedown condition ensures that there is no progressive plastic deformation of the component, but enhanced cyclic creep deformation is not restricted. Two methods are provided for estimating creep-fatigue crack growth, depending on whether the crack tip lies within or outside the zone of cyclic plasticity.

As R5 is an assessment guideline, there is no design margin built-in in its flaw evaluation procedure.

6.8.3 A16 Procedure of RCC-MR

RCC-MR is the French high temperature design code that provides design rules for fast breeder reactors, including high-temperature components. Appendix A16 of RCC-MR was developed to include leak-before-break (LBB) procedures and methods for defect assessment of components operating in the creep regime.

The A16 crack growth analysis is based on simplified analytical methods for C^* calculations. It is similar to the J integral calculations employed for flaw evaluations in Light Water Reactor applications, Marie et al. (2007). A16 has a wealth of formulas for determining the fracture mechanics parameters for specific components such as plates, pipes, and elbows. It employs a creep crack growth rate that is correlated to C^* using a power-law relation. When creep-fatigue loading is involved, the crack growth is calculated on a cycle-by-cycle basis where the fatigue and creep crack extensions are calculated independently. These independently calculated crack extensions are summed to the previous crack length to update the flaw geometry. This procedure is similar to the empirical crack extension evaluation method employed in ASME Section XI, Appendix C for fatigue and PWSCC crack growth calculations. The A16 procedure requires specific decomposition of the cycle to extract the part that effectively contributes to creep crack growth.

6.8.4 DOE/ASME Materials Project

During the early years of the evolution of the current NH, methodologies for evaluation of creep crack growth were in their infancy. However, there have been numerous advances in the technology in recent years, for both nuclear and non-nuclear applications. A key issue for nuclear applications is whether these methodologies are sufficiently well established that they can be implemented to give the required assurances without undue conservatism that would preclude designs and/or operating parameters that are actually not susceptible to premature failure. With this setting as the background, a new task (Task 8) for the DOE/ASME Materials Project was initiated in April 2008, and to be completed by June 2009, to address the NRC concern on the lack of quantitative flaw evaluation methodology in Subsection NH. The scope of Task 8 is summarized below.

- Review currently used methods for creep and creep-fatigue crack growth at discontinuities and in weldments to assess their applicability for design and in-service inspection assessment of Subsection NH components
- Include methods used in other nuclear standards such as R5, RCC-MR and KTA as well as those employed in assessments of non-nuclear equipment
- Consider currently approved materials for NH construction as well as potential additions such as Alloy 617 and 230, and a low carbon/high nitrogen version of 316 stainless steel
- Identify promising technologies and the testing required to implement the specific methodology in Subsection NH

- Prepare draft rules based on the above assessment for implementation in NH
- Develop rules that are based on existing data where feasible

6.8.5 Required R&D and Testing

While crack growth evaluation methods under pure creep conditions have been quite maturely developed, such is not the case when creep-fatigue loadings are involved. A more robust creep-fatigue crack growth database for both base metals and weldments is needed to support the development of more accurate flaw evaluation methods or to qualify/validate existing methods such as those in R5 and A16.

Existing creep-fatigue crack growth data are typically developed from cyclic loads with positive R-ratio and tensile hold periods. It is well known that creep-fatigue life of smooth specimens could be more limiting either under tensile hold or compressive hold, depending on the material. Thus, it is important to develop creep-fatigue crack growth data that also involve negative R-ratio and compressive hold periods.

Creep-fatigue crack growth data from structural testing are also required to support the qualification/validation of the treatment of structural and material discontinuities in any adopted flaw evaluation procedures.

As in the case of creep-fatigue design rules in uncracked structure, the current approach in establishing flaw evaluation procedures is based on empirical correlations. Thus a robust database and minimal data extrapolation are required in general for success. But current procedures are based on correlation and extrapolation of shorter-term accelerated data. Thus establishing confidence in the extrapolation is important for regulatory acceptance. R&D efforts in establishing crack growth mechanisms under creep-fatigue conditions from the materials science perspective are needed. This would help to provide rationale for data extrapolation.

In addition, material models, cyclic creep analysis methods, and methods for instability analysis due to enhanced crack growth in remaining ligaments, similar to the ASME Section XI flaw evaluation methods, will have to be developed to satisfy NRC requirement.

6.9 Data Extrapolation to 60 Years

The 60-year design life for the ARR presents a significant challenge to the high temperature structural design methodology. The current Subsection NH is applicable to the design life only up to 34 years. No experimental data contain test durations of 525,000 hours, and it is impractical to conduct such long-term tests in any types of testing. So far the longest creep tests for Grade 91 and Grade 92 steels have run up to 100,000 hours. It has been noted that there is a large drop in creep rupture strength in long-term tests for these high-Cr creep-resistant steels, which may result in overestimation of the long-term creep strength and allowable stress (Kimura 2005).

Though extrapolation of data is unavoidable, questions to be considered are to what extent data can be extrapolated, how to extrapolate, and if extrapolation can be justified. Three major extrapolation methods, namely, parametric methods, graphical methods, and algebraic methods have been developed. Each method may also be categorized as empirical or physical. The quality of a method can be judged by numerical accuracy, physical feasibility, minimum quantity of data required, and determination of material constants. For instance, the Larson-Miller Parameter is often used to describe the creep stress rupture data. The correlation between stress, temperature, and rupture time can only be used in the ranges

of test conditions where data are obtained. Extrapolation beyond these ranges, a common practice due to lack of long-term creep data, is generally inappropriate.

Several issues should be considered in data extrapolation:

- An understanding of the dominant deformation and fracture mechanism(s) over the entire service life is essential for safe extrapolation. When short-term creep data are used to derive the allowable stress or the design stress for long-term performance, the same creep mechanism must be operating over the entire range of service life.
- The exposure of metallic alloys to high temperature, sodium and neutron exposure for long periods of time will result in microstructural changes, leading to degradation in materials properties. Microstructural instability may change a classical creep behavior to a non-classical case, e.g. absence of steady-state creep. Marked changes in the slope of stress-rupture curves often indicate microstructural changes, and must be considered in data extrapolation. New advanced alloys rely on precise microstructure to achieve superior mechanical performance. Microstructural instability during service is especially serious in predicting the long-term performance based on their initial microstructural states of advanced creep-resistant alloys.
- Extrapolation of creep-fatigue data is a very significant challenge to the design, especially to the weldments. It is complicated by the fact that any creep-fatigue model must consider strain rate, stress relaxation during holds, the difference between tension and compression loading, and combinations of all of these effects.

A methodology based on accelerated evaluation approaches and analytical methods to characterize and predict the durability of materials over their service lives has been developed. An example is to use “accelerated exposures” to generate end-of-life microstructure or damage states for subsequent characterization tests so that the time required to expose materials to aging conditions is reduced. For accelerated test methods it is important to establish the equivalence between test progression and service exposure time. Prediction models developed to characterize the material response for long durations must be based on a fundamental understanding of materials response and degradation mechanisms, and must incorporate critical environmental factors such as temperature, stress, strain rate, concentrations of chemical agents, and synergistic effects.

7. EXPERIMENTAL FACILITIES

A variety of test facilities are needed for the development and evaluation of advanced materials in support of ARR design, licensing and construction. Fast-spectrum irradiation facility, general radiological test facility, sodium test facility, and creep-fatigue facility are the most critical needs. Due to significant loss of research capability in reactor technology area, restoration of key facilities in the previous U.S. reactor development program and successful international collaboration are essential. The current and future experimental facilities are identified, and discussed in the following sections.

7.1 Material Irradiation Facilities

Testing of structural materials for advanced sodium reactor applications requires fast-spectrum irradiation facilities. No sodium reactors are currently running in the United States to perform such material irradiation experiments. The two thermal reactors operational in the U.S., High Flux Isotope Reactor (HFIR) at the ORNL and Advanced Test Reactor (ATR) at the INL, are available for materials testing. Shielding of thermal flux may be required to tailor the reactor needs. The maximum neutron dose that can be reached at the HFIR is ≈ 18 dpa/yr in the target position, and 5-7 dpa/yr in the beryllium reflector positions, and the estimate maximum dose at the ATR is ≈ 10 dpa/yr.

Sodium reactors currently operational abroad provide opportunities for international collaborations to fill the gap of domestic fast test reactor needs. French PHENIX fast reactor, Experimental Fast Breeder Reactor, JOYO in Japan and Experimental Fast Breeder Reactor, BOR-60 in Russia have been used extensively as fuels and materials irradiation facilities in the past.

7.1.1 Domestic Irradiation Facilities

Two thermal research reactors are available for material irradiation testing in the U.S., the High Flux Isotope Reactor (HFIR) at the Oak Ridge National Laboratory (ORNL) and the Advanced Test Reactor (ATR) at the Idaho National Laboratory (INL). Detailed description of these two reactors is provided in the following sections.

High Flux Isotope Reactor (HFIR)

The High Flux Isotope Reactor (HFIR) is one of the most powerful research reactors in the world (www.ornl.gov). It is an 85-MW versatile materials test reactor with the peak thermal neutron flux of 2.6×10^{15} n/cm²-s. The HFIR uses highly enriched U-235 as the fuel and is moderated and cooled by light water. It has a central flux trap for high flux irradiations and isotope production, with the reactor core surrounded by a beryllium reflector, providing additional facilities for irradiation experiments. One fuel cycle of the HFIR normally consists of full-power operation for a period of 21-23 days at full power, followed by an end-of-cycle outage for refueling that lasts about 4-6 days. It is important to note that the start-up and shutdown of the HFIR is rapid and the operating power is exceptionally steady. This ensures specimen temperature is held constant during irradiation.

The HFIR has the capability and facilities for performing a wide variety of materials irradiation experiments. Major material irradiation facilities available at the HFIR include hydraulic tube facility and peripheral target positions in the target region, removable beryllium (RB) facilities and potential use of vertical experiment facilities. An overview of the materials irradiation facilities at the HFIR is given in Figure 7.1. These experimental facilities provide unique capability for both instrumented and uninstrumented materials irradiation tests with a broad range of neutron flux spectrum.

The target region located in the radial center of the reactor has the highest neutron flux levels varying from 1.1×10^{15} n/cm²-s ($E > 0.1$ MeV) at the reactor midplane to about 0.5×10^{15} n/cm²-sec at the top and bottom of the reactor. The axial distribution in neutron flux within the flux trap is given in Figure 7.2. The calculated gamma-heating rate in Al at the reactor midplane is about 37 W/g. Thirty-one target positions are provided in the flux trap, and six peripheral target positions (PPTs) provided for experiments at the outer radial edge of the flux trap. Both instrumented and uninstrumented experiments are possible in the target region. The fixed irradiation vehicles and rabbit irradiation vehicles provide flexibility and versatility for materials testing. The hydraulic tube positions can be utilized for irradiation times as short as 5 minutes.

Eight large removable beryllium (RB) facilities are located in the removable beryllium near the control region, referred to as the RB* positions (see Figure 7.1). Four small removable beryllium facilities are located in the removable beryllium near the control region. Neutron fast flux levels ($E > 0.1$ MeV) in the removable beryllium region vary from 0.2×10^{15} to 0.5×10^{15} n/cm²-s. The calculated gamma-heating rate in Al at the reactor midplane is about 15 W/g. The large RB* facilities have been used for fully instrumented experiments for the Fusion Materials Program.

The HFIR has been used extensively for materials irradiation testing for a number of the DOE-sponsored programs, including the Fusion Materials Program, GenIV Materials Program, Naval Reactor Programs, and the ITER Project, etc. The materials tested included austenitic stainless steels, ferritic/martensitic steels, and vanadium alloys. A variety of specimen types have been irradiated including sheet type tensile specimens, thermal diffusivity, compact disc fracture toughness, bend bars, pressurized creep tubes and TEM specimens, etc. The unique capability of uninstrumented rabbit capsules has provided an invaluable tool to perform irradiation in a fast, economic and effective way, and has made significant contributions to the knowledge base of irradiated materials. Past experience has proven the HFIR to be a highly valuable materials experiment facility.

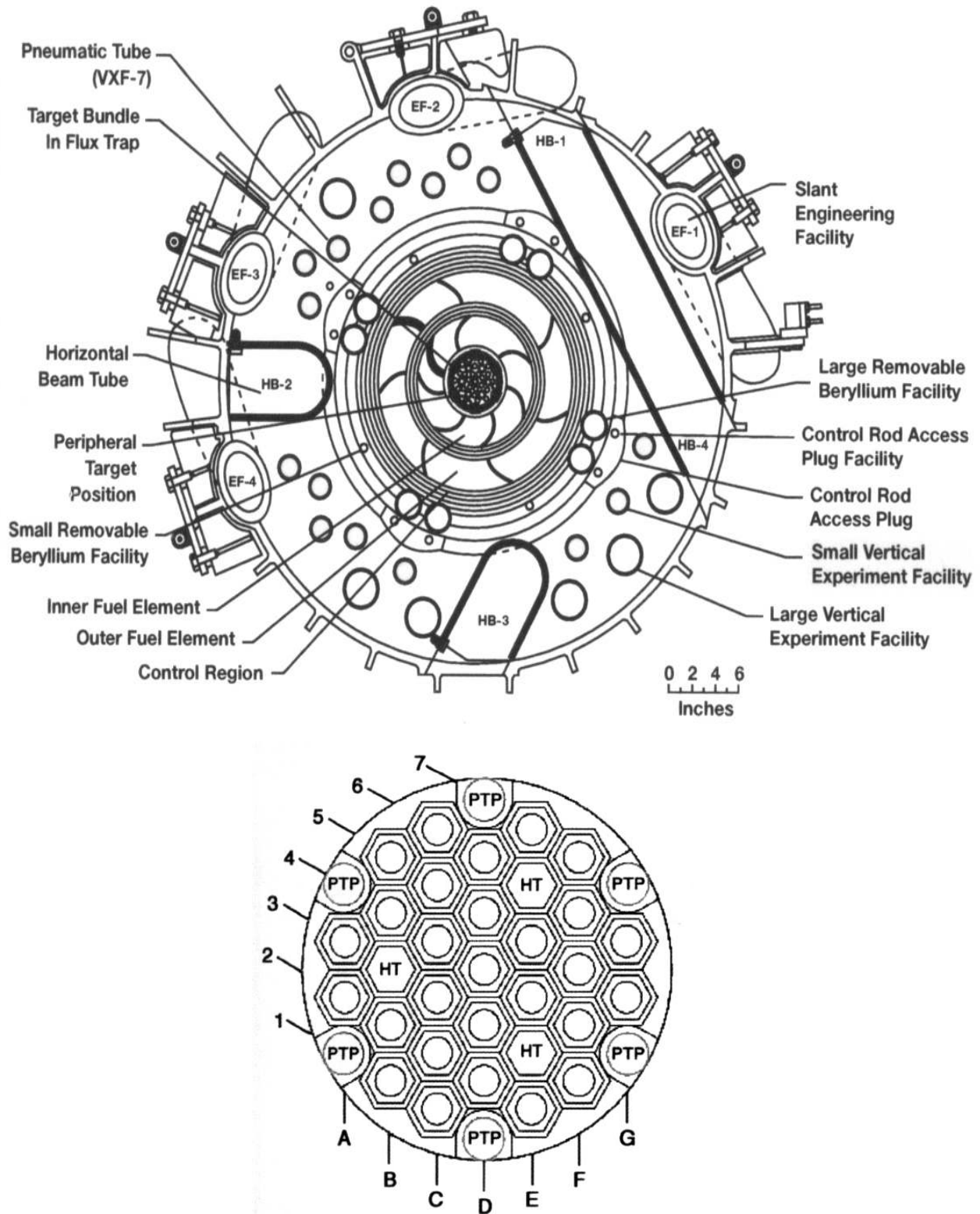


Figure 7.1. Overview of the materials irradiation facilities at the HFIR. (HT - hydraulic tube; PPT - peripheral target positions).

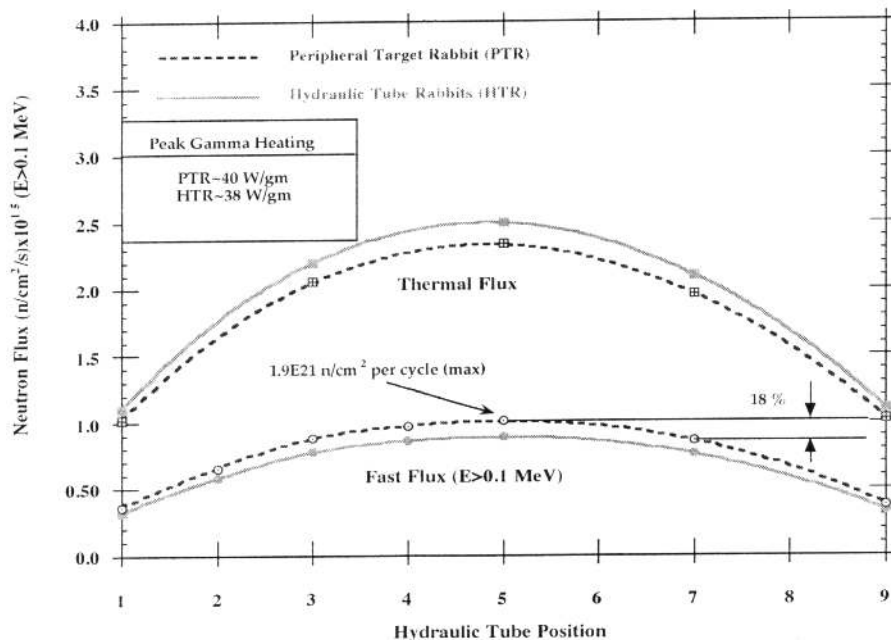


Figure 7.2. Axial variation in neutron flux for the HFIR at full-power (85 MW) operation.

Advanced Test Reactor (ATR)

The Advanced Test Reactor (ATR) is located at the Idaho National Laboratory and has been operating continuously since 1967. The ATR served primarily the U.S. Navy in the development and refinement of nuclear propulsion systems. There has been increased use of the ATR for government- and privately-sponsored research. In April 2007, the DOE designated the ATR as a National Scientific User Facility (NSFU) for nuclear fuels and materials research. The information about the ATR presented below can be found in the reference (FY2009 Advanced Test Reactor National Scientific User Facility Users' Guide, INL/EXT-08-14709).

The ATR is a thermal reactor cooled by pressurized (360 psig) water with an inlet temperature of 52°C and an outlet temperature of 71°C and with the maximum power of 250 MW. The ATR typically operates at much lower power levels. Table 7.1 summarizes the key operating parameters in the ATR.

A full cycle of the ATR ranges from 6 to 8 weeks. The outage between cycles is about one to two weeks. Neutron flux in the ATR varies from 2.5×10^{11} n/cm²-s (thermal) and 3.5×10^9 n/cm²-s (fast) in the outer tank position to 4.4×10^{14} n/cm²-s (thermal) and 2.2×10^{14} n/cm²-s (fast) in the flux trap. The axial distribution of neutron flux in the ATR center flux trap for the total reactor power of 125 MW is shown in Figure 7.3.

The ATR reactor core provides nine high-intensity neutron flux traps and 68 additional irradiation positions inside the reactor core reflector tank. Thirty-four additional low-flux irradiation positions are in two capsule irradiation tanks outside the core. Figure 7.5 illustrates the available irradiation test positions. The physical dimensions of the available test positions range from 0.659 to 5.00 in diameter. The ATR has capability to conduct both instrumented and passive irradiation experiments. It also has the Hydraulic Shuttle Irradiation System (HSIS), enabling test samples to be inserted and removed from the ATR during the reactor cycle, for test durations as short as a few hours.

Table 7.1. Key operating parameters at the ATR.

Reactor:	
Thermal power	250 MW _{th} ^a
Power density	1.0 MW/L
Maximum thermal neutron flux	1.0×10^{15} n/cm ² -sec ^b
Maximum fast flux	5.0×10^{14} n/cm ² -sec ^b
Number of flux traps	9
Number of experiment positions	68 ^c
Core:	
Number of fuel assemblies	40
Active length of assemblies	4 feet
Number of fuel plates per assembly	19
Uranium-235 content of an assembly	1,075 g
Total core load	43 kg ^d
Coolant:	
Design pressure	2.7 Mpa (390 psig)
Design temperature	115°C (240°F)
Reactor Coolant:	
Light water maximum coolant flow rate	3.09 m ³ /s (49,000 gpm)
Coolant temperature (operating)	<52°C (125°F) inlet, 71°C (160°F) outlet

a. Maximum design power. ATR is seldom operated above 110 MW_{th}
 b. Parameters are based on the full 250 MW_{th} power level and will be proportionally reduced for lower reactor power levels.
 c. Only 66 of these are available for irradiations.
 d. Total U-235 always less due to burn-up.

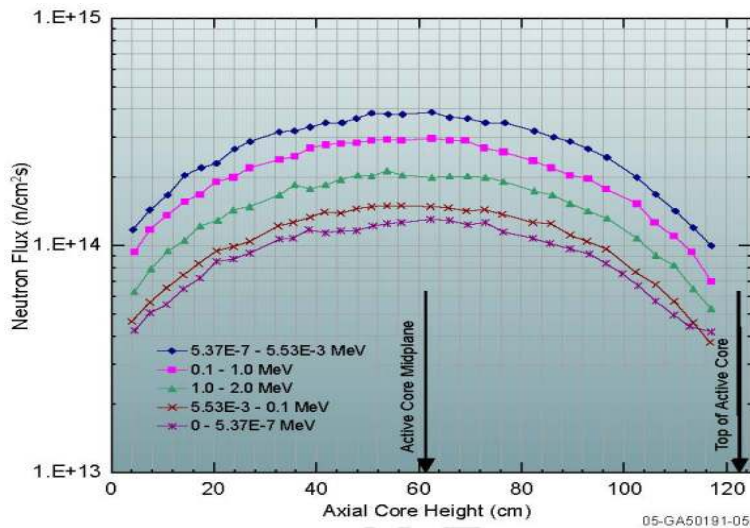


Figure 7.3. Axial distribution of neutron flux in the ATR center flux trap for total reactor power of 125 MW.

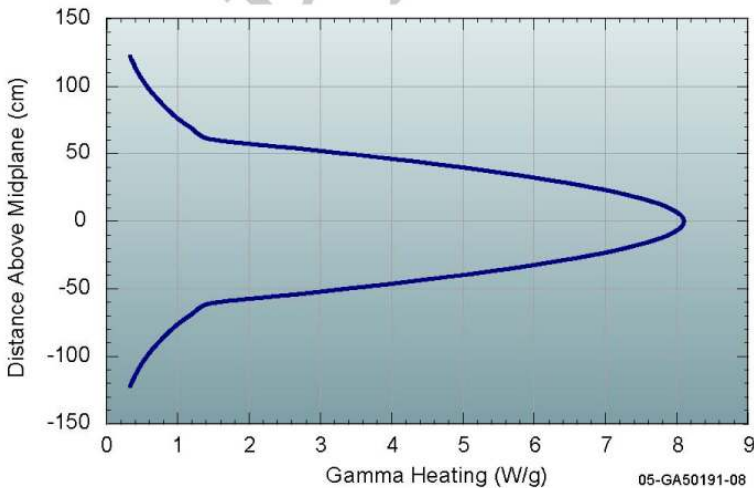


Figure 7.4. Typical gamma heating profile in the core with the reactor operating at 125 MW.

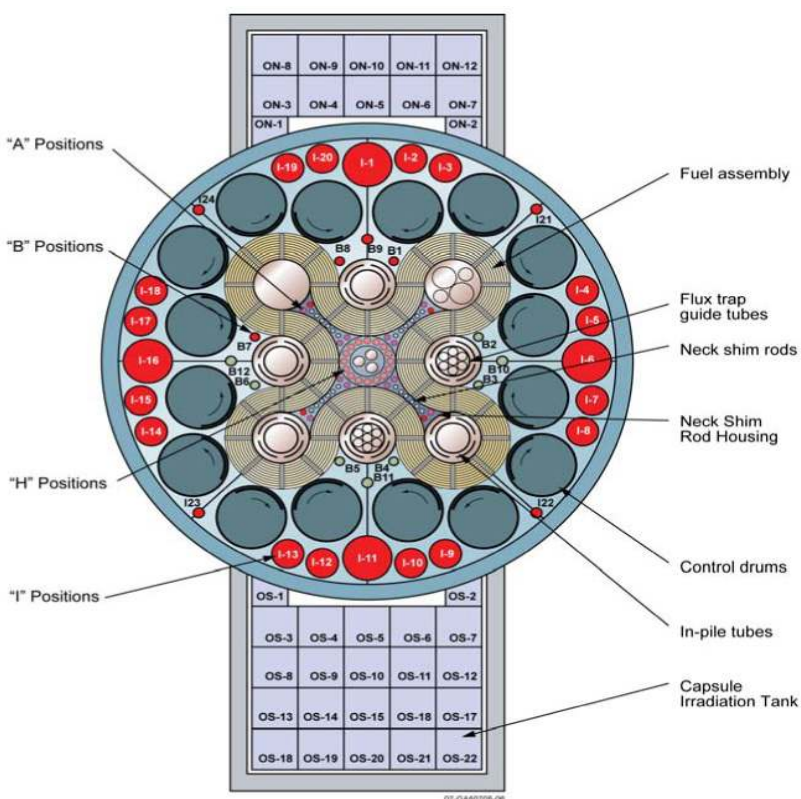


Figure 7.5. Irradiation positions at the ATR.

7.1.2 International Irradiation Facilities

Experimental FBR JOYO

JOYO is Japan’s first fast breeder reactor, located at Japan Atomic Energy Agency’s Oarai Research and Development Center. JOYO has played a significant role in advancement of fast reactor technology through its operation and experiment. It has also been used as an irradiation facility for the development of fuel and materials for fast reactors. The information about the JOYO reactor presented below is mainly taken from the reference (http://www.jaea.go.jp/04/o-arai/joyo_users_guide/index.html).

JOYO is a sodium-cooled experimental fast reactor fueled by uranium-plutonium mixed oxide (MOX). It achieved its first criticality on April 24, 1977, and started operation in 1979 with a reactor output of 50 MW, and later raised to 75 MW. The original core was replaced by a new core (MK-II core) with thermal power of 100MW in 1983 to allow for irradiation tests of fuel and materials. Joyo has been providing external users with opportunities for fast neutron irradiation since 1984. Upgrade of irradiation test capability was performed with the thermal power increase to 140 MW in the MK-III core to provide more irradiation spaces and an increase in fast neutron flux. The MK-III core has been operating since July, 2003. The key operating parameters of JOYO are summarized in Table 7.2.

The configuration of the JOYO core is shown in Figure 7.6. The radial distribution of fast neutron flux in the core is shown in Figure 7.7. As the position moves away from the core, the fraction of fast-energy neutron and the neutron flux level decrease. Relatively flat neutron energy distribution is available at the upper-core structure and the ex-vessel irradiation hole, which are apart from the core in the axial and radial directions, respectively (see Figure 7.8). The axial distributions of fast neutron flux at

the core center as well as of temperatures of coolant and sample inside the irradiation rig are shown in Figure 7.9. The maximum temperature in material irradiation at Joyo is approximately 750°C.

Table 7.2. Key operating parameters in JOYO

Reactor power	140 MWt
Maximum fast neutron flux ($E \geq 0.1\text{MeV}$)	$4.0 \times 10^{19} \text{ n} \cdot \text{m}^{-2} \cdot \text{s}^{-1}$
Primary coolant flow rate	2700 t /h
Coolant temperature (Inlet/Outlet)	350°C/500°C
Core height	500mm
Number of fuel subassemblies	85 in maximum
Reflector/Shielding subassembly	Stainless steel/B ₄ C
Installable number of irradiation rigs	21 in maximum
Pitch between subassemblies	81.5mm
Length of the rated power operation cycle	60 days/cycle in maximum

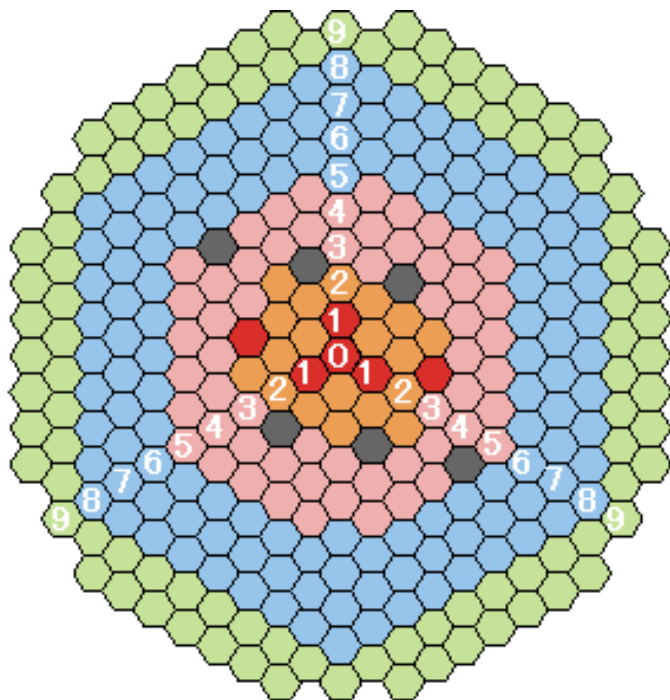


Figure 7.6. Configuration of JOYO MK-III core.

- Inner core fuel subassembly
- Control rod
- Outer core fuel subassembly
- Reflector
- Irradiation rig
- Shielding subassembly (B₄C)
- 1 Solid-white numbers represent the number of rows where subassemblies are installed.

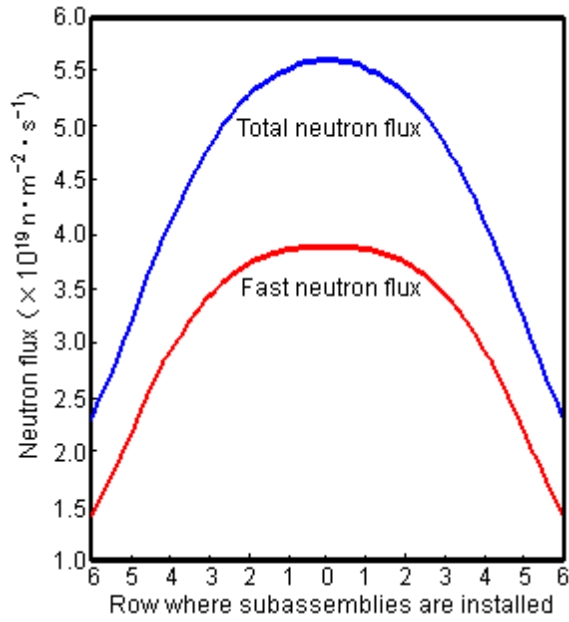


Figure 7.7. Radial distribution of fast neutron flux in the JOYO core.

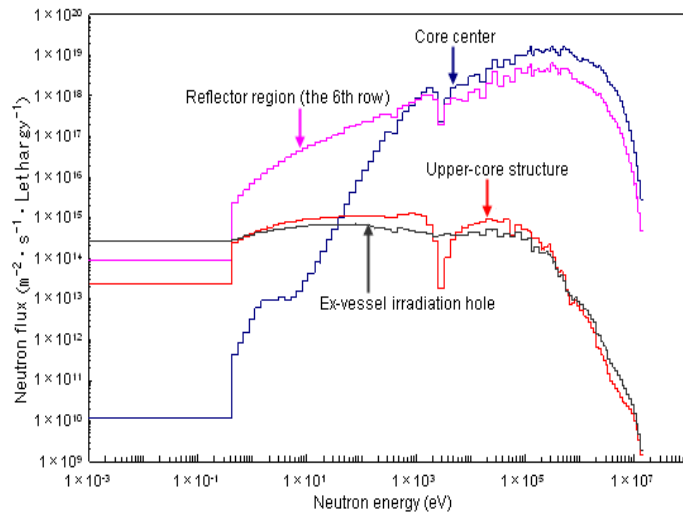


Figure 7.8. Neutron spectra at various positions in JOYO.

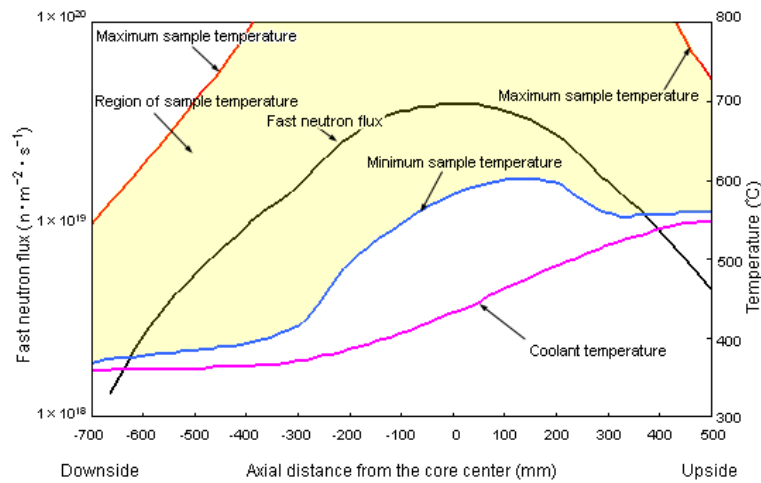


Figure 7.9. Axial distribution of neutron flux and temperature at the core center.

Two types of irradiation rigs are available in Joyo, i.e. offline irradiation rigs that need offline monitors to measure irradiation data, and online irradiation rigs, which allow online data measurement and/or temperature control. The offline irradiation rigs can be installed at any location in the core, while the locations for the online irradiation rigs are limited. Various types of irradiation rigs allowed in JOYO are shown in Figure 7.10. Typical offline/online irradiation rigs are described below.

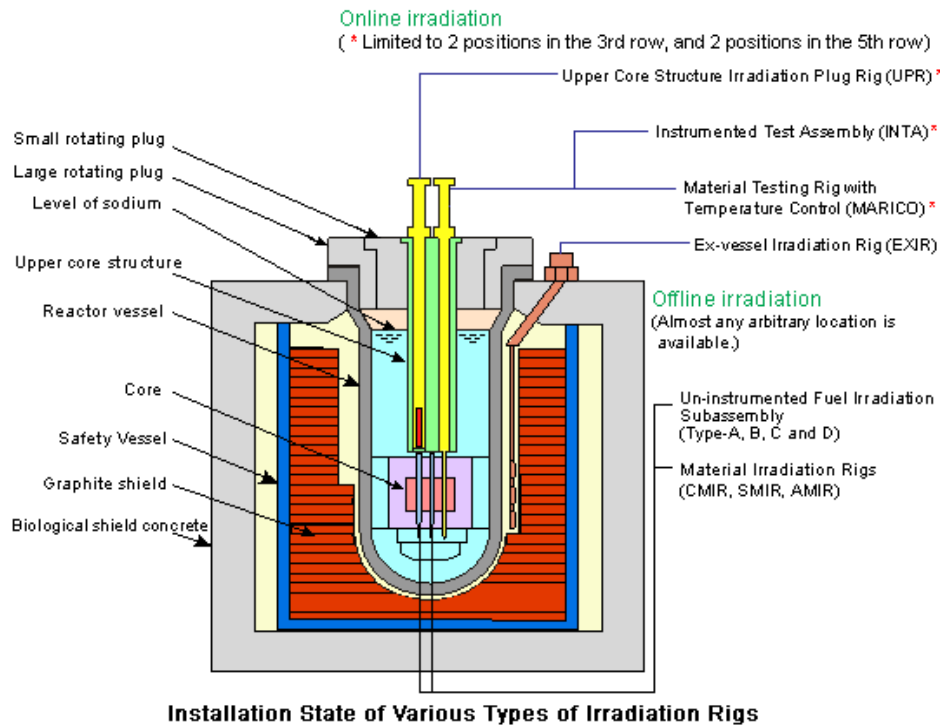


Figure 7.10. Various types of irradiation rigs at JOYO.

Materials Irradiation Rig (offline):

The material irradiation rigs are intended for use in obtaining data concerning the behavior of materials under fast neutron irradiation. They can be loaded in either the fuel or reflector regions. Samples are loaded in a holder or an irradiation capsule that is installed into any of six compartments. In addition, the irradiation capsule can be installed in the shaft center tube. A structural material irradiation rig is shown in Figure 7.11. An offline irradiation rig (shuttle-type irradiation rigs) can be disassembled after irradiation to remove the irradiated capsules, and reassembled after installing a new irradiation capsule for further irradiation.

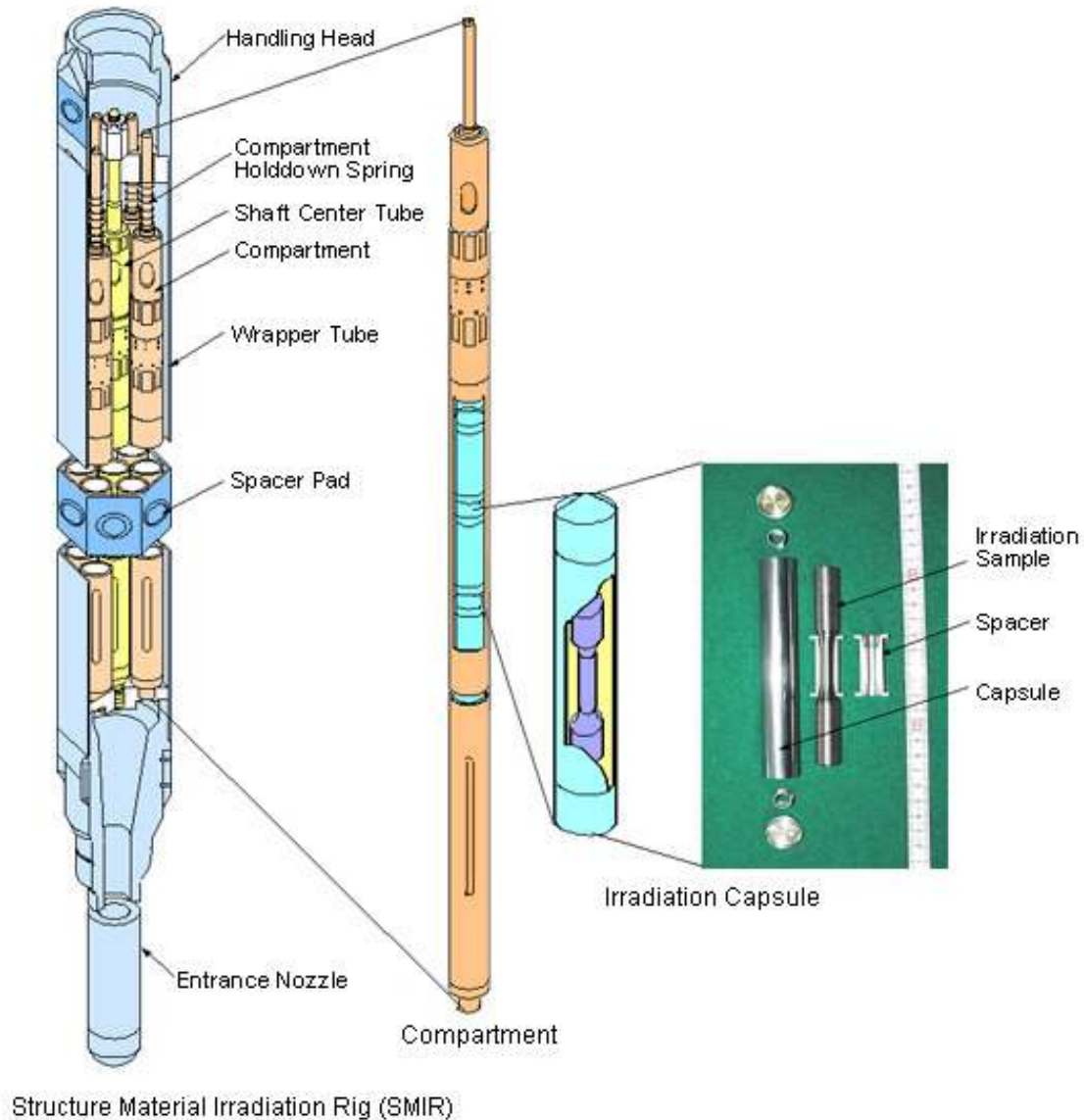
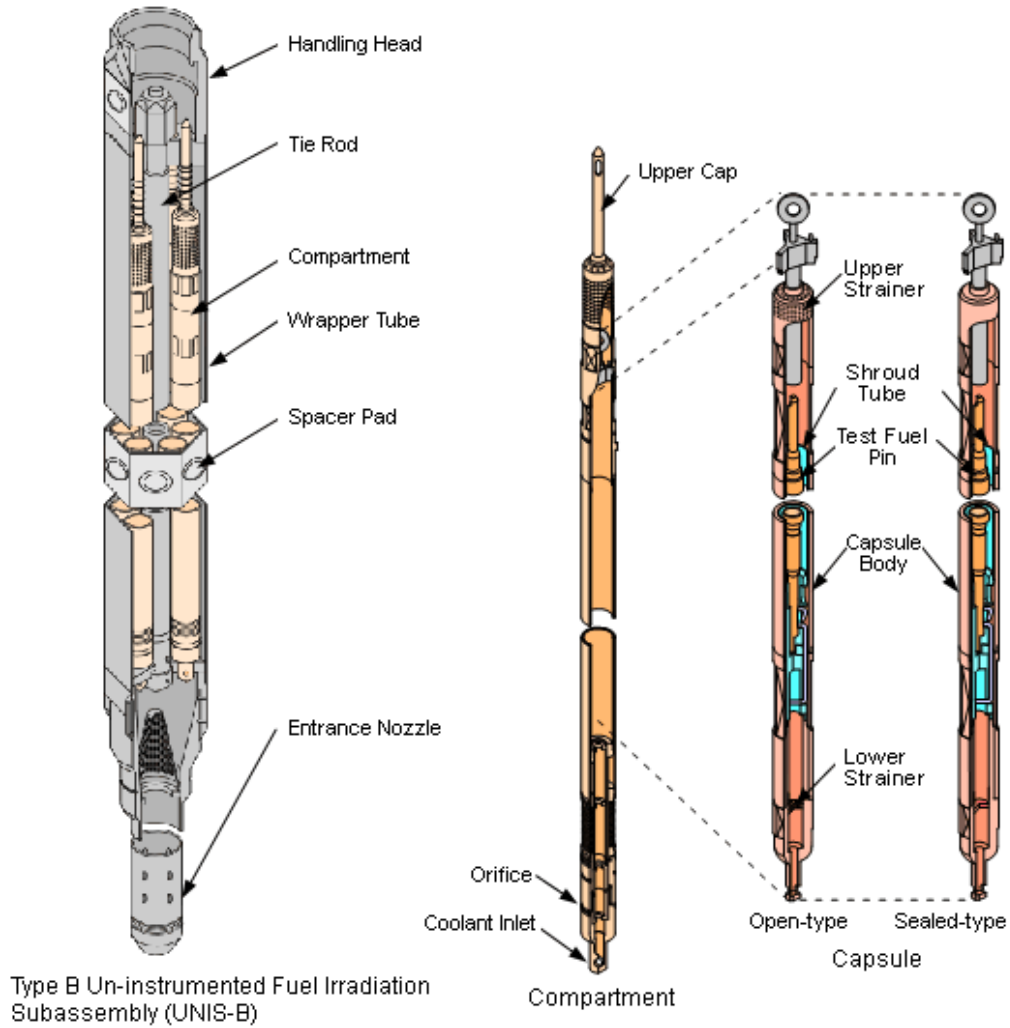


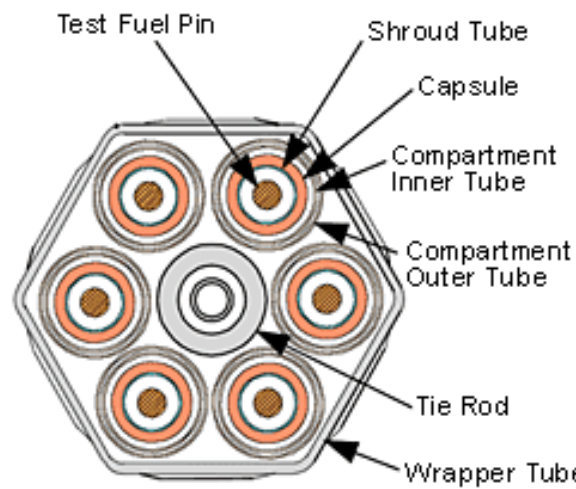
Figure 7.11. A structural material irradiation rig at JOYO.

Un-instrumented Fuel Irradiation Subassemblies (Offline):

The Un-instrumented Fuel Irradiation Subassembly (UNIS, Figure 7.12) is an irradiation rig for irradiating test fuel pins, and grouped into four types (type A, B, C and D) according to test purpose. The type-B UNIS (UNIS-B) is used primarily for successive irradiation testing of test fuel pins. It is possible to perform an interim inspection during the irradiation, evaluate the integrity of a selected sample fuel pin, and then reassemble the UNIS-B and reinstall it into the core. A parametric irradiation test can be performed using one UNIS-B by setting irradiation condition independently for each of the 6 compartments.



Type B Un-instrumented Fuel Irradiation Subassembly (UNIS-B)



Horizontal Cross Section of UNIS-B

Figure 7.12. Uninstrumented Fuel Irradiation Subassembly.

Upper Core Structure Irradiation Plug Rig (Online)

The Upper Core Structure Irradiation Plug Rig (UPR) (Figure 7.13) is used for irradiation testing of structure materials, including those of the reactor vessel, by installation at the upper-core structure of Joyo, and allows for the measuring of sample temperature during irradiation. Irradiation temperature can be controlled at desired temperatures above 500°C by applying an electric heater.

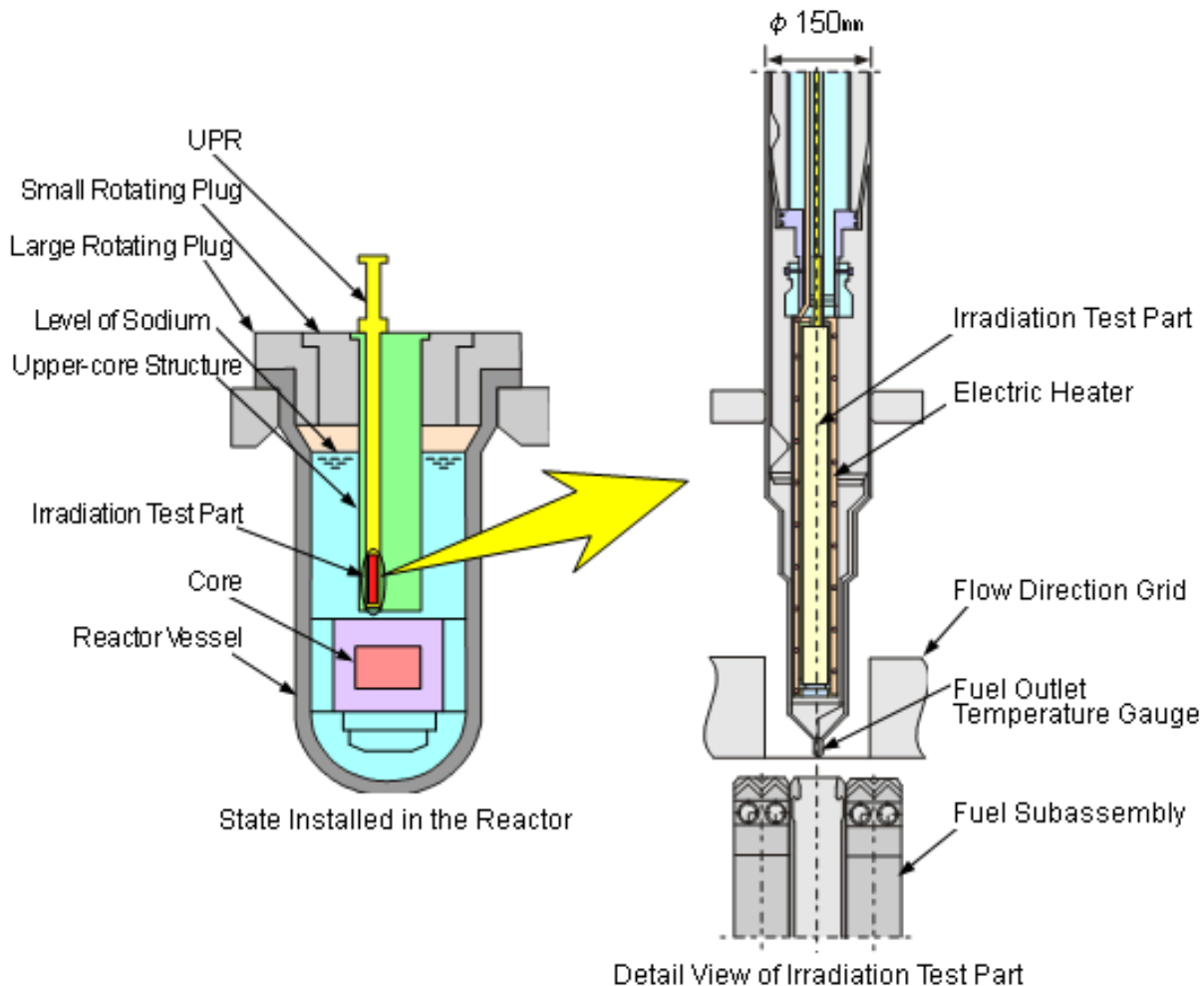


Figure 7.13. Upper Core Structure Irradiation Plug Rig (UPR)

Material Testing Rig with Temperature Control (Online)

The Material Testing Rig with Temperature Control (MARICO) (Figure 7.14) is an instrumented irradiation rig that allows for the irradiation of material under a controlled temperature. Temperature is controlled by adjusting the gas composition of a mixture of argon and helium. An electric heater can be installed to maintain the sample temperature at a constant independent of the reactor power.

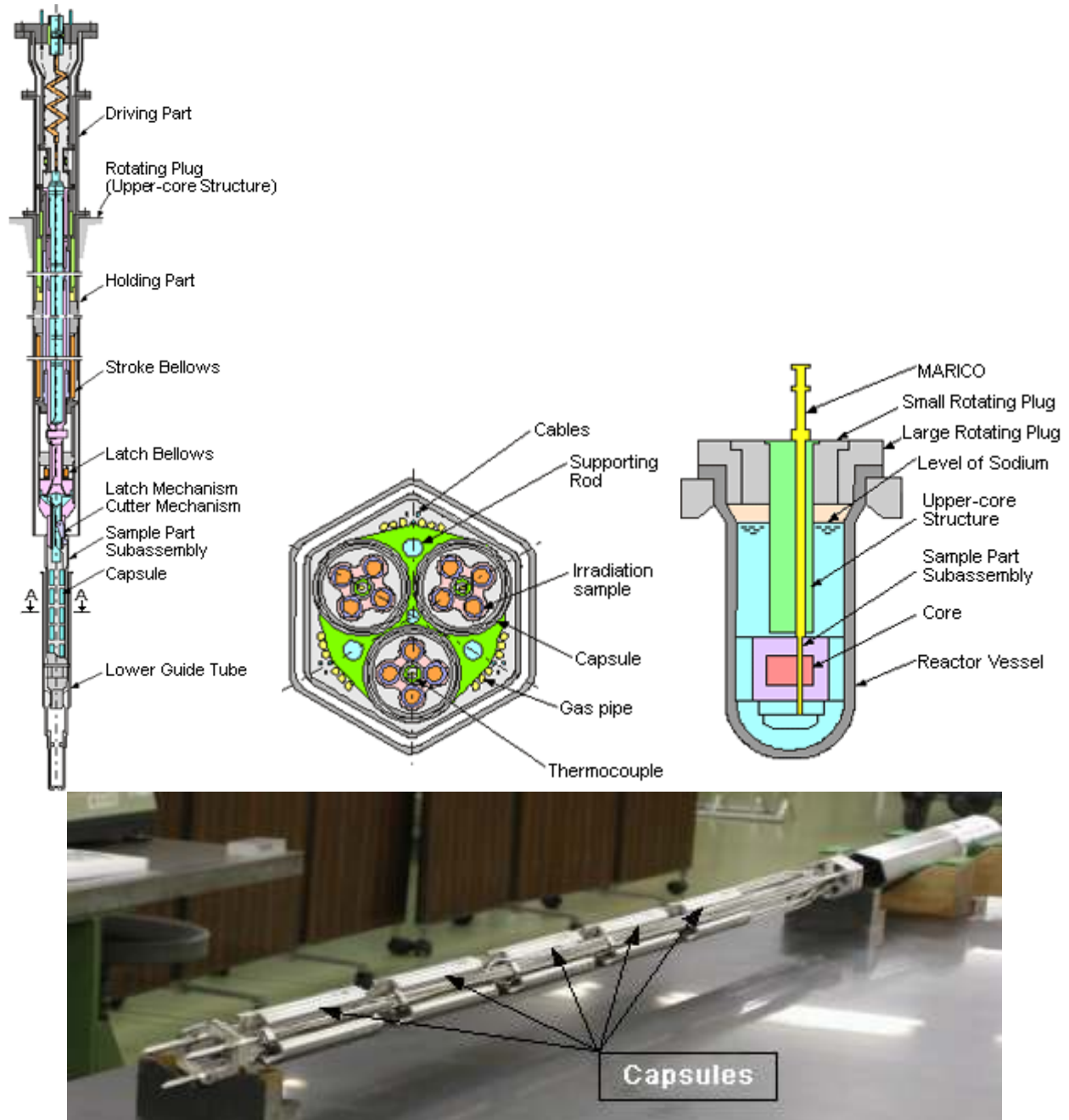


Figure 7.14. Material Testing Rig with Temperature Control (MARICO)

Ex-vessel Irradiation Rig (Online)

The Ex-vessel Irradiation Rig (EXIR) (Figure 7.15) is an instrumented irradiation rig for irradiation tests of reactor structural materials by utilizing the space between the reactor and safety vessels. In-situ loading can be realized by online pressurized gas, and temperatures can be maintained at 200 °C or above by electric heater.

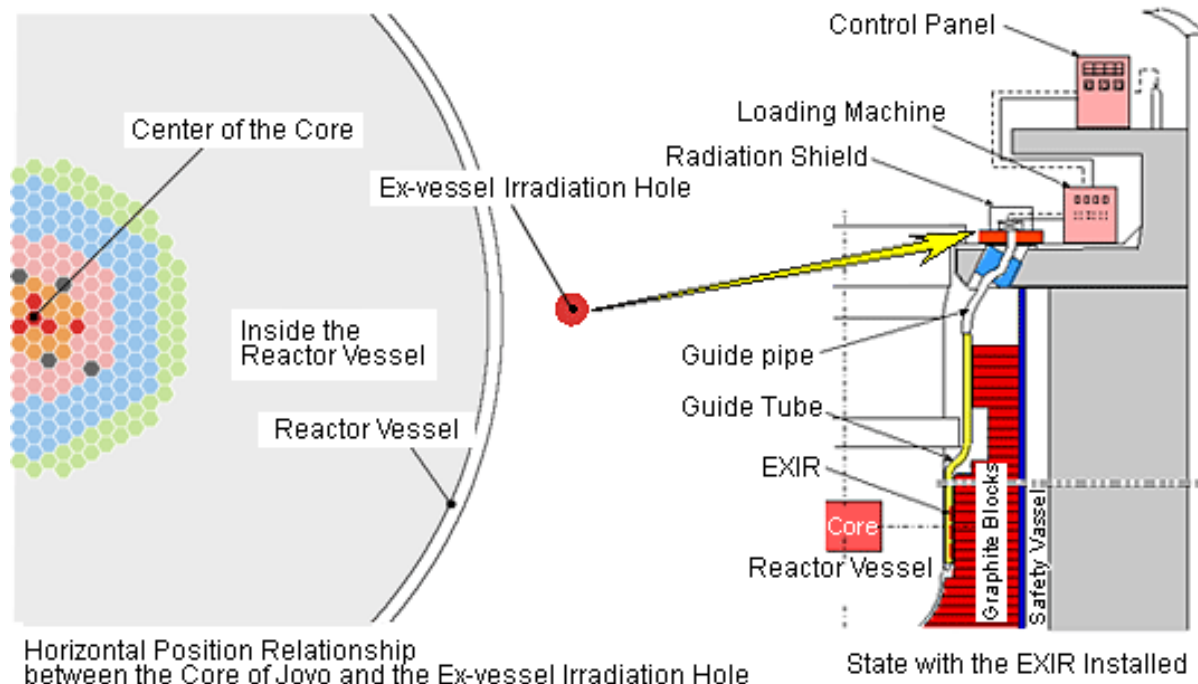


Figure 7.15. Online Ex-vessel Irradiation Rig.

In addition, related Post Irradiation Examination (PIE) facilities are located adjacent to Joyo, where various types of test equipment is installed in hot cells in order to accommodate the needs of various types of PIEs concerning fuel and material. Accordingly, a system that can perform a series of activities from irradiation to PIE and accommodate with a wide range of use patterns is provided.

Post Irradiation Examination Facilities

The PIE Facilities, including the Fuel Monitoring Facility (FMF), the Alpha-Gamma Facility (AGF) and the Material Monitoring Facility (MMF), are located adjacent to JOYO. Various types of PIEs include the estimation of Fission Product (FP) release behavior, metallography, mechanical properties and microstructural analysis of materials, as well as various tests and inspections of fuels and materials that are irradiated at Joyo. It is also possible to manufacture a fuel pin containing minor actinides at AGF, install it into a UNIS, and then irradiate it at Joyo. Successive irradiation by reinstalling a material sample that has undergone interim inspection into an irradiation rig is also possible.

Phenix Fast Breeder Reactor

Phenix is a prototype fast breeder reactor with a power capacity of 255 Mwe, located in the Marcoule nuclear site in France. It started commercial operation in 1974. The initial objective of Phenix reactor was to demonstrate fast breeder reactor technology. From 1992, the role of Phenix as an irradiation facility has been emphasized, particularly in support of the CEA R&D program on long-lived radioactive waste management. This program was further strengthened in 1998 to compensate for the shutdown of Super-Phenix. Since 1993, the reactor power has been limited to 350 MW(th) [145 MW(e)] on two secondary loop operations. A major renovation program was carried out in the plant from 1994 to 2003, involving safety upgrading, component inspections and repairs, and the 10-yr statutory maintenance. An extensive plant requalification program was carried out following the renovation work, and the plant resumed power operation in June 2003. As of 2004, its main use was investigation of

transmutation of nuclear waste, although it does also continue to generate electric power. Phénix is expected shutdown is July 2014. The U.S. DOE signed an agreement with France's Atomic Energy Commission (CEA) in 2004 to allow cooperation between the Department of Energy's (DOE) Office of Nuclear Energy, Science and Technology and the French Atomic Energy Commission. The agreement provides the DOE access to the PHENIX reactor.

BOR-60 Experimental Fast Reactor

Experimental fast reactor BOR-60 is a unique many-purpose facility. It is used for fuel, absorber, and structural material tests, isotopes production, tests of fast reactor components such as steam generators and sodium pumps, and also for heat and electricity production. BOR-60 is a sodium-cooled fast reactor with a thermal power of 60 MW. It has been in operation since 1969, an operation license until December 31, 2009. The replacement by the new sodium-cooled BOR-60M reactor is planned. The key operating parameters in BOR-60 are given in Table 7.3.

Table 7.3. Key operating parameters in BOR-60.

Reactor capacity	
thermal	60 MW
electrical	10 MW
Maximum neutron flux density	$3,7 \cdot 10^{15} \text{ sm}^{-2}\text{s}^{-1}$
Maximum specific power	1100 kW/l
Non-uniformity factor of heat rating	1,15
Average neutron flux density	0,45 MeV
Fuel	UO ₂ - PuO ₂
²³⁵ U enrichment	45 - 90 %
Fuel burn up rate	up to 6% per year
Neutron fluence per year	$5 \cdot 10^{22} \text{ sm}^{-2}$
Damage dose rate	up to 25 dpa /year
upper reflector	100mm
core	450mm
lower reflector	150mm
lower gas volume	300 mm
Coolant	sodium
Coolant temperature:	
at inlet in reactor	up to 330°C
at outlet of reactor	up to 530 °C
Microcompaign duration	up to 120 days
Reactor generates energy	≈265 days per year

BOR-60 has capability of “experimental cell” where the instrumented fuel or radiation material assemblies can be installed to obtain needed information during irradiation. Materials can be irradiated in a number of reactor cells and in 9 vertical dry channels placed outside the reactor vessel with diameter up to 270 mm and length of 700 mm. A variety of fuel types has been tested including oxides, metal, carbides and nitrides. A record high burnup level of about 35 at% has been successfully reached with an experimental MOX subassembly in BOR-60 while a lot of standard fuel pins have attained burnt levels of 25–30 at%. Structural materials tested at BOR-60 include structural reactor materials, electroinsulation, magnetic and hard melting materials for fusion reactors at temperature from 330 to 1000°C and damage dose up to 200 dpa. Experimental equipment and diagnostic and safety systems have also been tested in the first and the second sodium circuits of the facility. Five different type once-through steam generators including those for BN-600 and BN-350 were tested at the BOR-60 plant. Other testing include investigation and testing of liquid metal technology such as impurities and radionuclides trapping for coolant cleaning and personal dose rate decreasing, impurities control and investigation on transmutation and incineration of long-lived radionuclides from different reactor spent fuel.

7.2 Radiological Materials Test Facilities

Radiological materials test facilities are primarily located in the DOE national laboratories. The following section covers only those facilities that are being actively utilized.

7.2.1 Facility at Argonne National Laboratory

Irradiated Materials Laboratory (IML)

The IML at ANL’s Nuclear Engineering Division is used to conduct research on the behavior of nuclear reactor fuels and structural materials. The facility has also provided information for the development and testing of advanced alloy materials for the Department of Energy fusion program and the NRC light water reactor program. The laboratory is equipped for handling, testing, and analyzing irradiated materials. It consists of four air-atmosphere, centicurie beta/gamma hot cells. Each cell is equipped with movable doors that allow the cell equipment to be easily installed, removed, and reconfigured to support the mission of the cell. Testing capabilities include servo-hydraulic-driven tension/compression/cyclic testing machine tensile and creep-rupture testing, slow-strain-rate tensile testing (SSRT) up to 320°C in a controlled water environment, fracture toughness testing up to 320°C in a controlled water environment, and instrumented Charpy impact testing (drop-weight system) to -190°C. Sample preparation capabilities include a remotely operated electric discharge machine (EDM) for remote machining of precise test specimens from irradiated materials.

Electron Microscopy Laboratory for Irradiated Materials

The Electron Microscopy Laboratory for Irradiated Materials is dedicated to materials characterization using optical and electron microscopy. The laboratory is equipped with a shielded scanning electron microscope and a shield transmission electron microscope. Specimen preparation capability of irradiated materials includes jet polishing for preparation of TEM specimens, shielded glove boxes for preparing metallographic specimens and gold coater for preparing nonconductive specimens for electron beam analysis.

7.2.2 Facility at Idaho National Laboratory

Hot Fuel Examination Facility (HFEF)

The HFEF is located at the INL Materials and Fuels Complex. It is a large, heavily shielded, alpha-gamma hot cell facility designed for remote examination of highly irradiated fuel and structural materials. Its capabilities include nondestructive (dimensional measurements and neutron radiography) and destructive examination (such as mechanical testing or metallographic/ceramographic characterization). It can accept full-size light water reactor fuel assemblies.

The HFEF is comprised of two adjacent large, shielded hot cells in a three-story building, as well as a shielded metallographic loading box, an unshielded hot repair area and a waste characterization area. The main cell (argon atmosphere) has 15 workstations, each with a viewing window and a pair of remote manipulators. A decontamination cell (air atmosphere) has six similarly equipped workstations. The cells are equipped with overhead cranes and overhead electromechanical manipulators. Cell exhaust passes through two stages of HEPA filtration. The facility is linked to analytical laboratories and other facilities by pneumatic sample transfer lines. Each main cell work station has removable electrical and lighting feed-throughs that can be changed to accommodate the mission of the station. The main cell is equipped with two rapid insertion ports for quick transfer of small tools and items into the cell. The decontamination cell contains a spray chamber for decontaminating equipment and non-fissile material using a manipulator-held wand. Material handling takes place via a 750-lb electro-mechanical manipulator, a 5-ton crane and six sets of master-slave manipulators.

HFEF also has a 250 kW Training Research Isotope General Atomics reactor, for neutron radiography irradiation to examine internal features of fuel elements and assemblies.

Electron Microcopy Laboratory (EML)

The EML is a user facility dedicated to materials characterization using electron and optical microscopy. EML is a radiological materials area, permitting work to be performed with both radioactive and non-radioactive materials. A portion of the laboratory is dedicated to sample preparation, providing the researcher with facilities support, equipment, safety systems, and procedures to prepare samples of diverse materials for analysis. The three primary instruments in EML are a JEOL 2010 scanning transmission electron microscope (TEM), a JEOL JSM-7000f scanning electron microscope (SEM), and a Zeiss DSM 960a SEM.

7.2.3 Facility at Oak Ridge National Laboratory

Irradiated Materials Examination and Testing (IMET) Facility

The IMET hot cell facility is a Class III nuclear facility. These hot cells are the primary mechanical testing and examination facility for highly irradiated structural alloys and ceramics. The IMET facility is utilized by a number of programs, including DOE Office of Science (fusion energy sciences, HFIR surveillance program, SNS surveillance program), DOE Office of Nuclear Energy, Science and Technology, the Nuclear Regulatory Commission Heavy Section Steel Initiative, and NNSA Naval Reactors advanced materials programs. The six interconnected (shielded drawers/doors) steel-lined hot cells contain 320 square feet of work space and are maintained as a low alpha contamination facility (<70 dpm per 100 cm²) to facilitate transfer of specimens to other radiological laboratories after testing or sorting. An additional 600 square feet of work space for test equipment control systems and R&D staff work stations is located in a contamination-free area in front of the hot cells. The cells offer easy access

for equipment installation and maintenance via removable roof plates for large equipment and doors at the rear of the cells for smaller equipment and personnel entry. A bottom-loading carrier is used to transfer large quantities of radiological specimens into the cells via removable roof ports.

The hot cells are connected to the ORNL low-level liquid waste system. All of the cells are equipped with Level 8 (or better) manipulators. Video cameras and/or Kollmorgen wall periscopes are located in most of the cells to assist in visual identification of specimens and for equipment trouble shooting. The building exhaust is connected to a HEPA filtered ventilation system. Plant air, process water, liquid nitrogen, inert gas, and electrical power are available in all cells. Internet connections are used to transfer data from the equipment to internal and external users. The IMET facility also contains 60 storage wells capable of storing seven cans ($\approx 0.2 \text{ ft}^3$) in each well. A 5-ton capacity overhead crane is used for transferring the carrier between cell roof ports and the storage area. A second overhead crane (1-ton capacity) is available in Cell 6 for handling equipment and large pressure vessel sections. The building has a convenient loading area for receiving and shipping carriers. A radiological specimen preparation area is located adjacent to the hot cells, consisting of three shielded glove boxes and a chemical hood with HEPA ventilation and connections to the ORNL low-level liquid waste system. This specimen preparation facility is used for preparation of transmission electron microscopy specimens and other specialized activities. The most commonly conducted work includes mechanical testing including tensile tests, biaxial creep tests, fatigue tests, Charpy impact tests and fracture toughness tests, optical and scanning electron microscopy, densitometry, thermal and electrical conductivity.

Irradiated Fuels Examination Laboratory (IFEL)

The IFEL is a comprehensive facility for post-irradiation examination of nuclear fuels, including equipment for machining. Equipment is available for capsule gamma scanning, remote capsule disassembly, component metrology, metallography, ceramography, SEM/Microprobe examination, and radiochemistry.

Low Activation Materials Design and Analysis (LAMDA) Lab

The LAMDA facility is complementary to the hot cells facilities and allows for examination of low-activation materials without the need for remote manipulation. The LAMDA facilities include equipment for mechanical property testing as well as for chemical, electrical, and thermal property evaluations. Special facilities such as a clean room fitted with HEPA filtration and climate control for work with ceramics and composites. Additional equipment includes dedicated fume hoods for specimen cutting and grinding, equipment for cutting TEM disks, a Tenupol unit for thinning TEM disks to electron transparency, equipment for thinning of atom probe needles, and a resistivity system for determining the irradiation temperature of silicon carbide thermometers used in rabbit capsules of HFIR.

7.3 Sodium Facility for Materials Testing

Sodium as a heat transfer fluid in advanced reactors has significant influence on materials' performance, structural integrity and system design. Design data of sodium compatibility and mechanical properties in sodium environment are critical for reactor design, licensing and construction. Facilities for materials testing in sodium are required for evaluation of compatibility and mechanical properties of structural materials. A large number of sodium facilities were built in the U.S. during 1970s-80s for the development of fast breeder reactor technology. Due to the termination of the DOE Advanced Liquid Metal Reactor project, the sodium facilities have been severely degraded in recent years. Currently, very limited sodium facilities are operational in the U.S. Efforts to rebuild the sodium capability are underway in support of the developments of sodium technology for the AFCI ARR. The recent rewarded

DOE/AFCI project, “Sodium Compatibility of Advanced Reactor Materials” will initiate construction of thermal-gradient driven flowing loops and pumped sodium loops to examine sodium compatibility effects. International collaboration that provides access to the sodium facilities abroad is also an important step forward for the development of sodium reactor technology.

Sodium plugging test loop (SPTL) at ANL

The sodium plugging test loop at ANL was designed to investigate the possible plugging of narrow flow channels due to the presence of impurities (e.g. oxides) in flowing sodium. This new facility consists of a main sodium loop including three test sections, a bypass sodium loop including a cold trap/economizer assembly, and an auxiliary system composed of argon cover gas and vacuum lines. The main loop and the bypass loop are constructed from 0.5 inch OD, 0.049 in thick Type 316 stainless steel tubing. Other major components include three EM flow controllers, two EM pumps, five EM flow meters and expansion and dump tanks. The sodium loop system is about 1.8 m tall and is heated by a number of ceramic band heaters. The test sections simulate narrow flow channels of Heatric Printed Circuit Heat Exchangers™ with three different channel sizes. Test section 1 has 9 semi-circle, 2-mm diameter flow channels, test section 2 has 4 semi-circle, 4 mm diameter flow channels, and test section 3 has 3 semi-circle, 6-mm diameter flow channels. The three test sections are installed in parallel in the main loop. An assembly drawing of the SPTL loop is shown in Figure 7.16 (Cho, D., et al., Interim Report on Sodium Plugging Test, April 30, 2008).

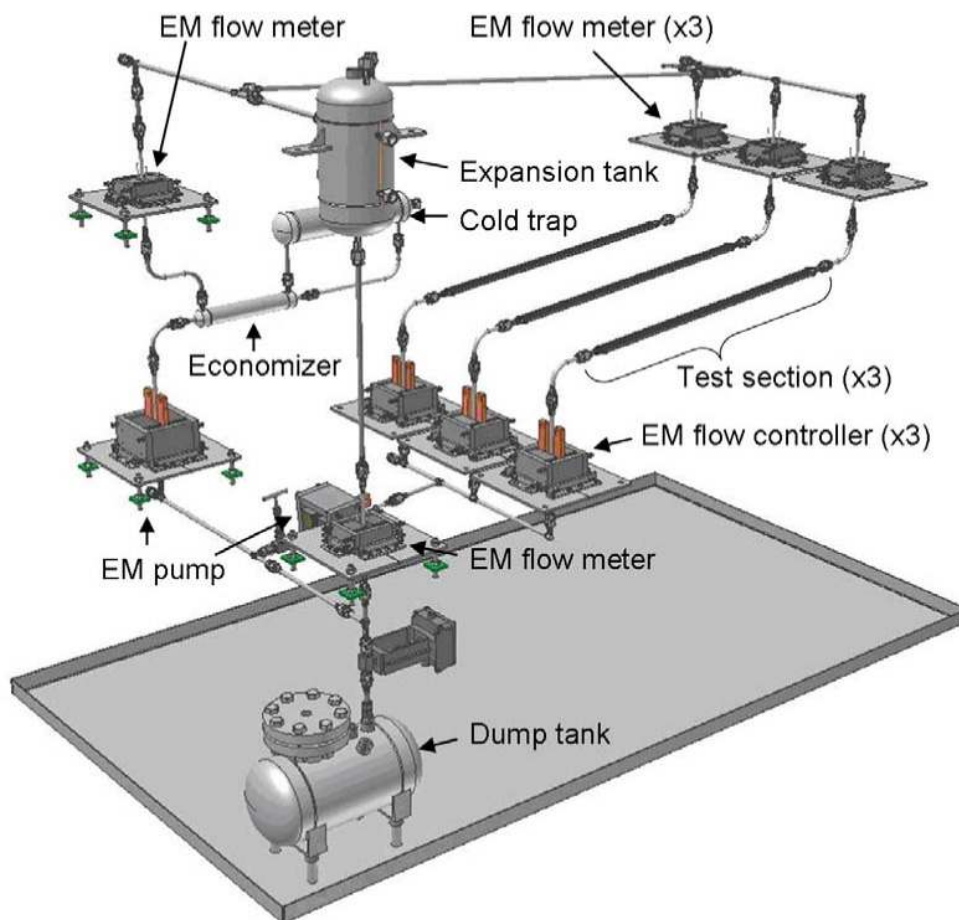


Figure 7.16. Assembly drawing of the SPTL loop at ANL.

Demonstration test runs have been conducted successfully with the test section temperatures up to 400-450°C. Though the loop was designed for materials testing, installation of a bypass section for materials study would be feasible and economical.

Components and Materials Evaluation Loop (CAMEL) at ANL

The closed sodium loop was used for isothermal testing of components, instrumentation, and materials as well as LMFBR core disruptive accident safety experiments. The loop had the design temperature of 540°C, 2.0 MPa (300 psi) maximum operating pressure, and 303 Liters (80 gallon) sodium inventory. It has 4-inch Schedule 40 stainless steel piping and optional tank-to-tank transfer of sodium driven by cover gas pressure differences with 14 liters/s (220 gallons per minute)/150 psi head EM pump. It can accommodate five vertical test sections up to 2.9 m (114 inches) in height.

The CAMEL loop has not been operated since 1986. Sodium is retained in a dump tank and cover gas has been maintained. Upgrades are required to make it operational.

Thermally Driven Sodium Loop at ORNL

A thermal driven sodium loop is proposed in the DOE AFCI awarded project "Sodium Compatibility of Advanced Reactor Materials". The loop will consist of a circuit with a hot leg and a cold leg operated at temperatures representative of the expected reactor system conditions utilizing high purity Na as a working fluid, with fluid flow driven by density gradient. The test system will be designed to accommodate additions of cold-traps and/or other system components as required and will be instrumented with thermocouples in wells protruding into the loop flow path as well as numerous external locations for precise monitoring. The loop will be primarily used for sodium compatibility studies of advanced structural materials for the ARR.

Sodium Pumped Loops at ANL and University of Wisconsin

The DOE AFCI awarded project also planned a series of sodium pumped loops to be built at ANL and University of Wisconsin. The pumped loops will make use of existing sodium handling capabilities at both locations. These loops would be constructed primarily from 1-inch pipe with bypass flows of 0.5 inch pipe for sodium clean up and flow control. The loop flow would be driven by an EM pump such that prototypic velocities could be achieved to mimic the conditions in a AFCI advanced reactor with sodium coolant. The facility would include a hot carbon filtration system and a cold trap to remove dissolved components. The hot leg test section would be placed on the left hand side of the loop and connect to the main loop with a series of grayloc fittings. This will allow an area change sufficient for the insertion of sample materials for testing on a ladder rack sample holder. The loop would also utilize EM or other flow meters to measure the velocity of the fluid. The test section will be designed capable of temperatures up to 650°C and heat can be removed on the right hand side with a series of copper cooling coils attached to the loop structure. A test section with a capability for material sample insertion could also be included on the cold side of the loop to study deposition of corrosion products, however the sodium will be continuously filtered through the carbon filter and cold trap.

International Collaboration

The Reactor Technology Working Group is pursuing joint research and development between the U.S. and Japan. The Material Test Facility in Sodium currently operating in Oarai Research and Development Center, Oarai, JAEA provides opportunities for international collaboration on key material

development areas. The facility was designed for studies of corrosion, tensile, creep, and fatigue behavior in sodium to evaluate high temperature strength of materials. Equipments include 2 fatigue test machines, 3 exposure pots, 5 creep test machines and 4 creep-fatigue test machines. Discussion of potential collaboration with other countries (e.g. France) is underway.

7.4 Creep-Fatigue Test Facility

Considering the critical needs of a large database on the creep-fatigue interaction issue in both conventional and advanced new alloys, the testing tasks are suggested to be executed in various national laboratories and research centers at universities to make full use of the existing capabilities and accelerate progress in the development and qualification of advanced materials.

7.4.1 Fatigue and Crack Growth Test Facility at ANL

The Corrosion and Mechanics of Materials Group in the Nuclear Engineering Division at ANL has long been involved in the testing, evaluation, licensing activities of reactor structural materials for government- and industry-sponsored programs. The Fatigue and Crack Growth Test Facility has four low-cycle test systems equipped with environmental chambers to conduct long-term fatigue, creep fatigue, and crack growth rate tests on structural materials. Sodium loops can be installed on the machines to conduct tests in sodium environments. The DOE Advanced Photon Source and Electron Microscopy Center at ANL provides expertise and state-of-art facility for microstructural characterization.

7.4.2 Creep-Fatigue Test Facility at INL

The Idaho National Laboratory has capabilities and facilities to conduct tensile testing, fracture testing and creep and creep-fatigue under controlled environments. Materials examined include oxide dispersion strengthened alloys, ferritic/martensitic alloys, advanced intermetallics, and high temperature Ni-base alloys.

7.4.3 Mechanical Property Test Facility at ORNL

High temperature testing facilities available at ORNL include:

- Creep frames
- Electro-mechanical testing machines
- Servo-hydraulic axial testing machines
- Large capacity (up to 220 kips) axial servo-hydraulic testing machines
- Axial/torsion servo-hydraulic testing machines
- Equipments to conduct tube burst tests
- Large capacity furnaces for long-term aging
- Charpy impact machines for testing from LN₂ to elevated temperatures

Test temperatures can be up to 1000°C. Different sources of heating (infrared, resistance and RF) are available. Under some conditions testing can be performed as high as 2000°C.

The types of mechanical properties tests that can be performed in air, using these equipments, include:

- creep tests
- relaxation tests
- fatigue tests

- creep-fatigue tests
- creep crack growth tests
- fatigue crack growth tests
- creep-fatigue crack growth tests
- thermo-mechanical fatigue tests
- axial tests (tensile, strain rate change, ratcheting, stress dip, etc.) to support material model development
- multiaxial tests (axial, torsion and internal pressurization of tubes) to support failure criteria development
- structural tests
 - tube burst
 - thermal shock
- fracture toughness tests
- J-R curve tests
- Charpy impact tests, standard size and subsize size specimens

Tests can be performed in high vacuum or inert gases.

8. SUMMARY

The AFCI program has selected a sodium-cooled reactor concept for actinide burning, commercial demonstration and superior safety and reliability of next-generation advanced reactors. Advanced materials are one of the key elements in advancing sodium reactor technology. Five different conceptual designs have been proposed, and all these reference design concepts favor austenitic stainless steels and ferritic/martensitic steels for the structural applications. So far only five materials are qualified for use in elevated-temperature nuclear structural components, including Type 304 SS, Type 316 SS, 2.25Cr-1Mo steels, mod.9Cr-1Mo steel, and Alloy 800H. Though there is extensive database and industrial experience with Type 304 and Type 316 austenitic stainless steels and 2.25Cr-1Mo and mod.9Cr-1Mo ferritic steels, advanced alloys with improved high temperature performance are desired for the economic competitiveness of advanced sodium reactor systems.

Selection and development of advanced materials must consider the unique characteristics in the structural design of advanced sodium-cooled reactors. Materials must be able to withstand long-term exposure to high temperature, sodium environment and neutron irradiation. Time-dependent deformation of creep, creep ratcheting and creep-fatigue interaction must be taken into account. The severe service conditions in advanced sodium reactors also demand improved high temperature design methodology and structural integrity criteria for robust reactor system designs. The current high temperature design methodology does not provide enough information to accommodate the structural design needs and advanced materials needs for ARR reactor systems.

It is recognized that the development and qualification of advanced materials and development of design methodologies for high temperature components are the major challenge facing advancement and deployment of sodium reactor technologies. As discussed in previous sections, time-dependent creep, creep-fatigue, and creeratcheting and effects of environments (temperature, sodium and neutron irradiation) are life-limiting factors for ARR structural designs. For code-qualified materials, a number of safety-related issues remained in the areas of weldments, environmental effects, data extrapolation to 60 years, inelastic analysis, notch weakening, thermal striping, etc. For new advanced alloys with improved strength properties and creep resistance, the available data are far more limited than what is needed for nuclear reactor applications. Improved high temperature design methodology is also required for these new alloys of which time-dependent material issues are more pronounced in terms of phase stability, phase transformation, grain boundary segregation, dissolution of strengthening phases, recovery and recrystallization. For both code-qualified alloys and new advanced alloys, it is important to identify the most critical and least resolved design and materials issues for ARR systems, and develop strategies that incorporate the key practical issues such as sodium compatibility, irradiation effects, creep, creep-fatigue, welding/joining, and fabrication/manufacturing to addresses both material needs and the need for high temperature design methodology.

In the following sections, material data requirements for reference and new advanced alloys are discussed based on the comprehensive assessments of their current status. Improvements in terms of high temperature design methodology are also addressed with the focus on the issues raised by the NRC.

8.1 Material Data Needs for Reference Alloys

Review of the existing database for Subsection NH materials has led to the conclusion that there is an extensive database and wide industrial experience with conventional austenitic stainless steels and ferritic steels. Though unique issues must be addressed for each individual material, there are common challenges facing all these alloys under ARR operating conditions. The major issues for consideration are:

- *Verification of allowable stresses for the 60-year design life*

The allowable stresses of structural alloys, such as yield strength value (S_y), design tensile strength value (S_u), design stress intensity value (S_m), maximum allowable stress intensity (S_0), allowable stress intensity value (S_t) and minimum stress to creep rupture (S_R) are provided for a 34-year design life in the current ASME Code. For ARR components, the 60-year or even beyond lifetime is expected. Additional long-term creep and creep-fatigue data are needed for reassessment and verification of allowables for the 60-year design life.

- *Long-term thermal aging effects*

The exposure of metallic materials to high temperature for long periods of time can lead to microstructural changes and result in degradation of material properties, especially material embrittlement. The fracture toughness after long-term thermal exposure must be evaluated to ensure no significant embrittlement issues. Degradation in yield, tensile, and creep strength due to long-term thermal aging should also be evaluated and incorporate in the design rules. Microstructural stability during long-term service is especially important to welds and heat affect zones.

- *Environmental Effects*

The ASME Code currently does not address environmental and neutron irradiation effects. These effects must be considered in ARR structural design and will be needed to meet regulatory requirements. Historically, industry and the DOE have addressed these issues outside of the ASME framework. Supplemental design criteria that incorporate environmental effects, particularly in creep-fatigue must be developed. Environment-related failure modes must be identified and neutron irradiation-induced embrittlement be considered. An extensive testing and evaluation program is needed to address the effects of high temperature, sodium exposure and neutron irradiation on the properties of structural materials to qualify them for the service conditions required in the ARR.

For each individual alloy, specific material performance issues and data needs are highlighted below.

Grade 91

The Grade 91 steel has significantly improved high temperature strength and creep resistance relative to low alloy steels, 2.25Cr-1Mo. The higher strength and better creep resistance allows thinner wall sections and therefore smaller thermal stresses in components and pipes. Grade 91 is a mature alloy in terms of fabrication, heat treatments, basic mechanical properties, joining technologies, etc. Nevertheless, most of these data have been developed and applied to thermal power boilers, of which materials are subjected to different temperature, loading and environmental conditions from what is expected in the ARR systems. For the ARR components that are often subjected to high-temperature, sodium exposure, neutron irradiation and cyclic thermal transients, the structural material is required to have excellent creep-fatigue resistance, sufficient fracture toughness, good sodium compatibility and radiation-tolerance.

One of the major differences in dealing with low alloy steels and high-Cr ferritic steels is the microstructural sensitivity of high-Cr steels. It should be noted that the superior properties of Grade 91 depend largely on the creation of precise microstructure of tempered martensite and precipitate particles

that give rise to high temperature strength and creep resistance. Failure to maintain such microstructure during fabrication and heat treatments and throughout the service life would seriously degrade the high temperature properties, and these issues have caused severe failures in the field. The exposure of Grade 91 steel to high temperature for long periods of time can lead to significant microstructural changes, resulting in degradation in mechanical performance, particularly the embrittlement. The microstructural stability, ductility, and toughness are especially required for pipes where leak-before-break has to be ensured. Long-term thermal aging data are needed for potential embrittlement during long-term service.

Some neutron irradiation data are available for Grade 91 from fusion reactor materials programs and previous liquid-metal fast breeder reactor programs. The emphasis of fusion reactor programs, however, was the low-temperature irradiation embrittlement in Grade 91. Irradiation data at temperatures specific to the ARR designs are required.

Corrosion damage in Grade 91 in sodium may not be significant based on limited experience. More data on high-Cr F/M steels in sodium are needed to draw firm conclusions. Decarburization/carburization and their effect on mechanical properties may be a more significant issue especially for components to be exposed in sodium for times up to 60 years. R&D on sodium effects in high-Cr F/M steels is required to provide design data and a better understanding that will be needed during licensing.

Weldments of Grade 91 are most problematic in applications of Grade 91 steel. The microstructure variations and stability in the weldments create complex issues, more so in large-size components. A number of component failures have occurred in fossil plants due to improper post-weld heat treatments, overheat, and long-term exposure at high temperatures. Lack of confidence in long-term performance of welds in advanced ferritic alloys is of particular concern. Premature Type IV cracking in the HAZs is a life-limiting failure mechanism. The causes and controls of Type IV cracking need to be well understood, and the issue should be adequately addressed in the design rules. The weld reduction factors for Grade 91 should be carefully evaluated, taking into account of long-term thermal aging effects, residual stress, Type IV cracking effects, stress redistribution during deformation, and multi-axial stress states. Creep-fatigue data of Grade 91 weldments are also lacking.

Creep-fatigue interaction represents the most complex form of high temperature behavior. The damage envelope for Grade 91 steel has put overly conservative load limits in the current ASME Code. It is noted that the inelastic and time-dependent deformation behavior of Grade 91 steel are substantially different from austenitic stainless steels. The current creep-fatigue design rules were developed based on creep-fatigue response of austenitic stainless steels. The unique deformation behavior of Grade 91, such as cyclic softening, stress relaxation during hold must be considered and modifications should be made to incorporate the deformation characteristics of Grade 91 steel. Due to anticipated thermal aging effects on microstructure and their influence on deformation mechanisms, additional creep-fatigue data are needed to evaluate and understand the damage processes. Materials design data to be used for structural designs must be assembled and evaluated to ensure the quality and traceability of the source test database. All existing and newly generated data and empirical relations to be used for developing high temperature design methodology and reactor design inputs must be qualified.

2.25Cr-1Mo Steels

There is a comprehensive database particularly for environmental effects in sodium, and also extensive industrial experience including nuclear reactor applications for low-alloy 2.25Cr-1Mo steels. However, 2.25Cr-1Mo steels have inferior high temperature strength and corrosion resistance in sodium environments compared with high-Cr ferritic/martensitic steels. 2.25Cr-1Mo steel has been increasingly replaced by high-strength high-Cr steels both in conventional power plants and in advanced nuclear

reactor systems. 2.25Cr-1Mo steels are not recommended to be a major structural alloy in the ARR reactor systems. However, there is some database for the V-modified 2.25Cr-1Mo steel (discussed in earlier sections of this report) and also has been Code qualified for non-nuclear applications. It may be of benefit to the ARR community to develop the needed additional data on this material and proceed to code qualify for use in nuclear systems.

Austenitic Stainless Steels

Austenitic stainless steels have been widely used in nuclear industry. There is an extensive database and industrial experience for both Types 304 and 316 stainless steels. Knowledge of their performance in sodium reactors is quite extensive as well. Compared to high-Cr F/M steels, austenitic stainless steels have better sodium compatibility, better microstructural stability, smaller heat variations, less sensitive to heat treatments, better control of quality of weldments, and ample experience with their applications in irradiation environments. However, austenitic stainless steels have lower thermal conductivities and higher thermal expansion coefficients, and therefore high thermal stresses in thick-wall components. Austenitic stainless steels are also more expensive than ferritic steels. For the ARR operating environments, there are few unresolved performance issues in Type 316SS. The primary need for the full qualification and licensing of 316SS for ARR applications is the assessment of their performance for times up to 60 years, especially for the environmental effects of sodium, thermal aging, and neutron irradiation.

Concerns were raised by the NRC regarding the reactor vessel made of austenitic stainless steels during the licensing review of the PRISM. The following issues need to be addressed in licensing of the ARR.

- Degradation of the reactor vessel when exposed to a flowing sodium environment due to transfer of carbon and nitrogen.
- Erosion of the vessel wall during transient situations should also be examined.
- The effects of neutron embrittlement need to be accounted for in the design and safety analysis.
- Sensitization and stress corrosion cracking at high temperatures, particularly during transient heatups

Type 316LN and 316FR (Japanese version of 316LN) are small variations to conventional Type 316 SS with lower carbon and higher nitrogen content. Type 316LN and 316FR have higher mechanical strength, good combination of strength and toughness, better resistance to stress corrosion cracking and hot cracking, good compatibility with sodium environment, less prone to irradiation damage of both base metal and weld metal over conventional Type 316SS. 316FR is a prime candidate for structural applications for reactor vessel and internals in the Japanese demonstration fast reactors. Type 316LN is a favorable structural alloy in European fast reactors, and a major structural alloy in fusion reactors (e.g. the ITER). A comprehensive database exists for Type 316LN and 316FR from the international fast and fusion reactor materials programs. 316LN is qualified in the French RCC-MR code. Strong interest has been expressed by the Japanese Fast Reactor Team to qualify 316FR in the ASME Code for elevated temperature structural use in advanced sodium reactors. The inclusion of 316LN or 316FR in Subsection NH will provide choices for selection of structural materials with better mechanical performance for the ARR designs in the U.S.

8.2 Material Data Needs for Advanced Alloys

The advanced alloy development involves modification of existing (with and without Code qualification) alloys through minor compositional changes and thermo-mechanical treatments for

improved high temperature performance. The conventional processes available for alloy development have been historically slow, taking decades to bring a new alloy to commercial market. However, given the computational tools currently available, a science-based approach for alloy improvement offers an opportunity to accelerate the alloy development process. Using computational thermodynamics and kinetic models, alloy composition and heat treatment can be optimized before alloys are even melted. Additionally, alloy compositions and treatments can be custom tailored for specific applications, which would minimize the number of trial heats required for optimization of the composition and also minimizes the tests needed to evaluate the properties. Moreover, such custom tailoring can be focused on the development of nanoscale features that are vital for improving the creep properties and irradiation resistance of the structural materials. Relative to materials that are ASME Code qualified, these techniques may allow for small modifications to approved alloys that may result in improved performance. Most probably there will be no need either for additional procedures for the Code qualification or for modifications to design methodology for the application of the new alloys. However, even if the original alloy (i.e., before modification) has sufficient database to address all qualification and licensing issues, the newly developed alloys (even with minor modification) have to undergo a detailed evaluation as if they are completely new alloys.

Four advanced alloys have been selected for further development in support of ARR. These alloys are advanced ferritic/martensitic steels, NF616, NF616+TMT, and advanced austenitic stainless steels, NF709 and HT-UPS. There has been increased usage of advanced austenitic alloys and high-Cr ferritic steels in conventional power plants. Unfortunately, the understanding of long-term issues such as creep, creep-fatigue and environmental effects are poorly understood. The neutron irradiation data of these advanced alloys are very limited, and the mechanical properties data in sodium environments are nearly zero. Significant R&D and testing are needed for the reactor design and alloy qualification. Development and qualification of new materials for use in Section III Subsection NH presents a significant challenge to the design. The time it will take for the acceptance of the new materials will require that the R&D program begin as early as possible and be continuous.

Specific data needs for these advanced alloys have been identified (Busby et al. 2008):

NF616

- Fracture toughness
- Impact testing
- Irradiation performance
- Creep-Fatigue
- Long-term aging/microstructure
- Corrosion/decarburization

NF616+TMT

- Derivation of thermomechanical treatment
- Tensile properties
- Creep properties
- Fracture toughness
- Impact testing
- Irradiation performance
- Fatigue and Creep-Fatigue
- Long-term aging/microstructure
- Corrosion/decarburization

NF709

- Fracture toughness
- Impact testing
- Irradiation performance
- Creep-Fatigue
- Welding
- Long-term aging/microstructure
- Corrosion and carburization/decarburization

HT-UPS

- Fracture toughness
- Impact testing
- Irradiation performance
- Creep-Fatigue
- Long-term aging/microstructure
- Corrosion and carburization/decarburization

8.3 High Temperature Design Methodology Needs

Development of improved high temperature design methodology for codification and licensing of materials used in ARR is a critical component in advanced materials programs. A number of prominent issues related to high temperature design methodology in the ARR component designs have been reviewed. The focus was on the nine areas identified by the NRC in the licensing review of the CRBRP, i.e. weldment safety evaluation, notch weakening effect, inelastic analysis, elastic follow-up in piping, creep-fatigue evaluation, plastic strain concentration factors, steam generator tubesheet evaluation, intermediate piping transition weld, and elevated-temperature seismic effects. The NRC also expressed significant concerns of environmental effects of sodium and neutron exposure on material performance. It is recognized that the major issues are common to all high temperature reactor concepts. The DOE and ASME have established a collaboration plan in support of codification and licensing of GenIV reactors. Tasks include review and assessment of ASME allowables, revision of code cases, creep-fatigue rules for existing code materials and advanced materials to be developed. Several design methodology issues that are encountered in the ARR reactor designs are being addressed for the GenIV reactors. Collaboration and coordination with GenIV code qualification programs will leverage the expertise and experience.

The ARR code qualification efforts should give special attention to the unique characteristics of ARR reactor design and operating environments. Sodium-cooled reactors use liquid metal as a coolant and operate at temperatures of $\approx 500-550^{\circ}\text{C}$. Environmental issues, particularly associated with long-term sodium exposure are unique to ARRs. Fast-spectrum irradiation damage and production of transmutation helium are also significantly different from what are experienced in other types of reactors including NGNP very high-temperature gas-cooled reactors. Low-pressure of sodium and high temperature operating conditions also allow thin-walled structures in the ARR. Thermal stresses are dominant in many components. Significant R&D efforts are needed in the following areas:

- Time-dependent deformation: creep and creep-fatigue and consideration of environmental effects
- Creep-fatigue design rules of weldments
- Data extrapolation from 34 years to 60 years
- Weldments and Type IV cracking
- Thermal striping
- Creep ratcheting
- Improvement in dealing with notch weakening effects

- Sodium effects
- Neutron irradiation effects under fast-spectrum irradiation
- Long-term thermal aging effects and synergistic effects of temperature, sodium and neutron irradiation

9. REFERENCES

- Abe, F., et al., *Int. J. Press. Ves. Pip.* 84 (2007) 44.
- Advanced High Temperature Plant,” in Proc. 5th Charles Parson 2000 Conference on Advanced Materials for 21st Century Turbines and Power Plant, 3-7 July, 2000, Churchill College, Cambridge, UK, p. 276.
- Alamo, A., J.L. Bertin, V.K. Shamardin, and P. Wident, *J Nucl. Mater.* 367-370 (2007) 54-59.
- Alexander, D. J., K. B. Alexander, M. K. Miller, and R. K. Nanstad, “Effects of Aging at 343C on type 308 Stainless Steel Weldments,” *Fatigue, Degradation, and Fracture – 1990*, W. H. Bamford, C. Becht IV, S. Bhandari, J. D. Gilman, L. A. James, and M. Prager, Eds., PVP-Vol. 195/MPC-Vol. 30, ASME, 1990, pp. 187-192.
- Alexander, K. B., M. K. Miller, D. J. Alexander, and R. K. Nanstad, ”A Microscopical Evaluation of Low Temperature Aging of Type 308 Stainless Steel Weldments,” *Mat. Sci. and Tech.*, v. 6, 1990, pp. 314-320.
- Alinger, M. J., G. R. Odette, G. E. Lucas, *J. Nucl. Mater.* 307-311, p. 484 (2002).
- Allen D. J., and A. Fleming, “Creep Performance of Similar and Dissimilar E911 Steel Weldments for Andrews, R. C. and L. H. Kirschler, “Design Properties of One Heat of 2 1/4Cr-1Mo Steel and 316 Stainless Steel in High Temperature Air, Helium and Sodium Environments,” USAEC Report MSAR 66-174, MSA Research Corporation, Evans City, PA (1966).
- ANL-ABR-1, “Advanced Burner Test Reactor Preconceptual Design Report,” Argonne National Laboratory (ANL-AFCI-173), Sept. 5, 2006.
- Apblett, Jr. W. R. and M. Matejic, “Extra Low C Ferritic Steels for High Temperature Sodium Service,” *Proc. Symp. on Low C and Stabilized 2¼% Cr-1% Mo Steels*, American Society for Metals, Metals Park, Ohio, p. 131 (1973).
- Arai, M., T. Ogata and A. Nitta, “Continuous observation of cavity growth and coalescence by creep-fatigue tests in SEM,” *Japan Society of Mechanical Engineers International Journal, Series A*, Vol. 39, No. 3, pp. 382-388, 1996.
- Argon, A.S., “Mechanisms and mechanics of fracture in creeping alloys,” in *Recent Advances in Creep & Fracture of Engineering Materials and Structures*, Eds., B. Wilshire and D.R.J. Owen, Pineridge Press, Swansea, UK, 1982.
- Asayama, T. and S. Hasebe, *Nucl. Eng. Des.* 195 (2000) 197.
- Asayama, T. and Y. Tachibana, “DOE/ASME Materials Project, Task 5 Final Report: Collect Available Creep-Fatigue Data and Study Existing Creep-Fatigue Evaluation Procedures for Grade 91 and Hastelloy XR,” 2007.
- Asayama, T., “DOE/ASME Materials Project, Task 10: Update and Improve Subsection NH – Alternative Simplified Creep-Fatigue Design Methods”, 2008.
- Asayama, T., *Nucl Eng. Des.* 198 (2000) 25.
- Asayama, T., Y. Abe, N. Miyaji, M. Koi, T. Furukawa, and E. Yoshida, “Evaluation Procedures for Irradiation Effects and Sodium Environmental Effects for the Structural Design of Japanese Fast Breeder Reactor,” *J. Pressure Vessel Technology*, 123, 49 (2001).
- Ashworth, M. A., D. I. R. Norris, and I. P. Jones, *J. Nucl. Mater.* 189 (1992) 289.
- ASM Handbook, 1990, 2, p. 617.
- ASME Boiler and Pressure Vessel Code, 2007 Edition.

ASME Code, Section II Part D, 2004.

ASME Subsection NH, 2007 Edition.

Atsumo, H., S. Yuhara, A. Maruyama, S. Kanoh, N. Aoki, and K. Mochizuki, "Sodium Compatibility and Corrosion Tests for Component Materials," Proc. Intl. Conf. on Liquid Metal Technology in Energy Production. CONF-760503-P2, 849 (1976).

Barabash, V. and ITER International Team, "Materials challenges for ITER – Current status and future activities," J. Nucl. Mater., 367-370, pp. 21-32, 2007.

Bass, "Comparative assessment of ductility exhaustion and time fraction creep damage evaluation procedures based on US creep-fatigue data for 316SS," 1987.

Bate, "Progress report on the inelastic analysis of the Eddystone steam pipe failure, SG-ETD Meeting Minutes, September 1988.

Bendick, W., in Creep and Fracture in High Temperature Components – Design and Life Assessment, ECCC Creep Conference, Sept. 2005, p.406.

Besson, M., P. Baque, L. Champeix, J. R. Donati, C. Oberlin, and P. Saint-Paul, "C Transfer Between 2¼Cr-1Mo Alloy and Austenitic Steels," Proc. Intl. Conf. on Liquid Metal Technology in Energy Production, CONF-760503-P2, 834 (1976).

Bestwick and Clayton, "Design methodology for creep fatigue assessment using creep ductility criteria, SG-ETD Meeting Minutes, September 1985.

Blackburn, L. D., Hanford Engineering Development Laboratory, Private Communication to V. K. Sikka, ORNL, 1975.

Blass, J. J., et al., "JAPC-USDOE Joint Study on Structural Design Methods and Data for Modified 9Cr-1Mo Steel," in Annual Report for the Period April 1, 1990 – March 31, 1991, ORNL/9CR/91-1, March 1991.

Blass, J. J., et al., "JAPC-USDOE Joint Study on Structural Design Methods and Data for Modified 9Cr-1Mo Steel," in Annual Report for the Period April 1, 1990 – March 31, 1991, ORNL/9CR/91-1, March 1991.

Bloom, E.E., J.T. Busby, C. E. Duty, P. J. Maziasz, T. E. McGreevy, B. E. Nelson, B. A. Pint, P. F. Tortorelli, and S. J. Zinkle, "Critical Questions in Materials Science and Engineering for Successful Development of Fusion Power," J. of Nucl. Materials, Vol 367-370 (2007), p. 1.

Booker, M. K., J. P. Strizak, and C. R. Brinkman, "Analysis of the Continuous Cycling Fatigue Behavior of Annealed 2 1/4Cr-1Mo Steel," Oak Ridge National Laboratory, ORNL-5593 (1979).

Brinkman, "The influence of hold time on the elevated temperature fatigue properties of steels and alloys – a literature review," 1969.

Brinkman, C. R., J. Pres. Ves. Tech. 123 (2001) 75.

Brinkman, C. R., M. K. Booker, and J. P. Strizak, "The Influence of Environment, Metallurgical Variables, and Prolonged Test Times on the Fatigue and Creep-Fatigue Behavior of Annealed 2 1/4Cr-1Mo Steel," Oak Ridge National Laboratory, ORNL-5625 (1980).

Buchkremer, H. P., P. J. Ennis, D. Stover, J. Mater. Process. Tech. 92-93 (1999) 368.

Busby, J. T. et al., "Candidate Developmental Alloys for Improved Structural Materials for Advanced Fast Reactors," ORNL/TM-2008/040, ORNL/GNEP/LTR-2008-023, Oak Ridge National Laboratory, Oak Ridge, TN, March 2008.

- Busby, J.T. and K.J. Leonard, "Space fission reactor structural materials: Choices past, present, and future," *J. of Metals*, April 2007, p. 20.
- Busby, J.T., C.E. Duty, K.J. Leonard, R.K. Nanstad, S.J. Pawel, and M.A. Sokolov, "Assessment of Structural and Clad Materials for Fission Surface Power Systems," ORNL/LTR/FSP/07-01, August 2007.
- Campbell, "Creep-fatigue interaction correlation for 304 stainless steel subjected to strain controlled cycling with hold times at peak strain," ASME Paper No. 71-PVP-6, 1971.
- Charnock, W., J. E. Cordwell, and P. Marshall, "The Influence of High Temperature Sodium on the Structure and Mechanical Properties of 9 Cr Steel," *Proc. Intl. Conf. on Ferritic Steels for Fast Reactor Steam Generators*, BNES, London, p. 310 (1978).
- Cho, D., et al, Interim Report on Sodium Plugging Test, April 30, 2008.
- Chopra, O. K. "Low Cycle Fatigue Behavior of Type 316 Stainless Steel in Sodium," in *Mechanical Properties Design Data Program: Annual Progress Report for the Period Ending January 1985*, ORNL/LMR/1MM-85/3, Oak Ridge National Laboratory, Oak Ridge, TN pp. 1.17-1.28, (1985).
- Chopra, O. K. and K. Natesan, "Representation of Elevated-Temperature Tensile Behavior of Type 304 Stainless Steel in a Sodium Environment," *J. Eng. Mater. Technol.* 99, 366 (1977).
- Chopra, O. K. and K. Natesan, unpublished data, Argonne National Laboratory (2007).
- Chopra, O. K., Argonne National Laboratory, unpublished report, 1985.
- Chopra, O. K., K. Natesan, and T. F. Kassner "Carbon and Nitrogen Transfer in Fe-9Cr-Mo Ferritic Steels Exposed to a Sodium Environment," *J. Nucl. Mater.* 96 (3), 269 (1981).
- Chopra, O. K., K. Natesan, and T. F. Kassner, "Compatibility of Ferritic Steels in a Sodium Environment," *Proc. Intl. Conf. on Liquid Metal Technology in Energy Production*, CONF-760503-P2, 730 (1976).
- Chopra, O. K., K. Natesan, and T. F. Kassner, Argonne National Laboratory, unpublished report, 1981.
- Chopra, O. K., K. Natesan, T. F. Kassner, and D. L. Smith, "Low Cycle Fatigue and Creep Fatigue Behavior of Type 304 Stainless Steel in a Sodium Environment," Argonne National Laboratory, ANL-82-19, (1982).
- Cohn, M. J., J. F. Henry, D. Nass, *J. Pres. Ves. Tch.* 127 (2005) 197.
- Cordovi, M. A., J.J.B. Rutherford, A. B. Wilder, and C. P. Weigel, "Effects of High-Temperature Steam Exposure on the Properties of Superheater Tube Alloys," pp. 8-55 in *Behavior of Superheater Alloys in High Temperature, High Pressure Steam*, The American Society of Mechanical Engineers, New York, 1968.
- Corum and Sartory, "Assessment of current high temperature design methodology based on structural failure tests, SG-ETD Meeting Minutes, June 1985
- Corum, "Summary of JAPC-USDOE Study on modified 9Cr 1Mo steel," SG-ETD Meeting Minutes, November 1991.
- Corum, "What evidence do we have for or against current linear damage procedure?" SG-ETD Meeting Minutes, November 1987.
- Cowgill, M. G., Sodium Effects on Mechanical Properties of Structural Materials," in *Mechanical Properties Design Data Program: Annual Progress Report for the Period Ending January 1985*, ORNL/LMR/1MM-85/3, Oak Ridge National Laboratory, Oak Ridge, TN pp. 6.2-6.13, (1985).
- Cullen, T. M., Combustion Engineering, Inc., Chattanooga, Tenn., private communications to V. K. Sikka, ORNL, August 1975.

- Date, S., H. Ishikawa, T. Otani, Y. Takahashi, T. Nakazawa, Nucl. Eng. Des. 238 (2008) 353.
- Date, S., H. Ishikawa, Y. Takahashi, T. Nakazawa, Nucl. Eng. Des. 238 (2008) 336.
- DeLong et al., "Operation experiences and reliability evaluation on main steam line pressure parts of Philadelphia Electric Co., Eddystone No. 1," SG-ETD Meeting Minutes, February 1988
- DeLong, J. F., J. E. Bynum, F. V. Ellis, M. H. Rafiee, W. F. Siddall, T. Daikoku, and T. Haneda, "Failure Investigation of Eddystone Main Steam Piping," Welding J. Res. Suppl., v. 64, 1985, pp. 271s-280s.
- DiStefano, J. R., et al., "Summary of Modified 9Cr-1Mo Steel Development Program: 1975 – 1985," ORNL-6303, Oak Ridge National Laboratory, Oak Ridge, TN, October 1986.
- Donoghue, J. E., J. N. Donohew, G. R. Golub, R. M. Kenneally, P. B. Moore, S. P. Sands, and B. A. Wetzel, "Preapplication Safety Evaluation Report for the Power Reactor Innovative Module (PRISM) Liquid-Metal Reactor," Final Report, Nuclear Regulatory Commission, NUREG-1368, 1994.
- Edmonds, D. P., D. M. Vandergriff, and R. J. Gray, "Effect of Delta Ferrite Content on the Mechanical Properties of E308-16 Stainless Steel Weld Metal; III. Supplemental Studies," Properties of Steel Weldments for Elevated Temperature Pressure Containment Applications, I G. V. Smith, Ed., MPC-9, ASME, 1978, pp. 47-61.
- Eggeler, G., N. Nilsvang, and B. Ilschner, Steel Research, 58, p. 97, 1987.
- Eggeler, G., A. Ramteke, M. Coleman, B. Chew, G. Peter, A. Burblies et al, Int. J. Press. Ves. Pip. 60 (1994) 237.
- Ehrlich, K., J. Konys, and L. Heikinheimo, "Materials for high performance light water reactors," J. of Nucl. Mater., 327 (2004), p. 140.
- Ellis, J. R., M. T. Jakub, C. E. Jaske, and D. A. Utah, "Elevated Temperature Fatigue and Creep-Fatigue Properties of Annealed 2 1/4Cr-1Mo Steel," Proc. ASME Symp. on Structural Material for Service and Elevated Temperatures in Nuclear Power Generation, MPC-1, 213 (1975).
- EnergySolutions, GNEP Deployment Studies, Overall Summary Report, Revision 1, DOE/NE/24503.1-1 Final Rev. 1, 2008.
- Ennis, P. J. and A. Czyrska-Filemonowicz, OMMI, v. 1, April, 2002, p.1.
- Ennis, P. J., A. Zielinska-Lipiec, O. Wachter, A. Czyrska-Filemonowicz, Acta Mater. 45 (1997) 4901.
- EPRI Performance Review of P/T91, Palo Alto, CA: 2002. 1004516.
- EPRI, Performance Review of P/T91 Steels, Palo Alto, CA, 2002. 1004516.
- European Creep Collaborative Committee (ECCC) Data Sheets 2005.
- Fahr, D., "Analysis of Stress-Strain Behavior of Type 316 Stainless Steel," ORNL/TM-4292, November 1973.
- Faulkner, R.G., S.Song, P.E.J. Flewitt, M. Victoria, P. Marmy, J. Nucl. Mater. 255, Issues 2- 3, (1998) 189-209.
- Flagella, P. N. "Low Cycle Fatigue Behavior of Type 316 Stainless Steel in a Flowing Sodium Environment," WAESD-NA-94000-15, Westinghouse Electric Corporation, Madison, PA (1983).
- Flagella, P. N. and J. R. Kahrs, "Low-Cycle Fatigue Testing in Flowing Sodium at Elevated Temperatures," Proc. Intl. Conf. on Liquid Metal Technology in Energy Production, CONF-760503-PI, 353 (1976).

Flagella, P. N., J. A. Denne, and R. A. Leisure, "Effects of Sodium Pre-Exposure on the Creep-Rupture Properties of Type 316 Stainless Steel in Flowing Sodium." Proc. Second Intl. Conf. on Liquid Metal Technology in Energy Production, CONF-800401-P2, pp 19.50-19.56 (1980).

Flagella, P. N., J. A. Denne, and S. L. Schrock, Mechanical Properties Test Data for Structural Materials Quarterly Progress Report for Period Ending January 31, 1978, ORNL-5380, 186, and Ending April 30, 1978, ORNL-5416, 239.

Francis, J.A., W. Mazur, and H.K.D.H. Bhadeshia, Mater. Sci Tech. 22 (2006) 1387.

Furukawa, T., E. Yoshida, S. Kato, R. Komine, "Effect of Sodium on Mechanical Strength of FBR Grade Type 316 Stainless Steel," ASME PVP, v. 373, 1998, p. 301.

Ganesan, V. and V. Ganesan, J. Nucl. Mater. 256 (1998) 69.

Garner, F. A. and D. Gelles "Neutron-Induced Swelling of Commercial Alloys at Very High Exposures," Effects of Radiation on Materials: 14th International Symposium (Volume II), ASTM STP 1046, N. H. Packan, R. E. Stoller, and A. S. Kumar, Eds., American Society of Testing and Materials, Philadelphia, 1990, pp. 673-683.

Garner, F. A., "Irradiation Performance of Cladding and Structural Steels in Liquid Metal Reactors," Chapter 6, Volume 10A, Nuclear Materials, Part 1, B. R. T. Frost, ed., Materials Science and Technology: A Comprehensive Treatment, R. W. Cahn, P. Haasen, and E. J. Kramer, eds., VCH publishers, Germany, 1994.

Garner, F.A., M.L. Hamilton, N.F. Panayotou and G.D. Johnson, J. Nucl. Mater. 103 & 104, 803, 1981.

GE Hitachi Nuclear Energy, GNEP Conceptual Design Studies: Summary (Non-Proprietary), Rev. 0, April 10, 2008.

Gelles, D.S., Pacific Northwest National Laboratory, unpublished research, 2008.

Gelles, D.S., J. Nucl. Mater, 225 (1995) 163-174.

Gelles, D.S., J. Nucl. Mater. 233-237 (1996) 291-298.

General Atomics, GNEP Deployment Studies: Executive Summary, PC-000555, Rev. 2, May 22, 2008.

Grossbeck, M.L., K. Ehrlich and C. Wassilew, An assessment of the tensile, irradiation creep, creep rupture, and fatigue behavior in austenitic stainless steels with emphasis on spectral effects, J. Nucl. Mater. 174 (1990) 264-281.

Haarmann, K., J.C. Vaillant, B. Vandenberghe, W. Bendick, and A. Arbab, The T91/P91 book Edition V&M, 2002.

Hald, J., in Creep and Fracture in High Temperature Components – Design and Life Assessment, ECCC Creep Conference, Sept. 2005, p. 20.

Harries, D.R., "Neutron irradiation-induced embrittlement in type 316 and other austenitic steels and alloys," J. Nucl. Mater. 82 (1979) 2-21.

Hattestrand, M. and H-O. Andren, Micron, 32, pp. 789-797, 2001.

Hattestrand, M., M. Schwind, H. Andren, Mater. Sci. Eng. A250 (1998) 27.

Hayes, W. C. and O. C. Shepard, "Corrosion and Decarburization of the Ferritic Chromium-Molybdenum Steels in a Sodium Coolant System," NAA- SR-2973, Atomic International (1958).

Henry, J., "Growing Experience with P91/T91 Forcing Essential Code Changes," Combined Cycle Journal, First Quarter 2005.

Hiltz, R. H., L. H. Kirschler, and R. C. Andrews, "Tensile Strength of Standard 2 1/4Cr-1Mo Steel after 10,000, 20,000, and 26,500 hour Exposures in 1050°F Sodium," MSAR 72-286, Mines Safety Appliances Research Corp., Evans City, PA (1972).

Hoke, J. and F. Eberle, "Experimental Superheater for Steam at 2000 psi and 1250°F – Report After 14,281 Hours of Operation," Trans. ASME 79(2): 307, February 1957.

Horak, J. A., V. K. Sikka, and D. T. Raske, "Review of Effects of Long-Term Aging on the Mechanical Properties and Microstructures of Types 304 and 316 Stainless Steel," International Conference on Nuclear Plant Aging, Availability Factor and Reliability Analysis, San Diego, CA, 3 July 1985.

Horsten, M. G., E. V. van Osch, D. S. Gelles, and M. L. Hamilton, "Irradiation Behavior of Ferritic-Martensitic 9-12% Cr Steels," Effects of Radiation on Materials: 19th International Symposium, ASTM STP 1366, M. L. Hamilton, A. S. Kumar, S. T. Rosinski, M. L. Grossbeck, Eds., American Society for Testing and Materials, West Conshohocken, PA 2000.

Hu, W.L. and D. S. Gelles, in Influence of Radiation on Material Properties: 13th International Symposium (Part II), ASTM STP 1175 (1987), p. 83.

Hu, W.L. and D.S. Gelles, "Miniature Charpy Impact Test Results for the Irradiated Ferritic Alloys HT-9 and Modified 9Cr-1Mo," pp.631-45 in Proceedings of Topical Conference on Ferritic Alloys for Use in Nuclear Energy Technologies, Snowbird, Utah, June 19-23, ed. J.W. Davis and D.J. Michel, TMS, New York, September 1984. (Taken from: J.R. DiStefano, et. al., "Summary of Modified 9Cr-1Mo Steel Development Program: 1975-1985," ORNL-6303, Oak Ridge National Laboratory, Oak Ridge, TN, October 1986).

Hucinska, J., 2003, "Advanced Vanadium Modified Steels for High Pressure Hydrogen Reactors," Advances in Materials Science, 4, pp. 21-27.

Husslage, W. and B. R. Drenth, in Proc. Second Intl. Conf. on Liquid Metal Technology in Energy Production, CONF-800401, p. 22-48 (1980).

Huthman, H., G. Menken, H. U. Borgstedt, T. Tass, in: Proceedings of the Second International Conference on Liquid Metal Technology in Energy Production, J. M. Dahlke (Ed.), Richland, Washington, vol. 2, p 19, 1980.

Idaho National Laboratory, FY2009 Advanced Test Reactor National Scientific User Facility Users' Guide, INL/EXT-08-14709, 2008.

Imgram, A. G., Ibarra, S., Prager, M., 1990, "A Vanadium Modified 2 1/4Cr-1Mo Steel with Superior Performance in Creep and Hydrogen Service," New Alloys for Pressure Vessels and Piping, PVP 201, MPC-3, pp. 1-28.

International Nuclear Recycling Alliance, Integrated U.S. Used Fuel Strategy – Analyses Performed by the International Nuclear Recycling Alliance, May 1, 2008.

Ishiguro, T., Murakami, Y., Ohnishi, K., and Watanabe, J., 1982, "A 2 1/4Cr-1Mo Pressure Vessel Steel with Improved Creep Rupture Strength," ASTM STP 755, pp. 129-147.

Isobe, N., M. Sukekawa, Y. Nakayama, S. Date, T. Ohtani, Y. Takahashi, N. Kasahara, H. Shibamoto, et al, Nucl. Eng. Des. 238 (2008) 347.

ITER Materials Properties Handbook (MPH), ITER Doc. G 74 MA 16 04-05-07 R0.1, (internal project document distributed to the ITER Participants).

Ito, T., S. Hagi, and Y. Wada, "Carburization and Denitrided Behavior of Modified SUS316 Steels in Sodium," Proc. The 28th Symposium on the High Temperature Strength of Materials, 1990, p. 101.

Ito, T., S. Kato, M. Aoki, E. Yoshida, T. Kobayashi, and Y. Wada, "Evaluation of Carburization and Decarburization Behavior of Fe-9Cr-Mo Ferritic Steels in Sodium Environments," *J. Nucl. Sc. and Technol.* 29 (4), 367 (1992).

James, L. A. and R. L. Knecht, "Fatigue-Crack Propagation Behavior of Type 304 Stainless Steel in a Liquid Sodium Environment," *Met. Trans.* 6A, 109 (1975).

James, L. A., *Scripta Met.* 10 (1976) 1039.

Japan Atomic Energy Agency (JAEA) Oarai Research and Development Center, http://www.jaea.go.jp/04/o-arai/joyo_users_guide/index.html.

Jetter, "Elevated temperature design – development and implementation of Code Case 1592," *Journal of Pressure Vessel Technology*, Vol. 98, pp. 222-229, 1976.

Jetter, "Elevated temperature design," lectures presented at Knolls Atomic Power Laboratory, June 2005.

Jetter, Personal communication, July 2008.

Jitsukawa, S., M. Tamura, B. van der Schaff, R.L. Klueh, A. Alamo, C. Petersen, M. Schirra, P. Spaetig, G.R. Odette, A.A. Tavassoli, K. Shiba, A. Kimura, *J. Nucl. Mater.* 307-311, Part 1, (2002), p179.

Jones, W. B., C. R. Hills, and D. H. Polonis, "Microstructural Evolution of Modified 9Cr-1Mo Steel," *Met. Trans. A*, 22A, May 1991, 1049-1058.

Kim, B. J., C. S. Jeong, and B. S. Lim, *Materials Science and Engineering A*, Vol. 483-484, pp. 544-546, 2008.

Kim, J. T., Kim, B. H., Kong, B. O., and Kim, D. J., 2006, "Effects of V and Carbides on the Temper Embrittlement of the 2.25Cr-1Mo Steel," PVP2006-ICPVT-11-93218, Proceedings of PVP2006-ICPVT-11, 2006 ASME Pressure Vessels and Piping Division Conference, July 23-27, 2006, Vancouver, BC, Canada.

Kimura, K., "Review of Allowable Stress and New Guideline of Long-term Creep Strength Assessment for High Cr-Ferritic Creep Resistant Steels," in *Creep and Fracture in High Temperature Components – Design and Life Assessment*, ECCC Creep Conference, Sept. 2005, p. 1007.

Kirschler, L. H. and R. C. Andrews, "Effect of High-Temperature Sodium on the Mechanical Properties of Candidate Alloys for the IMFBR Program," *Proc. Intl. Conf. on Sodium Technology and Fast Reactor Design*, ANL-7520, 41 (1968).

Kirschler, L. H., R. H. Hiltz, and S. J. Rodgers, "The Effect of High Temperature Sodium on the Mechanical Properties of Candidate Alloys for the LMFBR Program," USAEC Rep. MSAR 69-42, Mines Safety Appliances Research Corp., Evans City, PA (1969).

Klueh, R.L., "Reduced-activation bainitic and martensitic steels for nuclear fusion applications," *Curr. Opin. Solid State Mater. Sci.*, 8 (2004), p. 239.

Klueh, R. L. and D. J. Alexander, *J. Nucl. Mater.* 187 (1992) 60.

Klueh, R. L. and J. M. Vitek, "Elevated-Temperature Tensile Properties of Irradiated 9Cr-1MoVNb Steel," *J. Nucl. Mater.* 132, 127-31 (1985).

Klueh, R. L. and Swindeman, R. W., 1986, "The Microstructure and Mechanical Properties of a Modified 2.25Cr-1Mo Steel," *Metallurgical Transactions*, 17A, pp. 1027-1034.

Klueh, R. L., "Creep-Rupture Properties of Decarburized and Aged 2¼Cr-1Mo Steel," ORNL-5292 (1977).

Klueh, R. L., "Effect of C on the Mechanical Properties of 2¼Cr-1Mo Steel," ORNL-4922 (1973).

Klueh, R. L., "Effect of Sodium on the Mechanical Properties of 2 1/4Cr-1Mo Steel," Mechanical Properties Test Data for Structural Materials Quarterly Progress Report for Period Ending July 31, 1976, ORNL -5200, p. 181 (September 1976).

Klueh, R. L., D. R. Harries, High-Chromium Ferritic and Martensitic Steels for Nuclear Applications, West Conshohocken, Pennsylvania, American Society for Testing and Materials, 2001.

Klueh, R. L., *Inter. Mater. Rev.*, 50 (2005) 287.

Klueh, R.L. and A.T. Nelson, "Ferritic/Martensitic Steels for Next Generation Reactors", Proc.1st Symp. on Nuclear Fuels and Structural Materials for Next Generation Nuclear Reactors, *J.Nucl.Mater.* 371, Issues 1-3, pp 1-384, (2007).

Klueh, R.L., D.J. Alexander, in: Arvind S. Kumar, David S. Gelles, Randy K. Nanstad (Eds.), *Effects of Radiation on Materials: 16th International Symposium*, ASTM STP 1175, American Society for Testing and Materials, Philadelphia, 1994, p. 591.

Korcakova, L., J. Hald, and M. Somers, *Materials Characterization*, 47, pp. 111-117, 2001.

Krankota, J. L. and J. S. Armijo, "Influence of High Temperature Thermal and Sodium Exposure on the Mechanical Properties and Composition of Low C 2 1/4Cr-1Mo Steel," Proc. Symp. on Low C and Stabilized 2 1/4% Cr-1% Mo Steels, American Society for Metals, Metals Park, Ohio, p. 57 (1973).

Krankota, J. L. and J. S. Armijo, "The Kinetics of Decarburization of 2 1/4% Cr-1% Mo Steel in Sodium," *Nucl. Technol.* 24, 225 (1974).

Krankota, J. L. and K. D. Challenger, "Carbon Transport and Material Property Degradation in a Model of the Clinch Breeder Reactor Secondary Sodium System," Proc. Intl. Conf. on Liquid Metal Technology in Energy Production, CONF-760503-P2, 834 (1976).

Laha, K., K. S. Chandravathi, P. Parameswaran, K. Bhanu Sankara Rao, and S. L. Mannan, *Metallurgical and Materials Transactions A*, 38A, pp. 58-68, 2007.

Lauritzen, T., R.E. Blood, and S. Vaidyanathau, "Mechanical Properties of Reactor-Irradited HT-9: Effect of Thermomechanical Treatments," pp. 13-25 in *National Cladding/Duct Material Development Quarterly Technical Progress Letter*, October-November-December 1983, HEDL-TC-160-39, Hanford Engineering Development Laboratory, Richland, WA, 1984. (Taken from: J.R. DiStefano, et. al., "Summary of Modified 9Cr-1Mo Steel Development Program: 1975-1985," ORNL-6303, Oak Ridge National Laboratory, Oak Ridge, TN, October 1986).

Lauritzen, T., R.E. Blood, and S. Vaidyanathau, "Some Effects of Irradiation on the Tensile Properties of Modified 9Cr-1Mo," pp. 183-90 in *National Cladding/Duct Material Development Quarterly Technical Progress Letter*, January-February-March 1984, HEDL-TC-160-40, Hanford Engineering Development Laboratory, Richland, WA, 1984. (Taken from: J.R. DiStefano, et. al., "Summary of Modified 9Cr-1Mo Steel Development Program: 1975-1985," ORNL-6303, Oak Ridge National Laboratory, Oak Ridge, TN, October 1986).

Lee, E. H., P. J. Maziasz and A. F. Rowcliffe, "The Structure and Composition of Phases Occurring in Austenitic Stainless Steels in Thermal and Irradiation Environments," in *Phase Stability During Irradiation*, J. R. Holland, L. K. Mansur, and D. I. Potter, eds., The Metallurgical Society of AIME, 1981, Warrendale, Pennsylvania.

Licina, G. J. and P. Roy, "Effects of Thermally Aging and Decarburization on the mechanical Properties of 2 1/4Cr-1Mo Steel," Proc. Topical Conf. on Ferritic Alloys for Use in Nuclear Energy Technologies, The Metallurgical Society, Warrendale, PA, p. 443 (1984).

Licina, G. J. and P. Roy, *Effects of Thermal Aging and Decarburization on the Mechanical Properties of 2 1/4Cr-1Mo Steel*, CEFR-00617, August 1982.

Little, E. A., J. Nucl. Mater. 206, 324-334, 1993.

Lucas, G.E., "The evolution of mechanical property changes in irradiated austenitic stainless steel," J. Nucl. Mater. 206, 287-305, 1993.

Madden, P. K. and V. M. Callen, J. Nucl. Mater. 113, 46, 1983.

Maiya, P. S., "Effects of Wave Shape and Ultrahigh Vacuum on Elevated Temperature Low Cycle Fatigue in Type 304 Stainless Steel," Mater. Sci. Eng. 47, 13, 1981.

Majumdar, "Thermomechanical fatigue of type 304 stainless steel," SG-ETD Meeting Minutes, December 1990.

Majumdar, S. and P. S. Maiya, "A Mechanistic Model for Time-Dependent Fatigue," J. Eng. Mater. Technol. 102, 159, 1980.

Majumdar, S., "Application of the UK ductility exhaustion method to type 304 stainless steel data," SG-ETD Meeting Minutes, February 1993.

Makenas, B. J., J. F. Bates and J. W. Jost, "The Swelling Behavior of 20% CW 316 Stainless Steel Cladding With and Without Adjacent Fuel," Effects of Radiation on Materials: Eleventh Conference, ASTM STP 782, H. R. Brager and J. S. Perrin, Eds., American Society of Testing and Materials, pp. 17-29, 1982.

Maloy, S., "Advanced Core Materials Program Overview," presented at GNEP Advanced Materials Workshop, ORNL, July 2007.

Mannan, S. L., K. Bhanu Shankar Rao, M. Valsan, and A. Nagesha, "Strain Controlled Low Cycle Fatigue and Creep Fatigue Interaction Behavior of Modified 9Cr-1Mo Ferritic Steel," Trans. Indian Inst. Met. 58 (2-3), 159-168, 2005.

Mansur, L. K., Oak Ridge National Laboratory, unpublished report, 2005.

Mansur, L. K. and E. E. Bloom, "Radiation Effects in Reactor Structural Alloys," J. Metals, 23-31, 1982.

Mansur, L. K., "Mechanisms and Kinetics of Radiation Effects in Metals and Alloys," A chapter in the book, Kinetics of Non-Homogeneous Processes, edited by G. R. Freeman, Wiley-Interscience, New York, pp. 377-463, 1987.

Mansur, L. K., "Theory and experimental background on dimensional changes in irradiated alloys," J. Nucl. Mater. 216, 97-123, 1994.

Marie, S., S. Chapuliot, Y. Kayser, M.H. Lacire, B. Drubay, B. Barthelet, P. Le Delliou, V. Rougier, C. Naudin, P. Gilles, M. Triay, "French RSE-M and RCC-MR code appendices for flaw analysis: Presentation of the fracture parameters calculations – Part I: General review," International Journal of Pressure Vessels and Piping, Vol. 84, pp. 590-600, 2007.

Masuyama, F., "Creep Rupture Life and Design Factors for High Strength Ferritic Steels" in Creep and Fracture in High Temperature Components – Design and Life Assessment, ECCO Creep Conference, p. 981, 2005.

Masuyama, F., N. Nishimura, H. Haneda, F. V. Ellis, and J. F. Delong, "Investigation of the Deterioration Plus Restoration Behavior of Fourteen Heats of TP 316 Stainless Steel Removed From Eddystone Unit No. 1 Main Steam Lines After 130,520 Hours Service," Properties of Stainless Steels in Elevated Temperature Service, M. Prager, Ed., MPC-Vol. 26/PVP-vol. 132, ASME, pp. 173-187, 1987.

Mathew, M. D., S. Latha, K. Bhanu, S. Rao and S. L. Mannan, "Weld Strength Reduction and Creep Fracture in Nitrogen Alloyed 316 Stainless Steel Weldments" in Creep and Fracture in High Temperature Components – Design and Life Assessment, ECCO Creep Conference, p. 804, 2005.

Matsumoto, K., Y. Ohta, T. Kataoka, S. Yagi, K. Suzuke, T. Yukitoshi, T. Moroishi, K. Yoshikawa, and Y. Shida, "C Transfer Behavior of Materials for Liquid-Metal Fast Breeder Reactor Steam Generators," Nucl. Technol. 28, 452 (1976).

Maziasz, P. J., "Overview of microstructural evolution in neutron-irradiated austenitic stainless steels," J. Nucl. Mater. 205 (1993) 118-145.

Maziasz, P. J., ASTM-STP-979 (1989) p. 116-161.

Maziasz, P. J., J. P. Shingledecker, N. D. Evans, Y. Yamamoto, K. L. More, R. Trejo, and E. Lara-Curzio, Trans. ASME 129 (2007) 798.

Maziasz, P. J., JOM (1989) 14.

Menken, G., E. D. Grosser, and E. T. Hessen, "Corrosion and Creep Behavior of Ferritic Cr-Alloyed Steels in Sodium," Proc. Intl. Conf. on Ferritic Steels for Fast Reactor Steam Generators, BNES, London, p. 264 (1978).

Mills, W. J. "Effect of Loading Rate and Thermal Aging on the Fracture Toughness of Stainless Steel Alloys," Fracture Mechanics: Perspectives and Directions (Twentieth Symposium), ASTM STP 1020, R. P. Wei and R. P. Gangloff, Eds., ASTM, 1989, pp. 459-475.

Mills, W. J., "Fracture Toughness of Irradiated Stainless Steel Alloys," HEDL-SA-3471, Westinghouse Hanford Company, January 1986.

Mimura, H., M. Ohgami, H. Naoi, and T. Fujita, in High Temperature Materials for Power Engineering, Part I, Kluwer Academic Publishers, pp. 485-494, 1990.

Mimura, H., M. Ohgami, H. Naoi, and T. Fujita, in Materials for Advanced Power Engineering, p. 361, 1994.

Miyaji, N., Y. Abe, S. Ukai, S. Onose, J. Nucl. Mater. 271 and 272, 173, 1999.

Myers, J. "Effect of Ageing on the Mechanical Properties of 316 Weld Metals," Report TPRD/M/1502/R85, Central Electricity Generating Board, Marchwood Engineering Laboratories, July 1985.

Natesan, K. and T. F. Kassner, "Monitoring and Measurement of C Activity in Sodium Systems," Nucl. Technol. 19, 46, 1973.

Natesan, K., Argonne National Laboratory, unpublished report, 1983.

Natesan, K., D. L. Smith, T. F. Kassner, and O. K. Chopra, "Influence of Sodium Environment on the Tensile Behavior of Austenitic Stainless Steels," ASME Symp. on Structural Material for Service and Elevated Temperatures in Nuclear Power Generation, MPC-1, 302, 1975.

Natesan, K., M. Li, S. Majumdar, R. Nanstad, and T. -L. Sham, "Preliminary Assessment of Code Qualification for ABR Structural Materials," February 2008.

Natesan, K., O. K. Chopra, and T. F. Kassner, "Compatibility of Fe-2¼wt % Cr-1 wt % Mo Steel in a Sodium Environment," Nucl. Technol. 28, 441, 1976.

Natesan, K., O. K. Chopra, and T. F. Kassner, "Effect of Sodium on the Creep-Rupture Behavior of Type 304 Stainless Steel," Proc. Intl. Conf. on Liquid Metal Technology in Energy Production, CONF-760503-P1, 338, 1976.

Natesan, K., O. K. Chopra, and T. F. Kassner, "Influence of Sodium Environment on the Uniaxial Tensile Behavior of Titanium Modified Type 316 Stainless Steel," J. Nucl. Mater. 73, 137, 1978.

Natesan, K., O. K. Chopra, G. J. Zeman, D. L. Smith, and T. F. Kassner, "Effect of Sodium Environment on the Creep-Rupture and Low-Cycle Fatigue Behavior of Austenitic Stainless Steels," Proc. IAEA

Specialists Meeting on Properties of primary Circuit Structural Materials Including Environmental Effects, CONF-771052, 168, 1977.

Natesan, K., T. F. Kassner, and Che-Yu Li, "Effect of Sodium on Mechanical Properties and Friction-Wear Behavior of LMFBR Materials" Reactor Technol. 15, 244, 1972.

National Institute for Materials Science Fatigue Data Sheet, 2002.

Nielsen, H.S. and V. Tvergaard, "Intergranular fracture under creep-fatigue interaction," International Journal of Damage Mechanics, Vol. 7, pp. 3-23, 1998.

Nippon Steel Cooperation, Japan.

NUREG-0968, Safety Evaluation Report Related to the Construction of Clinch River Breeder Reactor Plant, Nuclear Regulatory Commission, USNRC Report, vol. 1, Main Report, March 1983.

NUREG-1368, Preapplication Safety Evaluation Report for the Power Reactor Innovative Small Module (PRISM) Liquid-Metal Reactor, Nuclear Regulatory Commission, USNRC Report, February 1994.

Pawel, J. E. et al., "Irradiation performance of stainless steels for ITER application," J. Nucl. Mater. 239, 126-131, 1996.

Pizzo, P. P. and L. V. Hampton, Influence of Decarburization on the Mechanical Properties of Isothermally Annealed 2 1/4Cr-1Mo Steel, GEFR-00448, April 1980.

Powell, R.W., Superalloys in the Fast Breeder Reactor, HEDL-SA-811, January 1976.

Prager, M., "Long-Term Studies of Strength and Toughness of an Advanced Steel," Fitness-for-Service Evaluations in Petroleum and Fossil Power Plants, PVP-Vol. 380, ASME, pp. 291-299, 1998.

Program for the Development of Design Data LMFBR Steam Generator Materials, USDOE Rep. GEFR-00067-2, General Electric Company, Sunnyvale, CA, 1978.

Raj, R., "Mechanisms of creep-fatigue interaction," in Flow and Fracture at Elevated Temperatures, Ed. R. Raj, American Society for Metals, Metals Park, OH, pp. 215-249, 1985.

RCC-MR, French Design Code for Fast Reactors issued by AFCEN (French Society for Design and Construction Rules for Nuclear Island Components).

Rensman, J-W, NRG Irradiation Testing; Report on 300C and 6-C irradiated RAFM steels, NRG Petten (20023/05.68497.P) 2005.

Rensman, J., J van Hoepen, B.M. Bakker, R. den Boef, P van den Broek, and E.D.L. van Essen, J. Nucl. Mater. 307-311, Part 1, p. 1113, 2002.

Rensman, J., J. van Hoepen, J.B. M. Bakker, R. den Boef, F.P. van den Broek, and E.D. L. Van Essen, J. Nucl. Mater. 307-311, 245, 2002.

Riou, "DOE/ASME Materials Project, Task 3 Final Report: Improvement of ASME NH for Grade 91 (Creep-fatigue)," 2007.

Rowcliffe, A. F. and M. L. Grossbeck, "The response of austenitic steels to radiation damage," J. Nucl. Mater. 122 & 123, 181-190, 1984.

Sanderson, S. J. and S. Jacques, "Some Elevated Temperature Tensile and Strain-Controlled Fatigue Properties for 9%Cr1%Mo Steel Heat Treated to Simulate Thick Section Material," Proc. IAEA Specialist Meeting on Mechanical Properties of Structural Materials Including Environmental Effects, Report IWGFR-49, pp. 601-611, 1984.

Sannier, J., O. Konovaltschikoff, D. Leclercq, and R. Darras, "Compatibility of Ferritic Steels with Liquid Sodium at High Temperatures," Conf. on Effects of Environment on Materials Properties in Nuclear Systems, BNES, London, p. 155, 1971.

Sartory, W. K., "Assessment of damage accumulation rules based on thermal shock tests of cylinders," UKAEA/USDOE Structural Integrity Specialists Meeting, Oak Ridge National Laboratory, October 14-16, 1987.

Sawada, K., K. Kubo, F. Abe, Mater. Sci. Eng. A319-321, 784, 2001.

Schaffernak, B., P. Hofer, and H. Cerjak, in Materials for Advanced Power Engineering, eds. J. Lecomte-Beckers, F. Schubert, P. J. Ennis, Energy Technology Series, Volume 5, Part I, pp. 123-138, 1998.

Schneider, H-C., B. Dafferner, J. Aktaa, J. Nucl. Mater. 321, p. 135, 2003.

Schrock, S. L., S. A. Shiels, and C. Bagnall, "C and Nitrogen Transport in Sodium Systems," Proc. Intl. Conf. on Liquid Metal Technology in Energy Production, CONF-760503-P2, 809, 1976.

Schubert, J., "Determination of Weld Strength Factors for the Creep Rupture Strength of Welded Joints," ECCC Creep Conference, London, Sept 12-14, 2005.

Severd, "Creep-fatigue assessment methods using elastic analysis results and adjustments," Journal of Pressure Vessel Technology, Vol. 113, 1991.

Shiba, K., M. Suzuki, A. Hishinuma, J Nucl. Mater. 233-237, p. 30, 1996.

Shibli, I. A., Performance of P91 Thick Section Welds, OMMI 1, 2002.

Shiels, S. A., C. Bagnall, and S. L. Schrock, "Interstitial Mass Transfer in Sodium Systems," Proc. Symp. on Chemical Aspects of Corrosion and Mass Transfer in Liquid Sodium, Detroit, 157, 1971.

Shoichi, K., Y. Eiichi, and A. Kazumi, Technical Report, Japan Nuclear Cycle Development Institute, JNC-TN-9400-2001-025, 2001.

Sikka, V. K. "Effects of Thermal Aging on the Mechanical Properties of Type 316 Stainless Steel – Elevated-Temperature Properties," ORNL/TM-8371, Oak Ridge National Laboratory, Oak Ridge, TN, 1982.

Sikka, V. K., "Development of Modified 9Cr-1Mo Steel for Elevated-Temperature Service," Proc. Topical Conf. on Ferritic Alloys for Use in Nuclear Energy Technologies, The Metallurgical Society, Warrendale, PA, p. 317, 1984.

Sikka, V. K., "Elevated Temperature Ductility of Types 304 and 316 Stainless Steel," ORNL/TM/6608, 1978.

Sikka, V. K., Oak Ridge National Laboratory, unpublished research, 1980.

Sikka, V. K., C. R. Brinkman, and H. E. McCoy, Jr., "Effect of Thermal Aging on the Tensile and Creep Properties of types 304 and 316 Stainless Steels," pp. 316-50 in Structural Material for Service at Elevated Temperatures in Nuclear Power Generation, MPC-1, A. O. Schaffer, Ed., The American Society of Mechanical Engineers, New York, 1975.

Sikka, V.K., Ward CT, Thomas KC. Modified 9Cr-1Mo steel—an improved alloy for steam generator application. In: Ferritic Steels for High-Temperature Applications, Proceedings of the ASM International Conference on Production, Fabrication Properties, and Applications of Ferritic Steels for High Temperature Applications, Metals Park, Ohio, USA: American Society for Metals; pp. 65-84, 1983.

Smith, "Strain based creep-fatigue procedure developed in UK for fast reactor design," SG-ETD Meeting Minutes, September 1989.

Smith, C. V., "Elevated-Temperature Properties of Chromium-Molybdenum Steels," ASTM DS6, 1953.

- Smith, D. L., G. J. Zeman, K. Natesan, and T. F. Kassner, "Influence of Low-Cycle Fatigue Behavior of Type 304 and 316 Stainless Steels," Proc. Intl. Conf. Liquid Metal Technology in Energy Production, CONF- 760503-P1, 359, 1976.
- Smith, D. L., K. Natesan, T. F. Kassner, and G. J. Zeman, "Effects of Sodium on the Low-Cycle Fatigue Behavior of Austenitic Stainless Steels," ASME Symp. on Structural Materials for Service at Elevated Temperatures in Nuclear Power Generation, MPC-1, 290, 1975.
- Smith, G. V., "Evaluation of the Elevated Temperature Tensile and Creep-rupture Properties of 3 to 9 Percent Chromium-Molybdenum Steels," ASTM DS58, 1975.
- Snyder, R. B., K. Natesan, and T. F. Kassner, "A Generalized Method of Computing C-Diffusion Profiles in Austenitic Stainless Steels Exposed to a Sodium Environment," ANL-8015 (1973); also "Kinetics of Carburization-Decarburization Process of Austenitic Stainless Steels in Sodium," J. Nucl. Mater. 50, 259 (1974).
- Snyder, R. B., K. Natesan, and T. F. Kassner, "An Analysis of C Transport in the EBR-II and FFTF Primary Sodium Systems," Proc. Intl. Conf. on Liquid Metal Technology in Energy Production, CONF-760503-P2, 826, 1976.
- Sourmail, T. and H.K.D.H. Bhadeshia, Metall. Mater. Trans. A, 36A, 23, 2005.
- Spaeder, C. E. and K. G. Brickner, Advances in the Technology of Stainless Steels and Related Alloys, ASTM STP 369, p. 143, 1965.
- Spalaris, C., K. D. Challenger, D. Dutina, and P. Roy, "Sodium Heated Steam Generators: Near Term and Projected Information Needs--Ferritic Steels," Proc. Intl. Conf. on Ferritic Steels for Fast Reactor Steam Generators, BNES, London, p. 55, 1978.
- Spencer, B.H. and F.A. Garner, J. Nucl. Mater, 283-287, 164-168, 2000.
- Sponseller, B. L., N. Semchyshen, and P. J. Grobner, "Effect of Low C Contents and Exposures to Liquid Sodium on Elevated Temperature Behavior of 2¼ wt % Cr-1 wt % Mo Steel," Proc. Symp. on Low C and Stabilized 2¼% Cr-1% Mo Steels, American Society for Metals, Metals Park, Ohio, p. 73, 1973.
- Steichen, J. M., Mechanical Properties of FFTF Primary Outlet Piping, HEDL-TME 75-15, January 1975.
- Sugiura, R. et al., Eng. Fract. Mech. 74, 868, 2007.
- Suzuki, T. and I. Mutoh, J. Nucl. Mater. 149, 41, 1987.
- Swindeman, R. W., "Construction of isochronous stress-strain curves for 9Cr-1Mo-V steel," PVP Vol.391, Advances in Life Prediction Methodology, ASME, 1999.
- Swindeman, R.W., and P. Maziasz, "Evaluation of advanced austenitic alloys relative to alloy design criteria for steam service," ORNL-6629, Oak Ridge National Laboratory, Oak Ridge, TN p. 199, 1990.
- Tachibana, Y., "High Temperature Structural Design Guideline of the HTTR Metallic Components," Presented at the Generation IV International Forum, Oak Ridge, TN, 2005
- Taguchi, "Current Japanese approach to creep-fatigue evaluation of modified 9Cr 1Mo steel, SG-ETD Meeting Minutes, March 1995.
- Takahashi, "Practical use of inelastic analysis method in FBR design," EPRI/CRIEP Joint Study Report, 1987.
- Takahashi, Y., H. Shibamoto, K. Inoue, Nucl. Eng. De. 238, 322, 2008.
- Tas, H., F. Casteels, and M. Schirra, "Influence of Dynamic Sodium on the Creep Properties of Stabilized Austenitic Steels," Proc. Intl. Conf. on Liquid Metal Technology in Energy Production, CONF-760503-P1, pp. 346-352, 1976.

- Tavassoli, A. A., *Fus. Eng. Des.* 29, 371, 1995.
- Tavassoli, A. A., *J. Nucl. Mater.* 367-370, 1316, 2007.
- Tavassoli, A. F., "Present limits and improvements of structural materials for fusion reactors--a review," *J. Nucl. Mater.* 302, 73-88, 2002.
- Tavassoli, F., Potential and limits of materials and tools: present limits and improvements (EU Fusion Materials Assessment meeting), FZK-Karlsruhe, 2001.
- Thorley, A. and C. Tyzack, "The Carburization of Stainless Steels in Sodium Containing C Impurities and Its Effect on Mechanical Properties," *Proc. Intl. Conf. on Effects of Environment on Materials Properties in Nuclear Systems*, BNES, London, 143, 1971.
- Thorley, A., B. Longson, and J. Prescott, "Effect of Exposure to Sodium on the Mechanical Properties and Structure of Some Ferritic, Austenitic and High Nickel Alloys," TRG-Report-1909, 1970.
- Tomkins, B., "The Interpretation of Elevated Temperature Fatigue Data," presented at Intl. Conf. on Fatigue Testing and Design, London, 1976.
- Tsuchida, Y., Inoue, T., and Suzuki, T., "Creep Rupture Strength of V-modified 2 ¼ Cr-1Mo Steel," *IJPVP*, 81, pp. 191-197, 2004.
- Tyzack, C. and A. W. Thorley, "Review of Corrosion and C Transport Behavior of Ferritic Materials Exposed to Sodium," *Proc. Intl. Conf. on Ferritic Steels for Fast Reactor Steam Generators*, BNES, London, p. 241, 1978.
- Uehira, A., S. Mizuta, S. Ukai and R. J. Puigh, "Irradiation creep of 11Cr-0.5Mo-2W,V,Nb ferritic-martensitic, modified 316, and 15Cr-20Ni austenitic S.S. irradiated in FFTF to 103-206 dpa," *J. Nucl. Mater.* 283-287, 396-399, 2000.
- Ukai, S., S. Mizuta, T. Kaito, H. Okada, *J. Nucl. Mater.* 278, 320, 2000.
- United States Steel Corporation, *Steels for Elevated Temperature Service*, ADUSS 43-1089-D4, Pittsburgh, 1972.
- Van Leeuwen, M. P. and L. Schra, "Parametric Analysis of the Effects of Prolonged Thermal Exposure on Material Strength," pp. 134.1-134.9 in *Int. Conf. Creep and Fatigue in Elevated Temperature Applications*, Vol. 1, published by Mechanical Engineering Publications, Ltd., for the Institution of Mechanical Engineers, London, 1975.
- Van Osch E. V., M. G. Horsten, and M. I. de Vries, "Irradiation testing of 316L(N)-IG austenitic stainless steel for ITER," *J. Nucl. Mater.* 258-263, 301-307, 1998).
- Van Osch, E.V., et al., Fracture toughness PWR internals, contribution to CEC contract PWR internals – Part 2, ECN-report, ECN-I-97-010, Petten, 1997.
- Vitek, J. M., S. A. David, D. J. Alexander, J. R. Keiser, and R. K. Nanstad, "Low Temperature Aging Behavior of Type 308 Stainless Steel Weld Metal," *Acta Metall. Mater.*, vol. 39, No. 4, pp. 503-516, 1991.
- Vitek, J. M., W. R. Corwin, R. L. Klueh and J. R. Hawthorne, *J. Nucl. Mater.* 141-143, 948, 1986.
- Vlasak, T., J. Hakl, A. S. Svum, "Influence of weld joint in 2.25Cr-1Mo steel on long-term creep strength reduction," ECCO Creep Conference, London, Sept 12-14, 2005.
- Vyrostkova, A., V. Homolova, J. Pecha, M. Svoboda, *Mater Sci. Eng.A*, 2007.
- Waddington, J. S. and M. V. Speight, *Trans. ANS* 33, 310, 1979.

Wareing et al., "Failure criteria during elevated temperature creep-fatigue cyclic of austenitic stainless steel," SG-ETD Meeting Minutes, November 1985.

Wood, D. S., "The effect of creep on the high strain fatigue behavior of a pressure vessel steel," Welding Journal Research Supplement, pp. 90s-96s, 1966.

Wood, D. S., "Effects of a Sodium Environment on the Mechanical Properties of Ferritic Steels," Proc. Intl. Conf. on Ferritic Steels for Fast Reactor Steam Generators, BNES, London, p. 293, 1978.

Wood, D. S., "Materials Data for High Temperature Design," Proc. Conf. on the Experience of Structural Validation in the Nuclear Energy Industry with Emphasis on High Temperature Design, Institution of Mechanical Engineers, London, p. 23, 1979.

Wood, D. S., A. B. Baldwin, F. W. Grounds, J. Wynn, E. G. Wilson, and J. Wareing, "Mechanical Properties Data on 9% Cr Steel," Proc. Intl. Conf. on Ferritic Steels for Fast Reactor Steam Generators, BNES, London, p. 189, 1978.

Wood, D. S., G. F. Slattery, J. Wynn, M. O. Connaughton, and M. H. Lambert, "Preliminary Results of Effect of Environment on the Low Cycle Fatigue Behavior of Type 316 Stainless Steel and 9% Cr Ferritic Steel," Conf. on Influence of Environment on Fatigue, London, 1977.

Wozadlo, G. P., L. V. Hampton, and P. Roy, "Decarburization and Thermal Aging – their Effect Upon 2 1/4Cr-1Mo Steel Mechanical Properties," in Proc. Second Intl. Conf. on Liquid Metal Technology in Energy Production, CONF-800401, p. 2-1, 1980.

Yamamoto, M. and T. Ogata, "Microscopic damage mechanism of Ni-based superalloy Inconel 738LC under creep-fatigue conditions," Journal of Engineering Materials and Technology, pp. 315-320, 2000.

Yamamoto, T., G.R. Odette, H. Kishimoto, J-W Rensman, P Miao, J.Nucl.Mater. 356, 27-49, 2006.

Yamamoto, Y., M. P. Brady, Z. P. Lu, P. J. Maziasz, et al, Science 316, 433, 2007.

Yescas, M. A. and P. F. Morris, in Creep and Fracture in High Temperature Components – Design and Life Assessment, ECCC Creep Conference, September 2005.

Yuhara, S. and H. Atsumo, "Creep and Creep-Rupture Properties of 2 1/4Cr-1Mo Steel for a Fast Breeder Reactor in High-Temperature Sodium," Proc. Intl. Conf. on Ferritic Steels for Fast Reactor Steam Generators, BNES, London, p. 300, 1978.

Yukawa, S. "Review and Evaluation of the Toughness of Austenitic Steels and Nickel Alloys After Long-Term Elevated Temperature Exposures," Welding Research Council Bulletin 378, Welding Research Council, New York, NY, January 1993.

Yukitoshi, T., K. Yoshikawa, K. Tokimasa, T. Kudo, Y. Shida, and Y. Inaba, "Development of 9 Cr-2 Mo Steel for Fast Breeder Reactor Steam Generators," Proc. Intl. Conf. on Ferritic Steels for Fast Reactor Steam Generators, BNES, London, p. 87, 1978.

Zeisloft, R. H., W. E. Leyda, and H. A. Domian, "Low C 2 1/4Cr-1Mo Steels," Proc. Symp. on Low C and Stabilized 2 1/4% Cr-1% Mo Steels, American Society for Metals, Metals Park, Ohio, p. 37, 1973.

Zeman, G. J. and D. L. Smith, "Low Cycle Fatigue Behavior of Type 304 and 316 Stainless Steels Tested in Sodium at 550°C," Nucl. Technol. 42, 82, 1979.

Zinkle, S. J., P. J. Maziasz, and R. E. Stoller, "Dose dependence of the microstructural evolution in neutron-irradiated austenitic stainless steel," J. Nucl. Mater. 206, 266-286, 1993.

Zinkle, S.J., L.J. Ott, D.T. Ingersoll, R.J. Ellis, and M.L. Grossbeck, "Overview of Materials Technology for Space Nuclear Power and Propulsion," Space Technology and Applications International Forum-STAIF 2002, Vol. 608, p. 1063, Melville, NY, USA, 2002.



Nuclear Engineering Division

Argonne National Laboratory
9700 South Cass Avenue, Bldg. 212
Argonne, IL 60439-4838

www.anl.gov



Argonne National Laboratory is a U.S. Department of Energy
laboratory managed by UChicago Argonne, LLC